GFZ

Helmholtz Centre POTSDAM

Hanbing Peng

Precise orbit determination of BDS-3 with inter-satellite links

Scientific Technical Report STR23/03

HELMHOLTZ
RESEARCH FOR GRAND CHALLENGES

Precise Orbit Determination of BDS-3 with Inter-Satellite Links

vorgelegt von

M. Sc.

Hanbing Peng

ORCID: 0009-0004-4236-0175

an der Fakultät VI - Planen Bauen Umwelt

der Technischen Universität Berlin

zur Erlangung des akademischen Grades

Doktor der Ingenieurwissenschaften

- Dr.-Ing. -

genehmigte Dissertation

Promotionsausschuss:

Vorsitzender: Prof. Dr. Dr. Frank Flechtner

Gutachter: Prof. Dr. Dr. h.c. Harald Schuh

Gutachter: Prof. Dr. Christoph Günther

Gutachter: Prof. Dr. Maorong Ge

Tag der wissenschaftlichen Aussprache: 23. Februar 2023

Berlin 2023

Acknowledgment

Abstract

BeiDou Navigation Satellite System (BDS), the Chinese component of Global Navigation Satellite Systems (GNSS), has come into operation and started to serve global users publicly since July 31, 2020. BDS-3, i.e., the latest development of BDS, provides many services not only the traditional Position, Navigation and Timing (PNT) but also several featured ones such as Satellite-Based Augmentation Service (SBAS), Precision Point Positioning (PPP), Short Message Communication Service (SMCS) and Search And Rescue (SAR). Precise and accurate orbit and clock products are the prerequisites of a GNSS to guarantee a high-quality service performance. BDS-3 is the first GNSS in which the Inter-Satellite-Link has been constellation-widely deployed. It has been preliminarily demonstrated that this new feature of BDS-3 improves the system's survivability as well as its independence on the ground tracking. This study is devoted to the Precise Orbit Determination (POD) of BDS-3 with newly available ISL observations.

The inherent incapability of ISL measurements of sensing the absolute variations of Right Ascension of the Ascending Nodes (RAANs) of satellite orbits hinders the autonomous orbit determination free from ground support. Different approaches to constrain the constellation rotation have been studied in the literature. On the other hand, orbit determination using only ISL observations can serve to evaluate the performance of the newly carried Inter-Satellite-Link payloads. Depending on the satellite, the post-fit RMS of ISL range observations is 4.2~10.5 cm. Eliminating the effects of constellation rotations, orbit precision based on ISL range observations is around 7.0, 4.6, and 3.5 cm in the along-track, cross-track, and radial direction, respectively. The clock observations of ISLs are used to synchronize the clocks of satellites within the constellation. The post-fit RMS of ISL clock observations ranges from ~2.9 cm to 10.0 cm, differing for satellites. For most satellites, similar precision of clock offsets as the IGS MGEX ACs' products can be obtained by ISL measurements, with STDs around 0.15 ~ 0.20 ns. Hardware delays of Inter-Satellite-Links estimated from the range and clock observations both show very good temporal stability, with a monthly average STD of 0.13 and 0.08 ns, respectively. Harmonic signals taking the orbit motion as the fundamental frequency are found in both the range and clock residuals. Although it turns out those harmonic signals only affect the results marginally, a Fourier-like periodic function model is proposed to absorb them and has been proved effective.

Several unresolved issues related to the POD of BDS-3 are investigated based on ground tracking data before studying the contributions of additional ISL observations. The effects of non-conservative perturbations from the Earth's albedo and antenna thrust are significant and, therefore, need to be considered in the POD of BDS-3. The applicability of different empirical Solar Radiation Pressure (SRP) models and the necessity of an extra a-priori box-wing model are evaluated. Generally, the ECOM2 model shows superiority over the ECOM1 model as for BDS-3 satellites. And if the ECOM2 model is adopted,

the additional a-priori box-wing model is unnecessary. In order to keep the backward compatibility of BDS-2, the strategy for integrated processing of BDS-2 and BDS-3, in which the legacy frequency combination B1I+B2I remains unchanged for BDS-2, is proposed and demonstrated.

The contributions of incorporating ISL observations to the POD of BDS-3 are assessed comprehensively. First, the benefits of additional ISL range measurements are demonstrated in cases of different ground tracking networks. Secondly, the somehow unexpected improvement in the orbit precision brought by incorporating ISL clock observations is displayed. Furthermore, integratedly processing the ISL derived range, ISL derived clock, and L-band ground tracking observations reduces the orbit DBD by ~39% and 42% in the along-track and radial directions, respectively, compared to using only ground-tracking data. Last but not least, the contributions of ISL measurements to the estimation of geodetic parameters are proved, especially for the geocenter coordinates. Strong correlations between empirical SRP parameters and the geocenter Z-component, which plague the community for a long time, are significantly reduced by adding ISL observations. The results are very promising not just in terms of establishing and maintaining a national BDS-based terrestrial reference frame but also improving the potential contribution of BDS via the IGS community to the International Terrestrial Reference Frame (ITRF).

Zusammenfassung

Das BeiDou Navigation Satellite System (BDS), die chinesische Komponente von Global Navigation Satellite Systems (GNSS), ist seit dem 31. Juli 2020 in Betrieb und dient weltweit Benutzern öffentlich. BDS-3, dh die neueste Entwicklung von BDS, bietet viele Dienste, nicht nur die traditionelle Position, Navigation und Zeitmessung (PNT), sondern auch mehrere Funktionen wie der satellitengestützte Augmentation Service (SBAS), Precision Point Positioning (PPP), Short Message Communication Service (SMCS) und Search And Rescue (SAR). Präzise und genaue Orbit- und Clock-Produkte sind die Voraussetzungen für ein GNSS, um eine qualitativ hochwertige Serviceleistung zu gewährleisten. BDS-3 ist das erste GNSS, bei dem der Inter-Satellite-Link konstellationsweit eingesetzt wurde. Es wurde vorläufig gezeigt, dass diese neue Funktion von BDS-3 die Überlebensfähigkeit des Systems sowie seine Unabhängigkeit von der Bodenverfolgung verbessert. Diese Studie widmet sich der Precise Orbit Determination (POD) von BDS-3 mit neu verfügbaren ISL-Beobachtungen.

Die inhärente Unfähigkeit von ISL-Messungen, die absoluten Variationen der Right Ascension of the Ascending Nodes (RAANs) von Satellitenumlaufbahnen zu erfassen, behindert die autonome Umlaufbahnbestimmung ohne Bodenunterstützung. In der Literatur wurden verschiedene Ansätze untersucht, um die Konstellationsrotation einzuschränken. Andererseits kann die Bestimmung der Umlaufbahn, die nur ISL-Beobachtungen verwendet, dazu dienen, die Leistung der neu beförderten Inter-Satellite-Link-Nutzlasten zu bewerten. Abhängig vom Satelliten beträgt der Post-Fit-RMS der ISL-Bereichsbeobachtungen 4,2 bis 10,5 cm. Unter Eliminierung der Auswirkungen von Konstellationsrotationen beträgt die Orbit-Präzision basierend auf ISL-Entfernungsbeobachtungen etwa 7,0, 4,6 bzw. 3,5 cm in Längs-, Quer- und Radialrichtung. Die Uhrenbeobachtungen von ISLs werden verwendet, um die Uhren von Satelliten innerhalb der Konstellation zu synchronisieren. Der Post-Fit-RMS von ISL-Uhrbeobachtungen reicht von ~2,9 cm bis 10,0 cm, unterschiedlich für Satelliten. Bei den meisten Satelliten kann durch ISL-Messungen eine ähnliche Genauigkeit der Taktverschiebungen wie bei den Produkten der IGS MGEX ACs mit STDs von etwa 0,15 bis 0,20 ns erreicht werden. Hardwareverzögerungen von Inter-Satellite-Links, die aus den Entfernungs- und Taktbeobachtungen geschätzt wurden, zeigen beide eine sehr gute zeitliche Stabilität mit einer monatlichen durchschnittlichen STD von 0,13 bzw. 0,08 ns. Harmonische Signale, die die Bahnbewegung als Grundfrequenz nehmen, werden sowohl in den Entfernungs- als auch in den Taktresten gefunden. Obwohl sich herausstellt, dass diese harmonischen Signale die Ergebnisse nur marginal beeinflussen, wird ein Fourier-ähnliches periodisches Funktionsmodell vorgeschlagen, um sie zu absorbieren und sich als effektiv erwiesen hat.

Mehrere ungelöste Probleme im Zusammenhang mit dem POD von BDS-3 werden auf der Grundlage von Bodenverfolgungsdaten untersucht, bevor die Beiträge zusätzlicher ISL-Beobachtungen untersucht

werden. Die Auswirkungen nicht-konservativer Störungen durch die Albedo der Erde und den Antennenschub sind signifikant und müssen daher im POD von BDS-3 berücksichtigt werden. Die Anwendbarkeit verschiedener empirischer Solar Radiation Pressure (SRP)-Modelle und die Notwendigkeit eines zusätzlichen a-priori-Box-Wing-Modells werden evaluiert. Im Allgemeinen zeigt das ECOM2-Modell eine Überlegenheit gegenüber dem ECOM1-Modell für BDS-3-Satelliten. Und wenn das ECOM2-Modell übernommen wird, ist das zusätzliche A-priori-Box-Wing-Modell überflüssig. Um die Abwärtskompatibilität von BDS-2 zu erhalten, wird die Strategie zur integrierten Verarbeitung von BDS-2 und BDS-3 vorgeschlagen und demonstriert, bei der die Legacy-Frequenzkombination B1I+B2I für BDS-2 unverändert bleibt.

Die Beiträge der Einbeziehung von ISL-Beobachtungen in den POD von BDS-3 werden umfassend bewertet. Zunächst werden die Vorteile zusätzlicher ISL-Entfernungsmessungen bei unterschiedlichen Bodenverfolgungsnetzwerken demonstriert. Zweitens wird die irgendwie unerwartete Verbesserung der Bahngenauigkeit durch die Einbeziehung von ISL-Uhrenbeobachtungen angezeigt. Darüber hinaus reduziert die integrierte Verarbeitung der ISL-abgeleiteten Entfernung, des ISL-abgeleiteten Takts und der L-Band-Bodenverfolgungsbeobachtungen die Bahn-DBD um ~39 % bzw . Nicht zuletzt werden die Beiträge von ISL-Messungen zur Schätzung geodätischer Parameter, insbesondere für die Geozentrumskoordinaten, nachgewiesen. Starke Korrelationen zwischen empirischen SRP-Parametern und der Geozentrum-Z-Komponente, die die Community schon lange plagen, werden durch das Hinzufügen von ISL-Beobachtungen deutlich reduziert. Die Ergebnisse sind nicht nur im Hinblick auf die Einrichtung und Aufrechterhaltung eines nationalen BDS-basierten terrestrischen Referenzrahmens sehr vielversprechend, sondern auch hinsichtlich der Verbesserung des potenziellen Beitrags von BDS über die IGS-Community zum International Terrestrial Reference Frame (ITRF).

Table of Contents

List of Figures

List of Tables

1 Introduction

1.1 Motivation

The development of the new generation of BeiDou Navigation Satellite System, i.e., the BDS-3, was completed on July 31, 2020. Besides many featured services compared to other GNSSs, the new payloads, Ka-band Inter-Satellite-Links, are firstly deployed to the entire constellation. With the capability of high bandwidth communication, satellites connected by Ka-band ISLs can exchange data timely among the whole constellation. Not limited by the coverage of the ground network, operational directives from the Operational Control System (OCS) can be uplinked to any specific satellite. The controllability of the space segment of BDS-3 is greatly improved. Ephemerides calculated in the OCS can also be updated promptly to all satellites in the constellation via the relaying through ISLs. The Issue Of Data (IOD) of the system can be shortened and guaranteed.

Another important functionality of Inter-Satellite-Links is the precise ranging between satellites. The quality of ephemerides determines the service performance of a GNSS. Without ISLs, ephemeris quality, in turn, depends to a large extent on the tracking coverage of the OCS ground network. The regionally distributed ground network of BDS compromised its global service performance, although services for the core area could be provided with high quality. By the ranging measurements of ISLs, autonomous ephemeris improvement can be realized. Once the necessary a priori information is uplinked to the constellation, the global nominal service performance of the system can be maintained for a long period without intense contact with the OCS. This not only alleviates the operation burden of the OCS but also eases the vulnerability of the system, which is particularly crucial for a strategic infrastructure like GNSS.

The conception of ISL was first proposed for the GPS in the 1980s and admired by subsequent GNSSs. However, BDS is the first GNSS that deploys the Inter-Satellite-Links constellation-wide. Many studies based on the real ISL data of BDS-3 have been published to validate the fulfillment of designed missions. Results prove the successfulness of this newly deployed GNSS payload. However, most of those researches are focused only on the enhancement of ISLs on the basic service performance of BDS or availability improvement of the system under unfavorable conditions. In fact, the ISLs could also benefit the system's services provided for applications requiring higher quality ephemerides. Moreover, because of the increased rigidity of the constellation brought by ISLs, errors imperceivable to legacy GNSS

L-band observations might expose. Compensating for the inherent weakness of L-band measurements, additional ISLs might extend the role of GNSS played in fundamental geodetic applications. Those aforementioned advantages of ISLs from BDS-3 are seldom addressed yet so far, which constitutes the motivations of this study.

1.2 Outline

The study, focusing on the precise orbit determination of BDS-3 using ISL observations, is briefly outlined as follows.

In the next chapter, the development history of BDS is shortly reviewed, followed by a thorough introduction of the current status of BDS, i.e., mainly the BDS-3, as to its different components. Emphasis is placed on the new payload of BDS-3, i.e., the Inter-Satellite-Link, including the ranging system, modelling of the original dual one-way pseudoranges, and the errors that affect the ISL measurements. The pre-processing to obtain the usually used derivation observations, which are also used in this study, is also introduced. Detailed mathematical models are presented with certain error analysis based on simulations. At the end of this chapter, several aspects related to the numerous numerical experiments shown in this study are briefed, such as the datasets, processing strategies, and evaluation approaches for the results.

In Chapter 3, orbit determination using only ISL range observations is investigated. First, the mathematical background of the unobservability of orbital elements is given. Then, comprehensive analyses are dedicated to the orbit determination results. Because of the lack of datum, precise satellite orbits within the Earth-Centered Earth-fixed coordinate system (ECEF) cannot be obtained, relying solely on the ISL measurements. However, the performance of ISLs of BDS-3 can be exhaustively examined through the free network adjustments. Characteristics of the residuals of ISL derived range observations of BDS-3 are analyzed. The orbit quality is assessed after eliminating the effect of the constellation rotation via Helmert transformations. The close relationship between the Z-axis rotation of the constellation and the changes of Right Ascension of the Ascending Nodes of satellite orbits is clearly revealed. Effects of hardware delays of Inter-Satellite-Links in the range observations are estimated. In addition, to cope with the harmonic signals found in the link residuals, a Fourier-like periodic function model is proposed to absorb those signals. The effectiveness of this model is assessed in different aspects.

Chapter 4 is devoted to time synchronization among satellites within the constellation using

ISL clock observations. After introducing the modelling of satellite clocks, clock estimation results using the ISL derived clock measurements of BDS-3 are detailedly inspected. The residuals of clock observations are presented. Estimates of clock offsets and rates are evaluated. Hardware delays of the Inter-Satellite-Links in the clock observations, which can be obtained by differencing the clock offsets with a reference solution from L-band observations, are calculated. The stability of those hardware delays is also presented. The periodic function model proposed in Chapter 3 is similarly employed to assimilate the harmonic signals existing in the ISL clock observations. The feasibility evaluation of the model for ISL clock observations is given.

In Chapter 5, several critical issues of BDS-3 orbit determination are settled based on ground tracking measurements before proceeding with the contribution of ISLs to the orbit determination. The significance of the effects of several non-conservative perturbations, such as the Earth's albedo and antenna thrust, is checked. Additionally, the applicability of different empirical Solar Radiation Pressure (SRP) models for BDS-3 satellites is compared through orbit determinations results. An innovative way to employ empirical SRP models, which takes the difference in suitability to satellites into account, is proposed. Effects of a priori SRP based on box-wing models in the orbit modelling of BDS-3 satellites are also evaluated. As the open service frequencies of BDS-3 have been changed in respect to BDS-2, the concern of backward compatibility of the system is addressed. The frequency choice for BDS-2 in the integrated processing of BDS-2+BDS-3 during the transition phase is extensively discussed. Receiver biases between BDS-2 and BDS-3 are also presented.

Chapter 6 is dedicated to analyzing and demonstrating the contributions of additional ISL observations to the orbit determination of BDS-3 satellites. First, the contribution of ISL derived range observations is studied in the cases of different ground tracking networks. Secondly, the benefit from ISL clock observations to the orbit improvement is explored. Before those investigations, impacts of harmonic signals in ISL observations are demonstrated along with the discussion of weight allocations. Finally, both the derived range and clock observations are integratedly processed with ground tracking data to research the augmentation brought by ISLs. Besides satellite orbits, the contribution of ISL observations to the estimation of geodetic parameters, such as Earth Rotation Parameters (ERPs), geocenter coordinates, and the network scale, are also underscored.

At last, some most important findings from this study are summarized in Chapter 7, together with a concise outlook for the research work in the short future.

2 The BeiDou Navigation Satellite System

2.1 Overview and Current Status

2.1.1 Overview

The building of the Chinese BeiDou Navigation Satellite System (BDS[1]) was initiated in the 1980s. A long-term development plan consisting of three steps has been clearly stated as the system expands. As the first step, a demonstration system comprising two Geostationary Earth Orbit (GEO) satellites[2] was built between 1994 and 2000. Two more GEO satellites[3] were launched as complementary or backup to the system in 2003 and 2007. The demonstration system was formerly called BeiDou-1 but is now more commonly abbreviated as BDS-1. The establishment of BDS-1 made China the third country possessing an independent satellite navigation system except for the United States and Russia. Services provided by BDS-1 included the Radio Determination Satellite Services (RDSS)(Rothblatt 1987), the Wide-Area Differential Services (WADS), the location report, and the Short Message Communication (SMC). The RDSSs of BDS-1, different from the Radio Navigation Satellite Service[4] (RNSS)(Matas 2011) provided by its successors, were active positioning and timing services. As GEO satellites have been normally used as communication platforms in space, featured services like SMC were inherently integrated into BDS-1. Services provided by BDS-1 were only available to China and its limited surrounding areas.

The second step was to construct a regional navigation satellite system (BDS-2), which started in 2004. The first BDS-2 satellite, well-known as the COMPASS-M1, was successfully put into the Medium Earth Orbit (MEO) on 14th April 2007 (UTC+8). The launch of COMPASS-M1 was mainly to provide a testbed for validations of hardware and technical solutions, such as domestic space-borne atomic clocks, realizations of precise orbit determination, and time synchronization. It also preserved the usage priority of radio frequencies, as the ITU (International Telecommunication Union) requires on-orbit broadcasting in allocated

---

[1] formerly named after the COMPASS, which was widely used in ancient China for navigation

[2] BeiDou-1A (COSPAR 2000-069A, launched on 2000/10/31 UTC+8) and BeiDou-1B (COSPAR 2000-082A, launched on 2000/12/21 UTC+8)

[3] BeiDou-1C (COSPAR 2003-021A, launched on 2003/05/25 UTC+8) and BeiDou-1D (COSPAR 2007-003A, launched on 2007/02/03 UTC+8)

[4] defined as Article 1.43 in the ITU Radio Regulations (Edition of 2020)

frequencies within a limited period. Except for GEOs used in BDS-1, Inclined Geosynchronous Orbit (IGSO) satellites are also included in BDS-2. The operational service of BDS-2 comprising 14 satellites, i.e., 5 GEOs+5 IGSOs+4 MEOs, was officially declared by the China Satellite Navigation Office (CSNO) on 27th December 2012. After that, another four BDS-2 satellites (two IGSOs and two GEOs) were launched for replacement and backup. Along with the legacy RDSS, the RNSS, which enables users to determine their positions, velocities, and times passively (i.e., the PNT service), is provided by BDS-2. Featured services such as the location report and SMC are also kept in BDS-2. The core service region has been extended to cover the most area within 55° S~55° N and 70° E~150° E[5] (CSNO 2013a).

A Global Navigation Satellite System (GNSS) is the target of the third step of BDS (BDS-3). The space segment of BDS-3 is designed to include five GEO, three IGSO, and 27 MEO satellites. Before deploying operational satellites, five BDS-3 experimental satellites were launched during 2015~2016. By those experimental satellites, tests on newly designed signals, indigenous onboard atomic clocks and CPUs[6], and new payloads, e.g., inter-satellite-links, have been intensively conducted. The BDS-3 basic system, including 1 GEO and 18 MEO satellites, was established and put into service on 27th December 2018. With additional 11 satellites, the worldwide operational service of BDS-3 was officially released on 31st July 2020. Besides the traditional PNT service, diverse featured functions are also provided by BDS-3, such as Ground Augmentation System (GAS), Precise Point Positioning (PPP), and Search And Rescue (SAR). The service region of SMC is also extended from regional in BDS-1 or BDS-2 (RSMC) to global in BDS-3 (GSMC) (CSNO 2021).

2.1.2 Current Status

2.1.2.1 Constellation

Up to December 2021, there are 46 operational BDS satellites in space, including 16 BDS-2 and 30 BDS-3 satellites. The BDS-2 constellation consists of six GEO, seven IGSO, and three MEO satellites, while the BDS-3 is composed of three GEO, three IGSO, and 24 MEO satellites. Full lists of BDS-2 and BDS-3 operational constellations as of December 2021 can be found in Appendix A.

---

[5] includes most of the Asia-Pacific region though the term itself does not have a clear-cut definition yet

[6] on SVN C101 (BDS-3S IGSO-1S or BDS-3 I1S, launched on 2015/03/30 UTC+8), two Loongson 1E and four Loongson 1F CPUs are carried. See http://news.sciencenet.cn/htmlnews/2015/4/317313.shtm (in Chinese), last accessed on 2021/11/24

All BDS satellites are equipped with Laser Retroreflector Arrays (LRA), designed by the Shanghai Astronomical Observatory (SHAO) of the Chinese Academy of Sciences (Zhang et al. 2014) for Satellite Laser Ranging (SLR). Except for precise orbit determination, SLR measurements are also used in assisting the time comparison between satellites and ground stations (i.e., Laser Time Transfer) (Meng et al. 2013) and validating orbits calculated based on L-band observations.

All BDS-1 and BDS-2 satellites were manufactured by the China Academy of Space Technology (CAST), affiliated with the China Aerospace Science and Technology Corporation (CASC). Starting with the experimental satellites, the second manufacturer is awarded the contract for fabricating BDS-3 satellites, i.e., the Shanghai Engineering Center for Microsatellites (SECM)[7].

Domestic atomic clocks onboard BDS satellites are made by CASC, the China Aerospace Science and Industry Corporation (CASIC), and SHAO. Four clocks based on Rubidium Atomic Frequency Standards (RAFSs) are carried onboard each BDS-2 satellite, one active, one hot backup, and two cold backups. The Passive Hydrogen Maser (PHM), fabricated by SHAO, was first tested on SVN C104, a BDS-3 experimental satellite. It is an IGSO satellite and was launched on September 30th, 2015[8]. Onboard BDS-3 operational satellites, both RAFS and PHM clocks are deployed (Pan et al. 2021).

The six BDS-2 GEO satellites are located at 58.75° E, 84° E, 110.5° E, 140° E, and 160° E, respectively, with an altitude of 35786 km above the Earth's equator. The three BDS-3 GEO satellites are located at 80° E, 110.5° E, and 140° E. An important role of GEO satellites since the BDS-1 is broadcasting augmentation and integrity information for signals of BDS as well as other GNSS, i.e., providing the WADS. Including the ground monitoring stations, control center, and the services, the WADS of BDS is generally called the BeiDou Satellite-Based Augmentation System (BDSBAS).

The seven BDS-2 IGSO satellites with an inclination of 55° are distributed on three planes. The geographic longitudes of the ascending nodes of the three IGSO satellites on the first plane are 95° E, 112° E, and 118° E. The geographic longitudes of the ascending nodes of the two IGSO satellites on the second plane are 95° E and 118° E. The geographic longitudes of the ascending nodes of the two IGSO satellites on the third plane are 95° E and 118° E (CSNO 2018a).

---

[7] renamed as Innovation Academy for Microsatellites of the Chinese Academy of Sciences (IAMCAS) since September 2017, http://www.microsate.com/

[8] http://www.beidou.gov.cn/yw/xwzx/lsxw/xwzx2015/201710/t20171010_1063.html (in Chinese), last accessed on 2021/11/23

The 24 MEO satellites of BDS-3 are deployed as a typical Walker Delta 55°: 24/3/1 constellation (Walker 1984; Yang et al. 2017c) at 21528 km above the Earth. A schematic diagram of the current BDS-3 MEO constellation is displayed in Figure 2.1.
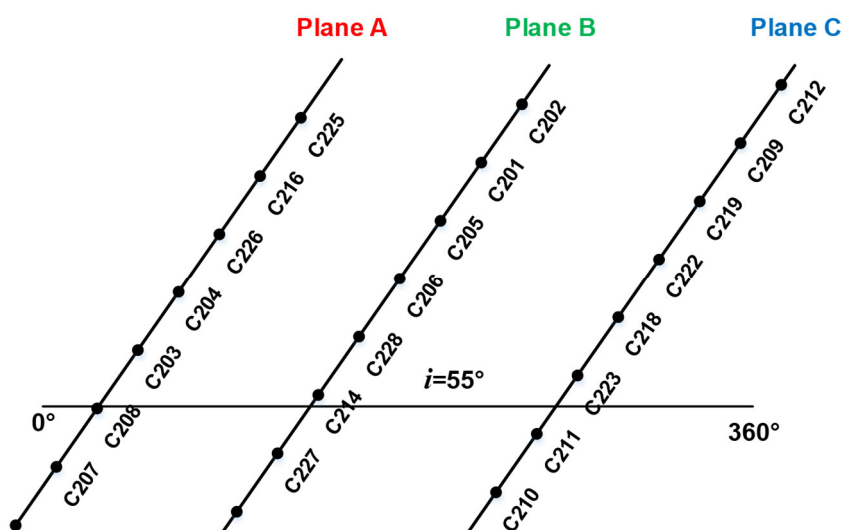
Figure 2.1 A schematic diagram of the current operational BDS-3 MEO constellation[9]

Perturbations of on-orbit satellites are closely related to the orbit planes. Orientations of orbit planes determine the variation of relative geometry between satellites and the Sun, which is currently the main perturbation source of GNSS satellites. Based on a calculation of orbits spanning the year 2019~2020, it is found that, among IGSO satellites, SVN C005, C009, C019, and C221 orbit on the same plane while SVN C008, C017, and C220 share another plane. Also, SVN C007 and C010 orbit together on a third IGSO plane. As for the BDS-3 IGSO satellite, SVN C224, its orbit plane is very similar to C007 and C010 while showing a small but distinct difference. For BDS-2 MEOs, SVN C012 and C013 are on Plane A[10] while C015 on Plane B[11] of the BDS-3 MEO constellation. Figure 2.2 displays the variations of Sun elevations above the orbit planes of several BDS satellites over the year 2019~2020. For satellites on the same orbit plane, the Sun's illumination changes during one solar cycle are basically the same. The period of this solar cycle, i.e., the revisit cycle of the Sun with respect to the orbit plane, is usually called the draconitic year.

---

[9] Until December 2021

[10] between slots A-6 and A-7, A-7 and A-8 for SVN C012 and SVN C013, respectively, according to https://igs.org/mgex/constellations/#beidou, last accessed on 2021/11/21

[11] between slots B-3 and B-4 for SVN C015, according to https://igs.org/mgex/constellations/#beidou, last accessed on 2021/11/21
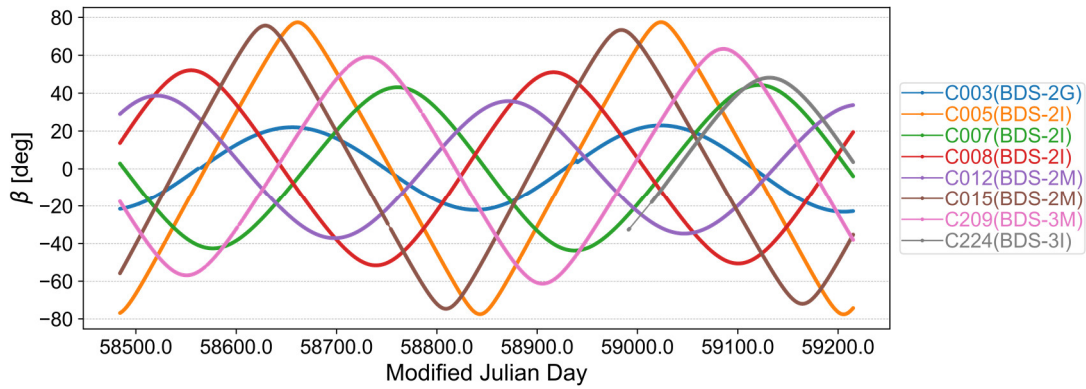
Figure 2.2 Sun elevation variations with respect to the orbit planes of several BDS satellites over the year 2019~2020

Yaw attitude control models of SVN C005 (BDS-2I PRN C06), C015 (BDS-2M PRN C14) and C017 (BDS-2I PRN C13) have been changed from the traditional YS/ON to a Galileo-like model, which is very similar to that of BDS-3 satellites.

2.1.2.2 Signals in Space

Initially, only the in-phase signals on frequencies B1 and B2 (i.e., B1I and B2I) (CSNO 2016) were assigned as the open service signals of BDS-2. The quadrature components on B1 and B2, as well as both the in-phase and quadrature components on B3, were reserved for the authorized service. Nevertheless, some researchers managed to decode some properties of the non-public B3I signal via measurements from high-gain antenna dishes(Grelier et al. 2007; Gao et al. 2009). Since the official release of the Interface Control Document (ICD) of the B3I signal in February of 2018 (CSNO 2018b), BDS-2 became the first GNSS providing public triple-frequency service signals on the whole system. Many studies have been devoted to exploring the benefits of a third GNSS open service signal (Tang et al. 2014; Teunissen et al. 2014; Li et al. 2015; Li et al. 2017; Li 2018).

New and advanced signal structure designs of BDS-3 not only improve the performance but also benefit compatibility and interoperability with other GNSS. Services signals of BDS are summarized in Appendix A. However, it should be mentioned that the architecture of signals of operational BDS-3 might not be exactly the same as the experimental satellites[12].

---

[12] http://www.csno-tarc.cn/en/system/constellation, last accessed on 2021/11/21

2.1.2.3 Ground Tracking Network

The Operation Control System (OCS) of BDS-2 consists of one master control station, 29 monitoring stations, and two time synchronization/uploading stations. Seven Type-A monitoring stations mainly provide measurements for orbits and ionospheric delays calculation. The 22 Type-B monitoring stations are used to generate augmentation and integrity information (Yang et al. 2017c).
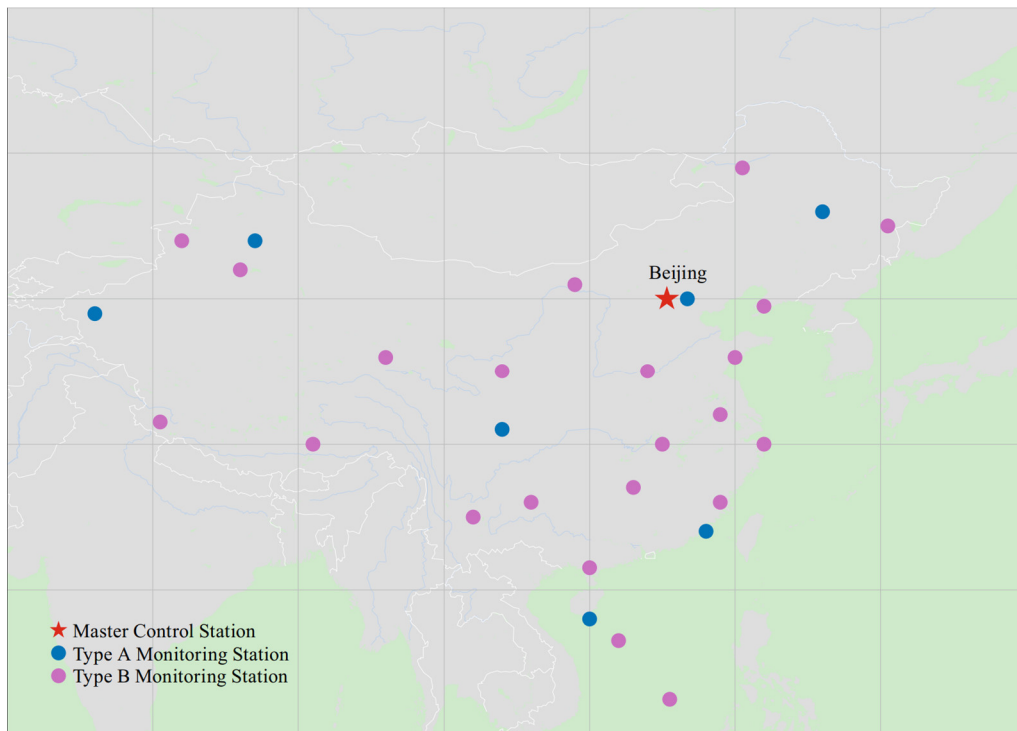
Figure 2.3 Master Control and Monitoring Stations of BDS-2 (Yang et al. 2017c)

The regional network limited to the territory can only provide less than 50% tracking coverage for BDS-2 MEOs (Zhou et al. 2012; Zhou et al. 2013).

In preparation for the 3rd International GNSS Service (IGS) reprocessing (repro3), i.e., the next IGS contribution to the ITRF 2020, many multi-GNSS antenna calibrations were released by IGS. Though BDS was not incorporated into the repro3, many antenna+radome combinations were also calibrated for BDS signals (See Table D-1 in Appendix D). For example, within a global network consisting of 151 stations that can track BDS-3 with B1I+B3I signals, 101 stations from 17 antenna+radome combinations have calibrations in the antenna file igsR3_2077.atx on DOY 335, 2019 (See Table D-2 in Appendix D). There are mainly two techniques for calibration, i.e., chamber and robot. (Villiger et al. 2020) compared the PCO up-components referring IF combination for GPS L1/L2, GLONASS L1/L2, and

Galileo E1/E5 obtained from those two calibration methods and found that, on average, the PCOs are consistent within 1 mm. However, for individual antenna types, the difference may reach up to 7 mm.

In the IGS antenna files, calibrations of only a small portion of BDS capable antenna+radome combinations are included (See Table D-3 in Appendix D). Without calibrated antenna offsets for ground stations, calibrations from GPS L1 and L2 are used for BDS B1 and B2/B3, respectively. Based on the comparisons of ionosphere-free (IF) linear combination PCOs of GPS L1+L2 with BDS B1+B3, an average and maximum difference of 9 and 34 mm can be found in the vertical direction (See Table D-4 in Appendix D).

2.2 Inter-Satellite Link

To improve the survivability of GPS in hostile environments or even high altitude nuclear bursts, the so-called Autonomous Navigation (AutoNav) capability was proposed and motivated. It required that the navigation accuracy, i.e., a User Range Error (URE) of 6 m, could be maintained for six months without any ground contact (Menn 1986; Ananda et al. 1990; Bernstein et al. 1993; Menn and Bernstein 1994). The AutoNav of GPS was realized via the Ultra High Frequency (UHF[13]) cross-link, which served the missions of inter-satellite ranging and communication. The UHF cross-link is a Time Division Multiple Access (TDMA) frequency-hopped data link. Initially, it was mainly designed for exchanging detected nuclear burst information between GPS satellites, which would be further disseminated on the 1381.05 MHz L_3 downlink. A modification to the Radio Frequency Data Unit (RFDU) was examined. It was evaluated to be able to provide one-way single frequency measurements with a 12 ns one-sigma uncertainty (Codik 1985). The AutoNav mode is not available in any current GPS satellites, nor will it be operational in the initial GPS IIIF SVs.[14]

One of the key payloads carried by BDS-3 experimental satellites is the inter-satellite-link[15]. The inter-satellite-link of BDS-3 utilizes the Ka-band[16] radio signal. The Ka-band is a portion of the microwave (300 MHz ~ 300 GHz) of the electromagnetic spectrum, the frequency range of which is 26.5~40 GHz. Correspondingly, the wavelength ranges from 7.5 ~ 11.3 mm.

---

[13] the ITU designation for radio frequency in the range 300 ~ 3000 MHz. See Recommendation ITU-R V.431-8 (08/2015).

[14] Refer to the minutes of the Public Interface Control Working Group and Open Forum published by the GPS Directorate in November 2019, https://www.gps.gov/technical/icwg/meetings/2019/09/minutes.pdf, last accessed on 2021/12/09. The specific section 6.3.5 for AutoNav in the GPS ICD IS-GPS-200M has been changed to <RESERVED>.

[15] To discriminate between the instrument and ranging or communication path, unless at the beginning of a sentence, only the latter is abbreviated in this study.

[16] i.e., Kurz-above band. It is an IEEE letter-band designation. The frequency range of the Ka-band spans the Super High Frequency (SHF, 3~30 GHz) and Extremely High Frequency (EHF, 30~300 GHz) bands of the ITU designation.

Through the carried phased array antenna, which can produce a beam-formed Ka-band signal by feeding single radiators with different phase shifts, BDS-3 satellites can establish ranging and communication links with each other and rapidly switch the beam direction to point to different companions (Yang et al. 2017a). Compared with mechanical steering antennas, electronically steered phased array antennas are more flexible and require less maintenance.

The first link was established between two BDS-3 experimental satellites, i.e., SVN C102 and C103, shortly after the launch [17]. Many studies have been reported based on the ISL measurements of BDS-3 experimental satellites. The linking scheme of BDS-3 is called the Concurrent Spatial Time Division system (Yang et al. 2017a). It means multiple links (but no more than half of all satellites in the constellation) between different satellite pairs may be established simultaneously. However, the inter-satellite-link of an individual satellite works mainly in the TDMA mode. According to a pre-defined routing schedule, links from one satellite are established with others sequentially within a designated time slot (Han et al. 2013; Yang et al. 2017b). Except for TDMA, continuous links between BDS-3 experimental satellites are also possible, e.g., M1S-M2S, M2S-I2S. Because of continuous and stable antenna offset corrections and stronger signals, resulting pseudoranges from continuous links show smaller noises than TDMA links (Pan et al. 2018). (Xie et al. 2019) showed that observations of inter-satellite links can greatly improve the POD precision for BDS-3, especially when there are only serval regional ground tracking stations used. (Wang et al. 2019) estimated the link-specific rather than satellite-specific hardware delays for ISL observations when used in POD. It shows an average decrease of 0.3 cm in the residuals compared to estimating satellite-specific hardware delays. And the difference of hardware delays derived from these two modelling strategies for a specific link ranges from 0.2 ns to 1.0 ns. Furthermore, Ka-band signal PCOs for BDS-3 satellites are also calibrated in the data processing. Although the average of the X-/Z-offset estimate series is close to the a-prior values, large time-variation exists in both estimate series. Orbit overlap difference decreased slightly when calibrating PCOs in processing. The SAR service provided by BDS-3 also relies on the Inter-Satellite Links of IGSO and MEO satellites (CSNO 2021).

2.2.1 Original Observations

The technical realization of BDS-3 inter-satellite-links is a dual one-way ranging system. A similar ranging scheme is also employed by the legacy Microwave Instrument (MWI) onboard

---

[17] http://www.beidou.gov.cn/yw/xwzx/lsxw/xwzx2015/201710/t20171010_1025.html (in Chinese), last accessed on 2021/11/23

GRACE/GRACE-FO satellites (Abich et al. 2019).

Assumed that, satellite i transmits an outward ranging signal at its apparent clock time t_1^i which is received by satellite j at its own apparent clock time t_2^j. Within a short period with respect to t_1^i, satellite i receives an inward ranging signal at its apparent clock time t_4^i which is, in turn, sent by satellite j at the apparent clock time t_3^j of satellite j. The two ranging processes between satellites i and j then constitute a complete dual one-way ranging. Each dual one-way ranging between linked satellites is designed to be finished within a short time window. For BDS-3, the time window of each dual one-way ranging is 3 seconds. Figure 2.4 shows the dual one-way ranging processes described above schematically. Apparent clocks of the two linked satellites and an imagined clock representing the system time are drawn for reference. Signal receipt and transmission epochs are indicated in all three clocks. Not all events are always taking place in the chronological order as indicated by the positions of their time tags on the timeline, as shown in Figure 2.4. For example, satellite j may also transmit the outward ranging signal before receiving the inward signal from satellite i.
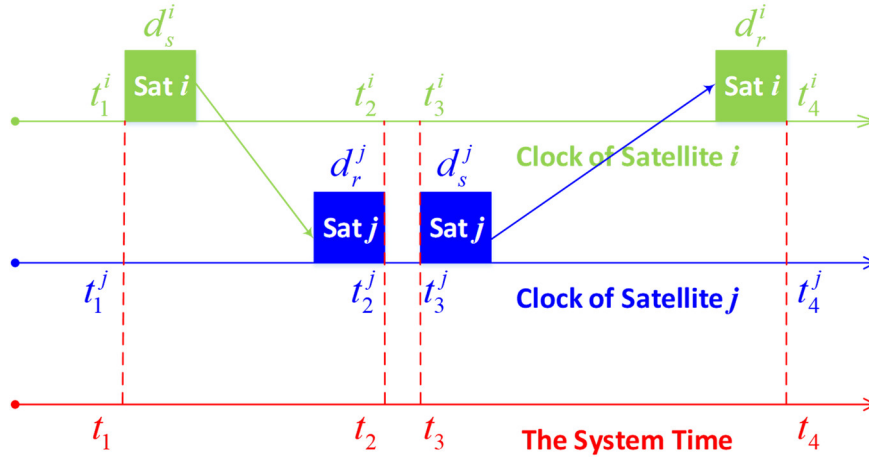
Figure 2.4 Schematic of the dual one-way ranging between two linked satellites

According to (Tang 2017), the difference between receipt epochs of those two one-way ranging signals is less than 3 seconds, i.e.

$$|t_4 - t_2| \leq 3 \text{ seconds} \tag{2.1}$$

The flight time of ISL signals between BDS satellites is 0.016~0.230 seconds (Zhou et al. 2018). Mathematically, the dual one-way ranging measurements of ISL can be described as following two observation equations

$$
\begin{aligned}
\rho^{i,j} &= \left\| X^j(t_2) - X^i(t_1) \right\| + c[\delta t^j(t_2) - \delta t^i(t_1)] + d_s^i + d_r^j + \varepsilon^{i,j} \\
\rho^{j,i} &= \left\| X^i(t_4) - X^j(t_3) \right\| + c[\delta t^i(t_4) - \delta t^j(t_3)] + d_s^j + d_r^i + \varepsilon^{j,i}
\end{aligned}
\tag{2.2}
$$

In Figure 2.4 and Equation (2.2), $\rho^{i,j}$ and $\rho^{j,i}$ are the one-way pseudorange observations

from satellite i to satellite j and from satellite j to satellite i. $\boldsymbol{X}^i(*)$ and $\boldsymbol{X}^j(*)$ are the position vectors of satellite i and j. t^i_* and t^j_* are event epochs given in the apparent clocks of satellite i and j, respectively. t_* denotes event epochs given in the imaginary system clock. $\delta t^i(*)$ are clock offsets of satellite i with respect to the system time, i.e.,

$$
\begin{aligned}
t^i_1 - \delta t^i(t^i_1) &= t_1 \\
t^i_4 - \delta t^i(t^i_4) &= t_4
\end{aligned}
\tag{2.3}
$$

$\delta t^j(*)$ are clock offset of satellite j with respect to the system time, i.e.,

$$
\begin{aligned}
t^j_2 - \delta t^j(t^j_2) &= t_2 \\
t^j_3 - \delta t^j(t^j_3) &= t_3
\end{aligned}
\tag{2.4}
$$

d^i_s and d^i_r are the transmission and receipt delays of the inter-satellite-link of satellite i. d^j_s and d^j_r are the transmission and receipt delays of the inter-satellite-link of satellite j. Hardware delays of inter-satellite-links are assumed to be constant over a typical processing session of 24~72 hours and therefore are not related to specific epochs in the observation equations. $\varepsilon^{i,j}$ and $\varepsilon^{j,i}$ denote other errors that affect the dual one-way ranging of ISLs, including inter-satellite-link antenna phase center corrections, relativistic effects, multi-path errors and random noises. The nominal random noise of Ka-band measurements is at the 10 cm level, according to (Pan et al. 2018). For links going through the Earth's atmosphere, atmospheric delays should also be considered.

Except for links between satellites, Ka-band links can also be established between satellites and ground stations that are equipped with inter-satellite-links, i.e., so-called anchor stations. Though it is somehow inconsistent with the literal meaning, those links are still called ISLs. It is not difficult to distinguish them from a real ISL according to the context. Observation equations for ISLs between satellites and ground stations are similar to Equation (2.2). Atmospheric delays always exist for those links. And except for the errors mentioned above, station-related corrections, e.g., tide displacements, should also be considered for ISLs between satellites and ground stations.

Based on the observation equations stated in Equation (2.2), original dual one-way ranging measurements of ISLs can be used directly to determine the orbits and clocks of BDS-3 satellites (Ruan et al. 2019).

2.2.2 Error Sources

2.2.2.1 Tropospheric Delay

For ISL ranging measurements, potential errors caused by the Earth's atmosphere depend on the actual signal transmission path between the linked pair of satellites. Figure 2.5 schematically illustrates an ISL between satellites above the Earth.
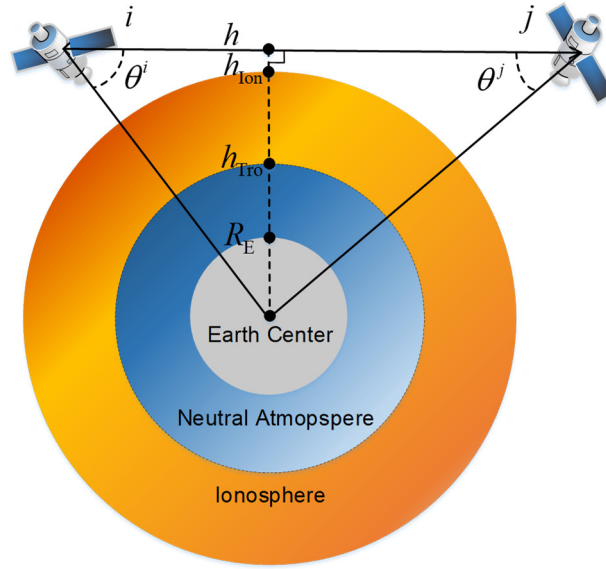
Figure 2.5 Schematic diagram of an Inter-Satellite Link between satellites above the Earth

In Figure 2.5, R_{E} denotes the Earth's radius. h_{Tro} and h_{Ion} are the geocentric heights of the top of the neutral atmosphere and ionosphere, respectively. θ_i and θ_j are the nadir angles of the ISL with respect to satellites i and j. Nadir angles of the ISL indicate the line-of-sight directions relative to the boresights of satellites and can be calculated based on satellites' positions via Equation (2.5).

$$\theta^i = \arccos(\frac{X^i - X^j}{\|X^i - X^j\|} \frac{X^i}{\|X^i\|})$$
$$\theta^j = \arccos(\frac{X^j - X^i}{\|X^j - X^i\|} \frac{X^j}{\|X^j\|})$$

(2.5)

h is the vertical distance between the line-of-sight of the ISL and the Earth's Center. It can be easily obtained by Equation (2.6).

$$h = \|X^i\|\sin\theta^i = \|X^j\|\sin\theta^j$$

(2.6)

This distance determines the visibility between satellites and whether the ISL ranging

observations are affected by the atmosphere of the Earth. As shown in Figure 2.5, the following criteria can be used to evaluate the visibility as well as potential error sources for ISL observations between two satellites at a specific epoch.

1) if $h < R_E$, because of the Earth's blockage, satellites i and j would be invisible to each other. Thus, an ISL between them is impossible.

2) if $R_E < h < h_{Tro}$, these satellites are visible to each other, and the ISL observations would be affected by both the neutral atmosphere and the ionosphere of the Earth.

3) if $h_{Tro} < h < h_{Ion}$, these satellites are visible to each other, and the ISL observations would be affected only by the ionosphere of the Earth.

4) if $h > h_{Ion}$, these satellites are visible to each other, and the Earth's atmosphere would not affect the ISL observations.

It should be mentioned that, except for the Earth's blockage, whether an inter-satellite linking could take place also depends on several other factors, e.g., the maximum beam angles of inter-satellite-link phased array antennas and routing schedules.

Tropospheric delays of radio signals[18] of the electromagnetic waves are non-dispersive and reach a magnitude of ~ 2.3 m at sea level (Petit and Luzum 2010). Therefore, models applied for L-band GNSS signals can be directly used for tropospheric delay corrections of Ka-band ISLs, i.e., models for the zenith hydrostatic delays (Saastamoinen 1972; Davis et al. 1985), horizontal tropospheric gradients (Chen and Herring 1997; Bar-Sever et al. 1998), mapping functions (Niell 1996; Niell 2001), and meteorological data (Boehm et al. 2007; Kouba 2009; Böhm et al. 2015).

2.2.2.2 Ionospheric Delay

For UHF links of GPS Block IIR, the ionospheric delays are 0~100 m with a mean delay of 20~30 m. The compensation for ionospheric delay by utilizing two frequencies made the measurements noisy because of the small frequency separation of only 15 MHz. Therefore, the dual-frequency combination was not routinely performed (Codik 1985; Ananda et al. 1990; Bernstein et al. 1993).

For Ka-band links between satellites and ground stations, assuming a high value of Slant Total Electron Content (STEC) S of

---

[18]   the lower frequency portion of the electromagnetic spectrum with the maximum frequency of 300 GHz.

$$S = \int_r^s N_e dl \approx 300 \times 10^{16} \text{ m}^{-2} \tag{2.7}$$

the signal delays in the distance caused by the first-order ionospheric term are around 8~16 cm, as shown in Figure 2.6. In Equation (2.7), $\boldsymbol{s}$ and $\boldsymbol{r}$ are the position vectors of the satellite at the signal transmission epoch and ground station at the signal receipt epoch, respectively. N_e denotes the number density of free electrons and dl is the differential length element. Higher-order terms of the ionospheric delay are increasingly less important for increasing frequencies (Petit and Luzum 2010). By taking a typical value reflecting the magnitude of the magnetic field modulus, the ratio of the second-order to first-order ionospheric delays can be approximated by

$$\frac{\delta\rho_{I,2}}{\delta\rho_{I,1}} \approx \frac{2.8 \times 10^5}{f} \tag{2.8}$$

where $\delta\rho_{I,1}$ and $\delta\rho_{I,2}$ are the first- and second-order ionospheric delays. This ratio for Ka-band signals is 7~11 × 10^{-6}. Therefore, second- or higher-order ionospheric delay terms in ranging observations of Ka-band ISLs between satellites and ground stations can be neglected. In enhanced environments like high altitude nuclear events, disturbances to the ionization of the plasmasphere may severely affect the measurement propagation delays. However, preliminary simulations only showed an insignificant degradation to the performance (Ananda et al. 1990).
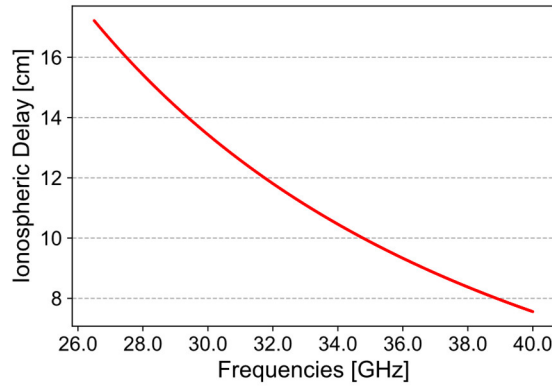
Figure 2.6 First-order ionospheric delays of Ka-band signals transmitted between satellites and ground stations

As for ISLs between satellites, as shown in Figure 2.5, only links passing through the Earth's atmosphere would suffer signal delays. To figure out the number of ISL observations affected by Earth's atmosphere, one week ISL measurements between BDS-3 MEO satellites are simulated. The maximum beam angle of 60 degrees was assumed in the simulation. Daily percentages of ISL observations affected by neutral atmosphere and ionosphere are shown in

Figure 2.7. Heights above the Earth surface of 50 km and 1000 km for the top of the troposphere and ionosphere are assumed, respectively. On average, only around 1.14% of daily ISL ranging signals would go through the ionosphere, among which 0.06% would also be affected by the neutral atmosphere. Due to such small portions, atmospheric corrections for ISL measurements between satellites are usually ignored.
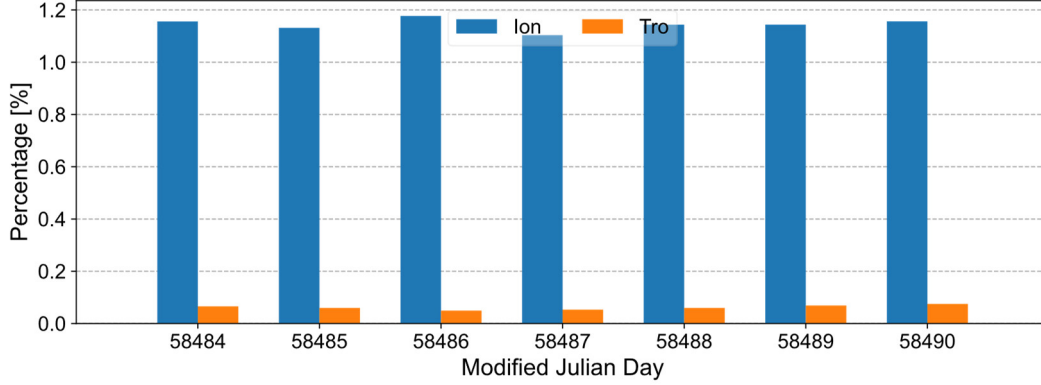
Figure 2.7 Daily percentage of ISL measurements affected by neutral atmosphere and ionosphere

2.2.2.3 Relativistic Effects

Relativistic effecs on the measurement model of the near-Earth satellite orbit determination problem are considered according to the recommendation from IERS Convention 2010 (Petit and Luzum 2010). These effects mainly include two parts. First part is the periodic effect due to the assumption of circular orbits, which can be calculated by

$$d\text{Rel1} = \frac{2}{c}(\boldsymbol{X}^{\text{Tran}}\dot{\boldsymbol{X}}^{\text{Tran}} - \boldsymbol{X}^{\text{Recv}}\dot{\boldsymbol{X}}^{\text{Recv}}) \tag{2.9}$$

where $\boldsymbol{X}^{\text{Tran}}$, $\dot{\boldsymbol{X}}^{\text{Tran}}$ are the position and velocity vectors of the transmitting satellite while $\boldsymbol{X}^{\text{Recv}}$, $\dot{\boldsymbol{X}}^{\text{Recv}}$ are that of the receiving satellite. The second part is the space-time curvature of the satellite signal due to the gravitational filed which can be expressed as

$$d\text{Rel2} = \frac{2GM_{\text{E}}}{c^2}\ln\frac{r_{\text{E,Tran}} + r_{\text{E,Recv}} + r_{\text{Tran,Recv}}}{r_{\text{E,Tran}} + r_{\text{E,Recv}} - r_{\text{Tran,Recv}}} \tag{2.10}$$

where $r_{\text{E,Tran}}$, $r_{\text{E,Recv}}$ are the distances between the Earth and the transmitting and receiving satellites, respectively. $r_{\text{Tran,Recv}}$ is the distance between the transmitting and receiving satellites. GM_{E} is the graviatational constant of the Earth. Figure 2.8 shows the quantity of these two parts of relativistic effects on BDS-3 ISL measurements, where different colors denote different links. It can be seen thant, the first part of the relativity corrections is within ±95 cm and differs largely from link to link. The second part is much smaller, around 1~4 cm.

18
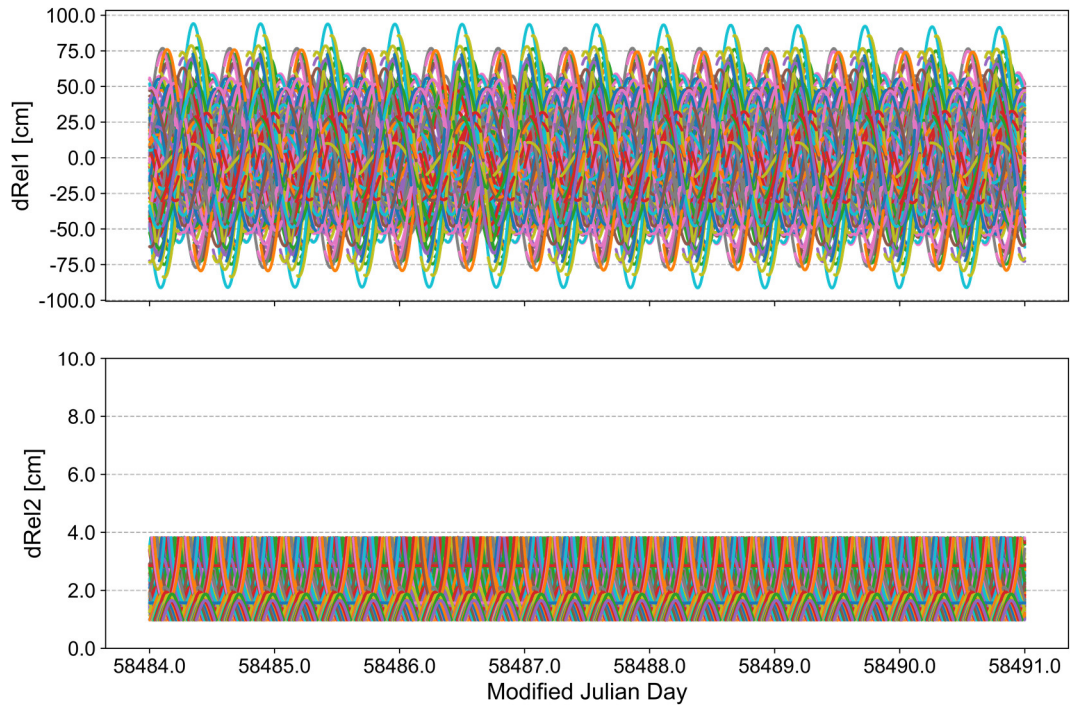
Figure 2.8 Relativistic effects on the measurements of BDS-3 Inter-Satellite Links

2.2.2.4 Other Errors

Other errors, such as Phase Center Offsets (PCO), are similar to the legacy L-band GNSS observations. The same models or procedures applied for the L-band GNSS observations can be used directly for ISL measurements. Therefore, detailed descriptions of them are omitted here.

2.2.3 Derived Observations

In order to run the orbit and clock improvements simultaneously as well as independently which is required by the limit of computation capacity onboard satellites, dual one-way ranging measurements of ISLs need to be decoupled via a preprocessing procedure. The decoupling of satellite orbit and clock information also avoids the mutual tangling of anomalies and errors (Ananda et al. 1990). In this preprocessing, dual one-way pseudoranges are converted into fictional instantaneous range and clock observations between linked satellites. Those instantaneous relative range and clock measurements are usually referred to as derived observations.

Let t be the epoch of the derived instantaneous pseudorange between the two linked satellites,

i.e., the so-called frame time in (Menn 1986; Ananda et al. 1990), observation equations of fictional instantaneous pseudoranges can be written as

$$\rho_*^{i,j} = \|X^j(t) - X^i(t)\| + c[\delta t^j(t) - \delta t^i(t)] + d_s^i + d_r^j + \varepsilon_*^{i,j}$$
$$\rho_*^{j,i} = \|X^i(t) - X^j(t)\| + c[\delta t^i(t) - \delta t^j(t)] + d_s^j + d_r^i + \varepsilon_*^{j,i}$$

(2.11)

where $\rho_*^{i,j}$ and $\rho_*^{j,i}$ are the instantaneous pseudoranges at epoch t. $\varepsilon_*^{i,j}$ and $\varepsilon_*^{j,i}$ denote the errors in those derived pseudorange measurements not shown in the equations. Except for the epoch time tag, other symbols have similar meanings as in the observation equations of original dual one-way measurements, i.e., Equation (2.2). Comparing Equation (2.2) with Equation (2.8), corrections applied to the raw one-way pseudoranges in order to obtain the instantaneous pseudoranges can be expressed as Equation (2.12)

$$\begin{aligned} \Delta\rho^{i,j} &= \rho_*^{i,j} - \rho^{i,j} \\ &= \|X^j(t) - X^i(t)\| - \|X^j(t_2) - X^i(t_1)\| + c[\delta t^j(t) - \delta t^j(t_2)] \\ &\quad - c[\delta t^i(t) - \delta t^i(t_1)] + (\varepsilon_*^{i,j} - \varepsilon^{i,j}) \\ \Delta\rho^{j,i} &= \rho_*^{j,i} - \rho^{j,i} \\ &= \|X^i(t) - X^j(t)\| - \|X^i(t_4) - X^j(t_3)\| + c[\delta t^i(t) - \delta t^i(t_4)] \\ &\quad - c[\delta t^j(t) - \delta t^j(t_3)] + (\varepsilon_*^{j,i} - \varepsilon^{j,i}) \end{aligned}$$

(2.12)

Differences of error terms between original and fictitious one-way pseudoranges can be ignored, i.e.,

$$\varepsilon_*^{i,j} - \varepsilon^{i,j} \approx 0, \ \varepsilon_*^{j,i} - \varepsilon^{j,i} \approx 0$$

(2.13)

According to the design of the ranging mechanism, differences of epochs between derived observations and original dual one-way observations are less than 3 seconds, i.e.

$$|t - t_2| \leq 3 \text{ seconds}$$
$$|t - t_4| \leq 3 \text{ seconds}$$

(2.14)

Expanding Equation (2.12) by Taylor series at epoch t and truncating them until the first order, the correction terms can be approximated as

$$\begin{aligned} \Delta\rho^{i,j} &\approx -(t_2 - t)e^{i,j}(t)V^j(t) + (t_1 - t)e^{i,j}(t)V^i(t) - c\dot{\delta t^j}(t)(t_2 - t) \\ &\quad + c\dot{\delta t^i}(t)(t_1 - t) \\ \Delta\rho^{j,i} &\approx -(t_3 - t)e^{i,j}(t)V^j(t) + (t_4 - t)e^{i,j}(t)V^i(t) + c\dot{\delta t^j}(t)(t_3 - t) \\ &\quad - c\dot{\delta t^i}(t)(t_4 - t) \end{aligned}$$

(2.15)

In Equation (2.15), $e^{i,j}(t)$ denotes the direction vector at epoch t pointing from satellite i to satellite j. $V^i(t)$, $V^j(t)$ are the velocity vectors of satellite i and j at epoch t while $\dot{\delta t^i}(t)$, $\dot{\delta t^j}(t)$ are their clock drifts. As the prediction accuracy within 3 seconds is no worse than 0.1 mm/s and 10^{-13} s/s for satellites' velocity and clock drift, respectively (Tang 2017; Tang et al. 2017; Pan et al. 2018; Tang et al. 2018), according to the law of error propagation,

20

$\Delta \rho^{i,j}$ and $\Delta \rho^{j,i}$ can be obtained with errors less than 1.0 cm.

Figure 2.9 shows the derivation errors caused by prediction errors of 0.1 mm/s in satellites' velocities and 10^{-13} s/s in clock drifts. The derivation interval, i.e., the epoch differences between derived and original observations, are assumed to be 3 seconds. It can be found that derivation errors less than 0.5 mm would be introduced by using predicted orbits and satellite clocks during the derivation.
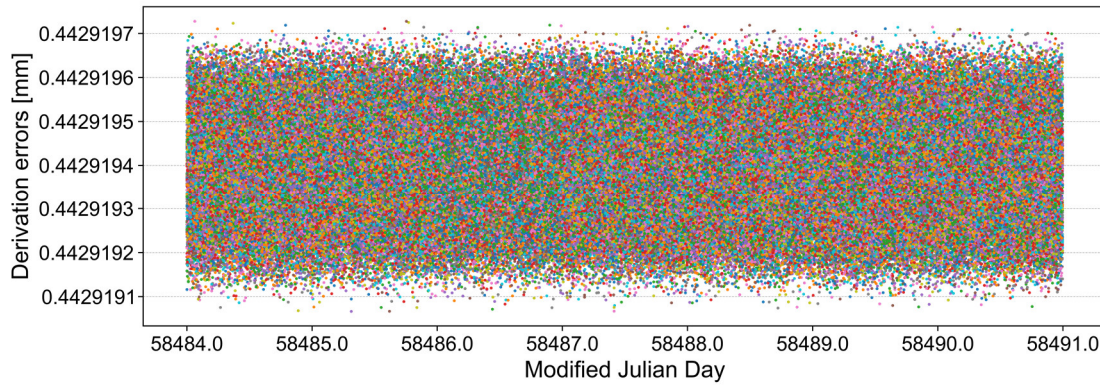
Figure 2.9 Derivation errors of ISL derived observations induced by prediction errors of 0.1 mm/s in satellites' velocities and 10^{-13} s/s in clock drifts when derivation intervals are 3 seconds

With longer derivation intervals, derivation error increases. However, as shown in Figure 2.10, even with derivation intervals of 10 seconds and clock drift prediction accuracy of one magnitude worse, i.e., 10^{-12} s/s (Yang et al. 2017a), the derivation errors would also not exceed 1.0 cm, only around 4.0 mm specifically. Thus, considering the precision of ISL measurements, the derivation errors can be safely neglected.
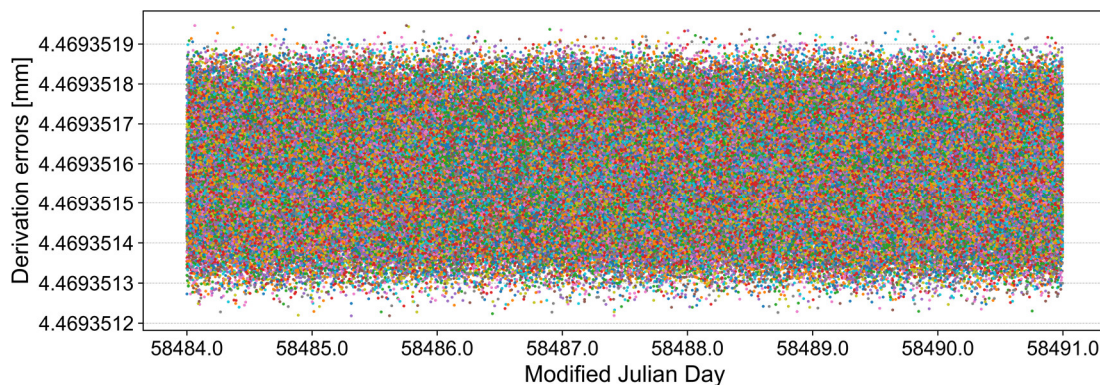
Figure 2.10 Derivation errors of ISL derived observations induced by prediction errors of 0.1 mm/s in satellites' velocities and 10^{-12} s/s in clock drifts when derivation intervals are 10 seconds

Note that, except for corrections to the original dual one-way measurements, epochs of ISL derived observations are also adjusted, i.e., taking derivation intervals into account. Depending on the magnitudes of individual onboard clock offsets, orbit differences caused by uncalibrated

time stamps of derived observations may reach from a few centimeters to several decimeters (Xia 2018).

2.2.3.1 Derived Range Observations

Omitting the epoch time t, by summing the two derived instantaneous pseudoranges as shown in Equation (2.11) gives the clock-free relative range observation ρ_+^{ij}

$$\rho_+^{ij} = \frac{\rho_*^{i,j} + \rho_*^{j,i}}{2} = \left\| X^j - X^i \right\| + \frac{d_s^i + d_r^i}{2} + \frac{d_s^j + d_r^j}{2} + \frac{\varepsilon_*^{i,j} + \varepsilon_*^{j,i}}{2} \qquad (2.16)$$

If only derived range observations are used, a parameter representing the sum of receiving and transmitting delay of the inter-satellite-link should be estimated for each satellite. Theoretically, derived range observations should have higher precision than original ones because of shrunk noises by $\sqrt{2}$ after the combination. Smaller polynomial fitting residuals were found for derived pseudoranges than the raw dual one-way ranging measurements (Zhou et al. 2018).

2.2.3.2 Derived Clock Observations

Similarly, the orbit-free relative clock observation ρ_-^{ij} can be obtained by differencing the two derived instantaneous pseudoranges

$$\rho_-^{ij} = \frac{\rho_*^{i,j} - \rho_*^{j,i}}{2} = c\left[\delta t^j - \delta t^i\right] + \frac{d_s^i - d_r^i}{2} - \frac{d_s^j - d_r^j}{2} + \frac{\varepsilon_*^{i,j} - \varepsilon_*^{j,i}}{2} \qquad (2.17)$$

The observation epoch t is omitted in Equation (2.17). As most common errors, such as the ionospheric delay, could be canceled out via subtraction, derived clock observations might show less noise than derived range observations.

Using only ISL derived clock observations, it is impossible to separate the hardware delays from satellite clock offsets because of the one-to-one correlations. However, if incorporating additional clock observations, like the L-band ground tracking measurements, hardware delays of inter-satellite-links can be obtained in the sense of relatively. Parameters implying the differences of receiving and transmitting delays of each satellite can be estimated. In this case, the rank deficiency of one degree of freedom due to datum missing can be eliminated by fixing the hardware delay of one satellite.

Mathematically, the orbit and clock information is fully decoupled through the derivation.

22

Combining the derived range and clock observations in a single estimator does not make any difference from processing them separately as there is no common unknown between those two observations. But if observations from the L-band ground tracking are also included, it might make sense to integratedly process the ISL derived range and clock measurements. The orbit and satellite clock information will be connected by the carrier phase and code pseudorange observations from the L-band ground tracking. Then, the receipt and transmission hardware delays of inter-satellite-links can also be parameterized individually, although one degree of freedom remains.

2.3 Data Processing

This section is dedicated to the introduction of datasets used for BDS-3 orbit determination in this study.

2.3.1 Used Datasets

2.3.1.1 Ka-band ISL

Observations of Ka-band ISLs of BDS-3 basic constellation during the period of DOY 335~365[19], 2019 were used. At that time, the basic constellation of BDS-3 contained 20 satellites, consisting of 18 MEOs and 2 IGSOs. Collected ISL observations are the derived range and clock observations as given in Equation (2.16) and Equation (2.17). Corrections such as phase center offsets of inter-satellite-link antennas, relativistic effects have been applied in the pre-processing for measurement derivations.

Figure 2.11 shows the nadir angles of all ISLs between BDS-3 MEO satellites during the considered session. The boresight angles of ISLs between BDS-3 MEO satellites range from 15° to 60°. By contrast, the nadir angles of ISLs between IGSOs and MEOs can be as small as 10° or even lower. For an ISL between an MEO satellite and an IGSO satellite, the nadir angle concerning the boresight of the IGSO satellite is always smaller because of the higher orbit altitude. Compared to the depression angle range of 32°~65° of GPS Block IIR UHF cross-links (Ananda et al. 1990), the beam extent of BDS-3 ISLs is wider, with a much smaller lower bound.

---

[19] i.e., 2019/12/01~2019/12/31, GPS Week 2082 0~ 2086 2, MJD 58818~58848
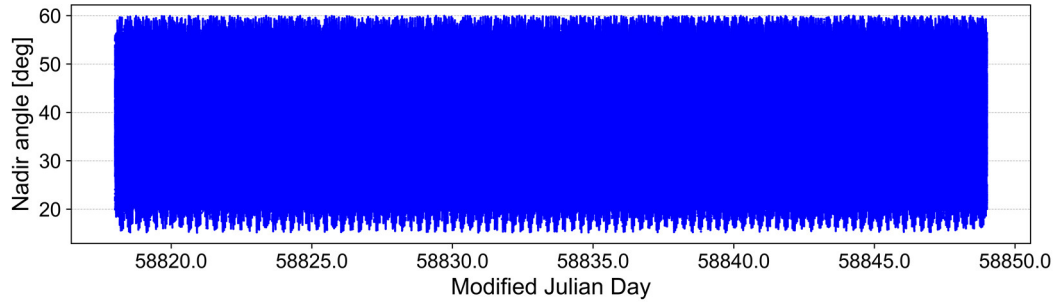
Figure 2.11 Nadir angles of ISLs between BDS-3 MEOs over DOY 335~365, 2019

Figure 2.12 shows the daily number of ISL derived observation pairs for each satellite over the one-month session. Each observation pair consists of one derived range and one derived clock measurements, which are resulted from the derivation of a set of dual one-way links. As each ISL involves two satellites, every observation pair has been counted twice, i.e., one for each of the two linked satellites. Except for the first four days, daily numbers of ISL observations for each satellite are stable. For MEO satellites, the daily number of link pairs is around 20000~22000. Relatively fewer ISLs are established for IGSO satellites, with a daily number of ISL pairs of ~18000.
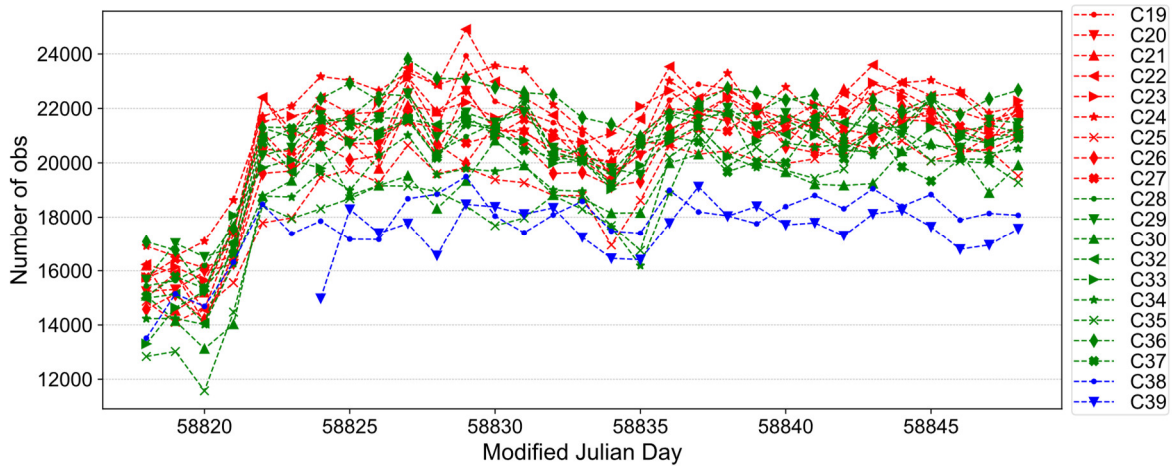
Figure 2.12 Daily number of ISL derived observation pairs of BDS-3 satellites over DOY 335~365, 2019

Ideally, every satellite can link with all other satellites in view. Regarding each different satellite pair as a different link, numbers of links for each BDS-3 satellite on DOY 335, 2019 are given in Figure 2.13. Links are distinguished by the type, i.e., intra-plane or inter-plane. The link numbers of each MEO satellite are similar, around 15~17. Among them, 13 links are established between different orbit planes while 2~4 are within the orbit plane. For the IGSO satellite C38, links with each of the 18 MEO satellites are established. For autonomous orbit determination, observations of inter-plane links contribute more than intra-plane link observations (Herklotz 1987). Figure 2.14 shows the percentages of intra- and inter-plane link

24

observations for each satellite on DOY 335, 2019. On average, intra-plane ISL observations account for 16%~32% for individual MEO satellites.
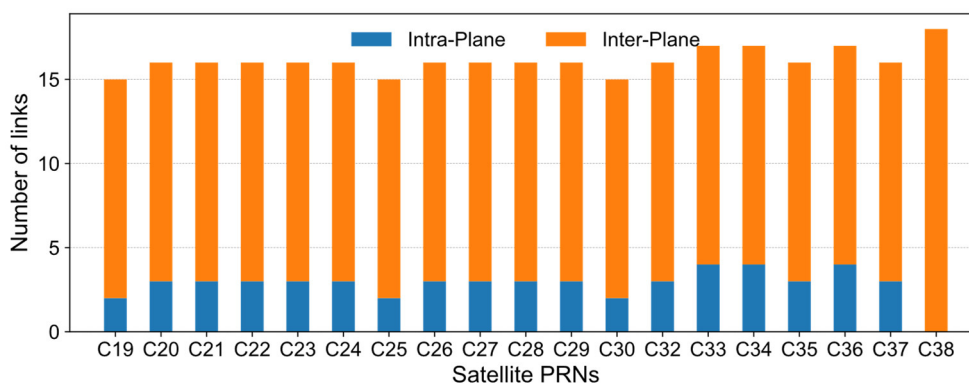
Figure 2.13 Number of intra- and inter-plane links for each BDS-3 satellite on DOY 335, 2019
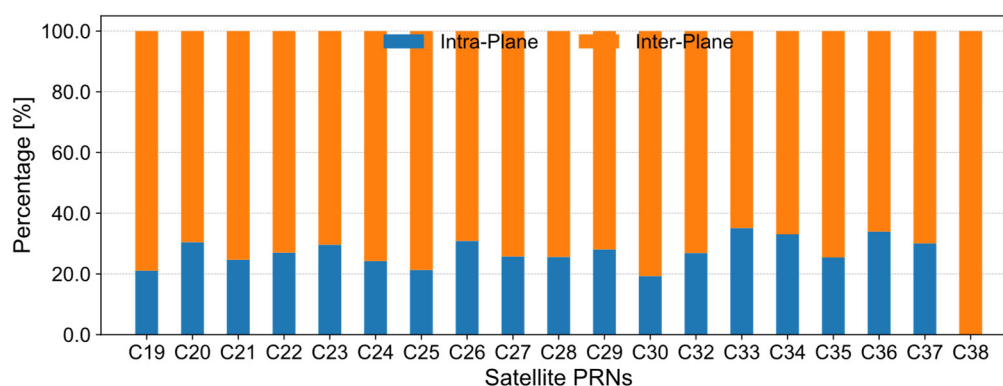
Figure 2.14 Percentages of intra- and inter-plane ISL observations for each BDS-3 satellite on DOY 335, 2019

To preliminarily evaluate the precision of ISL measurements of BDS-3, derived clock observations of each link were piece-wisely fitted by first-order polynomials. Fitting windows are of one-hour length. According to Equation (2.17), assuming the clock offsets and hardware delays of inter-satellite-links are absorbed by the polynomial models, the fitting residuals should mainly reflect the remaining errors persisting in the derived clock observations.

Polynomial fitting residuals of ISL derived clock observations of BDS-3 MEO satellites on DOY 335, 2019 are shown in Figure 2.15, Figure 2.16, and Figure 2.17. Satellites from different orbit planes are displayed separately. Fitting residuals of the IGSO satellite C38 are shown in Figure 2.18. Residual RMSs of satellites are labeled at the upper right corners within each axis. Most satellites' fitting RMSs are within 2~3 cm. However, the MEO satellite C23 shows relatively larger fitting residuals with a daily RMS of ~4.7 cm, which is attributed to a different technique status of its Inter-Satellite-Link payload in (Yang et al. 2021). Not much disparity regarding the magnitude of fitting residuals can be noticed between satellites from different MEO planes. On the other hand, satellite-specific distinctions are more visible. Satellites C24

and C37 on the MEO plane C show smaller fitting residuals compared to other satellites. For the IGSO satellite C38, it exhibits similar fitting residuals as most MEO satellites.
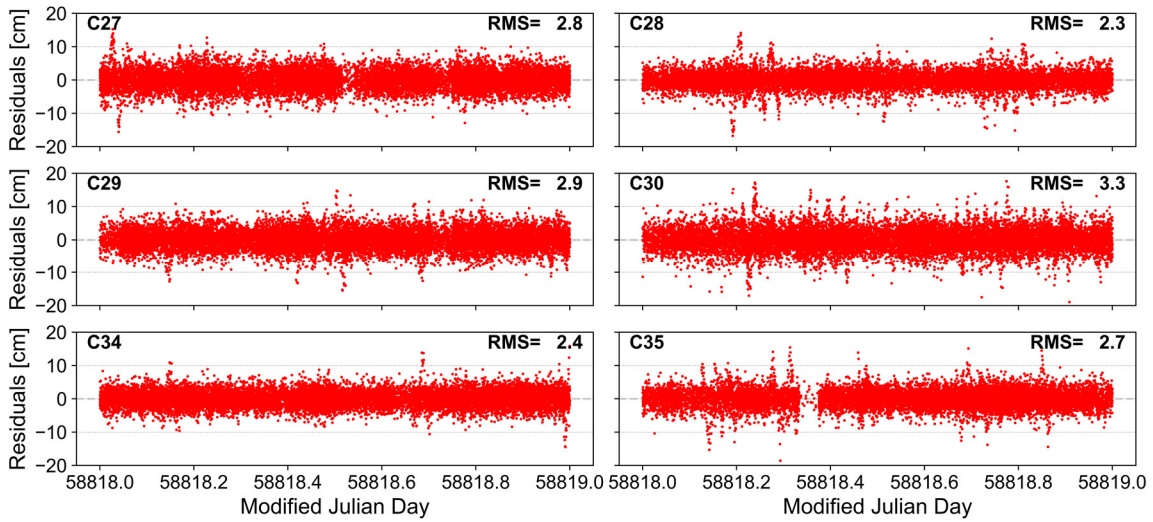
Figure 2.15 Polynomial fitting residuals of ISL derived clock observations of satellites from the BDS-3 MEO plane A
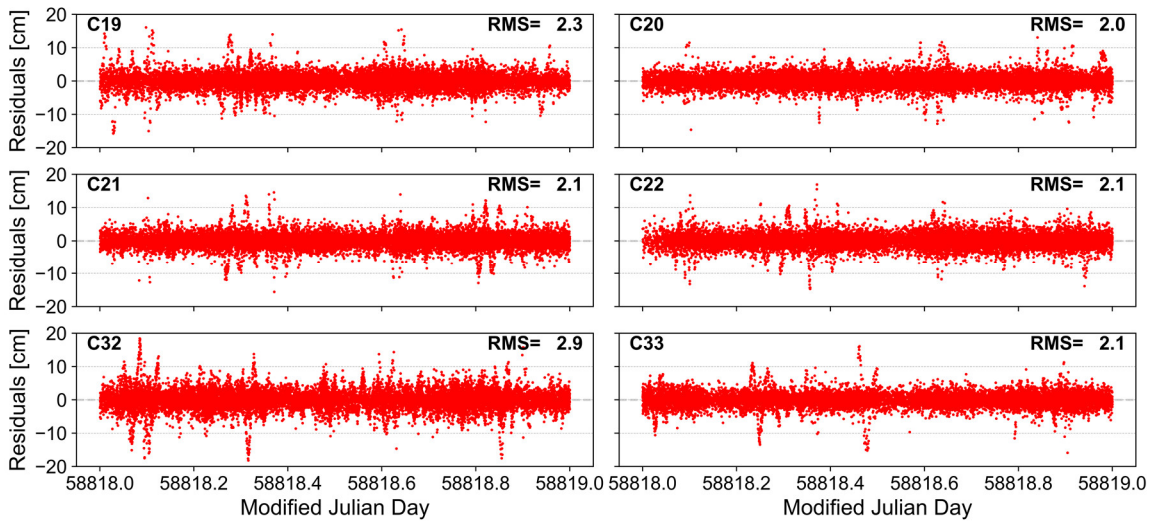
Figure 2.16 Polynomial fitting residuals of ISL derived clock observations of satellites from the BDS-3 MEO plane B
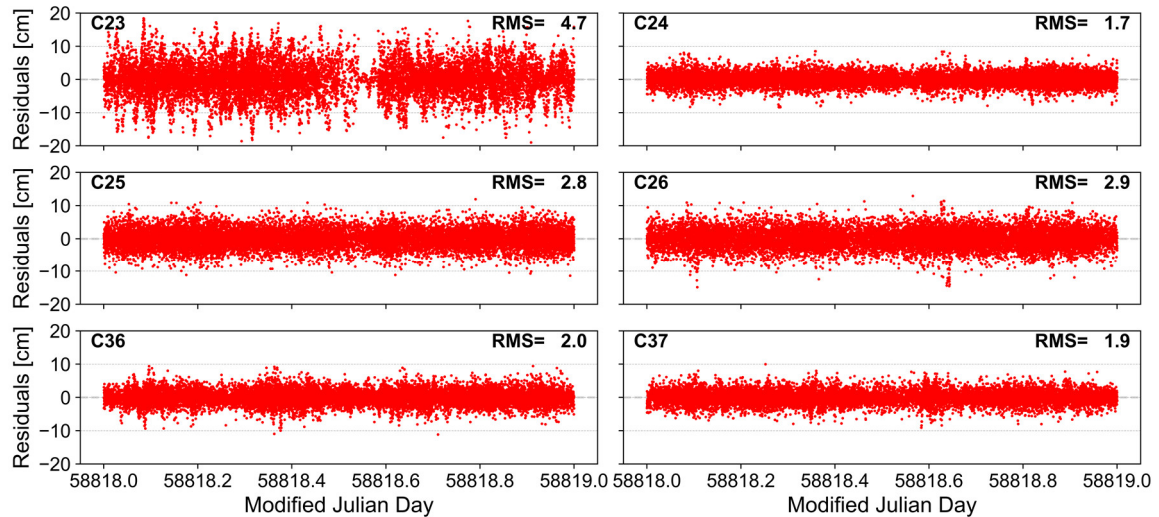
Figure 2.17 Polynomial fitting residuals of ISL derived clock observations of satellites from the BDS-3 MEO plane C
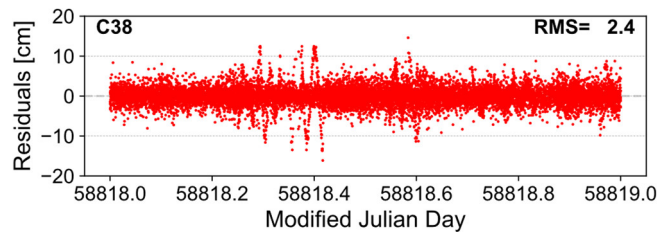
Figure 2.18 Polynomial fitting residuals of ISL derived clock observations of BDS-3 IGSO satellite C38

2.3.1.2 L-band Ground Tracking

Except for investigating several trivial issues related to the modelling of BDS-3 orbit determination, the L-band observations were mainly used in the contribution evaluation of BDS-3 ISL measurements. Therefore, the L-band ground tracking data collected by the IGS Multi-GNSS Experiment (MGEX) network[20] during the same period as the ISL observations, i.e., DOY 335~365, 2019, were used in this study. The geographic distribution of the ground tracking network of BDS-3 is given in Figure D-1 in Appendix D.

2.3.2 Processing Strategies

Since the first artificial satellite, Sputnik 1, launched on October 4, 1957, the theories and methods of precise orbit determination of Earth orbit satellites have been continuously

---

[20] International GNSS Service, Daily 30-second observation data, Greenbelt, MD, USA:NASA Crustal Dynamics Data Information System (CDDIS), Accessed March 24, 2020 at doi:10.5067/GNSS/gnss_daily_o_001.

improved and well established (Kaula 1966; Liu 1992; Jishen 1995; Liu 2000; Montenbruck and Gill 2000; Tapley et al. 2004; Milani and Gronchi 2010; Capderou 2014). Starting from the 1990s, with the expanding applications of GPS as well as the following GNSS in many scientific and industrial areas, basic theories of the data processing of GNSS L-band carrier phase and code pseudorange observations are well-shaped (Kleusberg and Teunissen 1996; Parkinson et al. 1996; Strang and Borre 1997; Hofmann-Wellenhof et al. 2001; Kaplan and Hegarty 2006; Hofmann-Wellenhof et al. 2008; Leick et al. 2015; Teunissen and Montenbruck 2017). Therefore, instead of repeating text and formulas, which can be easily found in plenty of valuable literature, the specific choices of different modelling and processing aspects made for this study are briefly introduced here. Unless otherwise mentioned within a specific context, the default dynamical and observational modellings and data processing strategies described in this section were always applied. Generally, recommendations from the International Earth Rotation and Reference Systems Service (IERS) Conventions 2010 (Petit and Luzum 2010) and the IGS third reprocessing[21] are followed as closely as possible.

For the L-band ground tracking, carrier phase and code pseudorange observations of the signals B1I and B3I are used in the form of undifferenced ionosphere-free combinations. Several effective pre-processing methods (Blewitt 1990; Deng 2008; Liu 2011; Cai et al. 2013) are used to detect blunders and cycle slips in the observations. Sampling intervals of raw observations stored in RINEX format[22] data files are 30 seconds. For orbit determination, a lower sampling rate is enough. Hence, the processing interval of 300 seconds is adopted. Each processing session is ~24 hours, i.e., from 00:00:00 to 23:55:00 GPST of each day. The cutoff elevation angle of 7° is applied for all ground stations. The same weighting scheme is used for carrier phase and code pseudorange observations, i.e.,

$$\sigma = \begin{cases} \sigma_0/(2\sin e) & e \le 30° \\ \sigma_0 & e > 30° \end{cases} \tag{2.18}$$

For observations with an elevation angle lower than 30°, a deweighting function inversely proportional to the sine of the elevation angle is imposed. In Equation (2.18), e is the elevation angle of observing line-of-sight. σ_0 is the a priori standard deviation of raw (uncombined) carrier phase or pseudorange measurements with elevation angles above 30°, which is set to be 0.01 cycle and 0.50 m, respectively. σ is the actually applied standard deviation for each observation.

The first-order ionospheric delays are eliminated by forming the so-called ionosphere-free

---

combinations of observations from the two frequencies. The second- or higher-order effects are ignored. The Saastammoinen model (Saastamoinen 1972; Davis et al. 1985) is used to calculate the a priori tropospheric zenith delay. The meteorological data are obtained based on the empirical GPT (Global Pressure and Temperature) model (Boehm et al. 2007). The relative humidity, which the GPT model does not provide, is assumed to be 60% at all ground stations. The Global Mapping Function (GMF) from (Boehm et al. 2006) is utilized to map the zenith delay to the line-of-sight direction. On top of the a priori model, the effect of the residual zenith wet component is absorbed by a piece-wise constant model at each station. The length of each piece is one hour. Additionally, the effects of atmospheric azimuthal asymmetry are accounted for by estimating daily horizontal gradients. The gradient mapping function from (Bar-Sever et al. 1998) is adopted.

Absolute calibration models (Schmid et al. 2007) from the IGS ANTEX[23] file igs14_2148.atx[24] are used for phase center offset and variation corrections of L-band transmitter and receiver antennas. For receiver antennas without available calibrations for BDS signal frequencies, corrections for GPS L1/L2 frequencies are used in stead. The time delay and space-time bending caused by the relativistic effect are considered according to the IERS Conventions 2010 (Petit and Luzum 2010). Phase wind-up effects, i.e., deviations of signals' polarization states from the designed pure Right-Hand Circularly Polarized (RHCP) signals, at the receiver antennas are corrected by models (Wu et al. 1993; Beyerle 2009).

The geodetic datum is realized by aligning the ground station coordinates to the IGS daily combination of AC (Analysis Center) global solutions[25] via the so-called No-Net-Translation (NNT) and No-Net-Rotation (NNR) conditions (Altamimi 2002; Altamimi et al. 2002). Constraints of the NNT and NNR conditions are 1.00 mm and 0.03 mas, respectively, i.e., equivalent to 1 mm at the Earth's equator. Eccentricities of receiver Antenna Reference Points (ARPs) with respect to the site markers are corrected according to the information given in the IGS Solution (Software/Technique) INdependent EXchange (SINEX) files or RINEX observation files. Displacements of the station reference points due to various effects are corrected, including the solid Earth tides, ocean loading, S_1-S_2 atmospheric pressure loading (Ray and Ponte 2003), and pole tides (Desai 2002; Desai et al. 2015). Non-tidal displacements associated with the changing environmental loads, such as that from atmosphere, ocean, and hydrology, are not considered.

---

[23] the ANTenna EXchange format, refer to https://files.igs.org/pub/data/format/antex14.txt, last accessed on 2021/11/30

[24] https://files.igs.org/pub/station/general/pcv_archive/igs14_2148.atx, last accessed on 2021/11/30

[25] International GNSS Service, Final Combined Station Positions/Velocities (no covariance matrix) Product, Greenbelt, MD, USA:NASA Crustal Dynamics Data Information System (CDDIS), Accessed November 30, 2021 at doi:10.5067/GNSS/gnss_igsssc_001.

The procedure of transformation between the International Terrestrial Reference System (ITRS) and the Geocentric Celestial Reference System (GCRS) conforms to the IERS Conventions 2010 (Petit and Luzum 2010). The International Astronomical Union (IAU) 2006/2000A precession-nutation model is applied along with the Celestial Intermediate Origin (CIO) based transformation method[26]. A priori Earth Orientation Parameters (EOPs) are taken from the standard rapid data finals2000A.all (IAU 2000)[27], which contains the values from IERS Bulletin A for x/y pole, UT1-UTC, Length Of Day (LOD), dX, and dY.

The conventional geopotential model up to degree and order 12 is used. It is based on the Earth Gravitational Model 2008 (EGM2008)[28] (Pavlis et al. 2008; Pavlis et al. 2012) but uses a different value for the degree 2 zonal term. In addition, secular rates for some of the low-degree coefficients are also accounted for. The adopted conventional tide-free degree 2 zonal coefficient at J2000.0 epoch is

$$\bar{C}_{20}^{tf} = -0.48416531 \times 10^{-3} \tag{2.19}$$

Secular rates of the $\bar{C}_{20}$ (Nerem et al. 1993), $\bar{C}_{30}$, and $\bar{C}_{40}$ (Cheng et al. 1997) coefficients are

$$
\begin{aligned}
d\bar{C}_{20}/dt &= 11.6 \times 10^{-12}/\text{year} \\
d\bar{C}_{30}/dt &= 4.9 \times 10^{-12}/\text{year} \\
d\bar{C}_{40}/dt &= 4.7 \times 10^{-12}/\text{year}
\end{aligned}
\tag{2.20}
$$

The changes in the free space potential induced by the Sun- and Moon-caused solid Earth tides are modeled as variations in the standard geopotential coefficients C_{nm} and S_{nm}. According to the IERS Convention 2010, the permanent deformation produced by the degree 2 zonal tide generating potential, which has a nonzero (time average) mean, is included in the calculation for the effect of solid Earth tides. The Finite Element Solutions 2004 (FES2004)[29] is adopted to calculate the dynamical effects of ocean tides, i.e., the periodic variations in the normalized Stokes' coefficients (Lyard et al. 2006). Pole tides generated by the centrifugal effect of the polar motion on the solid Earth and oceans are also considered. The perturbation of the solid Earth pole tide in the external potential is equivalent to changes in the geopotential coefficients C_{21} and S_{21}. As for the ocean pole tide, the self-consistent equilibrium model presented by (Desai 2002) and recommended by the IERS Convention 2010 (Petit and Luzum

---

[26] Software Routines from the IAU SOFA Collection were used. Copyright © International Astronomical Union Standards of Fundamental Astronomy (http://www.iausofa.org)

[27] available at https://datacenter.iers.org/data/latestVersion/finals.all.iau2000.txt or ftp://ftp.iers.org/products/eop/rapid/standard/finals2000A.all

[28] available at https://earth-info.nga.mil/php/download.php?file=egm-08spherical, last accessed on 2021/11/30

[29] available at ftp://tai.bipm.org/iers/conv2010/chapter6/tidemodels/fes2004_Cnm-Snm.dat, last accessed on 2021/11/30

2010) is used to calculate the perturbations to the normalized geopotential coefficients. Only the dominant terms, i.e., perturbations in $\bar{C}_{21}$ and $\bar{S}_{21}$, are taken into account.

Except for the central body Earth, gravitations from third bodies such as the Sun, Moon, Mercury, Venus, Mars, Jupiter, Saturn, Uranus, Neptune, and Pluto, are also considered. The planetary and lunar Development Ephemeris 405 (DE405) (Standish 1998) from the Jet Propulsion Laboratory (JPL)[30] is used to acquire orbits of those bodies. Non-conservative perturbations such as the direct Solar Radiation Pressure (SRP), Earth's albedo, and thrust of the GNSS transmitter antenna are detailedly discussed in Section 5.1. Satellite metadata required for the modelling of non-conservative forces is provided by IGS MGEX via the release igs_metadata_2144.snx. Shadows of the Earth and the Moon on the Sun are calculated based on the assumption of conical projections (Jishen 1995). Attitude models of BDS satellites from (Dilssner 2017; Kouba 2017a; Kouba 2017b; Dilssner et al. 2018; Lin et al. 2018; Wang et al. 2018; Xia et al. 2019) are considered. Dynamical effects of general relativistic on satellites' motion equations are considered, including the Schwarzschild terms, Lense-Thirring precession (frame-dragging), and geodesic precession (de Sitter) terms.

Broadcast ephemerides are fitted and then integrated to provide the a priori orbits (or reference orbits called in the literature). First-order orbit motion and variation equations are solved together by numerical methods. The single-step integrator Runge-Kutta-Fehlberg 6(7) (Fehlberg 1968; Fehlberg 1970; Liu 1998) is used for the start-up with an integration step of 2 seconds. Then, the linear multi-step methods Adams-Bashforth and Adams-Moulton are used in tandem as an 11th-order predictor-corrector procedure (Hairer et al. 1993; Liu 1998; Butcher 2016). The integration steps of multi-step methods are 60 seconds.

For orbits, the Day Boundary Discontinuity (DBD) serves as the internal precision indicator, while the SLR (Pearlman et al. 2002; Noll et al. 2019) data are utilized to assess the external accuracy of orbital radial components.

---

[30] more about Jet Propulsion Laboratory Development Ephemeris, refer to https://ssd.jpl.nasa.gov/planets/orbits.html, last accessed on 2021/11/30

3 Orbit Determination using ISL

3.1 Introduction

Onboard autonomous update of broadcast ephemerides is one of the most important missions for Inter-Satellite Links. After the Operational Control Segment uplinked the long-term predicted ephemerides, the space segment should be able to maintain the required navigation performance for several months without any ground contact via inter-satellite ranging and communicating.

Because of the insensitivity of inter-satellite ranging observations to rotation errors, the constellation would experience the problem of "entire rotation" or "longitude drift" (Menn and Bernstein 1994; Liu and Liu 2000; Liu et al. 2000). There are mainly two sources of those unobservable rotation errors. One part is from the uploaded reference orbits caused by the earth motion prediction and geopotential errors. The geopotential error results in prediction errors of the nodal precession of orbit planes (Bernstein et al. 1993). The onboard estimator induces another part of the rotation errors. Limited by the onboard hardware, an imperfectly modeled estimator potentially leads to spurious rotations, which might be particularly sensitive to measurement bias errors. Through properly constraining the estimator, the rotation errors can be limited to that inherent in the stored ephemerides (Menn and Bernstein 1994).

Many pieces of research have been devoted to eliminating the rank deficiency caused by the imperceptible constellation rotation, including constraining the orbit orientation elements (Chen et al. 2005a; Xia 2018), adding absolute direction measurements (Chen et al. 2005b).

In this chapter, to start with, the ephemeris observability issue of ISL range observations is discussed. Then, satellite orbits are determined using only ISL range measurements to examine the quality of BDS-3 ISL observations. Results are evaluated and analyzed in aspects of fitting residuals, orbit precision, and the stability of ISL hardware delays. In the end, harmonic signals found in the link residuals are investigated and modeled. Their effects on the orbit determination results are assessed.

3.2 Ephemeris Observability

3.2.1 Analytic Description

With the six Keplerian orbit elements denoted as

✦ a, the semi-major axis, i.e., the mean distance of the perigee and apogee of the orbit

✦ e, the eccentricity, a measure of the orbit's deviation from a circle

✦ Ω, the Right Ascension of the Ascending Node (RAAN) which indicates the angle between the vernal equinox and the point on the orbit at which the satellite crosses the equator from south to north

✦ i, the inclination which gives the angle of the intersection between the orbital plane and the equator

✦ ω, the argument of perigee, i.e., the angle between the direction of the ascending node and the direction of the perigee

✦ t_p, the time of perigee passage or M_0, the mean anomaly at the reference epoch t_0, both of which are directly linked to the mean anomaly M at current time t by either $M = n(t - t_p)$ or $M = M_0 + n(t - t_0)$ where n is the satellite's mean motion.

a satellite's position in the geocentric Equatorial Coordinate System (ECS) $\boldsymbol{X} = (x \quad y \quad z)^{\mathrm{T}}$ can be expressed as (Montenbruck and Gill 2000; Tapley et al. 2004)

$$\boldsymbol{X} = r \begin{pmatrix} \cos u \cos \Omega - \sin u \cos i \sin \Omega \\ \cos u \sin \Omega + \sin u \cos i \cos \Omega \\ \sin u \sin i \end{pmatrix} \tag{3.1}$$

where r and u are the geocentric distance and argument of latitude of the satellite respectively, which can be related to the Keplerian orbit elements via the following equations

$$r = a(1 - e\cos E) = \frac{a(1 - e^2)}{1 + e\cos v}$$

$$u = \omega + v$$

$$v = \arctan \frac{\sqrt{1 - e^2}\sin E}{\cos E - e} \tag{3.2}$$

$$E - e\sin E = M$$

In Equation (3.2), v and E denote the true and eccentric anomaly, respectively.

Assuming that there are two satellites whose positions in the geocentric ECS are $X_1 = (x_1 \quad y_1 \quad z_1)^T$ and $X_2 = (x_2 \quad y_2 \quad z_2)^T$, the geometric distance $l^{1,2}$ between them is

$$l^{1,2} = \sqrt{(x_1 - x_2)^2 + (y_1 - y_2)^2 + (z_1 - z_2)^2}$$
$$= \sqrt{r_1^2 + r_2^2 - 2r_1 r_2 \cos\alpha}$$

(3.3)

where the geocentric distances of the two satellites are r_1 and r_2, and the angle between their geocentric position vectors is α

$$\cos\alpha = \frac{X_1 \cdot X_2}{r_1 r_2}$$

(3.4)

Considering Equation (3.1), one finds (Zhang 2005; Xia 2018)

$$
\begin{aligned}
\cos\alpha &= (\cos u_1 \cos\Omega_1 - \sin u_1 \cos i_1 \sin\Omega_1)(\cos u_2 \cos\Omega_2 - \sin u_2 \cos i_2 \sin\Omega_2) \\
&\quad + (\cos u_1 \sin\Omega_1 + \sin u_1 \cos i_1 \cos\Omega_1)(\cos u_2 \sin\Omega_2 \\
&\quad + \sin u_2 \cos i_2 \cos\Omega_2) + \sin u_1 \sin i_1 \sin u_2 \sin i_2 \\
&= \cos u_1 \cos u_2 \cos(\Omega_2 - \Omega_1) + \sin u_1 \cos i_1 \sin u_2 \cos i_2 \cos(\Omega_2 - \Omega_1) \\
&\quad + \sin u_1 \cos u_2 \cos i_1 \sin(\Omega_2 - \Omega_1) \\
&\quad - \sin u_2 \cos u_1 \cos i_2 \sin(\Omega_2 - \Omega_1) + \sin u_1 \sin i_1 \sin u_2 \sin i_2
\end{aligned}
$$

(3.5)

As the geocentric distance r and argument of latitude u are both irrelevant to the RAAN Ω according to Equation (3.2), it shows in Equation (3.3 and (3.5) that only the relative variation of the RAANs instead of any of the absolute ones of those two satellites is observable from the ISL ranging observations. In other words, one can simultaneously change the RAANs of those two satellites while still getting the same relative ranging observations.

Followings are some discussions based on other assumed cases.

➤ if $\Omega_1 = \Omega_2$ or $|\Omega_1 - \Omega_2| = \pi$, it shows via

$$
\begin{aligned}
\cos\alpha &= \pm\cos u_1 \cos u_2 \pm \sin u_1 \cos i_1 \sin u_2 \cos i_2 + \sin u_1 \sin i_1 \sin u_2 \sin i_2 \\
&= \pm\cos u_1 \cos u_2 \pm \sin u_1 \sin u_2 \cos(i_1 \mp i_2)
\end{aligned}
$$

(3.6)

that decoupling of i_1 and i_2 is again not possible.

➤ if $\Omega_1 = \Omega_2$ and $i_1 = i_2$ (or $|\Omega_1 - \Omega_2| = \pi$ and $i_1 + i_2 = \pi$), i.e., the two satellites orbit on the same plane. One can rewrite Equation (3.5) as

$$
\begin{aligned}
\cos\alpha &= \pm\cos(u_2 \mp u_1) \\
&= \pm\cos(\omega_2 \mp \omega_1 + \nu_2 \mp \nu_1)
\end{aligned}
$$

(3.7)

Then the orbit inclinations are, similar to the case of RAANs, also totally unobservable while only the relative change of satellites' arguments of latitude can be sensed.

➤   if $\Omega_1 = \Omega_2$, $i_1 = i_2$ and $\omega_1 = \omega_2$, Equation (3.7) becomes

$$\cos\alpha = \cos(v_2 - v_1) \tag{3.8}$$

As a result, the arguments of perigees can not be observed in addition to the aforementioned elements.

So far, all those discussions are based on the assumption that only the central gravitational force exists, i.e., a Keplerian word. In the actual non-Keplerian space, differences of non-central forces acting on satellites can not be fully accommodated by a rotation if the constellation spins. In other words, inter-satellite range measurements might not be really the same after a constellation rotation because of the change of non-central forces. However, the resulting inter-satellite range differences are small compared to measurement noises and model imperfections. Hence, the constellation rotations are virtually still imperceptible (Menn and Bernstein 1994).

3.2.2 Correlations of Orbit Parameters

From the perspective of the least-square adjustment, the unobservability of RAANs is manifested by strong correlations of orbit parameters between satellites. These correlations can be more straightforwardly depicted by taking Keplerian elements as the initial state vectors to be estimated. Let A be the design matrix when taking an ISL pseudorange $\rho^{1,2}$ as the observation. The unknowns are the Keplerian elements at the reference epoch t_0, denoted as $k_{1,0}$ and $k_{2,0}$. Then, the A matrix with a dimension of 1×12 can be expressed as

$$A_{1 \times 12} = \frac{\partial \rho^{1,2}}{\partial(X_1, X_2)} \frac{\partial(X_1, X_2)}{\partial(k_1, k_2)} \frac{\partial(k_1, k_2)}{\partial(k_{1,0}, k_{2,0})} \tag{3.9}$$

where k_1 and k_2 are vectors of Keplerian elements of the two satellites at the observation epoch, $k_{*=1,2} = (a_*, e_*, \Omega_*, i_*, \omega_*, M_{0,*})^{\mathrm{T}}$. Ignoring some small perturbation terms and omitting the detailed derivation, partial derivatives regarding RAANs can be written as (Liu and Liu 2000)

$$A_3 = \frac{\partial \rho^{1,2}}{\partial \Omega_{1,0}} = y_1 x_2 - x_1 y_2$$
$$A_9 = \frac{\partial \rho^{1,2}}{\partial \Omega_{2,0}} = x_1 y_2 - y_1 x_2 \tag{3.10}$$

It can be found that partial derivatives with respect to the RAANs of the two satellites have the same value while opposite signs. The normal matrix of the equation system will be rank-deficient if applying no a priori constraints. Much like the well-known case of clock offsets,

➤   36

RAANs can not be determined in the absolute sense when using ISL observations solely.

To intuitively demonstrate the consequence of unobservable RAANs, correlations between orbit parameters of different satellites are checked and compared between processings of using L-band ground tracking data and using Ka-band ISL measurements. Although the Cartesian coordinates have been used for the initial state vectors of satellites' orbits due to the convenience of numerical implementations, it does not compromise much the essential conclusions drawn from the results. Except for initial state vectors, parameters of the adopted empirical SRP model, i.e., the ECOM1 (See Appendix B), are also shown for completeness. Figure 3.1 and Figure 3.2 display the correlations among orbit parameters of intra-plane satellite pair SVN C201-C202 (PRN C19-C20) and inter-plane satellite pair SVN C201-C203 (PRN C19-C27), respectively, on DOY 335, 2019 when using ground tracking observations. It shows that, for intra-plane satellites, correlations among orbit parameters are insignificant except for relatively higher correlations between several SRP parameters (e.g., D0 and Bc1). For inter-plane satellites, the orbit parameters of different satellites are almost totally uncorrelated with each other. Correlations of SRP parameters existing among intra-plane satellites also vanish.
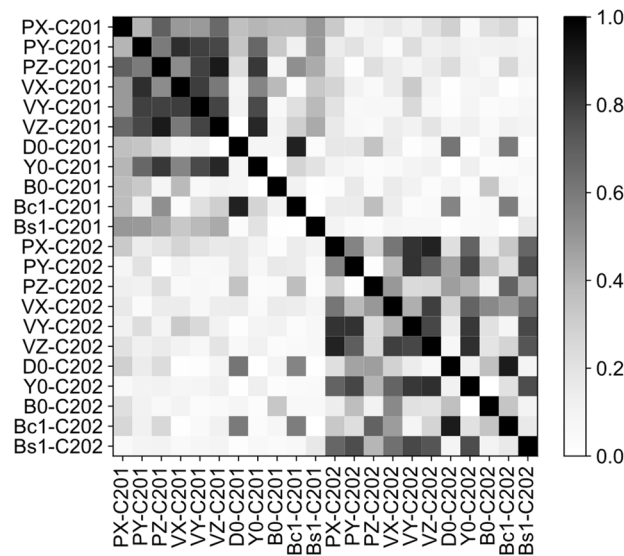
Figure 3.1 Correlations among orbit parameters of the intra-plane satellite pair SVN C201-C202 (PRN C19-C20) on DOY 335, 2019 when using ground tracking observations
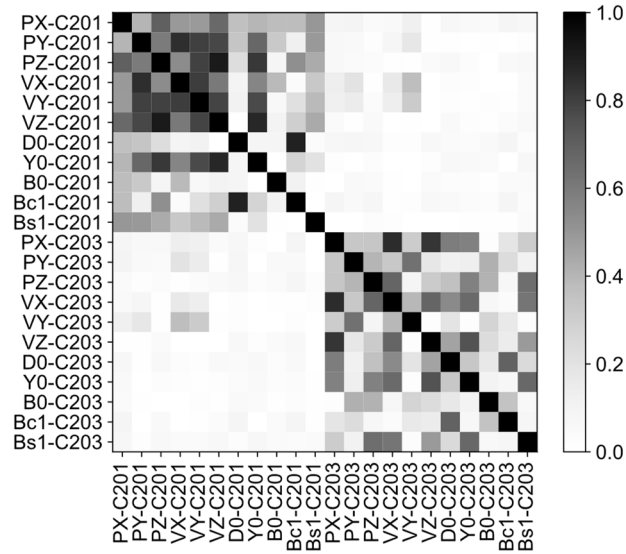
Figure 3.2 Correlations among orbit parameters of the inter-plane satellite pair SVN C201-C203 (PRN C19-C27) on DOY 335, 2019 when using ground tracking observations

Likewise, in the case of using ISL observations, the correlations among orbit parameters of the intra-plane satellite pair SVN C201-C202 (PRN C19-C20) and inter-plane satellite pair SVN C201-C203 (PRN C19-C27) on DOY 335, 2019 are shown in Figure 3.3 and Figure 3.4, respectively. Significant correlations of orbit parameters can be found for both intra- and inter-plane satellites. Those correlations mainly occur among the six initial state parameters. Additionally, an obvious increase in the correlations between the SRP parameter B0 and the initial state parameters can be observed compared to that of using ground tracking data, especially for inter-plane satellites. Furthermore, the individual satellite also shows prominent correlations between its initial state parameters.
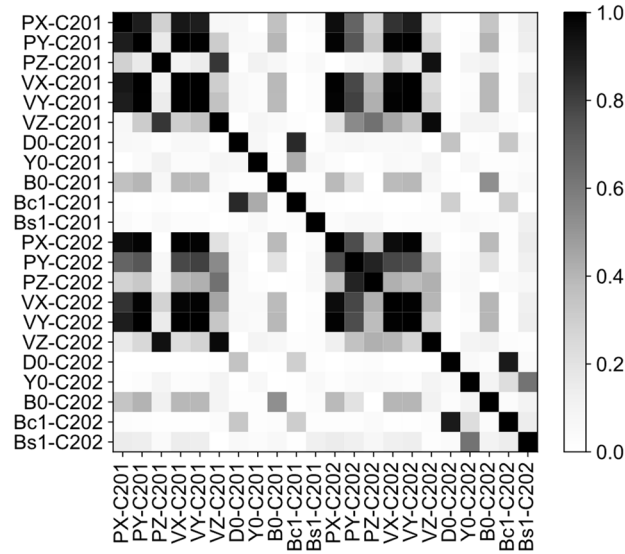
Figure 3.3 Correlations among orbit parameters of intra-plane satellite pair SVN C201-C202 (PRN C19-C20) on DOY 335, 2019 when using ISL
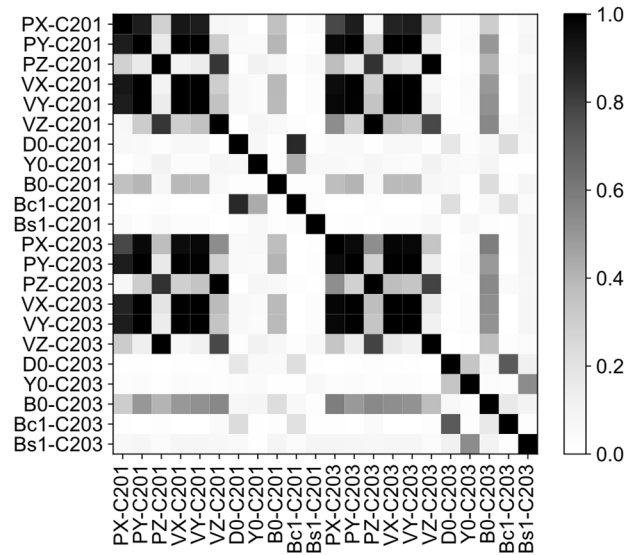
Figure 3.4 Correlations among orbit parameters of inter-plane satellite pair SVN C201-C203 (PRN C19-C27) on DOY 335, 2019 when using ISL

3.3 Orbit Determination

The ephemeris update procedure for the AutoNav mode runs actually in an onboard distributed processing system. Limited by the computation capability, only a sub-optimal solution can be obtained. Each satellite estimates only its own orbit and clock parameters using ISL measurements to other satellites in view (Ananda et al. 1990). However, for the performance evaluation and error analysis, a centralized processing system is more appropriate.

Orbit parameters of all satellites within the constellation are adjusted in a single estimator based on the whole set of ISL observations.

In this section, orbit determination results of BDS-3 satellites using the ISL derived range observations are analyzed detailedly. The observation equation, used ISL data, and adopted orbit modelling strategies are referred to Section 2.2 and 2.3. The a priori standard deviations of orbit initial state vectors are set to 10 km and 0.1 km/s for positions and velocities, respectively. Indeed, the a priori constraints are too pessimistic for broadcast ephemerides in most cases though preventing any severe contamination. By properly constraining the a priori orbits, the datum for RAANs can be provided. However, this is not the focus of this section. The homogeneous a priori standard deviation of 10 cm is used for the ISL observations of all satellites.

3.3.1 Fitting Residuals

Figure 3.5 displays the fitting residuals of ISL range observations resulting from BDS-3 orbit determination on DOY 335, 2019 (MJD 58818). Statistics of the residuals, i.e., the mean, STD, and RMS, are labeled at the top right corner of the figure. The overall RMS of residuals is 7.4 cm. And there is no significant bias found in the residual series. The number of valid observations of 142636 is also annotated on the figure. Over the entire month, the number of valid daily observations is between 142 and 212 thousand, with an average of 180 thousand. Besides, the residual histogram is presented in Figure 3.6. It shows a good unimodal symmetric distribution. Residuals of other daily sessions are not too dissimilar.
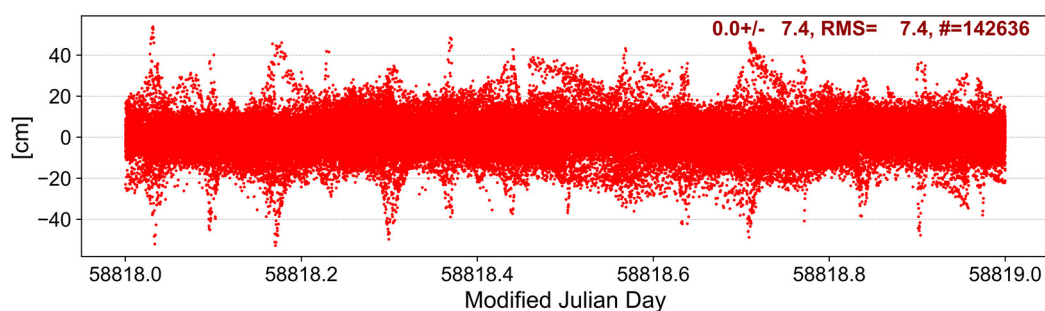
Figure 3.5 Fitting residuals of ISL range observations on DOY 335, 2019
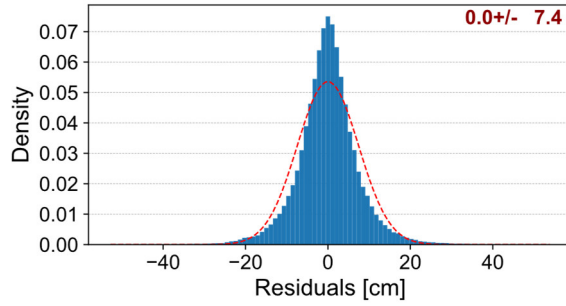
Figure 3.6 Histogram of ISL range observation fitting residuals on DOY 335, 2019

The daily RMSs of fitting residuals over the period of DOY 335~365, 2019 are shown in Figure 3.7. Basically, all the daily fitting RMSs are below 7.0 cm. The differences of fitting residual RMS among daily sessions are minor. The average daily fitting RMS is ~6.7 cm.
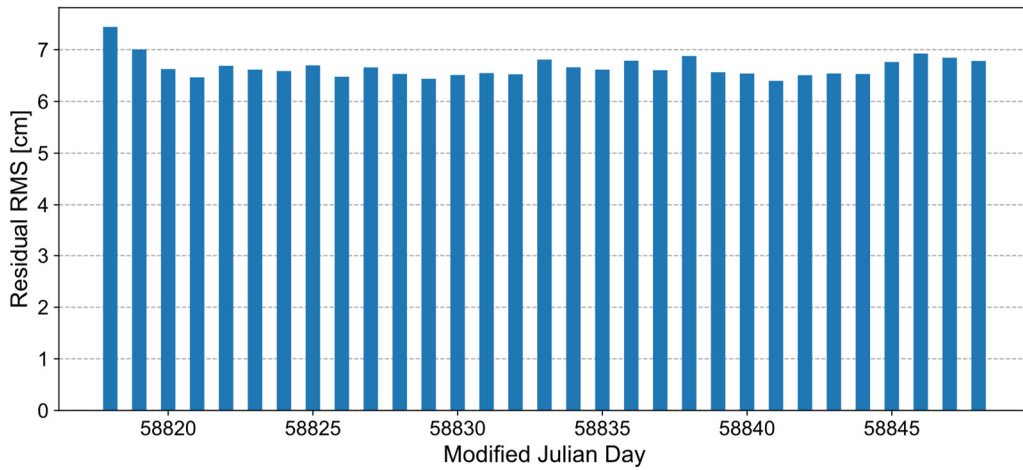
Figure 3.7 Daily fitting residual RMS of ISL range observations over DOY 335~365, 2019
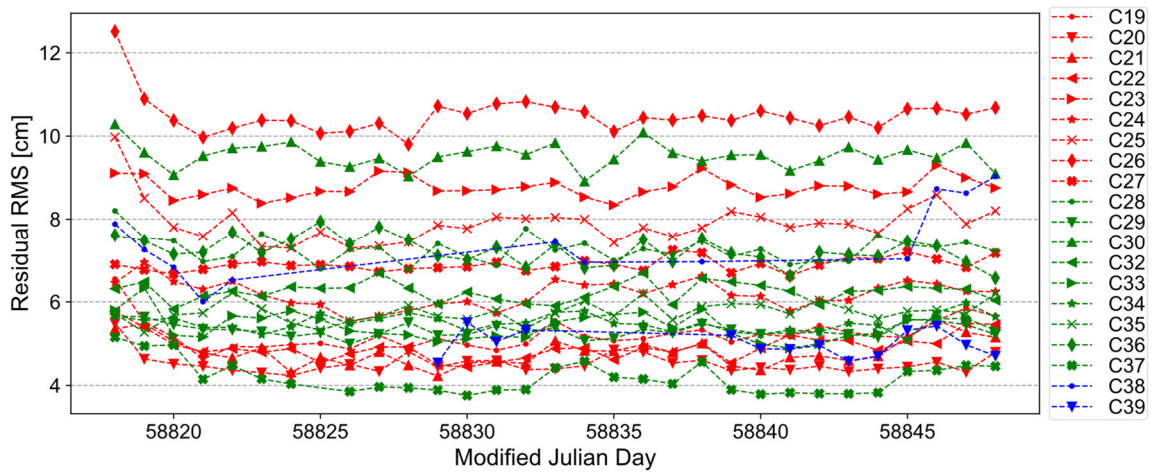
Figure 3.8 Daily fitting RMS of ISL range observations for each satellite over DOY 335~365, 2019
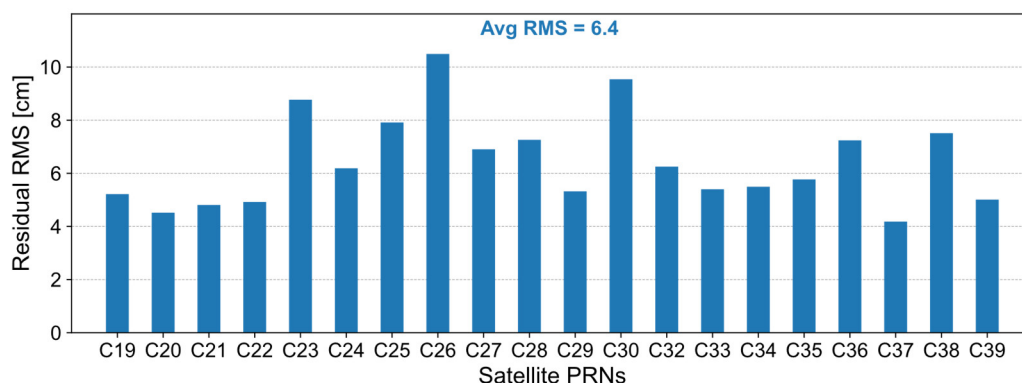
Figure 3.9 Overall fitting RMS of ISL range observations for each satellite over DOY 335~365, 2019

Figure 3.8 shows the daily fitting RMS series of ISL range observations for each satellite. And the overall RMSs for each satellite over the period of DOY 335~365, 2019 are presented in Figure 3.9. In Table 3-1, the values of overall fitting RMSs of each satellite are listed. For most satellites, the daily fitting RMSs are very stable. The fitting RMS of IGSO satellite C38 shows relatively significant variations. An increase of around 2 cm in the daily RMS can be observed for the last three days. Satellite C38 was absent in broadcast ephemerides for more than half of the 31 daily sessions. Thus, solutions from only 12 daily sessions are available for C38 because of the lack of a priori orbits. This may indicate some payload maintenances for C38 during this period which could also explain the unsteady ISL residuals.

The fitting residual RMS exhibits significant differences among satellites, which is probably caused by the different thermal noise levels of ISL receivers (Zhou et al. 2018). The satellite showing the smallest RMS is C37, around 4 cm. Satellite C26 has the largest RMS, which is more than 10 cm. The RMS of most satellites is 4~8 cm, and the constellation average is 6.44 cm. Satellite C23 and C30 also display relatively larger fitting residuals. Among the three BDS-3 MEO planes, satellites from plane B generally show smaller residuals compared to the other two planes (except for C37 of plane C).

Table 3-1 Overall fitting RMS of ISL range observations for each satellite over DOY 335~365, 2019

MEO Plane A		MEO Plane B		MEO Plane C		IGSOs	
PRN	RMS [cm]	PRN	RMS [cm]	PRN	RMS [cm]	PRN	RMS [cm]
C27	6.90	C19	5.22	C23	8.77	C38	7.51
C28	7.26	C20	4.52	C24	6.19	C39	5.01
C29	5.32	C21	4.81	C25	7.91		
C30	9.54	C22	4.92	C26	10.49		
C34	5.50	C32	6.25	C36	7.24		
C35	5.77	C33	5.40	C37	4.18		
Mean	6.72	Mean	5.19	Mean	7.46	Mean	6.26

Mean	6.44	

Since the derived observations have already been corrected for the ISL phase center errors, they should be free of any heterogeneous errors concerning the directions of links. To check for possible direction-dependent patterns, residuals of six satellites are plotted against their azimuth and nadir angles as in Figure 3.10. Each two of those satellites are from the same BDS-3 MEO orbit plane (See Figure 2.1, C28/C30 from plane A, C32/C33 from plane B, and C23/C26 from plane C) and exhibit the noisiest residuals among all satellites orbiting on the same plane. For none of these satellites, an obvious direction-related pattern can be found. For C26, it seems that a lot of noisier observations are concentrating within the region of azimuth 270°~90°, nadir 10°~35°. But if looked at closely, this should be more attributed to specific links rather than the satellite itself.
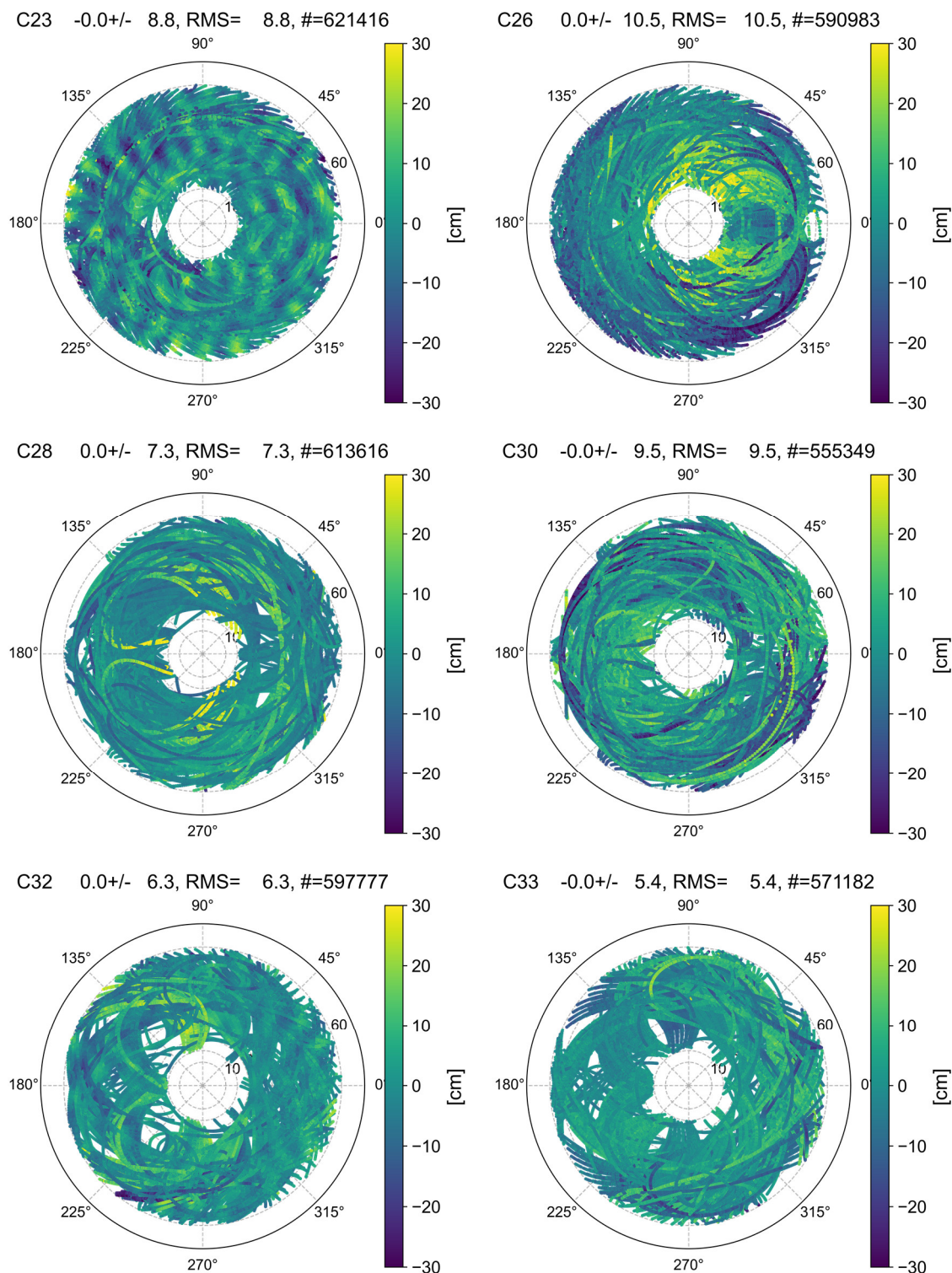
Figure 3.10 Sky plots of ISL range observation residuals of C23 and C26 (from plane C), C28 and C30 (from plane A), as well as C32 and C33 (from plane B)

In Figure 3.11, the overall RMSs of link residuals between each satellite pair are presented. Satellite PRNs labeled along the axes are colored differently to discriminate their orbiting plane. For individual satellites, the residuals hardly show significant differences between intra-and inter-plane links. Satellites with large residual RMS, e.g., C23, C26, and C30, show relatively

larger residuals when linked with whichever satellite. The three links with the largest residual RMS are related to C26, i.e., C26-C28, C26-C30, and C26-C27. The residual RMSs of those links are 16.7, 14.2, and 13.9 cm, respectively. As found earlier from the comparison of satellite residual RMSs, links involved satellites from plane B generally have smaller residuals.
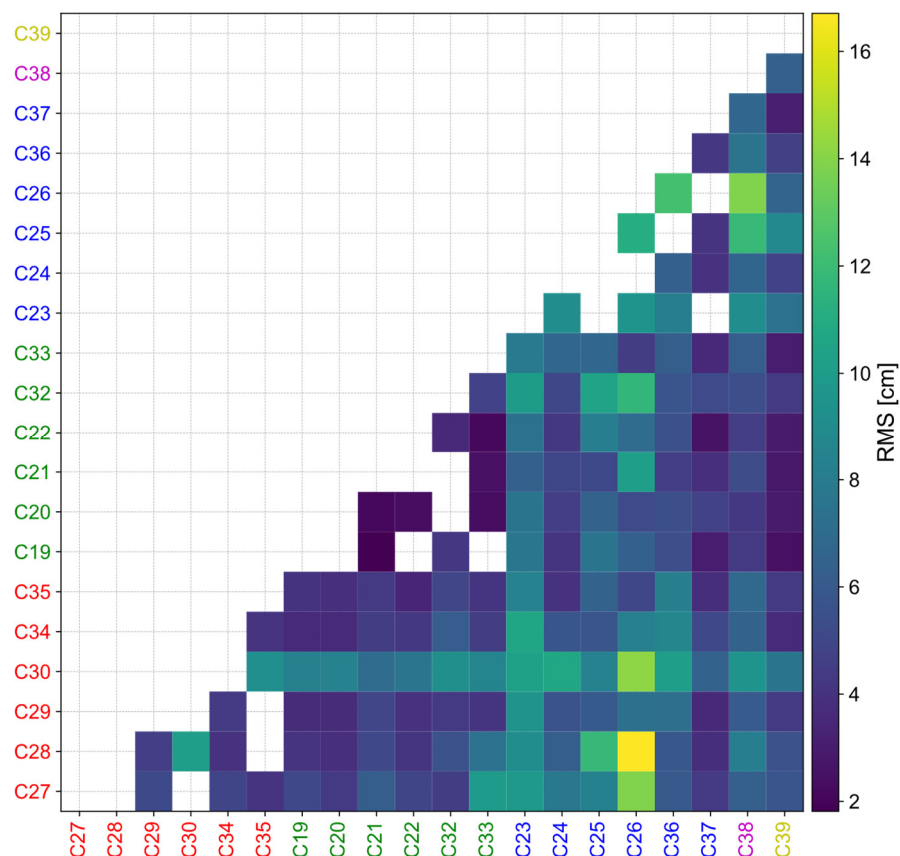
Figure 3.11 Overall RMS of link residuals between each satellite pair. Satellite PRNs labeled along axes are colored according to their orbit planes (Red, BDS-3 MEO plane A; Green, BDS-3 MEO plane B; Blue, BDS-3 MEO plane C; Others, BDS-3 IGSOs)

3.3.2 Orbits

Precisions of estimated orbits are usually evaluated by orbit differences between consecutive processing arcs at the boundary. In the case of a one-day processing arc, it is called the Day Boundary Differences (DBD). As satellites normally never "jump" suddenly from one place to another, the smoothness of calculated orbit arcs at the boundary should mainly reflect mismodelling stochastic errors. The first epoch of the second processing arc is usually taken as the boundary. In this chapter, each daily estimated orbit arc was extrapolated six epochs backward at the start and forward at the end of the observation session, so that the boundary is extended to a short arc that contains 12 epochs. Consequently, every two consecutive arcs

share a short overlapping arc of 12-epochs length. It should be noted that this approach for DBD calculation is limited within this chapter. In the other chapters of this study, a single epoch arc boundary was still adopted as the convention.

Figure 3.12 shows the overall DBD RMS of BDS-3 orbits estimated from ISL derived range observations during the period of DOY 335-365, 2019. The radial components are plotted along the y-axis on the left side, while the along-track, cross-track, and 1D components are presented using the y-axis on the right side for a better display. Note the different scales of those two axes. Due to the lack of observability, orbital along-track and cross-track components were basically not determined. Average RMSs of DBD in the orbital along-track and cross-track directions reach up to 373.32 and 371.40 m, respectively. However, the radial component RMS for most satellites is 2.22~4.21 cm. As analyzed in Sec 3.2, unlike orientations, sizes, i.e., semi-major axes of orbits, can still be observed by ISLs. The IGSO satellites C38 and C39 have apparently larger RMSs than BDS-3 MEOs, getting to 12.4 and 9.8 cm, respectively. Among the MEOs, the radial RMS of C30 with 7.3 cm is relatively larger than others.
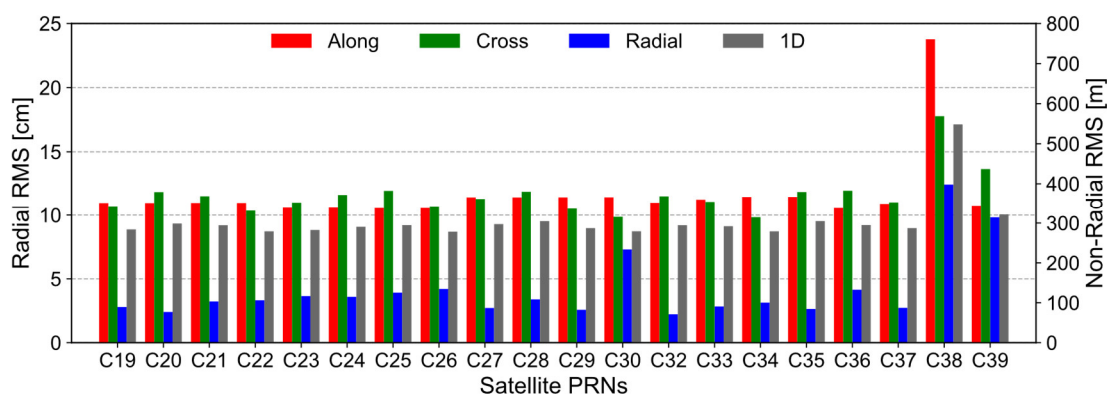
Figure 3.12 Overall orbit DBD RMS based on ISL relative range observations over DOY 335-365, 2019

Orbit rotations caused by the unobservability of RAANs when using ISL range measurements can be regarded as systematic errors. A Helmert transformation between the two sessions to be compared should eliminate or absorb most of them. Figure 3.13 presents the orbit DBD RMS after Helmert transformations were applied in the day boundary comparisons, which are 7.03, 4.56, and 3.54 cm on average in the orbital along-track, cross-track, and radial directions, respectively.
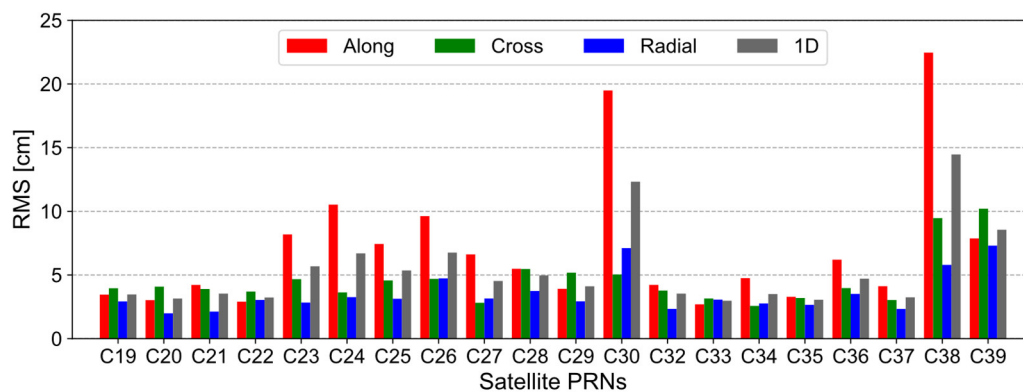
Figure 3.13 Overall orbit DBD RMS based on ISL range observations over DOY 335-365, 2019. Systematic differences between daily solutions were removed via Helmert transformations.

In Figure 3.14, the Helmert transformation parameters estimated from the comparison of day-boundary orbits are shown. Not surprisingly, the variation of the rotation components around the Z-axis is most significant.
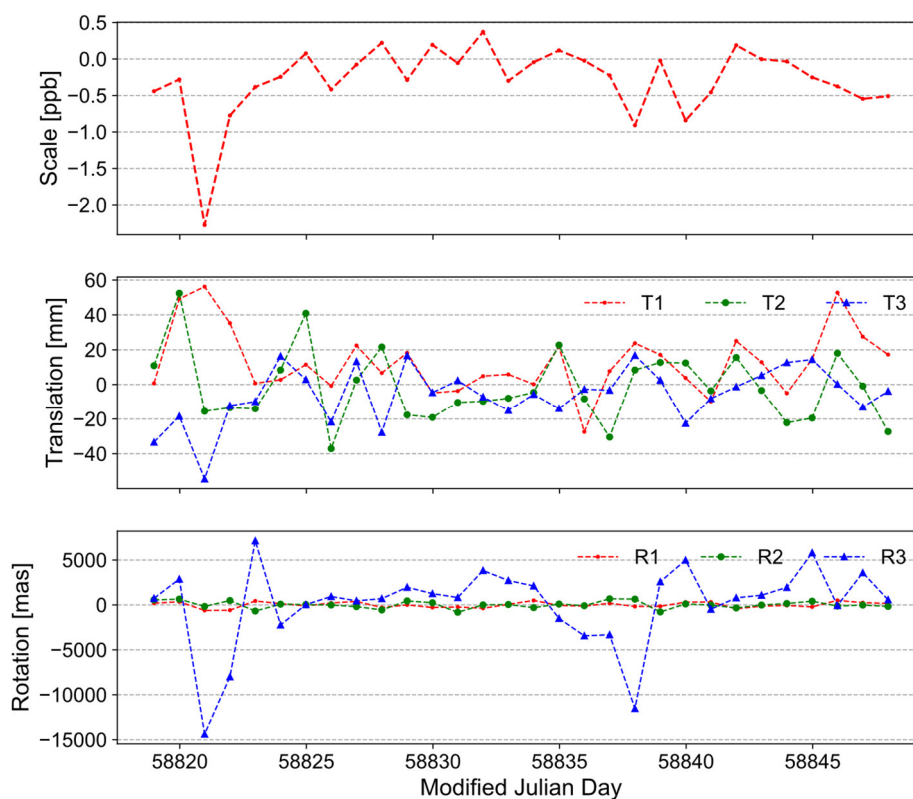
Figure 3.14 Helmert transformation parameters obtained from the comparisons of day boundary orbits

Additionally, the orbits estimated using only ISL observations were compared with those calculated by L-band ground tracking measurements. The 7-parameters Helmert transformation was applied in each daily comparison. Figure 3.15 shows the RMS of orbit differences between the ISL and ground tracking solutions over DOY 335-365, 2019.
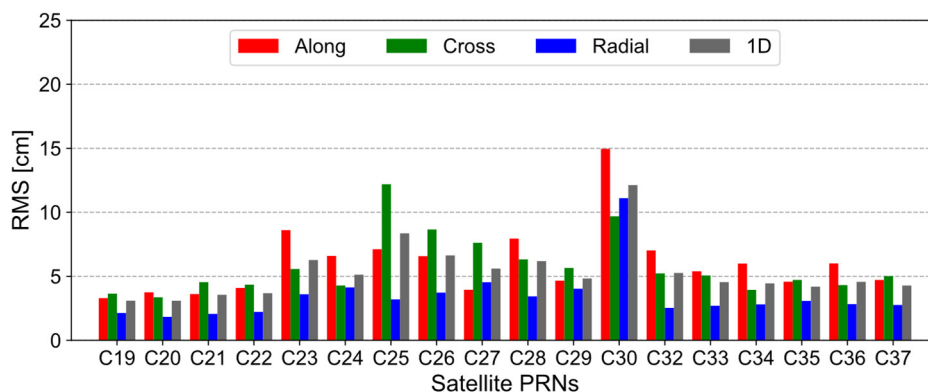
Figure 3.15 Orbit difference RMS between the ISL and ground tracking solutions over DOY 335-365, 2019. Systematic differences between ISL and ground tracking solutions were removed via Helmert transformations.

After removing the systematic errors induced by unobservability, the accuracy of orbits determined by ISLs can reach 6.05, 5.79, and 3.49 cm in the along-track, cross-track, and radial directions, respectively. The average 1-D RMS is ~5.33 cm. Except for C30, the radial RMS of all other satellites are within 5.0 cm. Similar to the case of DBD, satellite C30 shows a larger RMS than others.

The Helmert parameters calculated in the comparisons of ISL orbits with ground tracking orbits are displayed in Figure 3.16.
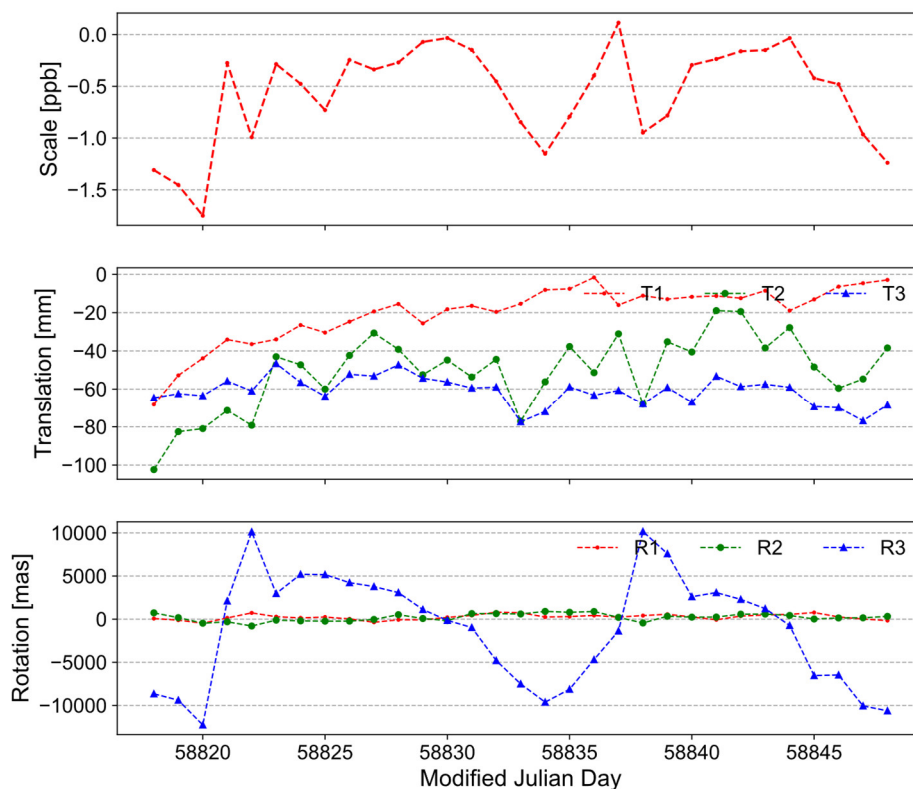
Figure 3.16 Helmert transformation parameters obtained from the comparisons of orbits estimated using ISLs with that estimated by ground tracking

Table 3-2 Statistics of Helmert transformation parameters calculated from the comparisons of orbits estimated using ISLs with that estimated by ground tracking

Helmert Parameters	Mean	STD	RMS
Scale [ppb]	-0.57	0.46	0.73
T1 [mm]	20.29	14.79	25.11
T2 [mm]	50.88	19.28	54.41
T3 [mm]	61.18	7.46	61.64
R1 [mas]	-238.50	315.04	395.13
R2 [mas]	-201.41	425.08	470.38
R3 [mas]	1201.84	6291.29	6405.06

Furthermore, the orbit RAANs of ISL orbits were compared to those of ground tracking orbits. The RAAN differences of three satellites, i.e., C19, C23, and C27 which are orbiting on different planes, are depicted in Figure 3.17. Despite slight differences among various orbit planes regarding the statistics, the variations of RAAN differences are highly consistent with the rotation Z-axis component obtained via the Helmert transformation, as shown in Figure 3.16.
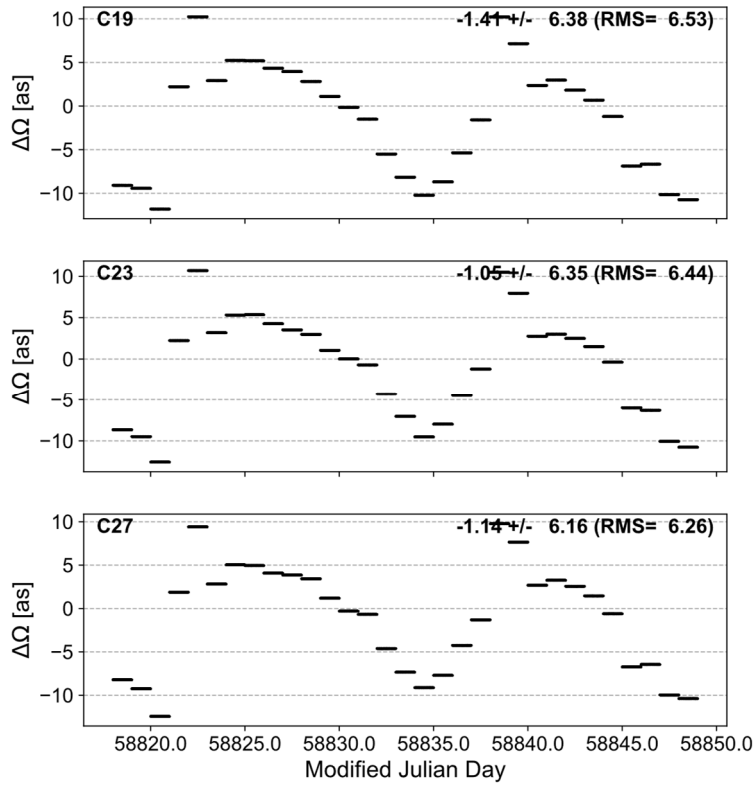
Figure 3.17 Orbit RAAN differences between ISL orbits and ground tracking orbits

3.3.3 Hardware Delays

As described in Equation (2.16), ISL hardware delays of satellites are estimated together with orbit parameters in the orbit determination. Those satellite-specific hardware delays estimated are the sum of the transmitting and receiving delays of ISL instruments. In Figure 3.18, the estimates of ISL hardware delays of each satellite are shown. Averages over the one-month session have been removed to exhibit only the variations. The averages of hardware delays over DOY 335~365, 2019, as well as their standard deviations are listed in Table 3-3. Satellites from different manufacturers are listed separately. Basically, except for satellite C39, variations of hardware delays during the one-month session are very small. However, some date-dependent deviations can still be clearly noted. For instance, daily solutions of MJD 58818~58822, 58833-58834, 58838, and 58845 deviate more from the averages. Among MEOs, satellite C23 gets the largest STD of 0.17 ns (~5.1 cm). On average, the overall stability of hardware delays for all satellites except for C39 is 0.13 ns (~3.9 cm). As only 14 daily solutions are obtained for satellite C39, the large STD of 0.42 ns (~12.6 cm) might not be so reliable.

To some extent, magnitudes of ISL hardware delays are related to the satellites' manufacturers. For satellites assembled by the CAST, except for C23, C32, and C36, the maximum difference

of ISL hardware delays among satellites is only 2.34 ns, i.e., the difference between C21 and C24. The hardware delays of IGSO satellites C38 and C39 are very close to that of most CAST-made MEO satellites. As to SECM-manufactured satellites, considerable differences are found among individual satellites. On the whole, except for C39, the stability of ISL hardware delays of satellites from CAST is similar to that of SECM satellites.
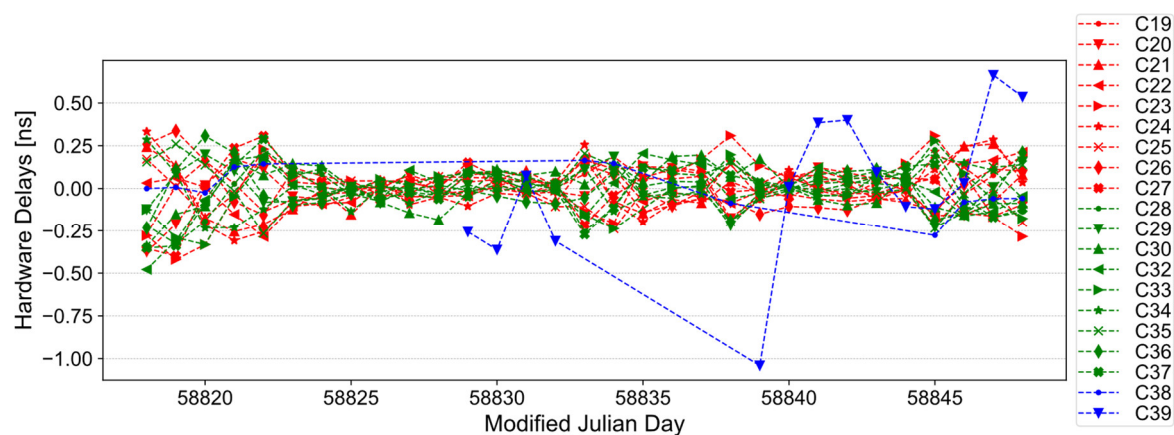
Figure 3.18 Estimated hardware delays in ISL range observations for the period of DOY 335~365, 2019. The overall satellite-specified average has been removed accordingly.

Table 3-3 Averages of ISL hardware delays in the range observations and their STDs over DOY 335~365, 2019

CAST			SECM		
PRN	Mean [ns]	STD [ns]	PRN	Mean [ns]	STD [ns]
C19	1192.42	0.11	C25	1949.87	0.11
C20	1192.82	0.12	C26	1956.05	0.12
C21	1192.09	0.13	C27	2124.01	0.14
C22	1192.68	0.10	C28	2494.07	0.13
C32	75536.29	0.14	C29	1990.35	0.10
C33	1193.47	0.14	C30	1995.01	0.13
C23	72967.09	0.17	C34	1990.83	0.11
C24	1194.43	0.15	C35	1992.69	0.11
C36	75545.20	0.12			
C37	1193.91	0.15			
C38	1198.57	0.12			
C39	1197.79	0.42			
Avg		**0.13**			**0.12**
Avg	0.13 (except for C39)				

3.4 Harmonic Signals in the Link Residuals

Figure 3.19 illustrates the residual series of ISL range observations of links C21-C29, C22-C30, and C28-C30 on DOY 335, 2019. There seems to be some periodic signals existing in the residuals series. Moreover, the characteristics of those signals differ from link to link. For link C28-C30, the signal runs approximately two cycles within the day, while it is almost four cycles for link C22-C30. The second cycle of the signal in link C22-C30 seems to have a smaller amplitude, indicating the signal may be composed of more than one periodic component. Despite much smaller amplitude, the periodic signal existing in the link C21-C29 is still very clear. Residuals series of many other links not showed here also exhibit similar signals. It should be noted that similar periodic signals were also found in the link residuals of BDS-3 experimental satellites (Xia 2018). But except for attributing it to errors in the a priori orbits, no further investigation was made. As more rigid than GNSS phase measurements, mismodelling errors are more visible in the residuals of ISL (Michalak et al. 2021).
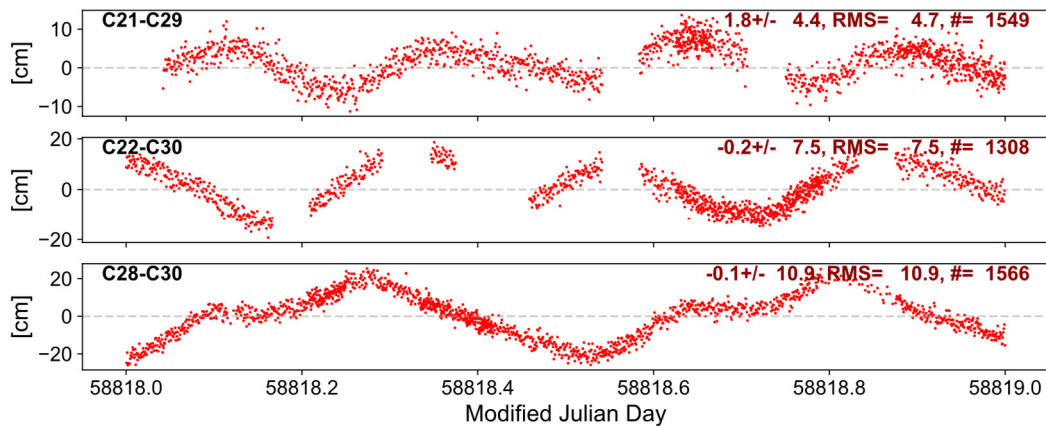
Figure 3.19 Rang residual series of link C21-C29, C22-C30, and C28-C30 on DOY 335, 2019

3.4.1 Spectrum Analysis on the Link Residuals

The Lomb-Scargle periodogram is a widely used statistical tool designed to detect periodic signals in unevenly spaced time series (Lomb 1976; Scargle 1982; VanderPlas 2018). It is suitable for analyzing the links residual series. Implementations from the community-developed core Python package for Astronomy (Collaboration et al. 2013; Price-Whelan et al. 2018) were used in this study.

Lomb-Scargle periodograms of ISL range residuals of links C19-C21, C20-C22, C24-C29, C25-C27, C26-C28, and C36-C37 on DOY 335, 2019 are given in Figure 3.20. For each link,

the variation of Lomb-Scargle power along the oscillation frequency is plotted as the solid blue line. The frequency with the maximum Lomb-Scargle power is annotated around the peak. The peak frequency is the frequency of a sinusoidal model that fits the residual series best. Additionally, the link residual series is displayed in an inset axis at the top right corner with its best-fit sinusoid plotted over. To quantitively exhibit the proportion of periodic errors, the RMSs of both the raw residuals and that obtained after removing the best-fit sinusoid are shown at the top left corner in red text and the bottom left corner in green text of the inset axis, respectively. Supplementarily labeled within the parentheses after the signal-free RMS text is the decreased percentage of the RMS.

Clear periodic signals can be found in all of those links' range residuals. Powers of peak frequencies are significantly higher than other sample frequencies, especially for links C19-C21, C20-C22, C24-C29, and C36-C37. After removing the best-fit signals, a convincing decrease of the residual RMS can be observed for all links, with a percentage of 20% ~ 75 %. Even for links with less noisy residuals, such as C19-C21 and C20-C22, eliminating the peak periodic signal reduces the RMS further.
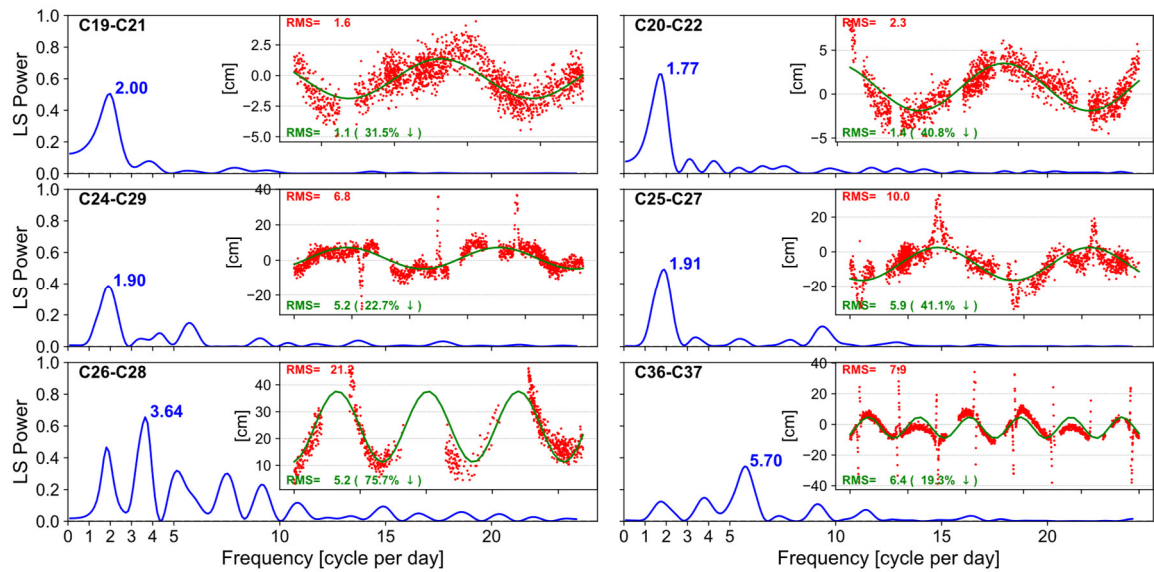
Figure 3.20 Lomb-Scargle periodograms of ISL range residuals of MEO-MEO links C19-C21, C20-C22, C24-C29, C25-C27, C26-C28, and C36-C37 on DOY 335, 2019

To obtain more sound estimates of periodic signal components, link residual series spanning the whole period considered in this study, i.e., DOY 335~365, 2019, were fitted using the Lomb-Scargle models. Results of the same links above are shown in Figure 3.21. The meanings of different parts of this figure are similar to that of Figure 3.20. Based on the extended series, periodic components in each link are more conspicuous. For links C19-C21, C20-C22, and C25-C27, there is only one dominant signal, while for links C26-C28 and C36-C37, two signals

with comparable power can be found. For many other links not shown here, usually, several signal components are found. If just removing the peak signal for the link, a reduction of 11%~71% in the residual RMS would be expected. For example, the overall RMS of link C26-C28 would decline by ~12 cm, from 16.7 to 4.9 cm.
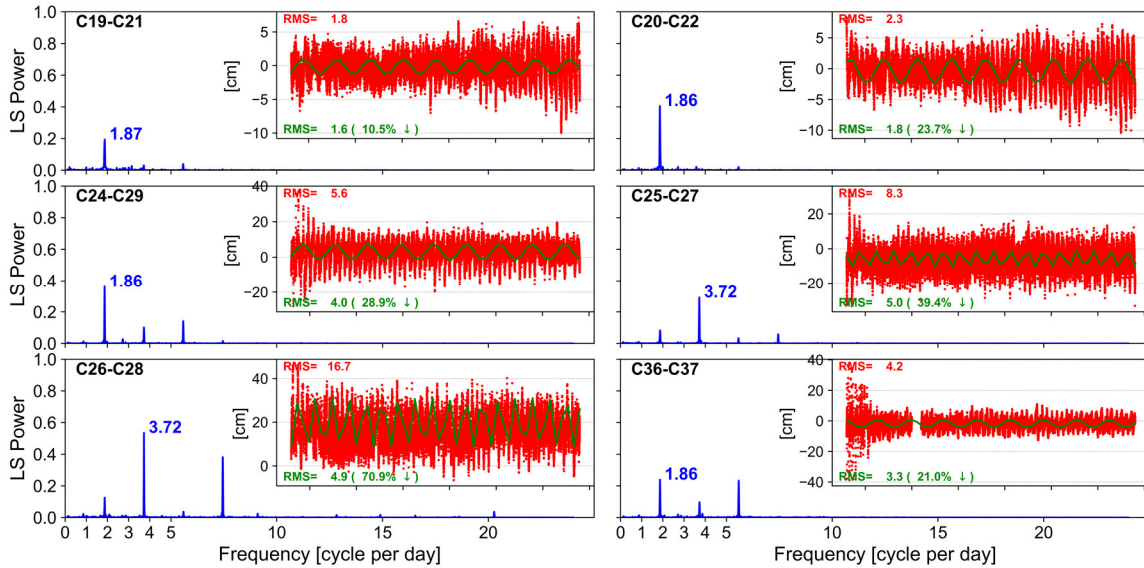
Figure 3.21 Lomb-Scargle periodograms of ISL range residuals of MEO-MEO links C19-C21, C20-C22, C24-C29, C25-C27, C26-C28, and C36-C37 for the period DOY 335~365, 2019

Regarding the frequencies of those periodic signals shown in Figure 3.21, it is not difficult to find that all of them are integral multiples of 1.86. Recalling the designed orbit height of BDS-3 MEOs, connections between those harmonic signals and satellites' orbit period of ~12 hours 53 minutes are obvious.

In Table 3-4, monthly averages of the frequencies (in cycles per day) and periods (in seconds) of orbit motions of BDS-3 MEOs are listed. Standard deviations indicating the stability of orbit periods for one month are also listed aside. Differences in orbit periods among individual BDS-3 MEO satellites are quite small. The shortest period, i.e., that of C30 is only less by 0.43 sec than the longest one, e.g., that of C20. For each satellite, the temporal variation of the orbit period is minor. The monthly stability for the whole constellation is ~ 3 sec. That may explain why the frequencies of periodic signals in different links share the same fundamental frequency and keep consistent over the whole month.

Table 3-4 Monthly means and their variations of orbit motions of BDS-3 MEOs

PRN	Frequency [cycle/d]	Period [sec]	STD [sec]	PRN	Frequency [cycle/d]	Period [sec]	STD [sec]
C19	1.862319	46393.78	2.99	C28	1.862329	46393.52	2.82
C20	1.862316	46393.86	2.99	C29	1.862330	46393.52	2.81

C21	1.862318	46393.78	2.99	C30	1.862333	46393.43	2.81
C22	1.862318	46393.78	2.99	C32	1.862317	46393.78	2.99
C23	1.862317	46393.78	3.00	C33	1.862319	46393.78	2.99
C24	1.862322	46393.69	3.00	C34	1.862327	46393.60	2.80
C25	1.862314	46393.86	3.01	C35	1.862330	46393.52	2.80
C26	1.862316	46393.86	3.01	C36	1.862317	46393.78	3.01
C27	1.862329	46393.52	2.82	C37	1.862320	46393.78	3.01

Knowing that those periodic signals resonate with the orbit motion, it is natural to consider modelling them by a harmonic function. The harmonic function model used in this study takes the orbit motion as its fundamental frequency, as described by Equation (3.11)

$$f(t) = \sum_{i=1}^{N} A_i \cos(s_i nt - \phi_i)$$

$$= \sum_{i=1}^{N} [A_i \sin\phi_i \sin(s_i nt) + A_i \cos\phi_i \cos(s_i nt)]$$

(3.11)

where N is the number of periodic signals to be considered; A_i, ϕ_i and s_i are the amplitude, initial phase, and number of Cycles Per orbit Revolution (CPR) for each signal, respectively; n denotes the mean motion of BDS-3 MEO satellites. Due to the negligible difference in orbit periods, a uniform orbit motion can be used for all links established between MEOs. It should be noted that, because an ISL hardware delay parameter is already included, as shown in Equation (2.16), a constant term is not necessary for the proposed model.

However, for MEO-IGSO links, as shown in Figure 3.22, signal components exhibited in the periodograms are not very clean. It might be caused by the different orbit motions between the two linked satellites. Also, the continuity of MEO-IGSO links is much worse than that of MEO-MEO links. This could also compromise the effectiveness of Lomb-Scargle fitting or even generate unreliable signals. Therefore, the proposed periodic function model was not applied on any MEO-IGSO links.

For the IGSO-IGSO link, i.e., C38-C39 shown in Figure 3.23, it also presents very clear resonance signals of odd CPRs. And the power decreases gradually at the medium-high frequency band. Though eliminating only the peak signal, i.e., the 3CPR signal would shrink the residuals by ~71%, this link was also not modeled in this study. A dedicated investigation on the IGSO-IGSO as well as MEO-IGSO links is reserved for further study.
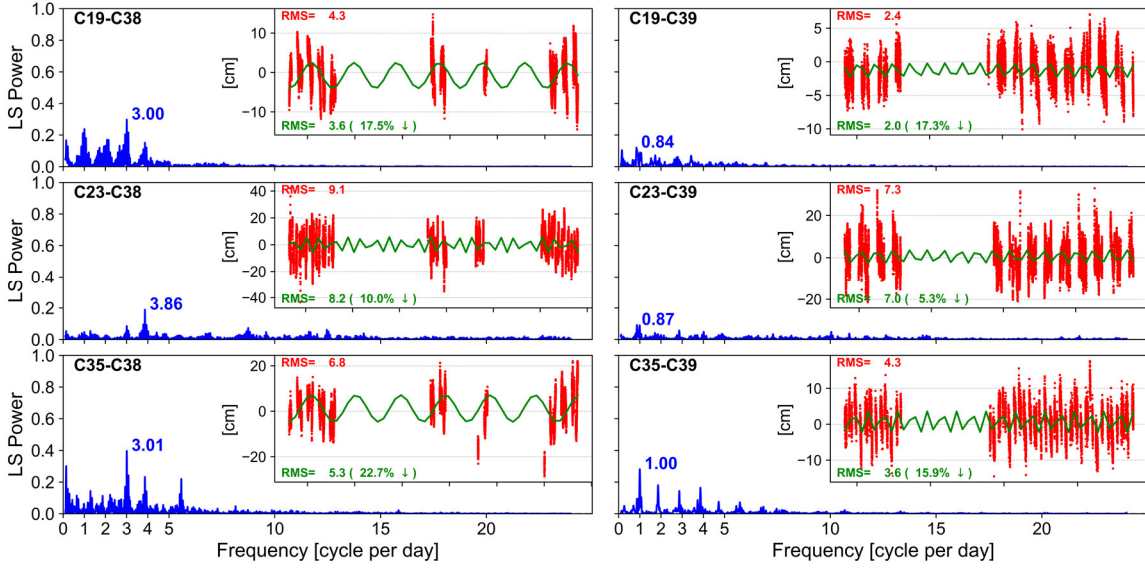
Figure 3.22 Lomb-Scargle periodograms of ISL range residuals of MEO-IGSO links C19-C38, C19-C39, C23-C38, C23-C39, C35-C38, and C35-C39 for the period DOY 335~365, 2019
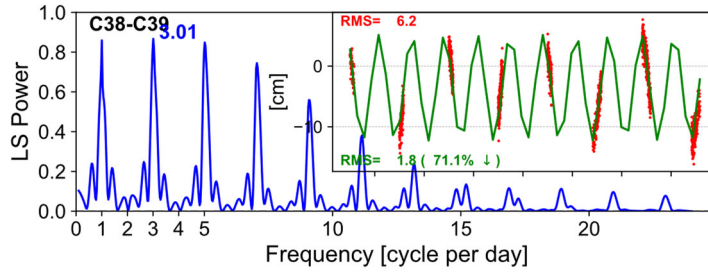
Figure 3.23 Lomb-Scargle periodograms of ISL range residuals of the IGSO-IGSO link C38-C39 for the period DOY 335~365, 2019

To verify the effectiveness of the proposed periodic function model in Equation (3.11), three specifically parameterized models with different periodic terms as listed in Table 3-5 have been examined. It should be mentioned that, except for 1CPR and 2CPR signals, several higher frequency components were also found for some links. Rather than completeness, a feasibility demonstration is more emphasized in this work. Therefore, the proposed model should work as well for other signals if proven to be effective for the signals considered here.

Table 3-5 Specific parameterization models for absorbing harmonic signals in the ISL range observations

Models	Number of signals considered	Signal frequencies [CPR]	Parameters to be estimated
Model 1	1	$s_1 = 1$	$A_1\sin\phi_1,\ A_1\cos\phi_1$
Model 2	1	$s_1 = 2$	$A_1\sin\phi_1,\ A_1\cos\phi_1$
Model 3	2	$s_1 = 1,\ s_2 = 2$	$A_1\sin\phi_1,\ A_1\cos\phi_1,$ $A_2\sin\phi_2,\ A_2\cos\phi_2$

3.4.2 Impact on Fitting Residuals

Figure 3.24 compares satellite residual RMS after applying different parameterized models on DOY 335, 2019. As could be expected, periodic function models reduce the residual RMS for all satellites. Because of different signal components existing in each link, the applicability of Model 1 and Model 2 differs from satellite to satellite. Using Model 3 is much better than any of the former two models. This is foreseeable as it absorbs both the 1CPR and 2CPR periodic signals. The range residual RMSs of most satellites are below or around 4 cm when Model 3 is adopted.
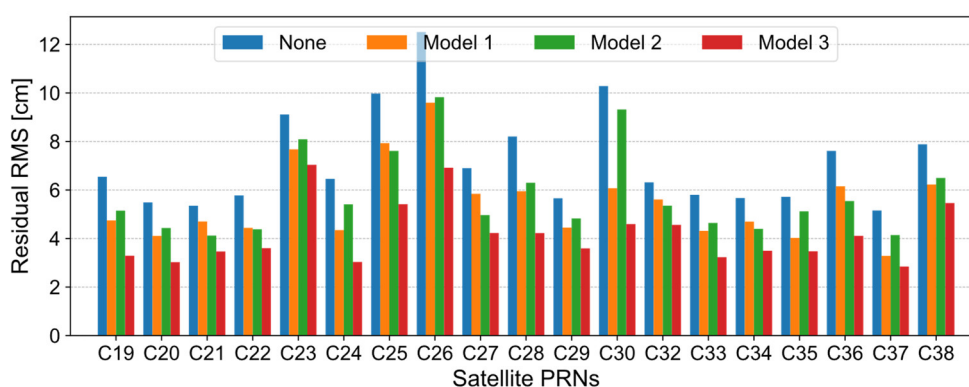
Figure 3.24 Satellite residual RMS of ISL range observations using different periodic function models on DOY 335, 2019

Satellite residual RMSs over the whole month of solutions with different periodic function models are listed in Table 3-6. Percentages of variations of satellite residual RMS with respect to that of the solution without any model applied are also given. On the whole, both Model 1 and Model 2 can mitigate ~16% of the satellite residuals. But for individual satellites, the capability of those two models is different. For example, for satellites C25 and C26, Model 2, which reduces the RMS by 24%~26%, works better than Model 1, with which only a 10%~12% decline was found. On the contrary, for C30, a decrease of more than 30% is observed when using Model 1, while only less than 10% decrement is obtained when Model 2 is adopted. Although C25 and C26 orbit on a different plane from C30, it is hard to attribute those divergences to satellites' orbit planes after a close comparison.

Capable of eliminating both the 1CPR and 2CPR signals, Model 3 decreases the satellite residual RMS by ~34% on average. A whole constellation RMS of 4.22 cm was reached. Although links established with IGSOs are not modeled, IGSO satellites, i.e., C38 and C39, also benefit from the wiping out of periodic errors in other links. Probably because of noisier observations than C39, relatively higher reductions were found for C38.

Table 3-6 Satellite residual RMS of ISL range observations over DOY 335~365, 2019 resulting from different periodic function models and their variation percentages wrt the solution without any model

PRN	Model 1		Model 2		Model 3	
	RMS [cm]	Change [%]	RMS [cm]	Change [%]	RMS [cm]	Change [%]
C19	4.31	-17.43	4.22	-19.16	3.28	-37.16
C20	3.58	-20.80	3.73	-17.48	2.73	-39.60
C21	4.05	-15.80	3.68	-23.49	2.98	-38.05
C22	4.05	-17.68	3.92	-20.33	3.07	-37.60
C23	7.48	-14.71	7.91	-9.81	6.60	-24.74
C24	4.84	-21.81	5.62	-9.21	4.01	-35.22
C25	7.07	-10.62	5.83	-26.30	4.88	-38.31
C26	9.20	-12.30	7.96	-24.12	6.53	-37.75
C27	6.04	-12.46	5.33	-22.75	4.45	-35.51
C28	5.96	-17.91	5.64	-22.31	4.19	-42.29
C29	4.66	-12.41	4.48	-15.79	3.72	-30.08
C30	6.42	-32.70	8.64	-9.43	5.22	-45.28
C32	5.40	-13.60	5.13	-17.92	4.31	-31.04
C33	4.43	-17.96	4.41	-18.33	3.33	-38.33
C34	4.91	-10.73	4.56	-17.09	3.96	-28.00
C35	4.42	-23.40	5.17	-10.40	3.78	-34.49
C36	6.03	-16.71	5.51	-23.90	4.08	-43.65
C37	3.25	-22.25	3.77	-9.81	2.83	-32.30
C38	6.07	-19.17	6.35	-15.45	5.71	-23.97
C39	4.65	-7.19	5.44	8.58	4.82	-3.79
Mean	5.34	-16.88	5.37	-16.22	4.22	-33.86

Figure 3.25 presents the histograms of decreased percentages of link residual RMS of solutions applying different periodic function models with respect to the solution with no model applied. As can be seen, compared to Model 1 and 2, range residuals of more links get remarkably reduced when Model 3 is used. Several links showing increased residuals, i.e., with a negative decrease percentage, are mostly from satellite C39, and the increments are less than 0.5 cm on average.
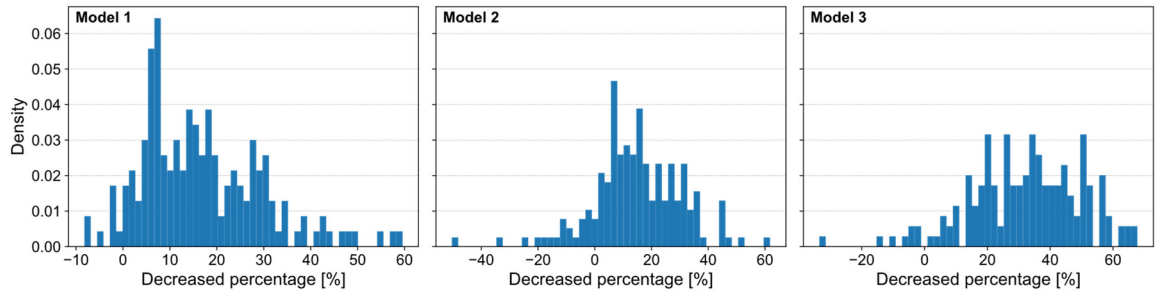
Figure 3.25 Histograms of decreased percentages of link residual RMS of solutions applying Model 1, Model 2, and Model 3 with respect to the original solution without any model

To intuitively demonstrate the success of the proposed model, Lomb-Scargle periodograms of range residuals of links C19-C24 and C22-C25 resulting from different models are displayed in Figure 3.26. The meanings of different parts of this figure are similar to that of Figure 3.20. It shows that all the examined models successfully filter out the parameterized periodic signals. Though some higher frequency signals persist even with Model 3 applied, like the 3CPR in C19-C24 and 4CPR in C22-C25, as mentioned earlier, this should not be a problem if extending the proposed model towards the high-frequency band.
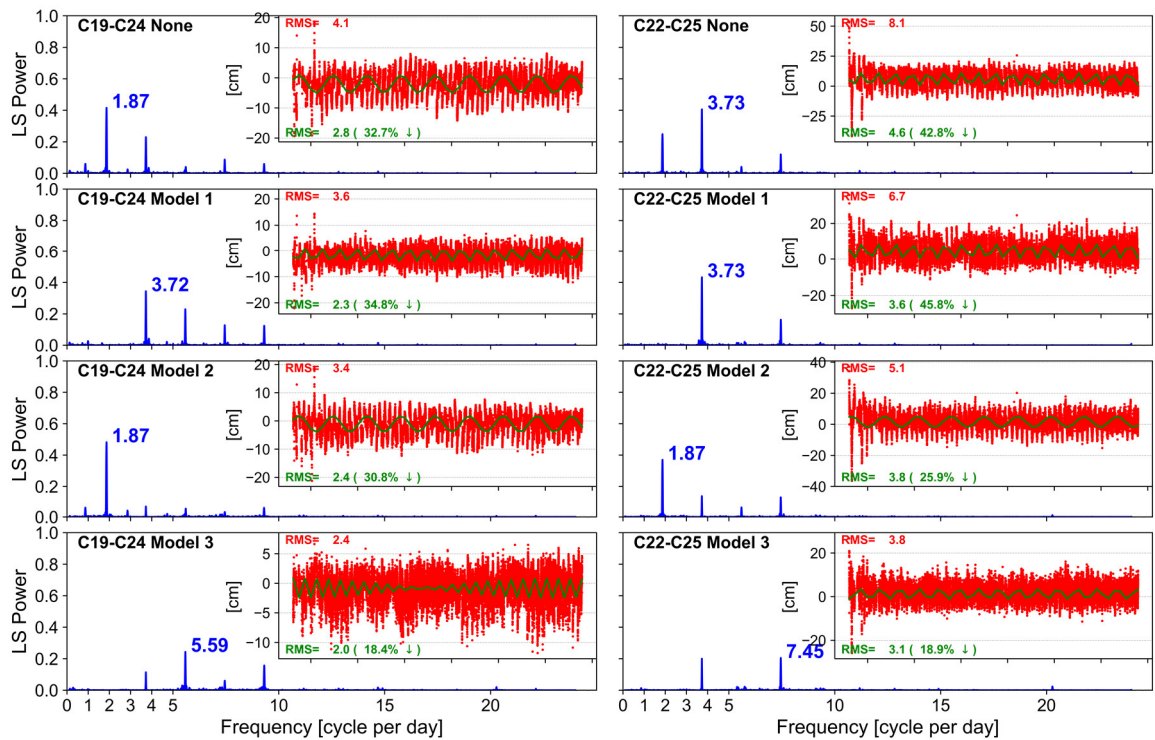
Figure 3.26 Lomb-Scargle periodograms of ISL range residuals of links C19-C24 and C22-C25 after applying different periodic function models

3.4.3 Impact on Orbits

Orbit DBDs from solutions with different periodic models were calculated in the same way as the solution without considering the harmonic signals. The comparison of DBD 1D RMSs for each satellite from different solutions is shown in Figure 3.27. The orbit DBD slightly increased for most satellites after applying the periodic function models, especially when Model 2 or 3 was used. However, a clear decrease can be noticed for satellites C23, C24, C30, C36, and C38 if applying Model 1. As a strong 1CPR signal exists in most C30 related links, removing this signal shrank the DBD 1D RMS by ~4 cm no matter by Model 1 or 3.
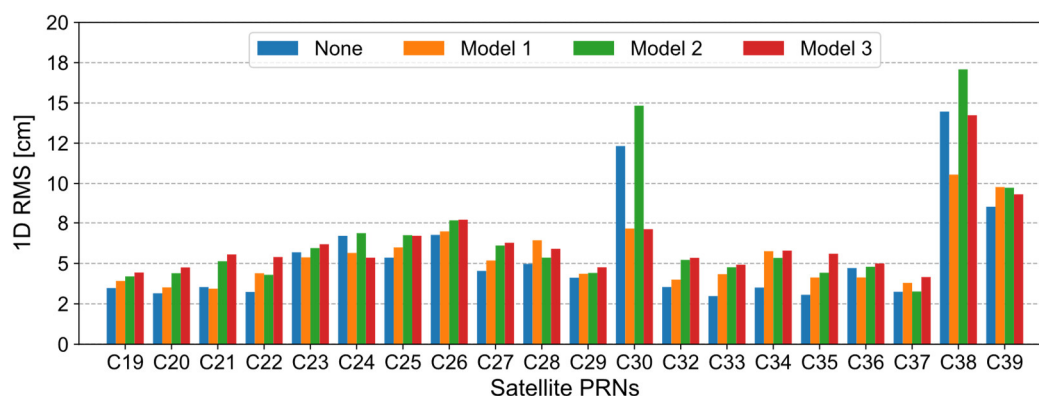
Figure 3.27 Comparisons of orbit DBD 1D RMS obtained from different periodic function models for DOY 335-365, 2019. Systematic differences between daily solutions were removed via Helmert transformations

Additionally, the ISL-based solutions were compared to the orbits determined by ground tracking. The Helmert transformations have been employed to eliminate the systematic errors in ISL-based orbits. In Figure 3.28, the orbit difference RMSs from various ISL solutions are displayed together for comparison. The comparing of each orbital direction, as well as the 1D RMS, are shown. Similar to the DBDs, except for satellite C30, 1D RMS of orbit differences are enlarged after considering the harmonic signals by the proposed periodic function models. Compared to Model 1, Model 2 and 3 even perform worse in this comparison. For most satellites, larger differences caused by Model 2 occur mainly in the orbital cross-track direction. In the case of Model 1, the notable increase of RMS is more found in the radial direction. But for satellites C19, C20, C21, C32, and C33, obvious increases can also be observed in the cross-track components. As Model 3 is virtually the combination of Model 1 and 2, basically, it rises the difference RMS whenever Model 1 or Model 2 does. Compared with the other two components, effects on the along-track direction are small for most satellites.
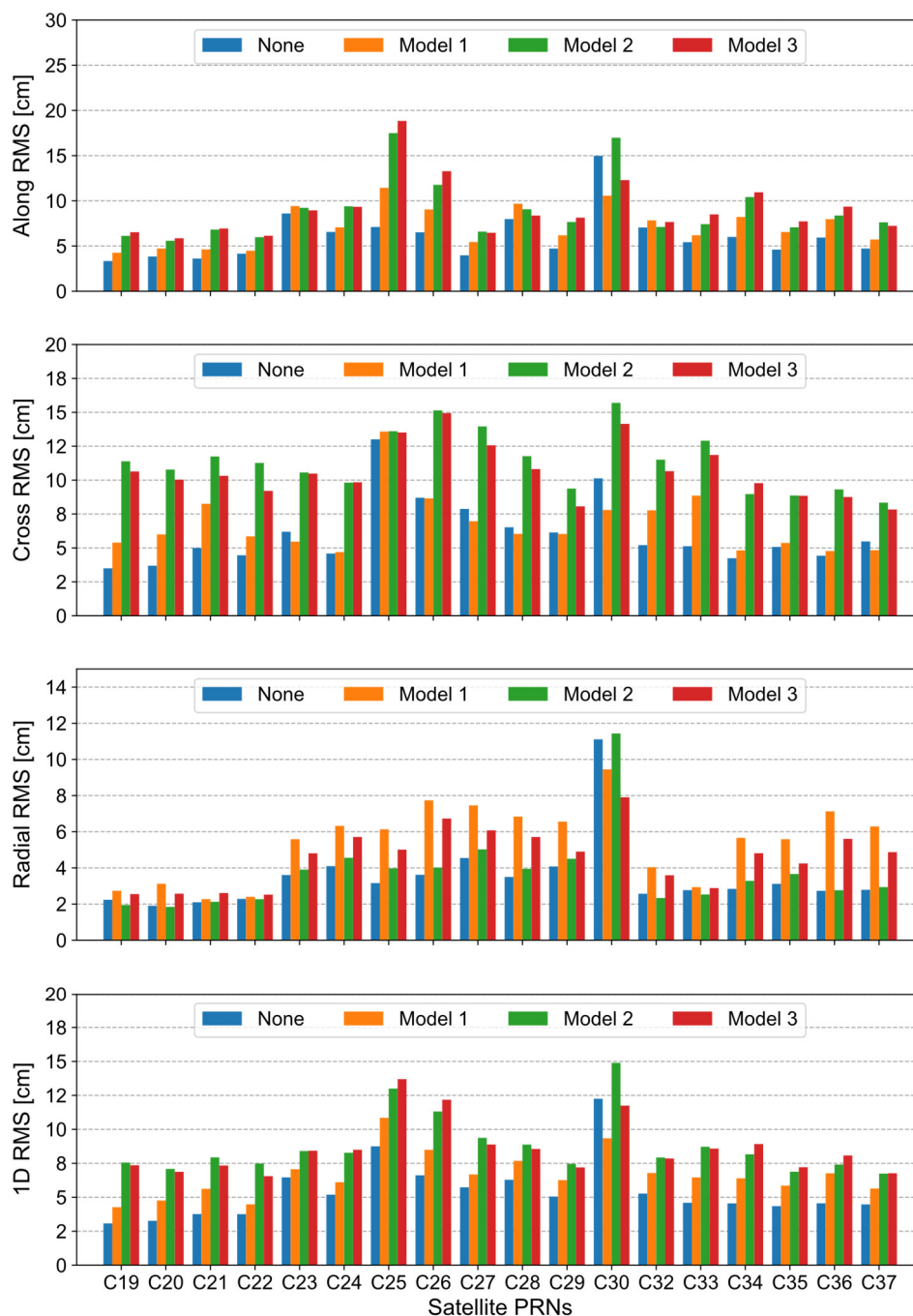
Figure 3.28 Comparison of differences of ISL-based orbits with respect to ground tracking-based orbits when applying various periodic function models for DOY 335~365, 2019. Systematic differences between ISL and ground tracking solutions were removed via Helmert transformations.

Figure 3.29 gives the systematic rotations of BDS-3 constellations between the ground tracking solution (**Grd**) and different ISL solutions. And the constellation rotations between individual ISL solutions are also presented for completeness. It shows that, after applying the periodic function models, the Z-axis rotation gets obviously stabilized. Especially when Model 1 is applied, the variation of the Z-axis rotation becomes much smaller. Comparisons between individual ISL solutions show that the constellation rotation is somehow very sensitive to the

periodic signals existing in the ISL range observations. Applying Model 2 rotates the entire constellation around the Z-axis more than Model 1 or 3. It might indicate a larger correlation between the constellation rotation and the 2CPR signals.
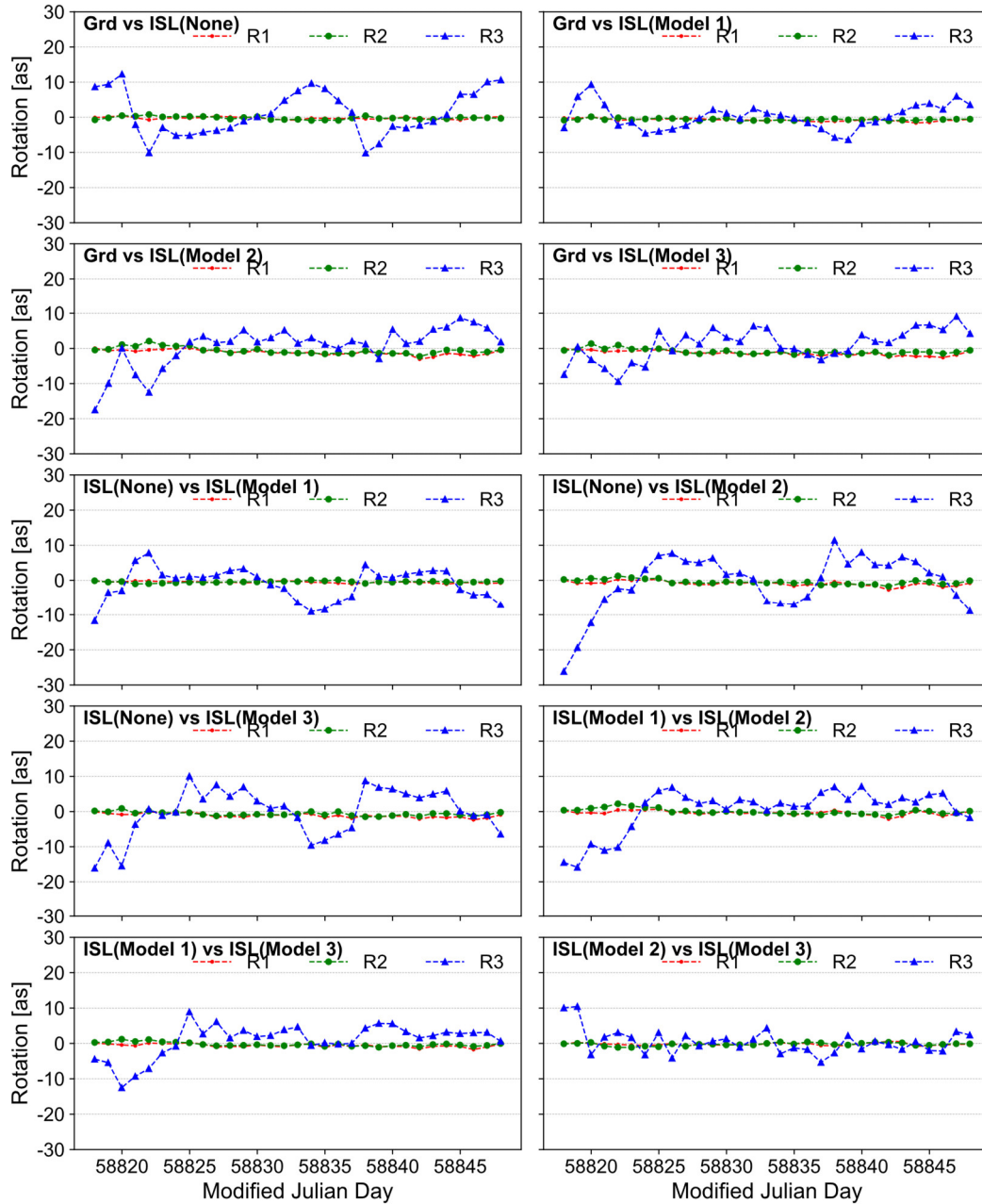
Figure 3.29 Systematic rotations among ground tracking solution (**Grd**) and different ISL solutions for DOY 335~365, 2019

3.4.4 Impact on Hardware Delays

Changes in the estimated values of ISL hardware delays reflect the systematic effects of those harmonic signals in the link residuals. Figure 3.30 gives the variations of mean values of ISL

hardware delays of each satellite after applying different periodic function models. Estimates of the solution without any model were taken as references.

The hardware delays of all MEOs but C26 are negatively shifted if modelling the harmonic signals by the proposed periodic function models. It means the harmonic signals found in the link residual do systematically affect the estimates of hardware delays. Average offsets for Model 1, 2, and 3 are -0.16, -0.16, and -0.17 ns, respectively. Hardware delay offsets are similar between Model 2 and 3 for most satellites. When applying Model 1, obviously different offsets of hardware delays were obtained for several satellites, such as C19, C20, C27, C28, C35, and C37. For C26, even the sign of the hardware delay variation is different from that of Model 2 and 3. The largest offsets are found for C24 when applying Model 1 and for C37 when Model 2 or 3 is used. For IGSOs, even though no periodic models were applied to their links in all solutions, slight changes in their hardware delays still can be observed.
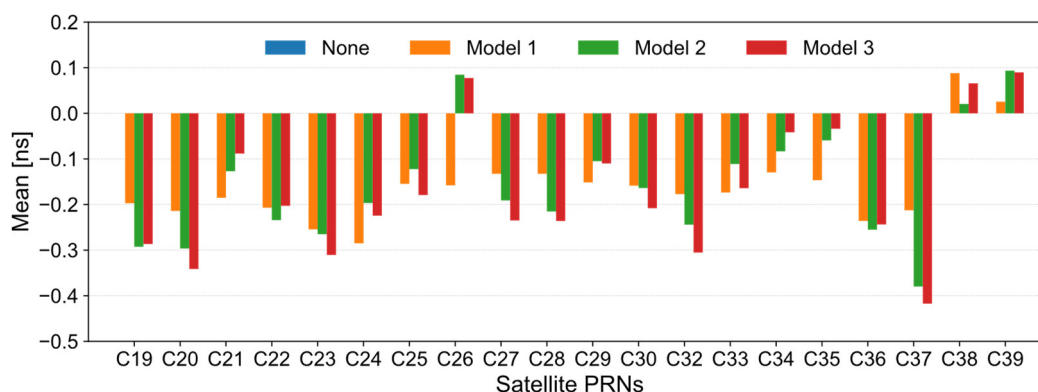
Figure 3.30 Variations of means of hardware delays of ISL range observations after employing different periodic function models over DOY 335~365, 2019

In Figure 3.32, the comparison of standard deviations of hardware delays obtained from different periodic models is presented. For BDS-3 MEOs, except for C25 and C26, the STDs of all other satellites get apparently reduced when considering Model 1. And the average STD of MEOs declines from 0.13 ns down to 0.10 ns. However, in Model 2, the hardware delay STDs of all MEOs are significantly increased, with an average STD of 0.32 ns. In Figure 3.31, ratios of a posteriori standard deviations of unit weights of solutions applying different models with respect to that of the solution without any model are presented along the left y-axis while the a posteriori standard deviations of the latter solution are showed along the right y-axis. As the strength of solutions with Model 2 should not be weaker than that with Model 1 because of the same amount of newly introduced parameters and similar a posteriori standard deviations, inferior results of solutions with Model 2 might indicate the existence of correlation between the hardware delays and the 2CPR terms of the periodic function model. Compared to Model 2, applying Model 3 gets slightly more stable hardware estimates for

MEOs, with an average STD of 0.25 ns. But it still degrades the solution in comparison with Model 1. It seems that the addition of the 1CPR terms could, to some degree, decrease the correlations between the 2CPR terms and hardware delay parameters. Otherwise, weakened estimates should be expected due to the doubled number of model parameters.
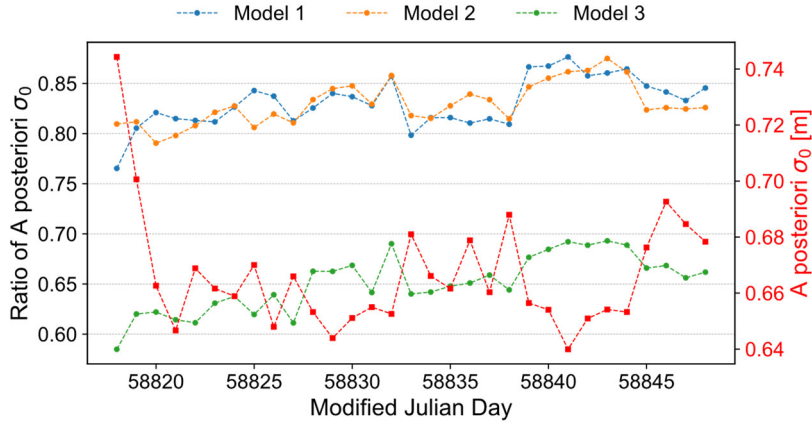
Figure 3.31 Ratios of a posteriori standard deviations of unit weights of solutions applying **Model 1**, **Model 2**, and **Model 3** with respect to the original solution without any model (**None**). A posteriori standard deviations of the unit weight of solution **None** are displayed using the y-axis on the right side.

As to IGSOs, small increases can be observed for C38 no matter which periodic model was adopted for MEO-MEO links. Conversely, for C39, slightly decreased STDs are found when applying Model 2 or 3.
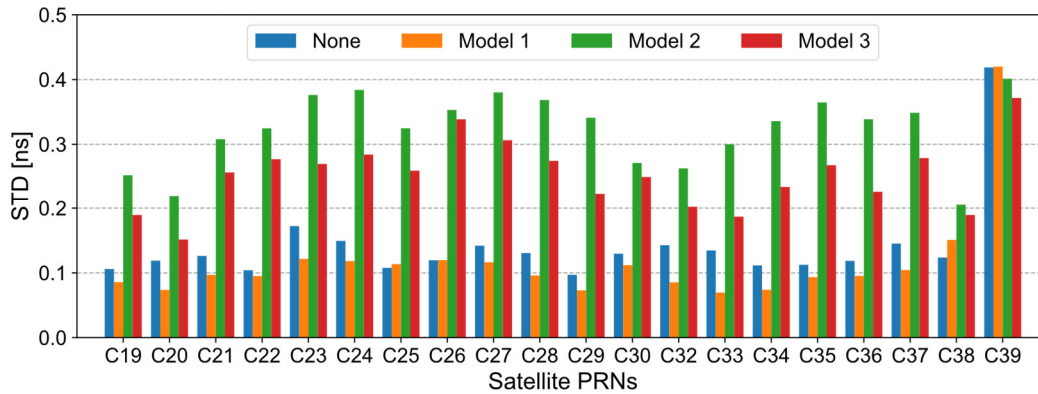
Figure 3.32 Comparison of STDs of hardware delays of ISL range observations resulting from different periodic function models over DOY 335~365, 2019

3.5 Conclusion

Because of imperceptible rotation errors, using ISL range observations solely could not accurately determine the orbits of BDS-3 satellites. But it provides the opportunity to investigate the performance of ISL itself comprehensively.

An average RMS of ~6.7 cm can be obtained for daily residuals of ISL range observations. Compared to insignificant daily variations, the fitting residuals show obvious differences between individual satellites. No apparent direction-dependent patterns were found for satellite residuals, indicating the proper dealing with the ISL phase center corrections in the derivation procedure of original measurements. Despite the lack of rotation datum, the radial component of orbit DBDs of most BDS-3 MEOs calculated by ISLs is only 2.22~4.21 cm. After eliminating constellation rotations by Helmert transformations, orbit DBD RMS in the orbital along-track, cross-track, and radial directions are 7.03, 4.56, and 3.54 cm on average. Compared to the orbits determined by ground trackings, the RMS in the along-track, cross-track, and radial directions reach 6.05, 5.79, and 3.49 cm, respectively, if the datum differences are mitigated. Estimates of ISL hardware delays in the range observations are pretty stable from day to day, and an overall STD of 0.13 ns (~4.0 cm) can be obtained over the one-month session.

Periodic signals resonating with the orbit motion are observed in ISL link residuals. Signal components existing in individual links are different. A periodic function model is proposed to absorb those systematic errors in ISL range observations. Results show that the proposed model can effectively mitigate the periodic signals for almost all links. Furthermore, if appropriately extended, some remaining high-frequency signals should also be easily wiped out by this periodic function model. It seems that the constellation rotation is very sensitive to those harmonic signals, which do affect the estimates of hardware delays systematically. Removing the 1CPR signals in the link observations apparently decreases the STDs of hardware delay estimates. However, possible correlations with other parameters should be properly dealt with before extending the proposed model towards the high-frequency band.

4 Time Synchronization using ISL

4.1 Introduction

Except for ranging measurements, relative clock offset observations are also obtained from the derivation of original ISL dual one-way rangings. The ISL clock observations are used to synchronize satellite clocks within the constellation when the system operates in the AutoNav mode (Martoccia et al. 1998; Wu 1999). In a hybrid mode, i.e., only a subconstellation has the AutoNav capability, the Operational Control Segment (OCS) is still needed to synchronize the time of the whole system (Ananda et al. 1990). With the OCS available, the utilization of ISLs might improve the clock estimation precision, reduce upload requirements, and provide an independent reference for the onboard diagnosis of ephemerides through inter-satellite ranging. With the addition of ISLs, clock tracking coverage of satellites can be greatly increased to overcome the limitation of the ground network, e.g., by more than 40% for BDS MEOs in the case of a regional network (Pan et al. 2018; Pan et al. 2021). In the normal operation, it can also compensate for the shortage of ground tracking to keep all satellites inter-connected when satellites are orbiting outside the territory coverage, especially for MEOs. Thus, timely updates of ephemeris can always be kept for every satellite. Currently, it is reported that the BDS-3 ISL observations are only used for clock estimation when the satellite is beyond the coverage of the ground tracking (Liu et al. 2020; Pan et al. 2021). The L-band Two-Way Satellite Time Frequency Transfer (TWSTFT) network serves to synchronize the clock of satellites that orbit above the territory with the system time (Liu et al. 2009; Tang et al. 2016; Zhou et al. 2016).

Pan et al. (2018) combined the Ka-band ISL and L-band TWSTFT observations to conduct time synchronization experiments for four BDS-3 experimental satellites. It demonstrated significant decreases of clock prediction errors with the addition of ISL, e.g., from 3.59 to 0.86 ns for M1S and from 1.94 to 0.57 ns for M2S. Clock offset estimation and prediction for BDS-3 using solely ISL observations were studied in (Pan et al. 2021). Ka-band links between the ground anchor station and satellites were utilized to synchronize the whole constellation with the system time of BDS, i.e., the BDST. Yang (2019) compared different datums in the time synchronization using ISL, namely a TWSTFT station, an ISL ground anchor station, and clock a priori information. Liu et al. (2020) showed that apparent constant or periodic closed-loop residuals exist in BDS-3 ISL relative clock observations. After aligning observations to integer-minute epochs through cubic spline interpolation, an adjustment model based on ISL closed-

loop residuals was proposed for the calculation of inter-satellite clock offsets.

At present, the ground tracking network of BDS is still confined within the territory of China. Whether the time synchronization realized solely by ISL measurements can reach similar performance as that by the ground tracking is critical for maintaining a spatially and temporally homogeneous service of BDS-3. This chapter is focused on time synchronization using only ISL clock observations. The datum issue for clock estimation, i.e., the so-called mean constellation clock or ensemble clock error in literature, is not covered here because of the lack of link observations from ground anchor stations. The unobservable constellation clock mean errors do not affect the user navigation performance. Using the L-band ground tracking measurements to provide the datum for clock estimation when ISLs are incorporated will be discussed in Section 6.2.

4.2 Satellite Clock Modelling

Because of one-to-one correlation with clock offset parameters, hardware delay parameters cannot be estimated directly from ISL clock measurements. Therefore, no parameters are set up to account for the hardware delays in the clock estimation based on only ISL observations.

Each ISL clock observation involves two independent satellite clock offset parameters regardless of the hardware delays. At each specific epoch, there is no more than one measurement for any satellites. It is impossible to estimate the clock offsets epoch-wisely by using white noise models as in the usual case of clock estimation based on ground tracking. In this study, Piece-Wise Polynomials (PWPs) stated by Equation (4.1) are used to model the time variations of BDS-3 satellite clocks when processing ISL observations.

$$\delta t^i(t) = a_0^i + a_1^i(t - t_0) + a_2^i(t - t_0)^2 + \cdots$$
$$\delta t^j(t) = a_0^j + a_1^j(t - t_0) + a_2^j(t - t_0)^2 + \cdots \tag{4.1}$$

In Equation (4.1), except for those symbols mentioned in former chapters, t_0 denotes the reference epoch of the PWP model. It is set as the start time of each piece-wise window. a_0^*, a_1^*, a_2^*, ... ($* = i, j$) are the coefficients of polynomials. Different from (Ruan et al. 2019), where only the offset parameters are estimated while the rates are fixed to a priori values, in this study, clock rates (even the rate drifts) are estimated together with the offsets instead of taken from predictions. Consequently, piece-wise windows can be set longer than just 1 min (limited by the precision of clock rate predictions) to accommodate as many ISL observations as possible within each modelling window.

4.3 Clock Estimation

Derived ISL clock observations of the period of DOY 335~365, 2019 were processed via a least-square estimator in batch mode to estimate satellite clocks of BDS-3. All observations were equally weighted. The length of each processing session was one day. Piece-wise windows of 300 seconds for satellite clock modelling were used. Due to the rank deficiency of one degree of freedom, daily broadcast clock corrections of satellite C19 were fixed as the reference. Thus, the clock offsets estimated are in the relative sense concerning the reference clock. The linear version of the PWP model described in Equation (4.1) was adopted for all clocks (except for the reference one) in all solutions unless otherwise mentioned. If required, the boundary continuity constraints can be easily applied to PWP models by employing pseudo-observation equations as

$$\begin{bmatrix} a_{0,k+1} \\ a_{1,k+1} \end{bmatrix} = \begin{bmatrix} 1 & \Delta t \\ 0 & 1 \end{bmatrix} \begin{bmatrix} a_{0,k} \\ a_{1,k} \end{bmatrix}, \Sigma_a = \begin{bmatrix} \sigma_{a_0}^2 & \sigma_{a_0}\sigma_{a_1} \\ \sigma_{a_1}\sigma_{a_0} & \sigma_{a_1}^2 \end{bmatrix} \tag{4.2}$$

where $[a_{0,k} \quad a_{1,k}]^\mathrm{T}$ and $[a_{0,k+1} \quad a_{1,k+1}]^\mathrm{T}$ are clock state vectors of two consecutive windows k and $k+1$. The Δt is the length of modelling windows, i.e., 5 min in this study. The variance-covariance matrix of these pseudo-observation equations is denoted as Σ_a with the a priori standard deviations of the offset and rate pseudo-observation equations designated as σ_{a_0} and σ_{a_1}, respectively. Thus, the additional normal matrix indicating the boundary constraints N_{BC} is

$$N_{\mathrm{BC}} = \begin{bmatrix} 1 & \Delta t & -1 & 0 \\ 0 & 1 & 0 & -1 \end{bmatrix}^\mathrm{T} \sigma_0^2 \Sigma_a^{-1} \begin{bmatrix} 1 & \Delta t & -1 & 0 \\ 0 & 1 & 0 & -1 \end{bmatrix} \tag{4.3}$$

where the σ_0 means the a priori standard deviation of the unit weight. In this study, the following variance-covariance matrix is practically used

$$\Sigma_a = \begin{bmatrix} 5000^2 & 0 \\ 0 & 300^2 \end{bmatrix} \tag{4.4}$$

i.e., very loose a priori constraints of σ_{a_0}=5000 m and σ_{a_1}=300 m/s are adopted, and the correlation between offset and rate pseudo-observation equations is ignored. Consequently, the boundary constraints N_{BC} can be written as

$$\boldsymbol{N}_{\mathrm{BC}} = \begin{bmatrix} \dfrac{\sigma_0^2}{\sigma_{a_0}^2} & \dfrac{\sigma_0^2 \Delta t}{\sigma_{a_0}^2} & -\dfrac{\sigma_0^2}{\sigma_{a_0}^2} & 0 \\[2ex] \dfrac{\sigma_0^2 \Delta t}{\sigma_{a_0}^2} & \dfrac{\sigma_0^2 \Delta t^2}{\sigma_{a_0}^2} + \dfrac{\sigma_0^2}{\sigma_{a_1}^2} & -\dfrac{\sigma_0^2 \Delta t}{\sigma_{a_0}^2} & -\dfrac{\sigma_0^2}{\sigma_{a_1}^2} \\[2ex] -\dfrac{\sigma_0^2}{\sigma_{a_0}^2} & -\dfrac{\sigma_0^2 \Delta t}{\sigma_{a_0}^2} & \dfrac{\sigma_0^2}{\sigma_{a_0}^2} & 0 \\[2ex] 0 & -\dfrac{\sigma_0^2}{\sigma_{a_1}^2} & 0 & \dfrac{\sigma_0^2}{\sigma_{a_1}^2} \end{bmatrix} \tag{4.5}$$

Because of indistinguishable from clock offsets (Menn 1986), i.e., the constant terms of the PWP models, no additional hardware delay parameter was set up in the clock estimation. However, under a certain assumption, it will not be difficult to acquire the hardware delays from the comparison of clock offset estimates with the ground tracking-based solution (See Section 4.3.3).

4.3.1 Fitting Residuals

Fitting residuals quantify the effectiveness of modelling as well as the precision of observations to a large extent. In Figure 4.1, fitting residuals of all used ISL clock observations of DOY 335, 2019 (MJD 58818) are shown as an example. As labeled at the bottom-right corner of the figure, there were 143855 valid observations used in the estimation, and the overall fitting RMS is ~5.2 cm. Almost all residuals are within ±20 cm. The histogram of the residuals (See Figure 4.2) shows an excellent unimodal symmetric distribution with a negligible mean of 1 mm. Moreover, the residuals' concentration is even better than a simulated normal distribution derived from the mean and standard deviation. Residual series from other daily sessions (not shown here) are similar.
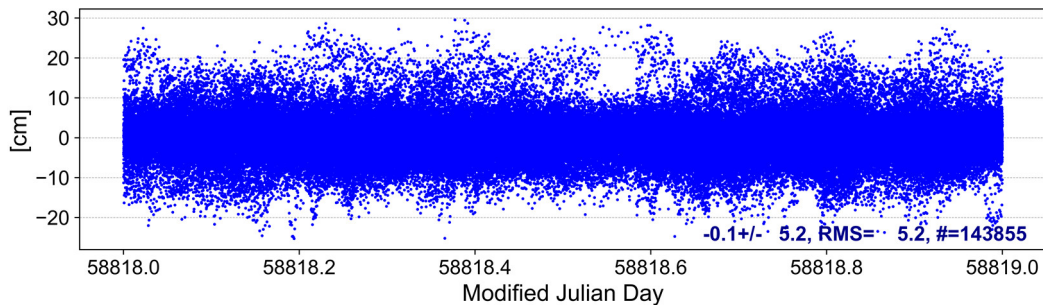
Figure 4.1 Fitting residuals of ISL relative clock observations on DOY 335,2019
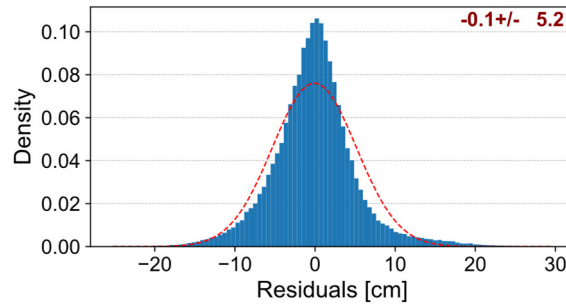
Figure 4.2 Histogram of fitting residuals of ISL relative clock observations on DOY 335, 2019

Figure 4.3 shows the daily fitting overall RMS over the whole period considered in this study. A fitting RMS of slightly larger than 5.0 cm can be guaranteed for all daily sessions. Differences among daily sessions are not significant. It can be regarded as one of the indicators of stable operation of ISL payloads in the system.
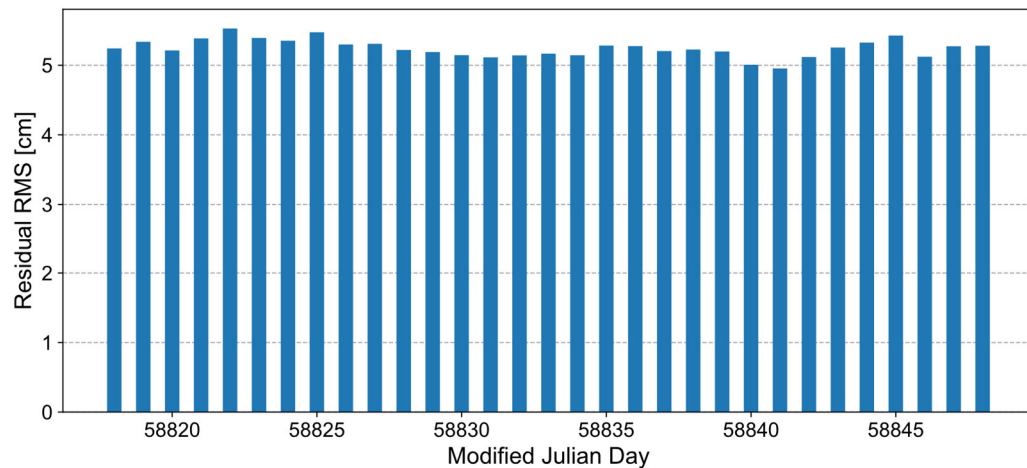
Figure 4.3 Daily fitting overall RMS of ISL relative clock observations over DOY 335~365, 2019

In contrast, between-satellite differences of fitting residuals are more apparent. The daily residual RMS series of each satellite are presented in Figure 4.4. Satellites' monthly overall RMSs are shown in Figure 4.5 and Table 4-1. The residual RMS difference between the best, i.e., satellite C37, and the worst, i.e., C26, reaches up to ~ 7.0 cm. Except for C26, clock observation residuals of C23 are also obviously larger than other satellites, which is similar to the case of range observations (See Figure 3.8). Unlike C26, the worse quality of ISL clock observations of satellite C23 is already revealed by the simple polynomial fitting, as shown in Figure 2.17. For satellite C30, its clock residual RMS is no longer significantly larger than most other satellites compared to its range observation residuals. Generally, clock observations have slightly smaller residuals than range observations. It probably should be attributed to the more flexible clock models, which have larger numbers of adjustable parameters. Besides, the cancellation of some common errors like ionospheric delays in the derivation could be another

reason (Ananda et al. 1990). For an individual satellite, like in the case of range measurements, the clock residual RMS still shows only marginal variations from one day to another.
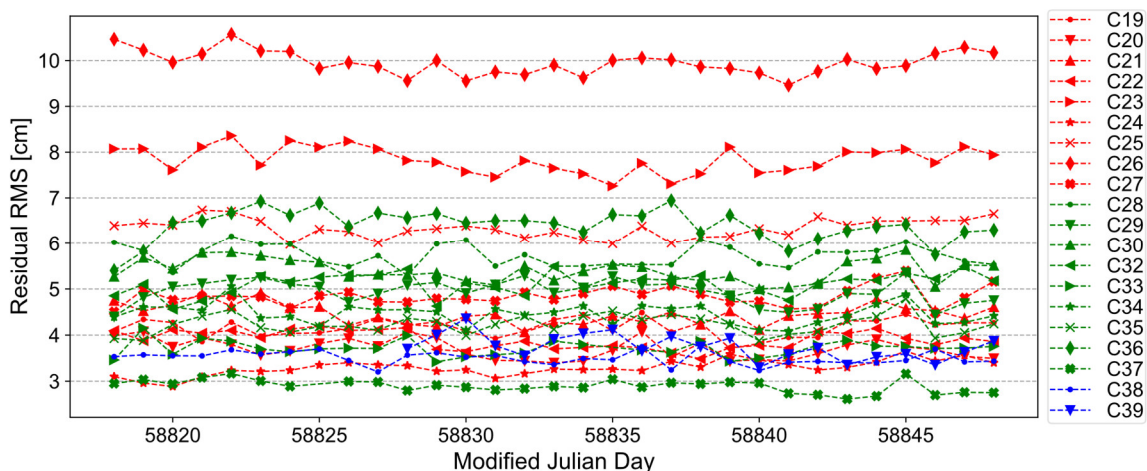
Figure 4.4 Daily fitting satellite RMS of ISL relative clock observations
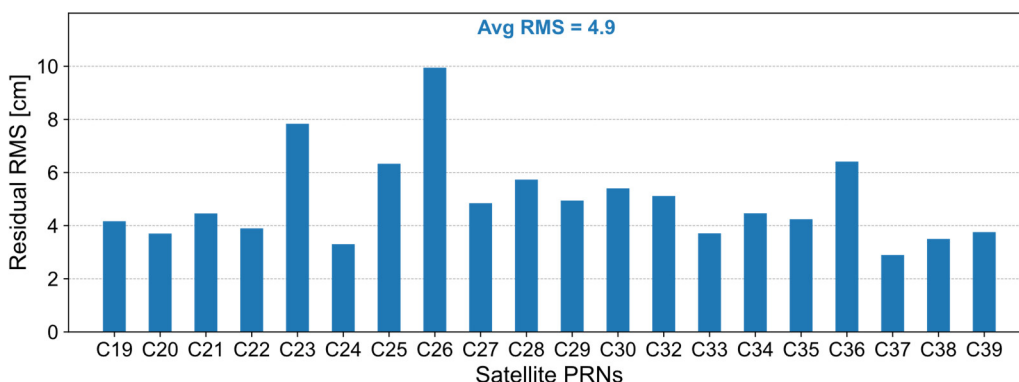
Figure 4.5 Fitting RMS of ISL relative clock observations for each satellite

To compare with other research, fitting RMSs of ISL clock observations over February 01~14, 2019 given in Table 3 from (Pan et al. 2021) are also listed in Table 4-1. Satellite C38 and C39 were omitted because of absence in either of these studies. In (Pan et al. 2021), a similar linear polynomial model with a fitting arc length of 1 min was adopted. From Table 4-1, except for C26 and C36, all other satellites have relatively smaller fitting residuals in this study. The average RMS is 5.08 cm against 7.79 cm in (Pan et al. 2021), about 2.7 cm less.

Table 4-1 Satellite residual RMS of ISL clock observations

PRN	RMS [cm]		PRN	RMS [cm]	
	(Pan et al. 2021)	this study		(Pan et al. 2021)	this study
C19	8.09	4.17	C28	6.90	5.73
C20	7.49	3.70	C29	6.60	4.94
C21	11.09	4.46	C30	7.49	5.40
C22	7.79	3.90	C32	6.60	5.12

C23	9.59	7.84	C33	8.69	3.71
C24	10.19	3.30	C34	6.90	4.47
C25	7.49	6.33	C35	6.60	4.24
C26	8.39	9.95	C36	6.30	6.41
C27	6.60	4.85	C37	7.49	2.90
Mean	7.79	5.08			

As the check did for range observations, fitting residuals of six satellites among which every two of them orbit on the same plane (See Figure 2.1, C29/C30 from plane A, C19/C20 from plane B while C23/C24 from plane C) are presented in the form of sky plots in Figure 4.6. Observations of one month can basically cover every corner of the sky for all satellites. From those sky plots, it hardly exhibits any obvious direction-dependent patterns. This somehow confirms the appropriate corrections of ISL phase center biases, which should have been applied in the pre-processing procedure when doing the observation derivations.
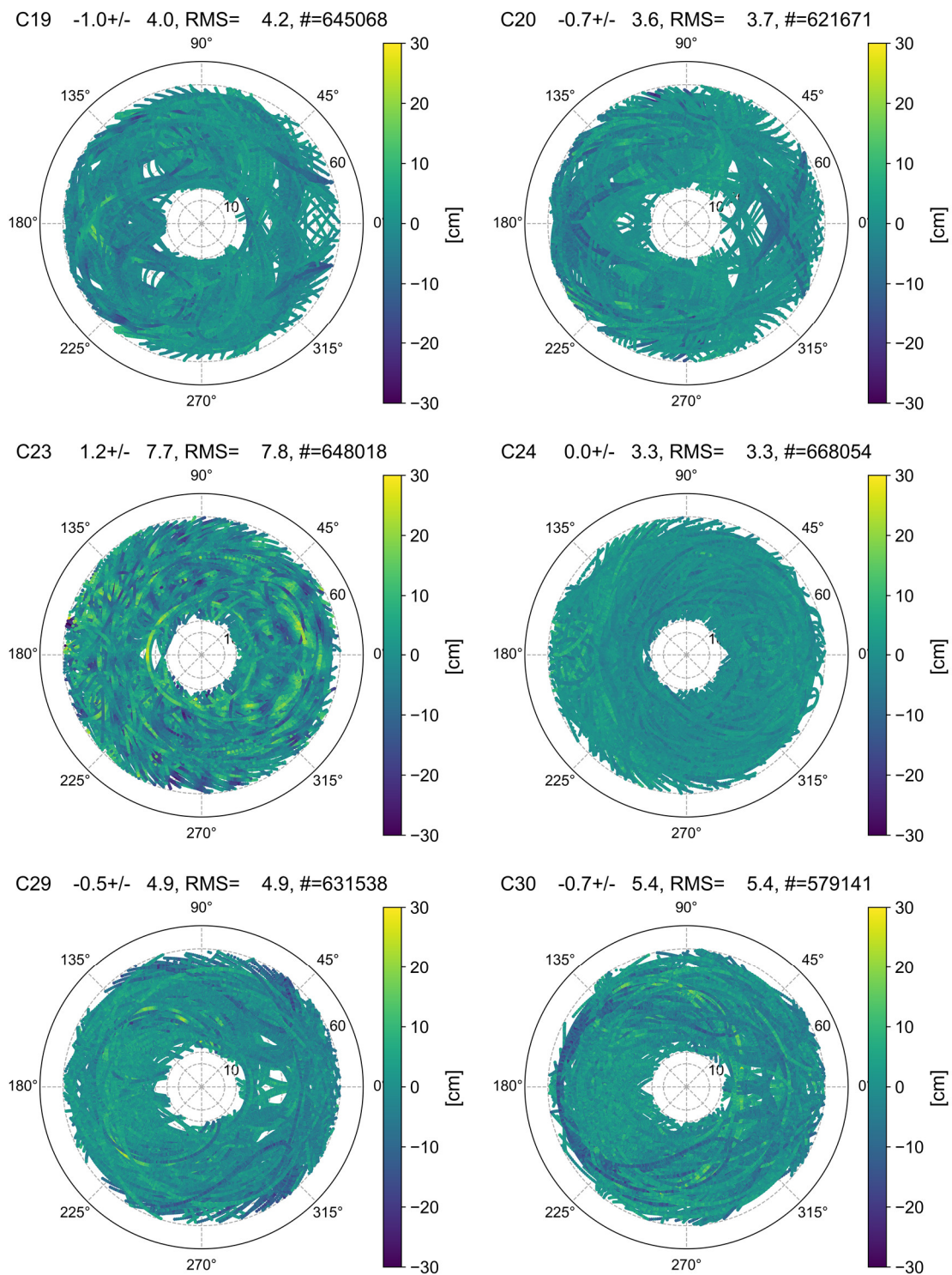
Figure 4.6 Sky plots of ISL clock observation residuals of C19 and C20 (from plane B), C23 and C24 (from plane C), as well as C29 and C30 (from plane A)

4.3.2 Clock Estimates

To investigate the precision of time synchronization realized by ISL, estimated clock

parameters are evaluated.

4.3.2.1 Clock Offsets

Presently, the precision of Ka-band ISL observations is still much lower than the L band carrier phases observations. Therefore, clock solutions obtained from ground tracking can be used as references to evaluate the quality of clock offsets estimated from ISLs.

Different clock solutions can be compared via a so-called twice-difference procedure meant to eliminate the effects of various clock datums used in the processing. Clock offset estimates were compared with MGEX Analysis Center (AC) Wuhan University's (WHU's) daily clock products. Clocks of satellite C21 were chosen as the reference when doing the twice-difference.

Figure 4.7 shows the daily STDs of clock offset differences for each satellite. Spikes occurring on MJD 58827 (DOY 344, 2019) and MJD 58845 (DOY 362, 2019) should be owned to WHU's clock products. Those spikes were not observed in an additional comparison with AC GFZ's products. Clock datum switches may be the possible causes as some jumps observed in the time series after the twice-difference. For most satellites, their STDs are between 0.15 ~ 0.20 ns. Standard deviations of satellite C30 are prominently larger than all other satellites.
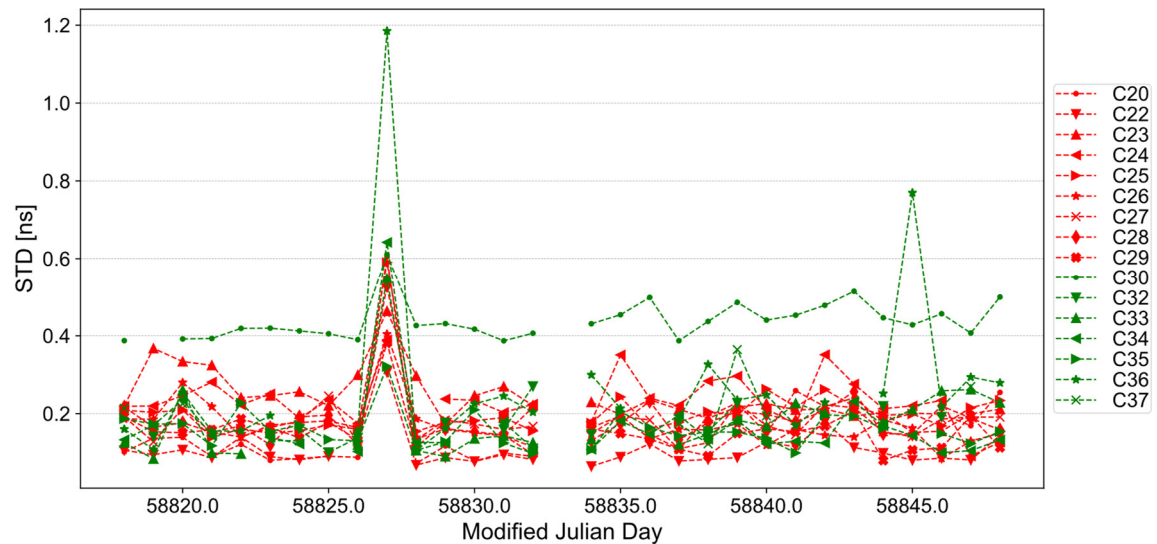
Figure 4.7 Daily standard derivations of clock offset difference wrt clock products from WHU

Furthermore, monthly averages of clock offset difference STDs for each satellite are listed in Table 4-2. Comparisons on MJD 58827 of all satellites and on MJD 58845 for C36 are omitted in the STD calculations. The same comparison conducted between MGEX ACs' products, i.e., WHU (wum) and GFZ (gbm), are also listed for reference. Though differences of ISL-generated clock offsets are smaller for most satellites (except for C23) when compared with

GFZ's product, those two comparisons should be regarded as at the similar level considering the precision of ISL observations. It shows that clock offsets of C20, C22, C29, C33, C34, C35, C36, C37 obtained from ISL have smaller STDs than other satellites. Compared to the difference between WHU's and GFZ's products, STDs of those satellites are only 0.01~0.02 ns larger. The standard deviation of C30 reaches up to 0.43 ns when compared with WHU's clock, 2~3 times larger than other satellites. Besides, satellites C23 and C24 also show slightly larger STDs than the remaining satellites. Similar research was published by (Yang et al. 2021). Compared to the results given in Table 3 from (Yang et al. 2021), generally smaller STDs have been obtained in this study. Interestingly, the STD of C30 was also found to be apparently larger than other satellites and reached 0.46 ns in (Yang et al. 2021).

Table 4-2 Monthly average STDs of offset difference between ISL-generated clock and MGEX ACs' daily products

PRN	STD[ns]			PRN	STD [ns]		
	ISL - wum	ISL - gbm	wum - gbm		ISL - wum	ISL - gbm	wum - gbm
C20	0.14	0.11	0.12	C29	0.15	0.13	0.14
C22	0.10	0.09	0.09	C30	0.43	0.41	0.11
C23	0.23	0.26	0.14	C32	0.17	0.15	0.12
C24	0.23	0.23	0.14	C33	0.16	0.12	0.14
C25	0.19	0.16	0.13	C34	0.15	0.15	0.14
C26	0.16	0.17	0.11	C35	0.15	0.14	0.15
C27	0.17	0.14	0.11	C36	0.21	0.19	0.19
C28	0.17	0.15	0.12	C37	0.19	0.19	0.19

4.3.2.2 Clock Rates

The rate stability of onboard atomic clocks is crucial to the AutoNav performance of BDS-3. As PWPs were employed to model the temporal variations of BDS-3 satellite clocks in this study, the 1st-degree terms of the models are virtually the clock rates. Clock rates estimated from ISL observations over one month are presented in Figure 4.8 for satellites C20, C25, C34, C35, C37, and C38.

Despite the noises, some even very slow drifts in the rates can be sensed from the estimates. It shows the capability of ISL observations for satellite clock rate estimation. As can be seen, the atomic clock onboard C20 shows a more significant rate change during this 31-days period compared to other satellites. Much smaller but still visible rate drifts can also be found for C25, C34, C35, and C38. For satellite C37, a clock rate jump (which is not found in the offsets) of

around $+7.93\times10^{-11}$ s/s was found during seconds 28800~29400 of MJD 58841 (DOY 358, 2019). But this clock frequency jump would not cause any significant errors for navigation service (Ananda et al. 1990). The clock rate estimates from Ka-band ISL observations are regarded as consistent with that from the L-band TWSFTF measurements. Comparisons of one-day results from estimation of 2-hour arcs in 2016 found that the boundary discontinuity of clock rates estimated from the TWSFTF for BDS-3 M1S was 4.39×10^{-14} s/s, and the difference between ISL-based and TWSFTF-based clock rates was 4.31×10^{-14} s/s (Pan et al. 2018).
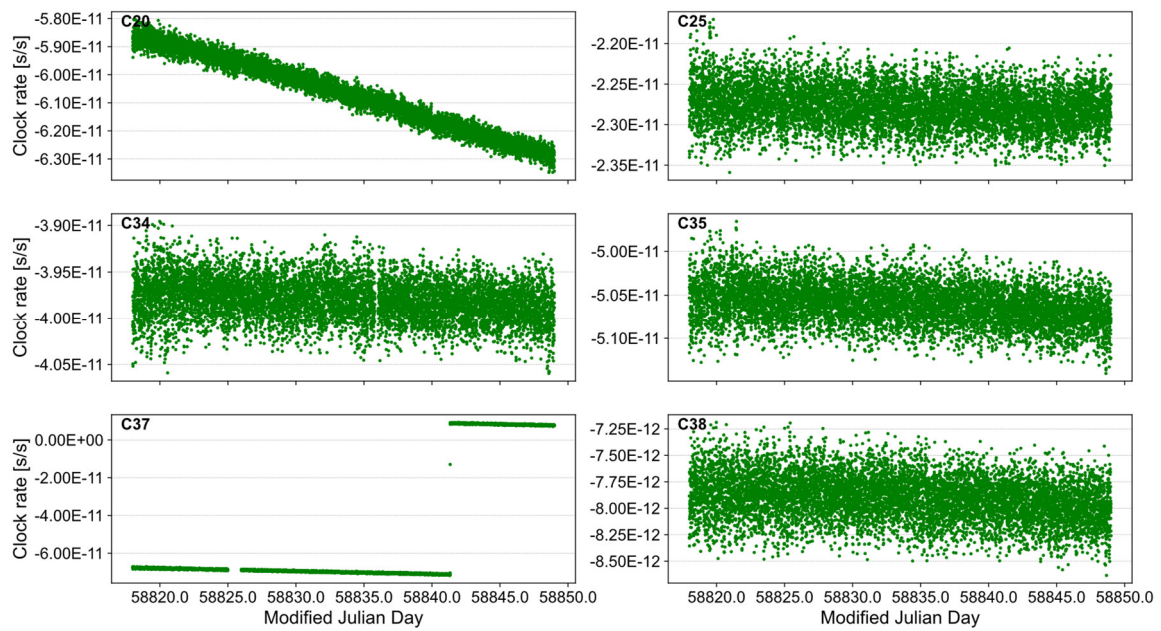
Figure 4.8 Satellite clock rates estimated from ISL clock observations

Likewise, clock rate estimates were linearly fitted to acquire rate drifts. Satellite C37 was excluded because of the rate jump, as mentioned above. A few outliers, no more than 1% on average for all satellites, were found and removed through a simple iterative robust fitting procedure. Parameters of the linear fitting models obtained are listed in Table 4-3 together with corresponding fitting RMSs.

Table 4-3 Satellite clock rate drifts acquired by fitting the estimated rate series to linear models over DOY 335-365, 2019

PRN	Clock rates $[10^{-12}$ s/s]	Clock rate drifts $[10^{-19}$ s/s²]	Fitting RMS $[10^{-13}$ s/s]	Operational Clock
C20	-58.48	-16.44	2.07	RAFS
C21	-39.19	-13.31	2.07	RAFS
C22	-67.10	-15.57	2.06	RAFS
C23	-5.58	-22.78	2.84	RAFS

C24	-12.06	-16.09	1.93	RAFS
C25	-22.70	-0.59	2.44	PHM
C26	3.99	-0.28	2.80	PHM
C27	-3.18	-0.74	2.14	PHM
C28	-3.22	-0.67	2.25	PHM
C29	-4.67	-0.69	2.28	PHM
C30	-3.82	-1.05	2.53	PHM
C32	-5.00	-20.76	2.08	RAFS
C33	-49.36	-12.96	2.01	RAFS
C34	-39.71	-0.70	2.09	PHM
C35	-50.49	-0.88	2.16	PHM
C36	3.39	-13.96	2.18	RAFS
C38	-7.82	-0.67	2.03	PHM
C39	-9.02	-11.10	2.04	PHM

Generally, satellites with RAFS clocks used as the nominal frequency standard, e.g., satellites C20-C24, have more than one magnitude larger clock rate drifts than that with PHM clocks. Rate drifts of RAFS clocks are -10 ~ -20×10^{-19} s/s^2, while for PHM clocks, they are around or mostly less than -1×10^{-19} s/s^2. However, for the IGSO satellite C39, despite of an operational PHM frequency source, it exhibited a similar drift as the best RAFS clock onboard C33. Except for C23 and C26, clock rate fitting RMSs of all other satellites are very close, around 1.9~2.5×10^{-13} s/s.

4.3.3 Hardware Delays

Under the assumption that the ISL hardware delays are constant during daily processing sessions, they can be obtained by differencing the clock offsets estimated from ISL observations with a reference solution. Clock offsets estimated based on ground tracking data were taken as the references solution to calculate the hardware delays in ISL clock observations. As the same satellite (i.e., C19) has been chosen as the datum clock in both the ground tracking and ISL solutions, daily means of clock offset differences can be regarded as the daily ISL hardware delays. Table 4-4 lists the monthly averages of satellite ISL hardware delays calculated in this way and their STDs over the period of DOY 335~365, 2019. And in Figure 4.9, standard deviations of daily hardware delays over this period are compared.

Table 4-4 Monthly averages and STDs of satellite hardware delays existing in the ISL clock observations

PRN	Mean [ns]	STD [ns]	PRN	Mean [ns]	STD [ns]

C20	29.86	0.06	C29	-35.27	0.09
C21	8.66	0.07	C30	-66.14	0.10
C22	13.82	0.06	C32	-60.82	0.06
C23	36.80	0.06	C33	-160.14	0.09
C24	-11.90	0.12	C34	-55.58	0.08
C25	-35.15	0.09	C35	-43.85	0.07
C26	-47.73	0.08	C36	-90.50	0.08
C27	-46.33	0.11	C37	-73.45	0.07
C28	-54.50	0.07	**Avg**		0.08
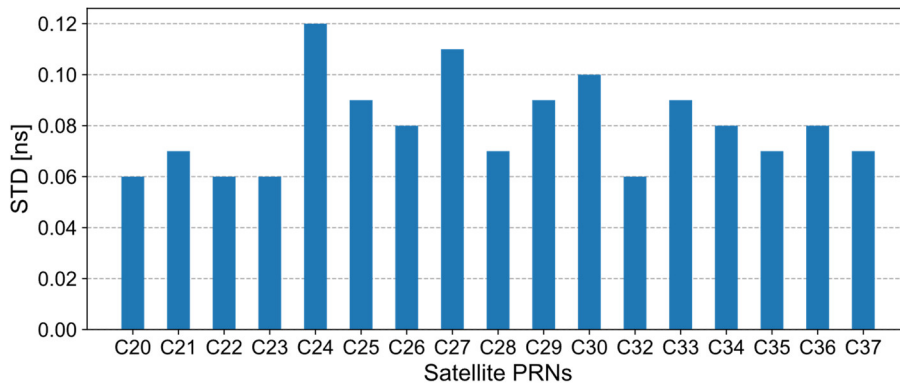
Figure 4.9 Standard deviations of daily hardware delays in the ISL clock observations over DOY 335~365, 2019

Two things should be noted here. Firstly, as integrated with clock offsets estimated from ground tracking data, transmitter delays of L band signals also contribute to the averages obtained here. Secondly, all hardware delays acquired are relative to the datum satellite C19 because of the rank deficiency. It shows that the hardware delays contained in ISL clock observations are quite stable. For most satellites, the STD is below 0.10 ns (~3.0 cm). The maximum STD from satellite C24 is less than 0.12 ns (~3.6 cm). The average of STDs of the whole constellation is around 0.08 ns (~2.4 cm). Note that the daily variations of the L-band transmitting delays might also contribute, if any.

4.4 Harmonic Signals in Link Residuals

Similar to range observations, residuals of ISL clock observations also appear to contain some prominent periodic signals. According to (Martoccia et al. 1998), orbitally-induced temperature fluctuations may result in cyclic errors varying at the orbital period. This could be one of the possible reasons of periodic signals found in ISL residuals here but yet to be verified.

4.4.1 Spectrum Analysis on the Link Residuals

Lomb-Scargle periodograms of fitting residuals of link C19-C25, C21-C28, C22-C37, C24-C36, and C34-C37 on DOY 335, 2019 (MJD 58818) are shown in Figure 4.10 as examples. All those links show significant either 1CPR (~1.86) or 2CPR (~3.72) harmonic signals concerning the orbital frequency of BDS-3 MEOs. With a coarse estimation, the RMS of link residuals would decrease by as much as ~58% for C21-C28 if those periodic errors were removed or appropriately modeled. Although the significance differs from one link to another, analogous periodic signals can be observed for all other MEO-MEO ISLs not shown here. Noticeable reductions of link residuals could be expected if eliminating those systematic errors.
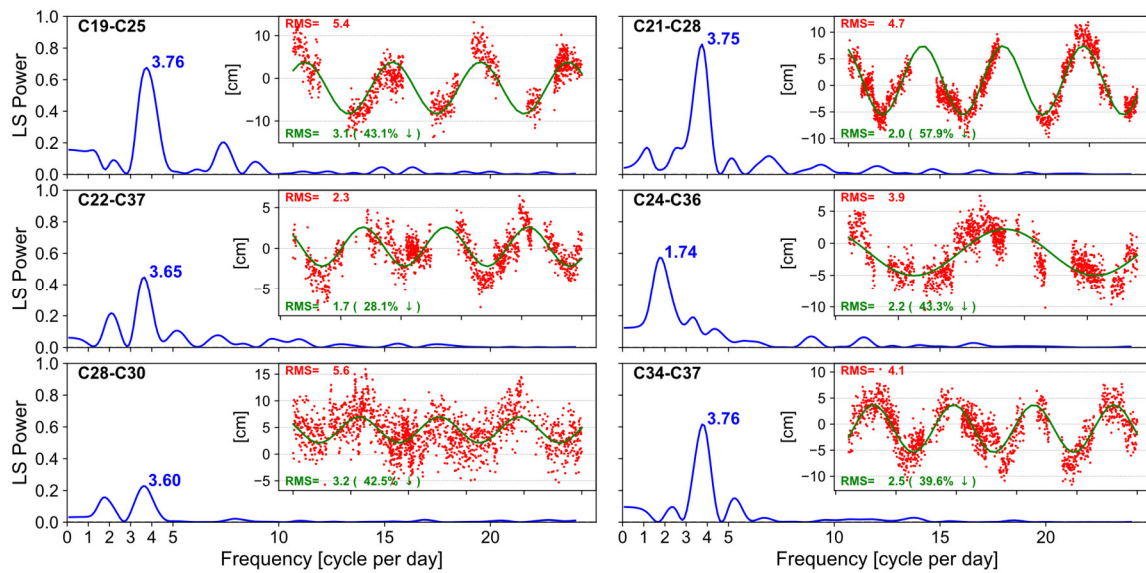
Figure 4.10 Lomb-Scargle periodograms of ISL clock residuals of links C19-C25, C21-C28, C22-C37, C24-C36, C28-C30, and C34-C37 on DOY 335, 2019

To obtain more accurate estimates of the frequencies of those periodic signals in link residuals, residual series spanning the whole period considered (i.e., DOY 335~365, 2019) were fitted using the Lomb-Scargle models. Figure 4.11 shows the periodograms resulting from the whole month fitting for the same example links given in Figure 4.10. In the extended fitting, periodic components resonating with the orbital frequency are more explicit. Peak significances of 2CPR signals reach 0.7~0.8 for links C19-C25 and C21-C28. For link C24-C36, the 1CPR component is found to be the dominant signal, with a significance of ~0.5.
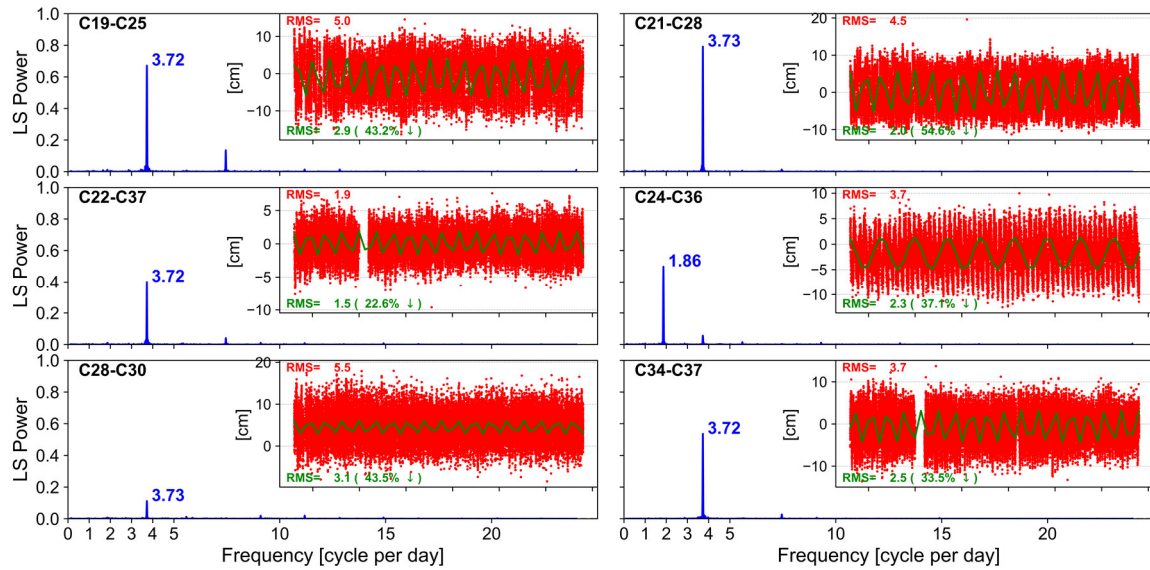
Figure 4.11 Lomb-Scargle Periodograms of link residuals of clock measurements for the period DOY 335~365, 2019

Given such a high similarity, it may indicate the coupling of ISL range and clock observations. In Figure 4.12, the daily calculated Pearson product-moment correlation coefficients[1] of ISL range and clock residuals are illustrated. It shows that high correlations between the derived range and clock observations exist for most links. For lots of links, the correlation coefficients are as high as more than ±0.50, and even high correlation coefficients greater than ±0.75 can be found for several links. It indicates that the range and clock measurements have not been fully decoupled as intended, at least in the sense of the precision of several centimeters.
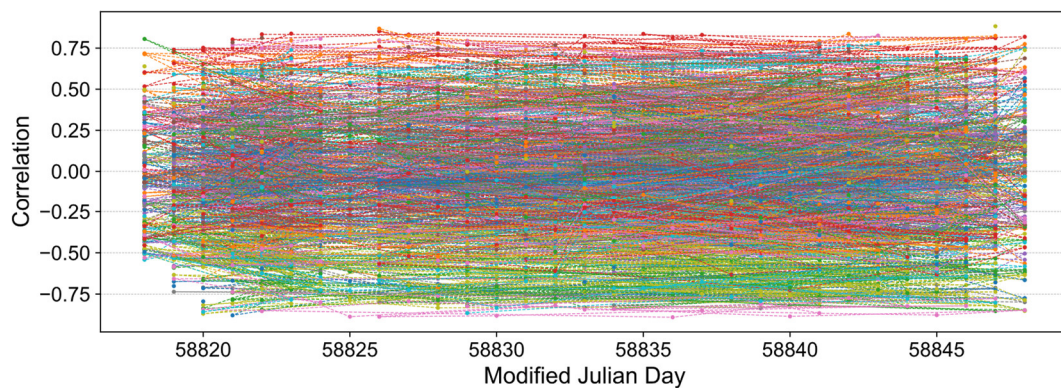
Figure 4.12 Daily correlation coefficients of ISL range and clock residuals. Each colored series represents an individual link, i.e., one satellite pair.

Much like in the case of ISL range observations, the same Fourier-like periodic function model as described in Equation (3.11) has been adopted to account for the harmonic signals found in clock observations. The periodic model was applied link-wisely and only limited to ISLs

---

[1] https://en.wikipedia.org/wiki/Pearson_correlation_coefficient

established between MEOs. Differently parameterized models as listed in Table 3-5 were employed respectively for comparisons. Effects of the application of those models on fitting residuals and estimates of clock offsets and hardware delays are analyzed and presented in the following.

4.4.2 Impact on Fitting Residuals

In Figure 4.13, residual RMS of each satellite on DOY 335, 2019 resulting from different periodic function models are presented. After applying the periodic models, noticeable reductions of fitting residuals can be observed for all satellites. Because for most links (more than 60% of all), the 2CPR component is the dominant signal, more considerable residual decreases are found when using Model 2 other than Model 1 for all but C38 satellites. Links involved C38 have different signal frequencies due to the distinct orbit period of the IGSO. Therefore, those periodic models were not applied to any ISLs of C38. Nevertheless, a slight decrease in the residuals of C38 can also be noted.

Even considering only the 1CPR terms, residuals of several satellites shrunk clearly, e.g., C23, C26, and C28. Using Model 3, which accounts for both the 1CPR and 2CPR signals, gets the smallest residuals for all satellites.
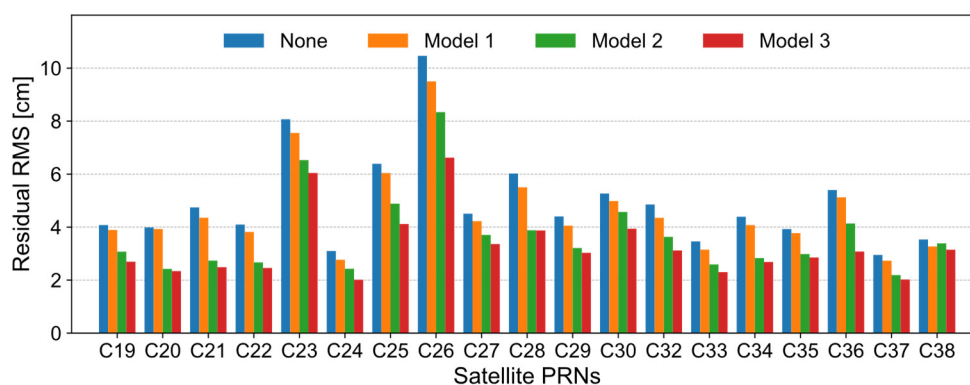
Figure 4.13 Satellite residual RMS of ISL clock observations resulting from different periodic function models on DOY 335, 2019

Table 4-5 summarizes the satellite residuals RMS from different periodic function models and their change percentages with respect to the solution ignoring the harmonic signals over the whole 31 days' session. An average decrease of 4% is found if only accounting for the 1CPR terms in the periodic function models. The 2CPR signals account for ~23% of the residual errors in ISL clock observations. The RMS of lower than 3.0 cm can be obtained for several satellites, like C20, C21, C22, C24, C33, and C37when eliminating the effects of the 2CPR components. The average RMS of the whole constellation declines down to 3.82 cm. Further

slight cutback can be found if both the 1CPR and 2CPR terms are contained in the periodic models. Then an average fitting RMS of 3.65 cm can be expected.

Table 4-5 Satellite residual RMS of ISL clock observations resulting from different periodic function models and their change percentages with respect to the solution ignoring the harmonic signals over DOY 335~365, 2019

PRN	Model 1		Model 2		Model 3	
	RMS [cm]	Change [%]	RMS [cm]	Change [%]	RMS [cm]	Change [%]
C19	4.02	-3.60	3.14	-24.70	3.02	-27.58
C20	3.58	-3.24	2.47	-33.24	2.37	-35.95
C21	4.26	-4.48	2.60	-41.70	2.52	-43.50
C22	3.71	-4.87	2.70	-30.77	2.55	-34.62
C23	7.50	-4.34	6.62	-15.56	6.29	-19.77
C24	3.09	-6.36	2.82	-14.55	2.63	-20.30
C25	6.13	-3.16	5.00	-21.01	4.83	-23.70
C26	9.60	-3.52	8.13	-18.29	7.72	-22.41
C27	4.73	-2.47	3.95	-18.56	3.83	-21.03
C28	5.54	-3.32	3.88	-32.29	3.67	-35.95
C29	4.81	-2.63	3.48	-29.55	3.39	-31.38
C30	5.27	-2.41	4.69	-13.15	4.57	-15.37
C32	4.79	-6.45	3.87	-24.41	3.56	-30.47
C33	3.49	-5.93	2.68	-27.76	2.50	-32.61
C34	4.30	-3.80	3.13	-29.98	3.03	-32.21
C35	4.11	-3.07	3.19	-24.76	3.10	-26.89
C36	6.10	-4.84	4.83	-24.65	4.53	-29.33
C37	2.80	-3.45	2.34	-19.31	2.26	-22.07
C38	3.37	-3.71	3.33	-4.86	3.19	-8.86
C39	3.57	-5.05	3.58	-4.79	3.37	-10.37
Average	4.74	-4.03	3.82	-22.69	3.65	-26.22

To graphically demonstrate the effectiveness of the proposed periodic models, residuals series of links C19-C25 and C24-C36 after applying different models are shown in Figure 4.14. As can be seen, applying Model 1 does not change the residuals too much for link C19-C25 because of its dominant 2CPR signal (See Figure 4.11). However, when Model 2 is used, the peak signal vanishes immediately. In the case of link C24-C36, the phenomenon is opposite due to a different peak frequency. Although there are still some remaining periodic components according to the Lomb-Scargle fitting, adopting Model 3 can wipe out the most

significant signals and make a pretty flat periodogram.
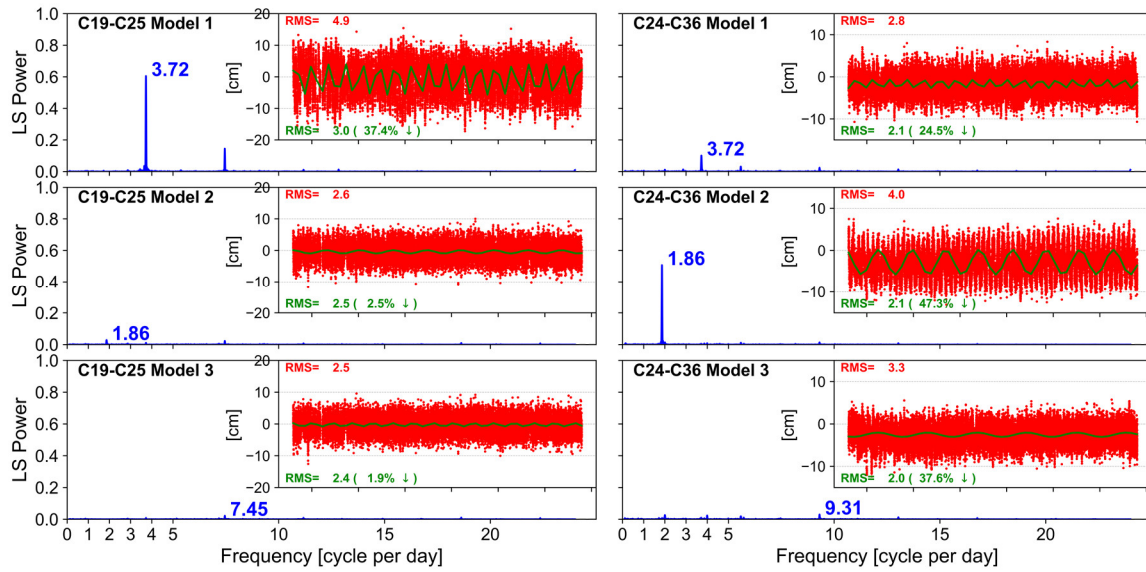
Figure 4.14 Lomb-Scargle Periodograms of clock residuals of link C19-C25 and C24-C36 after applying different periodic function models

4.4.3 Impact on Clock Estimates

Figure 4.15 and Figure 4.16 illustrate the STDs of clock offsets estimated by employing different periodic function models when compared with MGEX AC WHU's and GFZ's daily clock products, respectively.
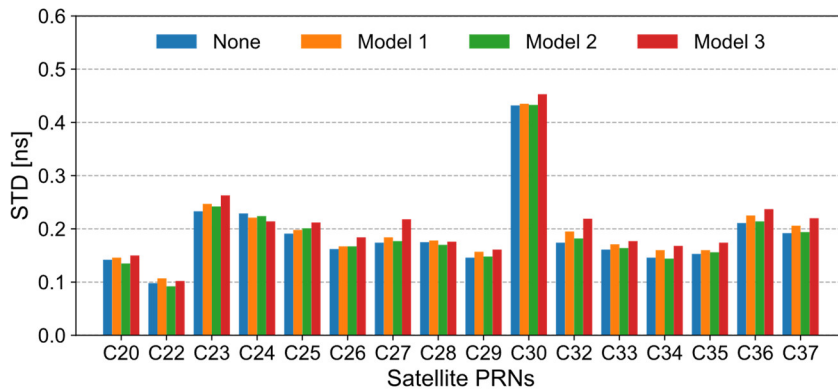
Figure 4.15 Monthly averages of clock offset difference STDs from solutions employing different periodic function models when compared with MGEX AC WHU's daily clock products
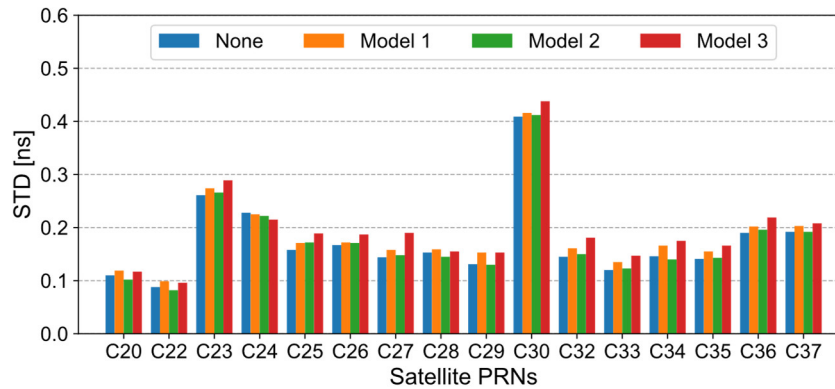
Figure 4.16 Monthly averages of clock offset difference STDs from solutions employing different periodic function models when compared with MGEX AC GFZ's daily clock products

No matter which external products were taken as references, it generally shows minor differences among various periodic models applied. Using Model 1 slightly increases the STDs in both comparisons for most satellites but not when Model 2 was adopted. As mentioned earlier, only a few out of all links show a strong 1CPR signal as the peak frequency. Failing to absorb much of the systematic errors, those additional introduced parameters due to Model 1 may weaken the solution. Applying Model 3 did not further reduce the STDs of clock offsets for most satellites when compared with external clock solutions. Similar to Model 1, clock offset difference STDs of several satellites get marginally increased when using Model 3. However, taking the precision of ISL observations into account, it is hard to conclude Model 3 as a degraded solution.

4.4.4 Impact on Hardware Delays

Hardware delays existing in the ISL clock observations were calculated for different solutions in the same way as described in Sec. 4.3.3. The comparison of monthly averages of hardware delays from solutions with various periodic models applied is illustrated in Figure 4.17. And the same comparison for STDs of hardware delays over DOY 335~365, 2019 is also presented in Figure 4.18.
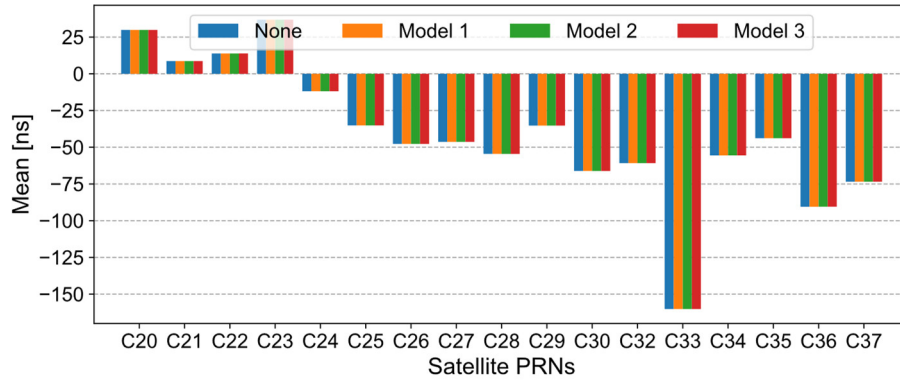
Figure 4.17 Comparison of means of ISL clock hardware delays estimated by employing different periodic function models
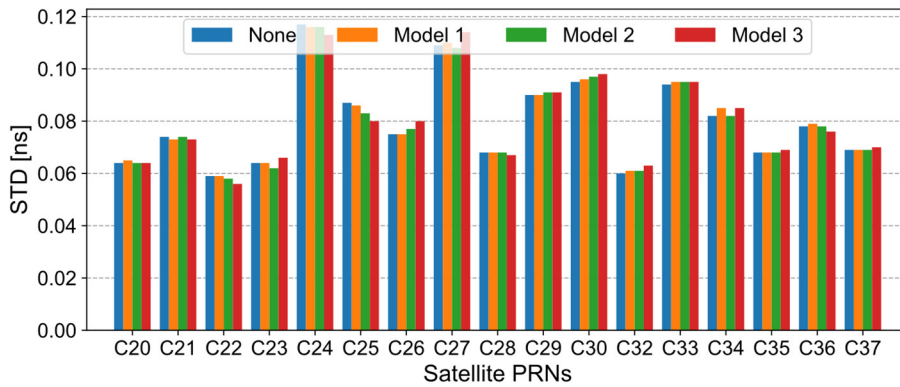
Figure 4.18 Comparison of STDs of ISL clock hardware delays estimated by employing different periodic function models

From Figure 4.17, the periodic signals in the clock observations have barely any noticeable effects on the estimates of hardware delays. Whether using a model or not, those systematic errors found in the fitting residuals do not change the obtained hardware delays. The negligible differences of STDs of hardware delays among different solutions confirm the harmlessness of those periodic signals.

4.5 Conclusion

Though in the sense of relative, clock estimation using only ISL without any support from the ground is an effective way to evaluate the time synchronization precision of BDS-3's AutoNav function.

Differing from satellite to satellite, an average fitting RMS of ~5.1 cm was obtained for ISL clock observations. Daily fitting residuals do not show much variation but a similar unimodal symmetric distribution. For individual satellites, no apparent directional errors can be recognized from their fitting residuals.

For most satellites, clock offset precision of 0.15 ~ 0.20 ns can be obtained relying only on ISL observations. And the clock rates can also be estimated with reasonable precision. Hardware delays existing in the ISL clock observations are found to be very stable. The average STD over one month is ~ 0.08 ns.

Similar to the range observations, residuals from most links show significant periodic signals resonating at the orbital frequency. It shows high correlations between the range and clock observations for most links. Considering that only a few links show peak significance at the 1CPR frequency, a Fourier-like periodic function model only accounting for the dominant 2CPR terms can greatly reduce those systematic errors. Nevertheless, a model taking all resonance frequencies into account can almost absorb all those periodic errors. Besides decreasing the fitting residuals, getting those periodic errors adequately modeled benefits the clock offset and hardware estimates marginally.

5 BDS-3 Orbit Determination with Ground Tracking

Before investigating orbit improvements contributed by additional ISL observations, it would be better to have an impression about the orbit quality obtained by ground tracking only. And any ambiguity about the dynamic modelling, which is irrelevant to specific observations used, should be clarified. Concerns like these constitute the motivation of this chapter.

The main part of the BDS-3 space segment is an MEO constellation. A similar design is also commonly used in other satellite navigation systems. Theoretically, there should not be too many differences in the dynamic and geometric modelling of orbit determination between BDS-3 and other GNSS, like GPS or Galileo, when using the L-band carrier phase and code pseudorange observations from ground tracking. However, as a newly emerged GNSS, some characteristic issues about its precise orbit determination are not settled yet.

Modelling of non-conservative forces is cumbersome for precise orbit determination of GNSS. Impacts of non-conservative perturbations on satellite orbits are closely related to the physical specifications of satellites. Thus, different satellite systems might suffer diversely from the deficiency of orbit modelling. The accuracy of satellites' a priori physical parameters required to model non-conservative perturbations might also be a concern. Quantitative analysis and check of these impacts for BDS-3 are necessary if targeting highly accurate orbits.

Another special concern about BDS-3 results from the switching of service frequencies, i.e., from the legacy B1I+B2I of BDS-2 to B1I+B3I. Precise products of GNSS serving high-demand users are always connected to specific service signals. To keep the backward compatibility, a smooth transition of services from BDS-2 to BDS-3 should be considered.

Hence, in this chapter, the effects of several critical non-conservative perturbations on the orbits of BDS-3 satellites are investigated. Following that, the possible choice of frequencies used in the combined orbit determination of BDS-2 and BDS-3 is discussed.

5.1 Non-Conservative Perturbations

5.1.1 Earth's Albedo

Earth's albedo, which originates indirectly from solar radiation, has been distinguished from

the direct solar radiation pressure as an additional non-negligible perturbation source of GNSS orbits(Hugentobler et al. 2009; Rodríguez-Solano 2009; Rodríguez-Solano et al. 2011a). It includes the effects of reflected visible light and emitted infrared radiation of the total solar radiation that reaches the Earth. In principle, the direct solar radiation pressure and Earth's albedo accelerate satellites' motion in a very similar manner except for different radiation directions. Calculating satellite accelerations caused by Earth's albedo requires the modelling of Earth radiation and satellite's geometric structure as well as its optical properties. In (Rodríguez-Solano 2009), detailed descriptions of the development of both analytical and numerical Earth radiation models were presented. It concludes that the simple analytical Earth radiation model has a similar performance as numerical models in the case of GPS-like satellites.

In this section, the effect of considering Earth's albedo on the orbits of BDS-3 is analyzed. Without repeating the model building procedure, the analytical Earth radiation model expressed as Equation (2.40) in (Rodríguez-Solano 2009) is adopted. For satellites on medium or high Earth orbits, the combined irradiance of Earth reflection and emission can be analytically approximated by

$$\boldsymbol{E}_{\mathrm{Alb}}(\psi, h) = \frac{\pi R_{\mathrm{E}}^2 E_{\mathrm{sun}}}{(R_{\mathrm{E}} + h)^2} \left[\frac{2\alpha}{3\pi^2} \big((\pi - \psi) \cos\psi + \sin\psi \big) + \frac{1-\alpha}{4\pi} \right] \boldsymbol{r} \tag{5.1}$$

where $\boldsymbol{E}_{\mathrm{Alb}}(\psi, h)$ means the irradiance of the Earth at a certain satellite altitude and relative positions of satellite, Earth and Sun (in W/m²); R_{E} is Earth's mean radius (6371 km); E_{sun} is the irradiance from the Sun at the Earth distance, i.e., the solar constant (1367 W/m²); h is the satellite's orbit altitude ($h \gg R_{\mathrm{E}}$); α is Earth's bond albedo, i.e., the ratio of reflected radiant power to incident radiant power of the Earth; ψ is the satellite–Earth-Sun angle; $\boldsymbol{r}$ is the satellite direction vector. For a specific part of the satellite with surface area of A_0 which is illuminated by the Earth, the generated force can be calculated as $\boldsymbol{F}_{\mathrm{Alb}}(\psi, h) = A_0 \cdot \boldsymbol{E}_{\mathrm{Alb}}(\psi, h)/c$. When using an analytical model, satellite models are also required in the calculation. As will be discussed in a later section for the modelling of direct SRP, parameters of satellite models released by the China Satellite Navigation Office (CSNO) are used here. As for the modelling of direct SRP here, the same empirical model was used in different solutions discussed in this section.

Figure 5.1 shows the accelerations caused by Earth's albedo for BDS-3 MEO satellites C22, C23, C26, and C30. Note that satellites C22 and C23 are from the same manufacturer but orbiting on different planes. It is the same case for satellites C26 and C30 while opposite for satellites C23 and C26 which orbit on the same plane but have different manufacturers. It shows that, depending on the fabricators (which means probably diverse physical specifications

of satellites) and orbiting planes, accelerations caused by Earth's albedo can reach up to 2~3 nm/s² for BDS-3 MEOs. The acceleration acts mainly in the orbital radial direction and shows both a short periodic and a secular variation. In fact, this secular variation is part of another long periodic change along with the Sun's position (Rodríguez-Solano 2009).
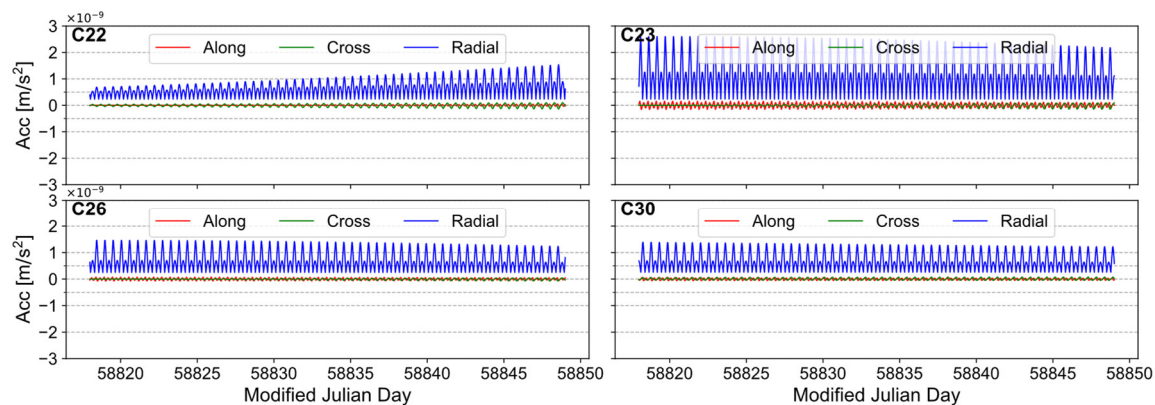
Figure 5.1 Accelerations caused by Earth's albedo for BDS-3 MEO satellites C22, C23, C26, and C30

Orbit variations of satellites C22, C23, C26, and C30 after considering Earth's albedo are illustrated in Figure 5.2. In the left panels, differences between solutions considering and ignoring Earth's albedo are displayed for various orbital components. Orbital radial variations are also plotted in the right panels in a so-called Sun-fixed system. The Sun-fixed system consists of the Sun's elevation angle above the satellite's orbit plane (β) and the satellite's orbit angle relative to the projection of the Sun (usually called the Noon) on the orbit plane (Δμ). In Figure 5.3, orbit difference RMS of BDS-3 MEOs between solutions considering and ignoring Earth's albedo are exhibited.

As shown for GPS in (Rodríguez-Solano 2009), the main effect of Earth's albedo is a contraction of the orbit, i.e., the reduction of the orbital radial component. Impacts on the along-track and cross-track components have only a size of around one-third of that in the radial direction and behavior more like noise. A clear dependence on the satellite's orbit angle can be observed in the radial variations. At the vicinity of the orbit Noon (i.e., -90°≤Δμ≤90°), the orbital radial deformation increases obviously. As satellites orbit above the illuminated part of the Earth during this period, both the reflected visible and emitted infrared radiation contribute to the perturbation (Rodríguez-Solano 2009). Moreover, the impact on orbital radials from Earth's albedo decreases as the Sun's elevation increases (see satellite C22, for instance). Generally, the magnitude of radial reduction for BDS-3 MEOs is 1.4 ~ 2.6 cm, with an average of ~1.7 cm. Effects in the along-track and radial directions are only 0.6 and 0.5 cm, respectively. Satellites C23, C24, C36, and C37 exhibit larger effects than other satellites. Impacts of Earth's albedo on the orbit precision and accuracy will be presented in the next

91

section.
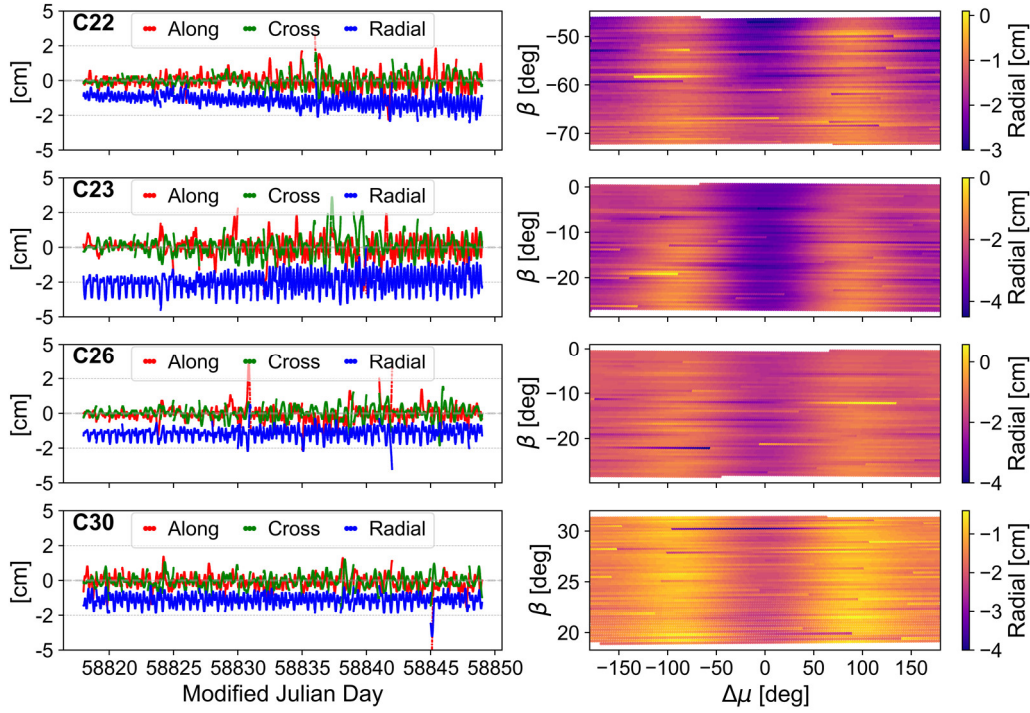
Figure 5.2 Orbit variations of BDS-3 MEO satellites C22, C23, C26, and C30 after considering Earth's albedo.
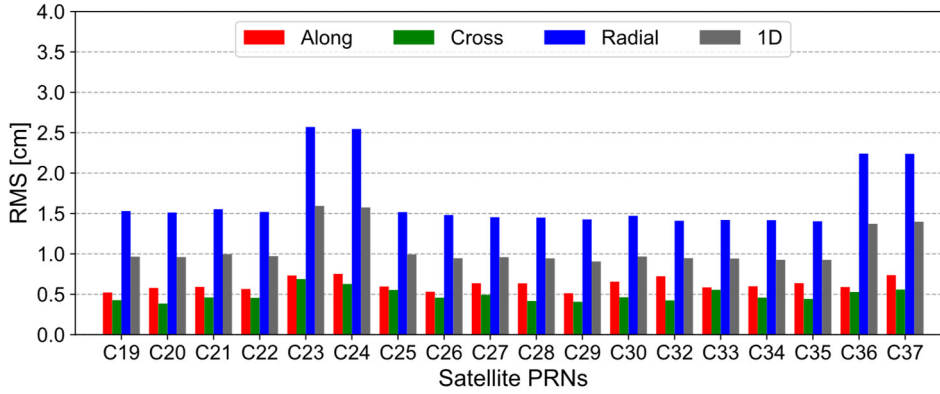
Figure 5.3 RMS of BDS-3 orbit difference between solutions considering and ignoring Earth's albedo

5.1.2 Antenna Thrust

With some reasonable assumptions, the acceleration induced by GNSS navigation antenna thrust arises only along the radial direction of the satellite and can be expressed as (Milani et al. 1987; Ziebart et al. 2007; Steigenberger et al. 2018)

$$\boldsymbol{a}_{\mathrm{Ant}} = \frac{P}{c \cdot m} \cdot \frac{\boldsymbol{X}_{\mathrm{Sat}}}{\|\boldsymbol{X}_{\mathrm{Sat}}\|} \tag{5.2}$$

where P and m denote the transmit power (in Watt) and mass (in kilogram) of the satellite; c is the speed of light in vacuum; X_{Sat} is the vector of the satellite's position. Similar to Earth's albedo, antenna thrust acceleration mainly induces a decrease in the orbit radius. The radial reduction Δr is proportional to the magnitude of the acceleration and inverse of the square of the satellite's mean motion n (Milani et al. 1987; Steigenberger et al. 2018)

$$\Delta r = -\frac{1}{3n^2}\|a_{Ant}\| \tag{5.3}$$

Based on the transmit power data collected by IGS MGEX (See Table A-4 in Appendix A), if applying the simplified antenna thrust model, an antenna thrust acceleration of 0.9~1.1 nm/s² and consequently a change of -1.6~-2.0 cm in the orbital radius can be expected for BDS-3 MEO satellites, as showed in Figure 5.4. Satellites manufactured by CAST have slightly larger accelerations than SECM-produced satellites because of 30 W higher transmit power. Small differences within the same group are due to slightly various satellite masses.
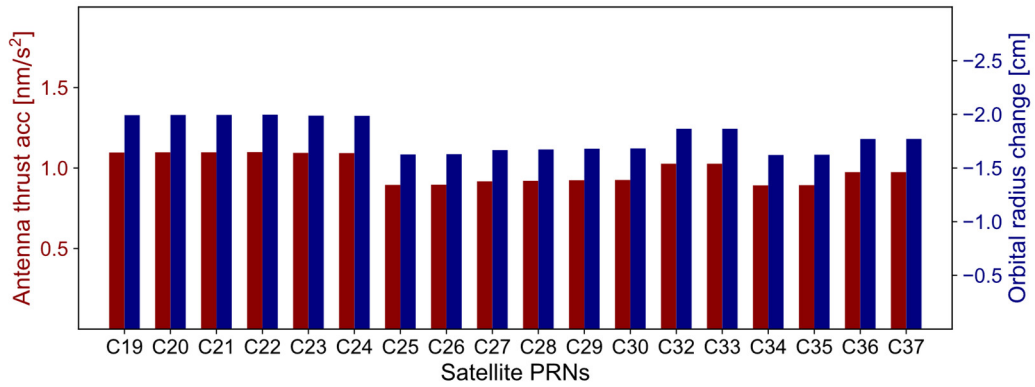
Figure 5.4 Antenna thrust induced acceleration (left y-axis) and its effect on the orbit radius of BDS-3 satellites based on a simplified model (right y-axis)

Figure 5.5 shows the orbit differences between considering and ignoring the perturbation caused by antenna thrust. As expected, the antenna thrust impacts mainly the orbit radial component. It causes an almost constant reduction of the radius of the orbit. The radial shrink of CAST satellites is 1.7~1.9 cm, while that of SECM satellites is ~1.6 cm, just coinciding with the prediction. A radial acceleration can also indirectly affect the other two components except for the radial one of the satellite's position. However, compared to Earth's albedo, antenna thrust has much smaller effects in the along- and cross-track directions of BDS-3 MEOs' orbits.
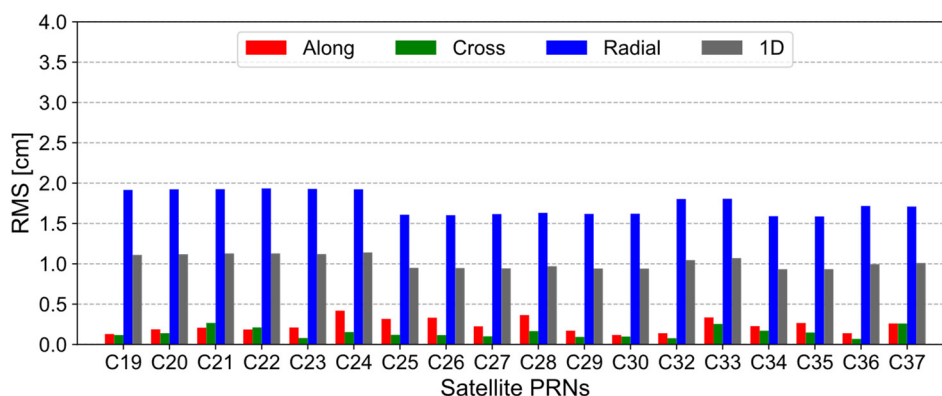
Figure 5.5 RMS of BDS-3 orbit differences between solutions considering and ignoring antenna thrust

In Figure 5.6, combined effects of Earth's albedo and antenna thrust perturbations are exhibited. It shows that the combined effects of those two dissipative forces on the orbit radial component are ~3.4 cm on average and can reach up to 4.0~4.5 cm for several CAST satellites.
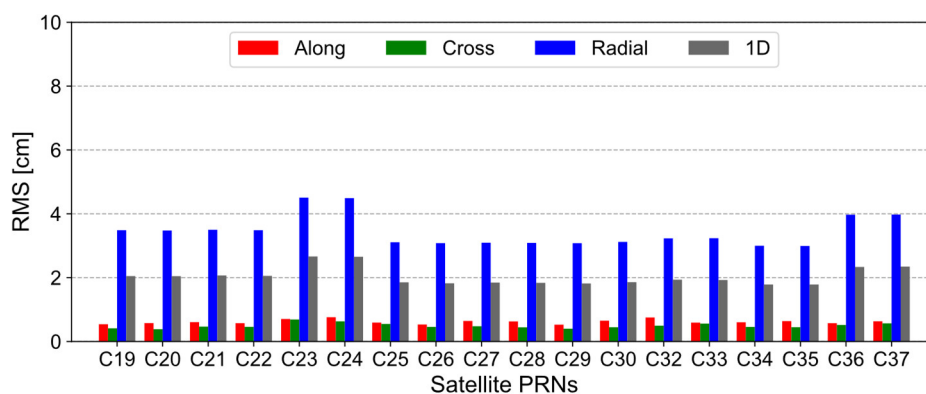
Figure 5.6 RMS of BDS-3 orbit differences between solutions considering and ignoring both Earth's albedo and antenna thrust

Only knowing the effect of perturbations does not guarantee the correct modelling of them. Orbit precision and accuracy should be examined to evaluate the properness of those perturbation models. In Figure 5.7, orbit DBD 1D RMS of solutions ignoring both Earth's albedo and antenna thrust (**None**), considering one of them (**Alb** or **Ant**), and considering both (**Alb+Ant**) are compared.

It seems that antenna thrust barely affects the internal precision of satellite orbits. After considering the effect of Earth's albedo, a small decrease, mainly in the orbital cross-track and radial directions, of the orbit DBD can be found for most satellites. As the constant terms in the D and B directions of the empirical SRP model (discussed in the next section) can partially compensate for the ignored Earth's albedo (Hugentobler et al. 2009), its actual impact might not be fully revealed when such an empirical SRP model is applied. Taking both Earth's albedo and antenna thrust into account produces basically the same orbit precision as only considering the former perturbation.

Statistics of orbit SLR residuals of those different solutions are compared in Figure 5.8. The SLR residuals were calculated in the way of observed minus computed (OmC). Not surprisingly, orbit radial reductions resulting from Earth's albedo and antenna thrust are directly reflected in the change of SLR residual biases. Because of opposite signs, the magnitude of SLR biases of C29 and C30 decrease while those of C20 and C21 increase after considering those perturbations. These significant biases in the SLR residuals were found by chance to be probably related to the uncertainty of offset corrections of Laser Retroreflector Arrays (LRA) onboard satellites.

The CSNO released LRA offsets of BDS-3 satellites were incorporated into the IGS MGEX metadata and, consequently, were used in this study. When using the LRA offsets listed in (Yan et al. 2019)(see Table A-3 in Appendix A), reductions in the magnitudes of SLR residual means of 4.2 and 2.6 cm, which coincide with the Z-offset differences between those two sources, were found for CAST satellites C20/C21, and SECM satellites C29/C30, respectively. The standard deviations of SLR residuals are not affected. It may need further investigation to validate the correctness of the CSNO released data. Nevertheless, in this study, using the IGS MGEX metadata is still insisted on, as inaccurate LRA offsets basically would only affect the biases of orbit SLR residuals. It should be mentioned that, even if the biases caused by the possible errors in the LAR offsets are considered, there are still remaining biases of 2.0 cm for satellite C20 and 1.8 cm for satellite C21 after modelling both Earth's albedo and antenna thrust. These biases are -1.3 and -1.6 cm before considering any of those two perturbations. Similar to the case reported by (Steigenberger et al. 2018) for the antenna thrust, considering it does not always decrease the SLR biases, e.g., Galileo Full Operational Capability (FOC) satellites, for which the SLR biases increase obviously after applying the antenna thrust model. For the two SECM satellites, C29 and C30, though reduced by 3 cm after considering Earth's albedo and antenna thrust, apparent biases can still be observed in the orbit SLR residuals. Additionally, unlike shown in orbit DBDs, satellites C29 and C30 exhibit obviously worse accuracy than C20 and C21. To sum up, the necessity of modelling the perturbations caused by Earth's albedo and antenna thrust for BDS-3 is confirmed and will be included in all following solutions in this study.
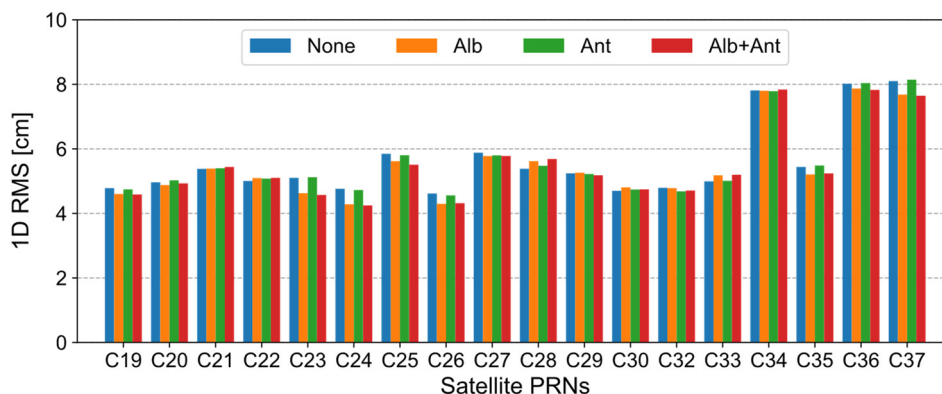
Figure 5.7 Comparisons of orbit DBD 1D RMS of solutions ignoring both Earth's albedo and antenna thrust (**None**), considering only Earth's albedo (**Alb**), considering only antenna thrust (**Ant**), and considering both of them (**Alb+Ant**)
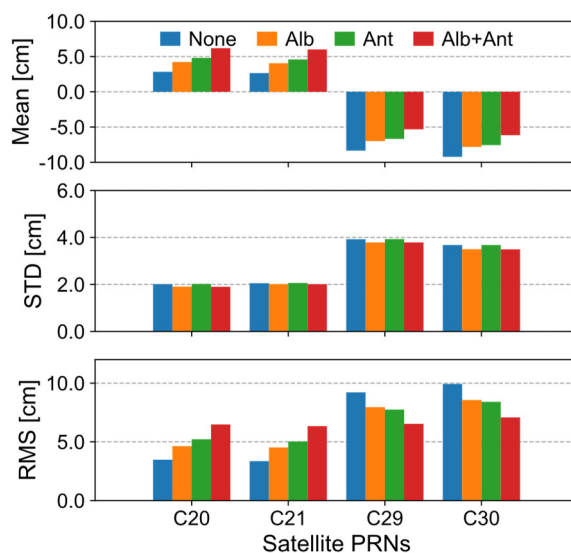
Figure 5.8 Comparisons of orbit SLR residuals of solutions ignoring both Earth's albedo and antenna thrust (**None**), considering only Earth's albedo (**Alb**), considering only antenna thrust (**Ant**), and considering both of them (**Alb+Ant**)

5.1.3 Solar Radiation Pressure

Considering the difficulty of modelling and magnitude of effects, direct Solar Radiation Pressure (SRP) is currently the most critical non-conservative perturbation for GNSS orbits. For a fresh GNSS like BDS, insufficiently accumulated studies in this aspect still can not recommend an optimal SRP model. This section focuses on choosing appropriate empirical SRP models and analyzing the necessity and impact of a priori analytical models for BDS-3.

5.1.3.1 Empirical Model

Inspired by the modelling of residual errors from Earth's gravity field (Colombo 1989), an empirical SRP model with similar Fourier formation while targeting the Sun instead of the Earth as the error source has been firstly proposed by (Beutler et al. 1994). After that, this so-called Empirical CODE Orbit Model (ECOM) has evolved into diverse variants that differ in the angular argument, number and frequency of periodic terms in one or several directions. Rather than giving detailed descriptions of all those differently parameterized ECOMs, literature in which the two mostly used models were proposed is listed here for reference. These are the commonly called ECOM1 (assigned as **E1P5** here because of five estimated parameters) (Springer et al. 1999) and the newly updated ECOM2 (Arnold et al. 2015). For ECOM2, the two recommended parameterizations annotated as D2B1 and D4B1 in that study are examined here and assigned as **E2P7** and **E2P9**, respectively, to discriminate the number of estimated parameters. Mathematical expressions of those ECOMs considered in this study are put in Appendix B.

Figure 5.9 compares the orbit DBD 1D RMS of solutions that apply different ECOMs for SRP modelling. Comparisons of statistics of orbit SLR residuals for those different solutions are displayed in Figure 5.10.
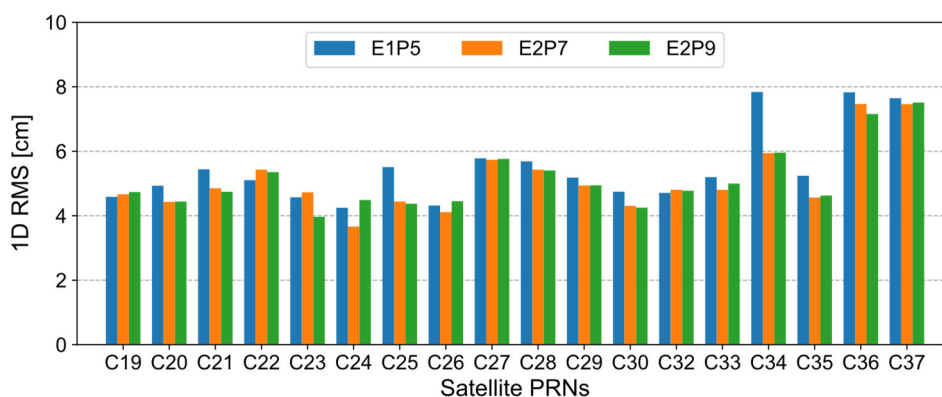
Figure 5.9 Orbit DBD 1D RMS of solutions with E1P5, E2P7, and E2P9 applied for SRP modelling
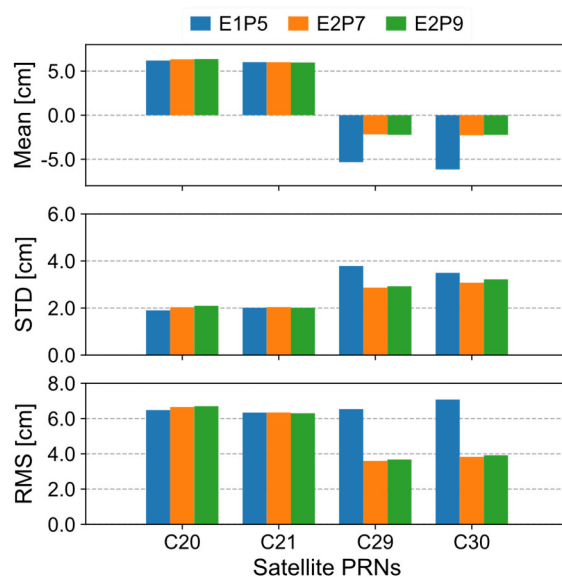
Figure 5.10 Statistics of orbit SLR residuals of solutions with E1P5, E2P7, and E2P9 applied for SRP modelling

It can be found that, except for satellites C23 and C24, very similar orbit performance can be obtained by using E2P7 or E2P9 for most BDS-3 MEO satellites. Clear reductions in the orbit DBD can be observed for several satellites, such as C21, C25, C34, and C35 when switching the ECOM from E1P5 to E2P7 or E2P9. However, for some other satellites, e.g., C27 and C32, the orbit precision is marginally affected by the different choices of empirical SRP models. Connections between those characteristics about applicability and the manufacturers or orbit planes of satellites are not very clear. In general, using E2P7 generates orbit with slightly better precision than E2P9.

As shown in Figure 5.10, applying E2P7 or E2P9 decreases the orbit SLR residual offsets by around 3.1 and 3.9 cm for the two SECM satellites, i.e., C29 and C30. This might be attributed to the additional 2CPR terms in the direction facing the Sun included in those ECOMs. Furthermore, if the possible errors in the LRA corrections (See Section 5.1.2) can be confirmed, orbit SLR residual offsets of C29 and C30 will almost vanish, with a remaining amount of only 0.5 and 0.3 cm, respectively. Standard deviations of orbit SLR residuals of satellites C29 and C30 also get reduced when using E2P7 or E2P9. But for the two CAST satellites, i.e., C20 and C21, not much influence on the orbit accuracy can be noticed for different empirical SRP models.

From the comparison, it shows some diversity among satellites about the applicability of different ECOMs. A natural consideration is to choose the "best fit" model for each individual satellite. With simple picking criteria based on the comparisons of orbit DBD and SLR residuals, the satellite-specific empirical SRP models are obtained for BDS-3 MEOs, as listed

in Table 5-1.

Table 5-1 Satellite-specific ECOMs for BDS-3 MEO satellites concluded from the comparisons of orbit DBD and SLR residuals

ECOMs	E1P5	E2P7	E2P9
Satellites applied	C19, C22, C27, C32	C20, C21, C24, C25, C26, C28, C29, C30, C33, C34, C35, C37	C23, C36

For the sake of simplification, those satellite-specific ECOMs are annotated as **SatE** when referring to SRP models in the following part of this study. It should be mentioned that, instead of a new model, it is more appropriate to regard **SatE** as a new way to apply different ECOMs for BDS-3 satellites. In Figure 5.11, orbit DBD 1D RMS of the solution adopting SatE is compared with the previously mentioned four models. And orbit DBD 1D RMS of all solutions are given in Table 5-2. Comparisons of orbit SLR residual statistics for those models are displayed in Figure 5.12.
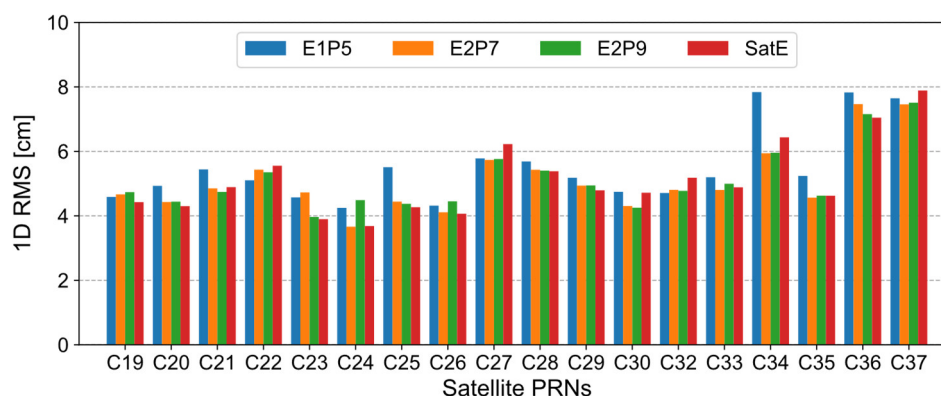
Figure 5.11 Comparisons of orbit DBD 1D RMS of the solution adopting **SatE** with solutions applying the other four models

Table 5-2 Orbit DBD 1D RMS of solutions with different empirical SRP models [cm]

PRN	E1P5	E2P7	E2P9	SatE
C19	4.59	4.67	4.74	4.43
C20	4.93	4.43	4.44	4.30
C21	5.44	4.85	4.74	4.89
C22	5.10	5.43	5.35	5.55
C23	4.57	4.73	3.97	3.90
C24	4.25	3.66	4.49	3.68
C25	5.51	4.44	4.37	4.27
C26	4.32	4.11	4.45	4.06
C27	5.78	5.73	5.76	6.23
C28	5.69	5.43	5.40	5.38

C29	5.18	4.94	4.94	4.79
C30	4.75	4.30	4.25	4.72
C32	4.71	4.81	4.78	5.18
C33	5.20	4.80	5.00	4.89
C34	7.84	5.94	5.96	6.43
C35	5.24	4.56	4.63	4.62
C36	7.83	7.47	7.16	7.05
C37	7.65	7.46	7.51	7.89
Mean	5.48	5.10	5.11	5.13

Although for some satellites, the solution adopting SatE as the SRP model shows the smallest orbit DBD, in general, it shows similar orbit precision as E2P7 and E2P9. This may indicate correlations of orbit parameters among satellites in the constellation, which compromises the effectiveness of independent modelling for individual satellites by empirical models. Similar conclusions can be drawn from the comparisons of orbit SLR residuals, as shown in Figure 5.12. Except for E1P5, the other three solutions get comparable quality for orbits of BDS-3 MEOs. From Figure 5.13, which shows the SLR residual variations against the Earth-satellite-Sun angle ε for those four solutions, dependences of residuals on the ε are eased up for C29 and C30 by switching from E1P5 to E2P7, E2P9, or SatE.
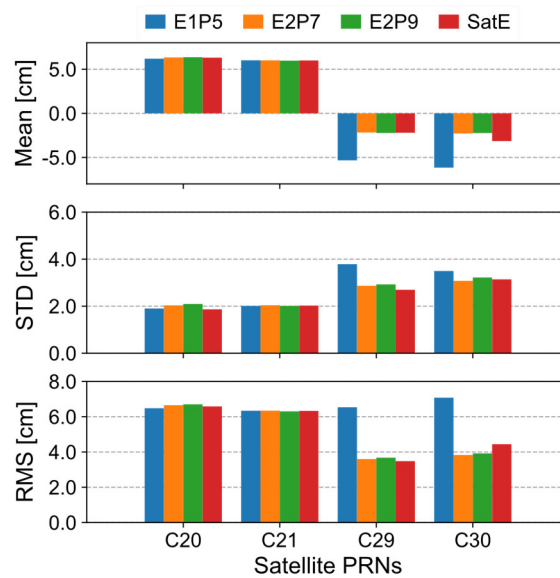
Figure 5.12 Comparisons of orbit SLR residuals of the solution adopting **SatE** with solutions applying the other four models
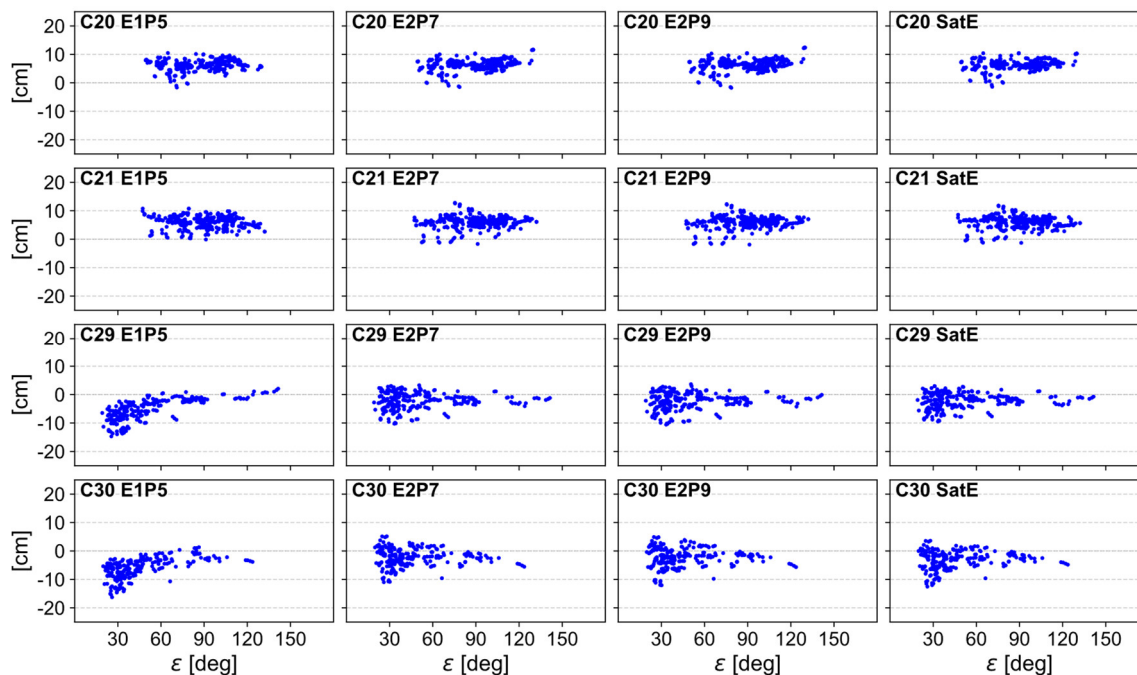
Figure 5.13 Variations of orbit SLR residuals along with the Earth-satellite-Sun angle ε of solutions with different empirical SRP models

5.1.3.2 Analytical Model

Analytical SRP models have been proposed to describe the interaction between direct solar radiation and satellite surfaces in a physically meaningful way (Milani et al. 1987). Usually, the satellite's shape is simplified as a box with two wings in an analytical model, which is, therefore, called the box-wing model. Another analytical model aimed to cope with a high-level complexity in the spacecraft structure was also proposed (Ziebart 2001). But in this study, the discussion is limited to the former one, i.e., the box-wing model. The box-wing model was found to be effective for reducing the spurious periodic signals in geodetic time series derived from GPS (Rodríguez-Solano et al. 2011b; Rodríguez-Solano et al. 2012) and BDS (Bingbing et al. 2022). However, the performance of box-wing models easily suffers from inaccurate a priori information about the satellite's physical specifications, such as its structures, dimensions, and optical properties. Dimensions and absorptivities of satellite bodies and solar panels of BDS-2/BDS-3 IGSO and MEO satellites have been released by CSNO[1]. Although either the specularities or diffusivities are further required by box-wing models, based on guessed values for these missing properties, it still makes sense to check the accuracy of those released parameters by applying them in orbit determinations. Effects of incorporating a priori box-

---

[1] http://www.beidou.gov.cn/yw/gfgg/201912/t20191209_19613.html/ W020200323534413073762.zip, last accessed on 2021/11/19.

wing models based on those released satellite parameters are investigated in this section. Parameters released by CSNO, guessed values for missing properties as well as related considerations about that are summarized in Appendix C for reference.

Figure 5.14 compares the orbit DBD 1D RMS of solutions combining the a priori box-wing model with different ECOMs. Orbit DBD 1D RMS of all solutions are listed in Table 5-3. Compared with Table 5-2, effects of the a-prior box-wing model on orbit DBD can be noticed for individual satellites, especially in the case of using E1P5 as the empirical SRP model. The direction of DBD changes (i.e., increasing or decreasing) depends on specific satellites, and it is not easy to conclude whether this is closely related to satellite types. For example, orbit DBD of CAST satellites C19, C20, C21, and C22 show slight increases after adding the a priori box-wing model while C23, C24, C36, and C37, which are from the same manufacturer, exhibit clear reduction. For SECM satellites, except for negligible increments found for C26, C27, and C30, orbit DBDs of the other five satellites are reduced by the a priori box-wing model. On average, the orbit DBD 1D RMS only decreases by around 0.1 cm after using the a priori box-wing model in addition to E1P5. As for the other three models, i.e., E2P7, E2P9, and SatE, impacts of the a priori box-wing model are very small for all satellites. As a result, with the a priori box-wing model, using E2P7, E2P9, and SatE can all get slightly smaller orbit DBD than E1P5.
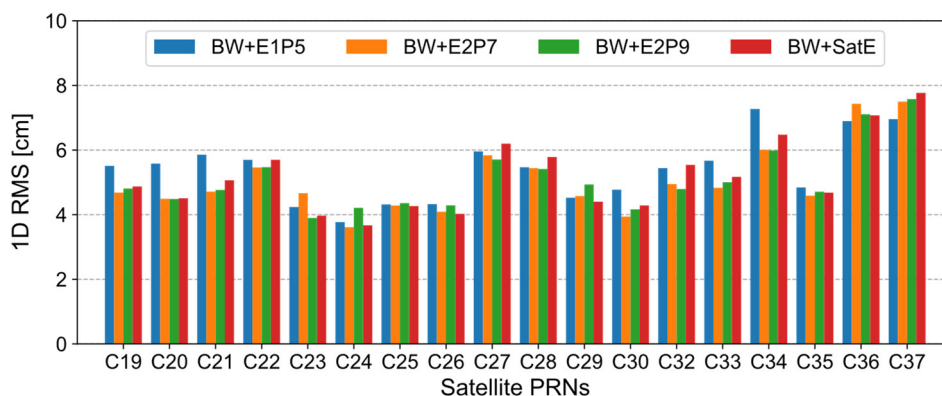
Figure 5.14 Comparisons of orbit DBD 1D RMS of solutions combining the a priori box-wing model with different empirical SRP models

Table 5-3 Orbit DBD 1D RMS of solutions combining the a priori box-wing model with different empirical SRP models [cm]

PRN	BW+E1P5	BW+E2P7	BW+E2P9	BW+SatE
C19	5.51	4.68	4.81	4.87
C20	5.58	4.49	4.48	4.51
C21	5.85	4.71	4.77	5.07
C22	5.70	5.46	5.47	5.70

C23	4.24	4.66	3.90	3.97
C24	3.77	3.61	4.21	3.67
C25	4.32	4.28	4.36	4.27
C26	4.33	4.09	4.29	4.03
C27	5.96	5.84	5.71	6.20
C28	5.47	5.44	5.41	5.79
C29	4.52	4.57	4.93	4.40
C30	4.77	3.94	4.16	4.28
C32	5.44	4.95	4.79	5.54
C33	5.67	4.83	5.00	5.17
C34	7.27	6.01	5.99	6.48
C35	4.84	4.59	4.71	4.68
C36	6.90	7.43	7.11	7.07
C37	6.96	7.50	7.58	7.77
Mean	5.39	5.06	5.09	5.19

In Figure 5.15, statistics of orbit SLR residuals of solutions combining the a priori box-wing model with different empirical SRP models are compared. Figure 5.16 shows the SLR residual variations along with the Earth-satellite-Sun angle ε for all solutions. For satellites C20 and C21, adding the a priori box-wing model hardly changes the orbital radial accuracy, no matter which ECOM is used. But for C29 and C30, compared to Figure 5.13, the a priori box-wing model clearly mitigates the ε angle dependence in the SLR residuals when using E1P5, which results in improved radial accuracy. When using E2P7, E2P9, or SatE, no significant difference can be noticed in the SLR residuals after adding the a priori box-wing model. Regardless of the offsets affected by the uncertainty of LRA corrections, STDs of SLR residuals are comparable among those solutions, with a maximum difference of ~0.6 cm. To sum up, similar orbit radial accuracy can be obtained among different empirical models if using the additional a priori box-wing model. And the orbit quality differences among solutions E2P7, E2P9, and SatE are also very small. Therefore, in the following processing of this study, the SatE is used for direct SRP modelling if not otherwise mentioned.
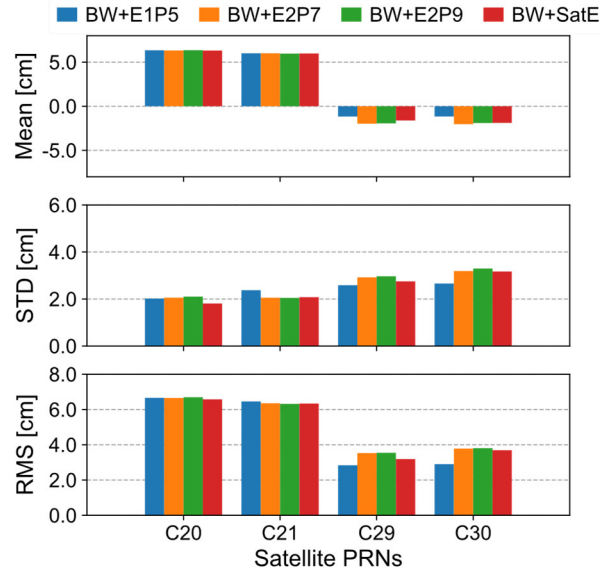
Figure 5.15 Comparisons of orbit SLR residual RMS of solutions combining the a priori box-wing model with different empirical SRP models
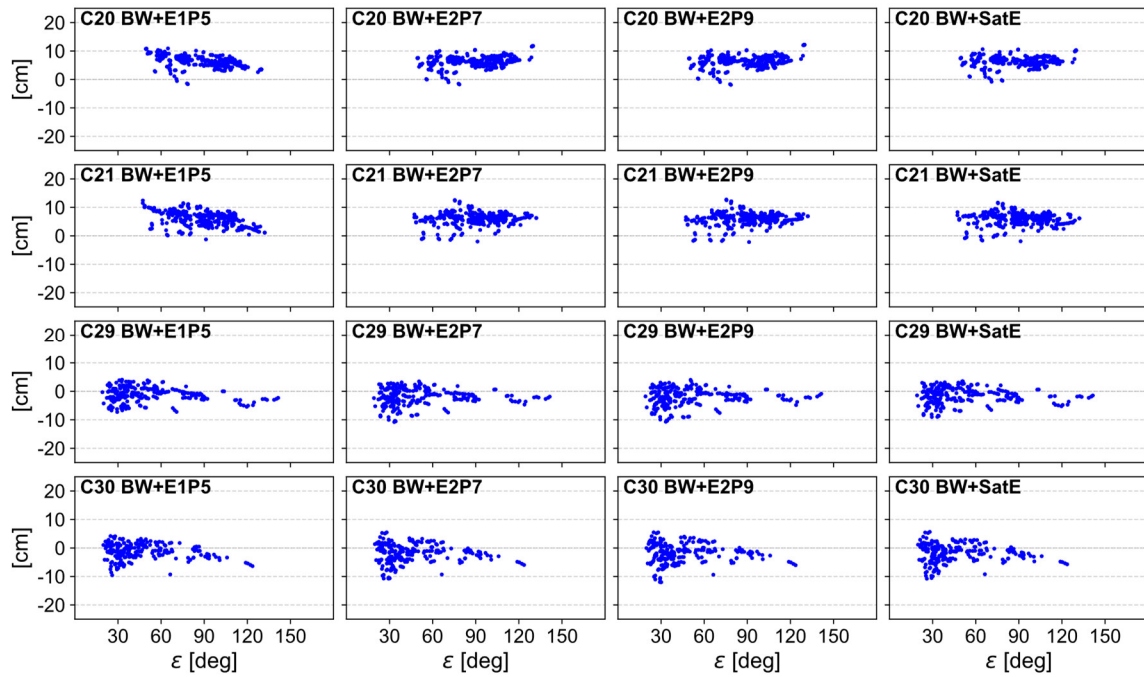
Figure 5.16 Variations of orbit SLR residuals along with the Earth-satellite-Sun angle ε of solutions combining the a priori box-wing model with different empirical SRP models

5.2 Integrated Processing of BDS-2 and BDS-3

The open service signals of BDS-3 are B1I and B3I (CSNO 2018b; CSNO 2019), which differ from the legacy B1I and B2I signals of BDS-2 (CSNO 2016). With the official release of the Interface Control Document (ICD), receivers can be updated to track BDS-2 satellites with

the B3I signal as well, making a common dual-frequency tracking between BDS-2 and BDS-3 possible. However, according to the published ICDs, there seem to be some design updates in the common signals of BDS-3. For example, in the B1I/B2I ICD of BDS-2 (CSNO 2016), the modulation mode of transmitted signals is QPSK (Quadrature Phase Shift Keying), while in a newer version ICD of B1I (CSNO 2019), the modulation mode was changed to BPSK (Binary Phase Shift Keying). It should be investigated if the common B1I+B3I signals are still the same between BDS-2 and BDS-3 after a signal design revision.

For a receiver *r*, which is capable of tracking both BDS-2 and BDS-3 satellites, the observation equation of BDS-2 ionosphere-free pseudorange (denoted as PC$_2$) measurements can be written as

$$
\begin{aligned}
PC_{r,2}^{\text{BDS}-2} = {} & \rho_r^{\text{BDS}-2} + \left(c\delta t_r + \Delta_{r,PC_2}\right) - \left(c\delta t^{\text{BDS}-2} - \Delta^{\text{BDS}-2,PC_2}\right) + m_r^{\text{BDS}-2}T \\
& + \varepsilon_{\text{BDS}-2,PC_2}
\end{aligned}
\tag{5.4}
$$

and for ionosphere-free carrier phase (denoted as LC$_2$) observations, it reads

$$
\begin{aligned}
LC_{r,2}^{\text{BDS}-2} = {} & \rho_r^{\text{BDS}-2} + \left(c\delta t_r + \Delta_{r,PC_2}\right) - \left(c\delta t^{\text{BDS}-2} - \Delta^{\text{BDS}-2,PC_2}\right) + m_r^{\text{BDS}-2}T \\
& + \left[\left(\Delta^{\text{BDS}-2,LC_2} - \Delta^{\text{BDS}-2,PC_2} - \Delta_{r,PC_2} + \Delta_{r,LC_2}\right) + \lambda_{LC_2}N_{r,LC_2}^{\text{BDS}-2}\right] \\
& + \varepsilon_{\text{BDS}-2,LC_2}
\end{aligned}
\tag{5.5}
$$

As for BDS-3 satellites, observation equations of ionosphere-free pseudoranges (denoted as PC$_3$) and carrier phases (denoted as LC$_3$) can be expressed with similar notations by Equation (5.6)

$$
\begin{aligned}
PC_{r,3}^{\text{BDS}-3} = {} & \rho_r^{\text{BDS}-3} + \left(c\delta t_r + \Delta_{r,PC_2}\right) - \left(c\delta t^{\text{BDS}-3} - \Delta^{\text{BDS}-3,PC_3}\right) + m_r^{\text{BDS}-3}T \\
& + \left(\Delta_{r,PC_3} - \Delta_{r,PC_2}\right) + \varepsilon_{\text{BDS}-3,PC_3}
\end{aligned}
\tag{5.6}
$$

and Equation (5.7), respectively

$$
\begin{aligned}
LC_{r,3}^{\text{BDS}-3} = {} & \rho_r^{\text{BDS}-3} + \left(c\delta t_r + \Delta_{r,PC_2}\right) - \left(c\delta t^{\text{BDS}-3} - \Delta^{\text{BDS}-3,PC_3}\right) + m_r^{\text{BDS}-3}T \\
& + \left[\left(\Delta^{\text{BDS}-3,LC_3} - \Delta^{\text{BDS}-3,PC_3} - \Delta_{r,PC_3} + \Delta_{r,LC_3}\right) + \lambda_{LC_3}N_{r,LC_3}^{\text{BDS}-3}\right] \\
& + \left(\Delta_{r,PC_3} - \Delta_{r,PC_2}\right) + \varepsilon_{\text{BDS}-3,LC_3}
\end{aligned}
\tag{5.7}
$$

In Equations (5.4)-(5.7), ρ_r^* (* = BDS-2 or BDS-3) is the actual distance between the phase center of the receiver antenna at the signal receipt time and that of the BDS-2/BDS-3 satellite transmitting antenna at the signal transmission time; δt_r is the receiver clock offset with respect to the reference clock(s) at the signal receipt time; δt^* (* = BDS-2 or BDS-3) is the BDS-2/BDS-3 satellite clock offset with respect to the reference clock(s) at the signal transmission time; $\Delta_{r,*}$ (* = PC$_2$, LC$_2$, PC$_3$, or LC$_3$) is the ionosphere-free combination of receiver hardware delays in the code pseudorange or carries phase observations of the two

frequencies used for BDS-2 or BDS-3; Analogously, $\Delta^{*,\&}$ (when $*$ = BDS-2, $\&$ = PC_2 or LC_2; when $*$= BDS-3, $\&$ = PC_3 or LC_3) is the ionosphere-free combination of transmitter hardware delays; m_r^* ($*$ = BDS-2 or BDS-3) is the function for mapping the tropospheric zenith delay T to the direction of the line-of-sight; λ_* ($*$ = LC_2 or LC_3) is the ionosphere-free combination of wavelengths of the two frequencies used for BDS-2 or BDS-3; $N_{r,\&}^*$ (when $*$ = BDS-2, $\&$ = LC_2; when $*$= BDS-3, $\&$ = LC_3) is the ionosphere-free combination of integer ambiguities in the two single-frequency carrier phase observations of BDS-2 or BDS-3. Other terms indicating various error sources not mentioned are denoted as $\varepsilon_{*,\&}$ (when $*$ = BDS-2, $\&$ = PC_2 or LC_2; when $*$= BDS-3, $\&$ = PC_3 or LC_3), which includes but is not limited to receiver and transmitter phase center offsets, relativistic effects, multipath effects, and noises; c is the speed of light in vacuum.

Clock offsets are always coupled with hardware delays. For a specific receiver, the hardware delays of BDS-3 are not necessarily the same as that of BDS-2, even for the common frequency because of the new design of signals. Observation equations of BDS-3 as expressed in Equation (5.6) and (5.7) are formularized in the form of taking receiver clock offsets of BDS-2 as local references. The term $(\Delta_{r,PC_3} - \Delta_{r,PC_2})$, referred as receiver bias between BDS-2 and BDS-3 in this study, is explicitly set up to consider the possible difference of receiver hardware delays between BDS-2 and BDS-3.

As a new generation of the space segment of BDS, BDS-3 should be incorporated with BDS-2 as a whole system. Not just from the point of view of the development and maintenance of the system, it also benefits the users in aspects like service quality and continuity. Integrated processing of BDS-2 and BDS-3 improves the overall orbit performance of BDS, especially for BDS-2 satellites. Figure 5.17 shows the comparison of orbit DBD RMS of BDS-2 of solutions with and without incorporating BDS-3 into the orbit determination. In Figure 5.18, statistics of orbit SLR residuals of BDS-2 are compared. Clear improvements in the orbit precision and accuracy can be observed when integrating the orbit determination of BDS-2 and BDS-3. In this comparison, observations of signals B1I and B3I were used for BDS-2, and the concern about the signal choice for BDS-2 will be addressed later.
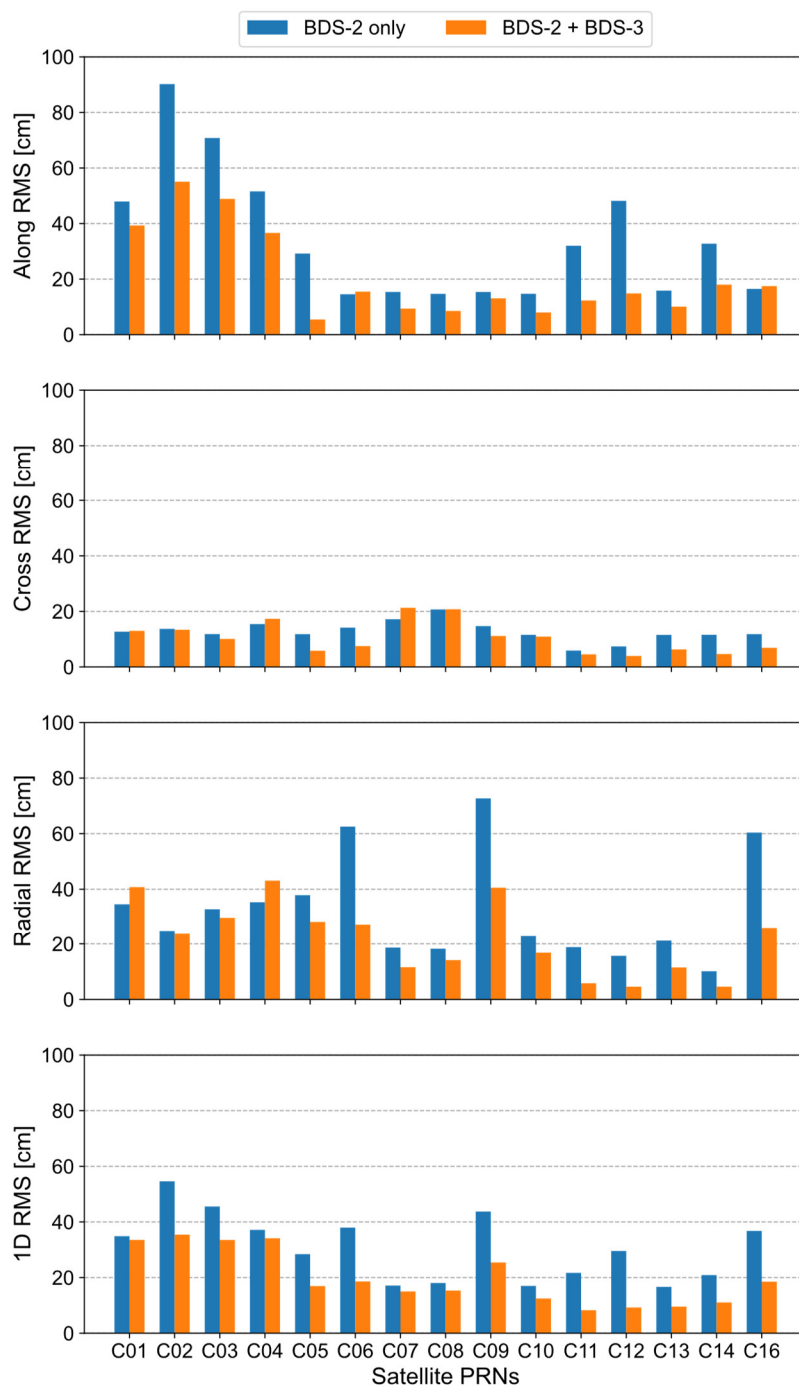
Figure 5.17 Comparisons of orbit DBD RMS of BDS-2 obtained from **BDS-2 only** processing and **BDS-2+BDS-3** integrated processing
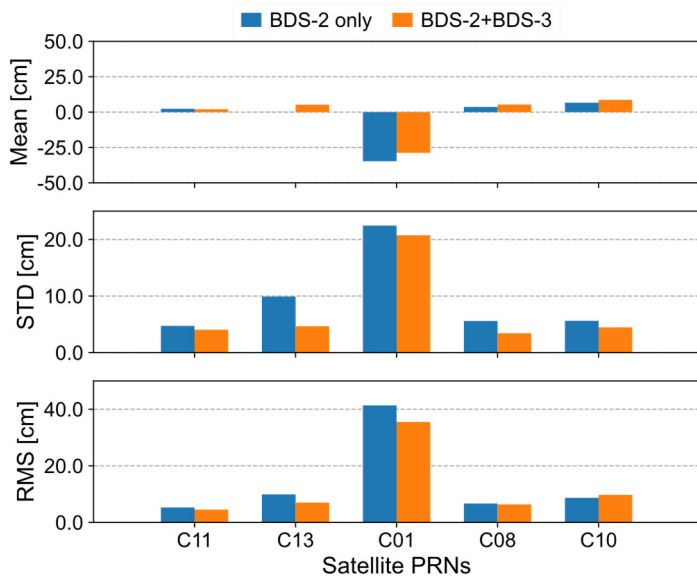
Figure 5.18 Comparisons of orbit SLR residual statistics of BDS-2 obtained from **BDS-2 only** processing and **BDS-2+BDS-3** integrated processing

During the transition phase from BDS-2 to BDS-3, BDS-2 satellites were more tracked at the B1+B2 than B1+B3 frequencies by the ground network, as shown in Figure 5.19[2].
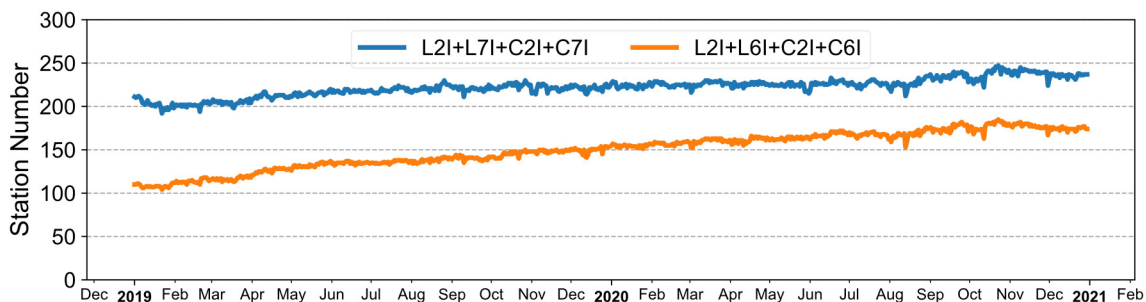
Figure 5.19 Number of IGS MGEX stations that can receive dual-frequency carrier phase and code pseudorange observations of B1I+B2I and B1I+B3I of BDS-2 during 2019~2020

Although those additional stations are mainly clustered in Europe (See Figure D-1 in Appendix D), using B1I+B2I can still get better orbit results for BDS-2. In Figure 5.20 and Figure 5.21, orbit DBD 1D RMS and SLR residual RMS of BDS-2 resulting from processings based on B1I+B3I and B1I+B2I are compared. Noticeable benefits can be found by using B1I+B2I for the orbit determination of BDS-2 in comparison to using B1I+B3I

In the following parts of this section, the choice between B1I+B2I and B1I+B3I for BDS-2 is discussed in the context of integrated processing of BDS-2 and BDS-3.

---

[2] Daily station numbers were obtained by checking RINEX observation files available at the CDDIS data center (https://cddis.nasa.gov/archive/). A simple criteria related to minimum number of observed satellites and epochs was applied to pick out sites that can actually track BDS-2 satellites.
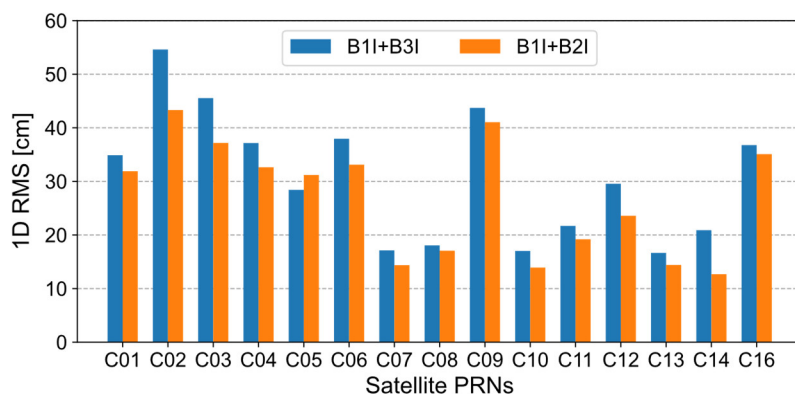
Figure 5.20 Comparison of orbit DBD 1D RMS of BDS-2 obtained from processings using B1I+B3I and B1I+B2I
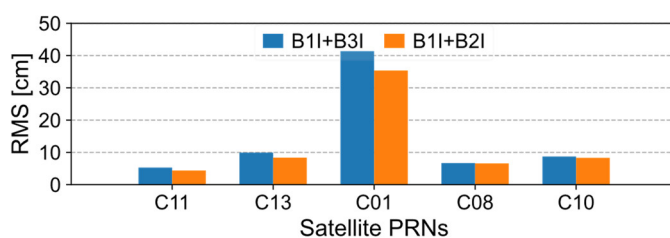
Figure 5.21 Comparison of orbit SLR residual RMS of BDS-2 obtained from processings using B1I+B3I and B1I+B2I

5.2.1 Use B1I+B3I for BDS-2

In (Li et al. 2019), it was concluded that there is no obvious systematic bias between experimental BDS-3 satellites and BDS-2 satellites as for the common B1I+B3I signals by comparing estimated receiver clock offsets and DCBs. That conclusion was based on four BDS-3 experimental satellites. However, there might be a different situation for the operational BDS-3 space segment. Moreover, comparison results from only three international GNSS Monitoring and Assessment System (iGMAS) stations equipped with the same receivers was exhibited in (Li et al. 2019). Thoroughly checking for all available receivers is necessary for a more solid conclusion. Therefore, in this section, two solutions differing on whether the possible receiver biases between BDS-2 and BDS-3 are estimated in the integrated processing are compared. Firstly, orbits are evaluated to examine the necessity of considering those receiver biases as well as their impact on the integrated orbit determination. Then, the estimated receiver biases are inspected to verify their existence or significance and magnitudes.

5.2.1.1 Orbits

In the processing for orbit determination, ambiguities that existed in the carrier phase observations are fixed in the form of double-difference to exploit the profit of accurate carrier phase measurements. The integer characteristics of the doubled-differenced ambiguities can only be warranted under the assumption that receiver hardware delays of signals from those two satellites which are differenced at the station are the same. If there are receiver biases between BDS-2 and BDS-3 in the common B1I+B3I signals, theoretically, inter-satellite differences should be only conducted within BDS-2 or BDS-3 instead of between them. For this reason, the concern about the effect of ignoring receiver biases between BDS-2 and BDS-3 in mapping double-differenced ambiguities is also checked here. Thus, three integrated BDS-2+BDS-3 orbit determination solutions are compared, i.e., ignoring possible receiver biases totally (**IgnBias**), considering the receiver biases by estimating them in the processing but still regarding BDS-2 and BDS-3 as a whole system in the ambiguity fixing (**EstBias**), and in addition to estimating the receiver biases, separately forming double-differenced ambiguities for BDS-2 and BDS-3 when doing ambiguity fixing (**EstBias_Amb**).

In Figure 5.22, orbit DBD 1D RMS of BDS-2 satellites are compared among those three solutions. The same comparisons for BDS-3 satellites are shown in Figure 5.23. Comparisons of orbit SLR residual RMS are given in Figure 5.24. For BDS-2, estimating the additional receiver bias parameters seems to weaken the solution, especially for GEO and MEO satellites. An increase in the orbit DBD can be noticed for those satellites, like C11, C12, and C14, after considering the possible receiver biases between BDS-2 and BDS-3. As for BDS-2 IGSO, only minor impacts on the orbits can be found. While for BDS-3, most satellites show small reductions in the orbit DBD after estimating the receiver bias parameters. Compared with MEOs of BDS-2, BDS-3 MEOs get stronger support from the ground tracking at the frequencies B1I and B3I. When estimating the receiver bias parameters, which are determined by observations from both BDS-2 and BDS-3, solutions of satellites that contribute fewer measurements are more possibly weakened. Whether considering the B1I+B3I receiver biases between BDS-2 and BDS-3 during the ambiguity fixing does not affect the orbits very much. In other words, even if there are receiver biases in the common B1I+B3I signals between BDS-2 and BDS-3, they still can be approximately regarded as one whole system when forming the double-differenced ambiguities due to negligible effects. From Figure 5.24, increases in the orbit SLR residuals can be observed for BDS-2 IGSOs, such as C13 and C10, after estimating the receiver bias parameters. Effects of those receiver biases on the orbit accuracy of BDS-3 are negligible, which means not discriminating BDS-2 and BDS-3 in the ambiguity fixing barely

changes the orbit accuracy.
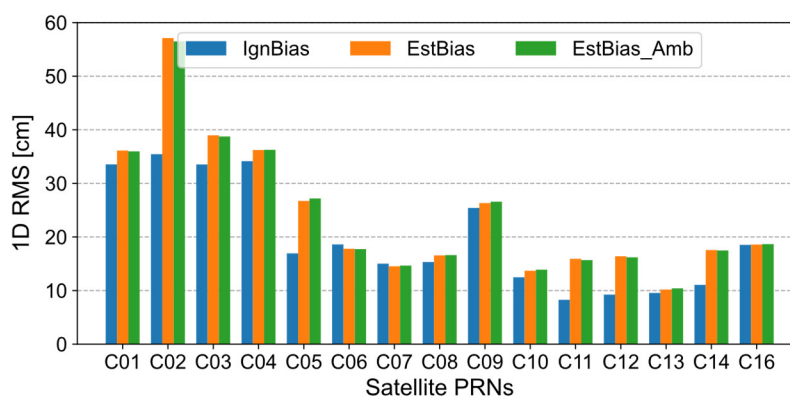
Figure 5.22 Comparisons of BDS-2 orbit DBD 1D RMS of integrated solutions **IgnBias**, **EstBias**, and **EstBias_Amb**
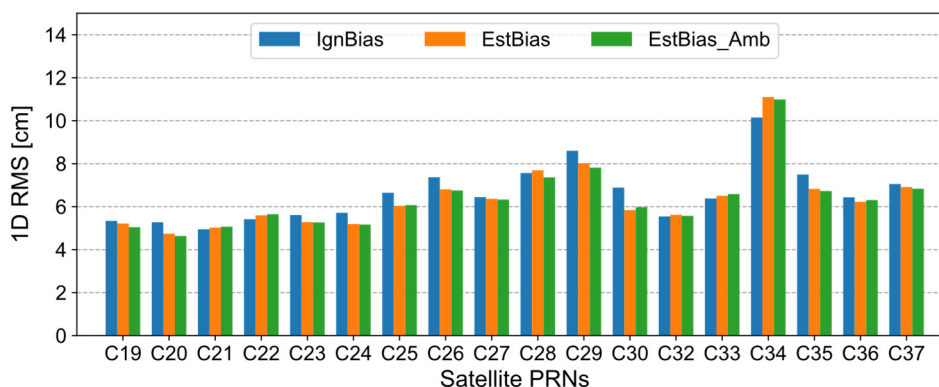
Figure 5.23 Comparisons of BDS-3 orbit DBD 1D RMS of integrated solutions **IgnBias**, **EstBias**, and **EstBias_Amb**
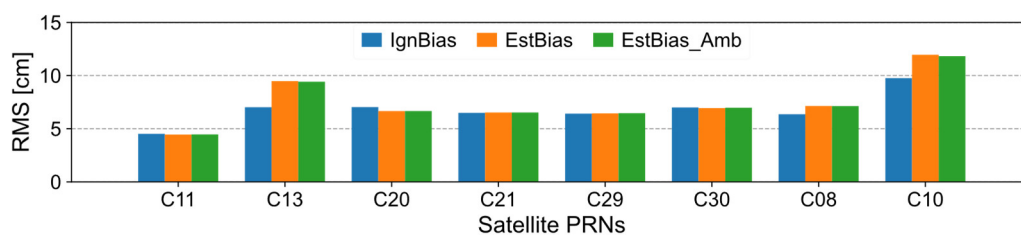
Figure 5.24 Comparisons of orbit SLR residuals RMS of integrated solutions **IgnBias**, **EstBias**, and **EstBias_Amb**

5.2.1.2 Receiver Biases

In Figure 5.25, estimates and formal errors of B1I+B3I receiver biases between BDS-2 and BDS-3 are displayed as blue bars and red error bars, respectively. The solution of DOY 345, 2019 is shown as an example. Labeled along the x-axis is the station code list, sorted first by receiver types and then within each group of the same receiver, by antenna types equipped at

sites.

Receivers of those stations are mainly from three manufacturers, i.e., JAVAD, Septentrio, and Trimble. The receiver bias shows highly correlated with the manufacturer, by which the estimates are distinctly divided into three groups. Biases of JAVAD and Septentrio receivers have opposite signs, and both generally show good uniformity within the group. For most receivers from those two companies, the biases are within ±5 ns, and on average, JAVAD receivers show slightly larger biases than Septentrio. However, for Trimble receivers, the bias estimates show large variations among individual stations. The largest bias from station MCHL reaches ~21.8 ns while the smallest, only around -0.1ns, from station FTNA is negligible if taking its formal error into account.
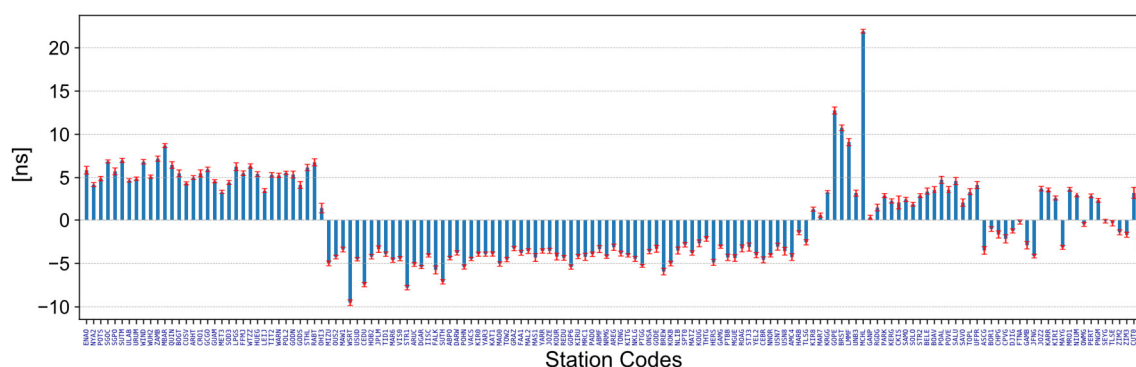
Figure 5.25 Estimates and formal errors of B1I+B3I receiver biases between BDS-2 and BDS-3 on DOY 345, 2019

The relatively small formal errors indicate significant differences in hardware delays of B1I+B3I between BDS-2 and BDS-3 for most receivers. Additionally, as all stations also track GPS, the receiver biases between BDS-2 and BDS-3 can be calculated indirectly by incorporating GPS observations into the processing. This can also serve as a cross-validation of the existence of those receiver biases. In integrated processing of BDS-2, BDS-3, and GPS observations, B1I+B3I receiver biases with respect to GPS signals of BDS-2 and BDS-3 were estimated separately. Those two sets of biases were then differenced at each station to calculate the biases between BDS-2 and BDS-3. Figure 5.26 shows the B1I+B3I receiver biases between BDS-2 and BDS-3 calculated indirectly by incorporating GPS observation for DOY 345, 2019. It shows basically the same results as displayed in Figure 5.25 for all stations. This could further confirm the existence of receiver biases between BDS-2 and BDS-3 for the common B1I+B3I signals.
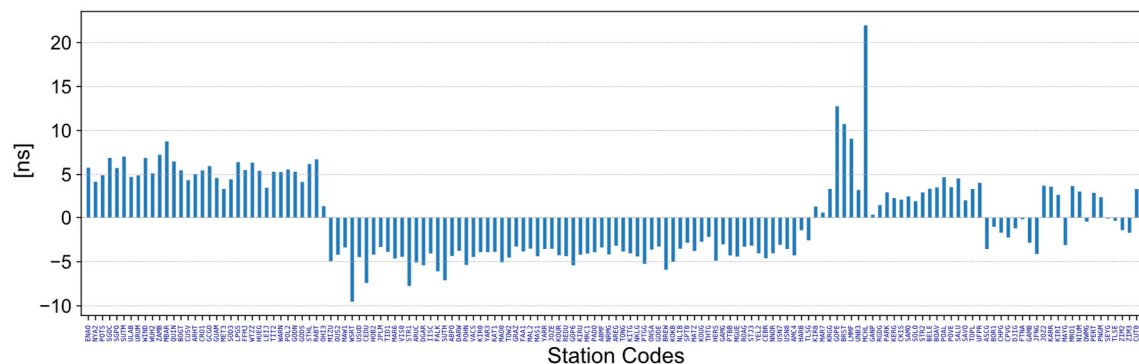
Figure 5.26 Indirectly calculated B1I+B3I receiver biases between BDS-2 and BDS-3 on DOY 345, 2019

In Figure 5.27, estimates of B1I+B3I receiver biases between BDS-2 and BDS-3 over DOY 335~365, 2019 are shown. Daily estimate series are given for each station in the upper panel, while in the lower panel, means and STDs of every station over DOY 335~365, 2019 are shown as blue bars and red error bars, respectively. As the zero-mean constraint was applied in the estimation to eliminate the rank deficiency of one degree of freedom, there might be some jumps of estimates between daily sessions caused by the variation of stations included in processing. The method suggested by (Sanz et al. 2017) was used to align bias estimates. As can be seen, the variations of estimates are generally very small. Even for Trimble receivers, the bias magnitude is very different from station to station, but all individual biases are pretty stable. The overall average of STDs is ~0.4 ns.
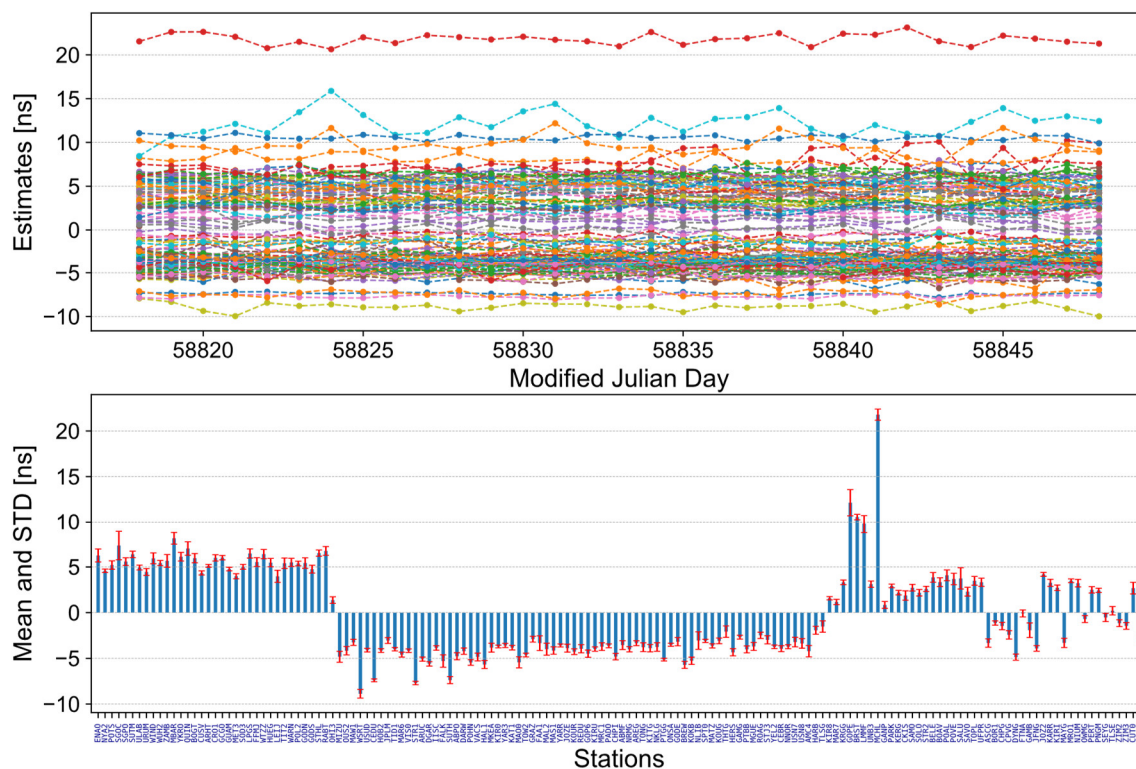
Figure 5.27 Estimated B1I+B3I receiver biases between BDS-2 and BDS-3 over DOY 335~365, 2019

5.2.2 Use B1I+B2I for BDS-2

If there is a receiver bias for the common signals between BDS-2 and BDS-3, receiver biases between different signals of BDS-2 and BDS-3 probably should always be considered. Therefore, when using B1I+B2I for BDS-2 satellites in the integrated processing, parameters for considering the receiver biases between BDS-2 and BDS-3 were always estimated.

5.2.2.1 Orbits

In this part, the difference in orbit performance between solutions using B1I+B3I and B1I+B2I for BDS-2 are focused on. Figure 5.28 shows comparisons of BDS-2 orbit DBD 1D RMS between solutions using B1I+B3I and B1I+B2I for BDS-2 satellites in the integrated processing. In Figure 5.29, similar comparisons for BDS-3 satellites are shown. Figure 5.30 compares the orbit SLR residual RMS for these two different processings.

The main benefit of using the legacy B1I+B2I for BDS-2 in the integrated processing is backward compatibility. Especially for the future re-processing of historical BDS observations, it can be a solution for obtaining a continuous and consistent time series. However, from

114

comparisons of orbit precision and accuracy, using B1I+B2I for BDS-2 can also slightly improve the orbit performance, not just for BDS-2 but also for BDS-3. For most BDS-2 and BDS-3 satellites, small reductions can be observed in the orbit DBD. Only tiny decreases are found in the SLR residuals of BDS-3 orbit, but for BDS-2 satellites, the improvement of orbit accuracy is noticeable.
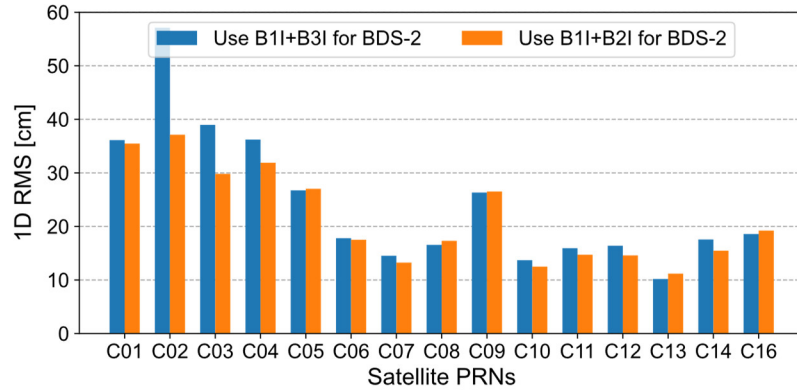
Figure 5.28 Comparisons of BDS-2 orbit DBD 1D RMS between solutions using B1I+B2I and B1I+B3I for BDS-2 in the integrated processing of BDS-2+BDS-3
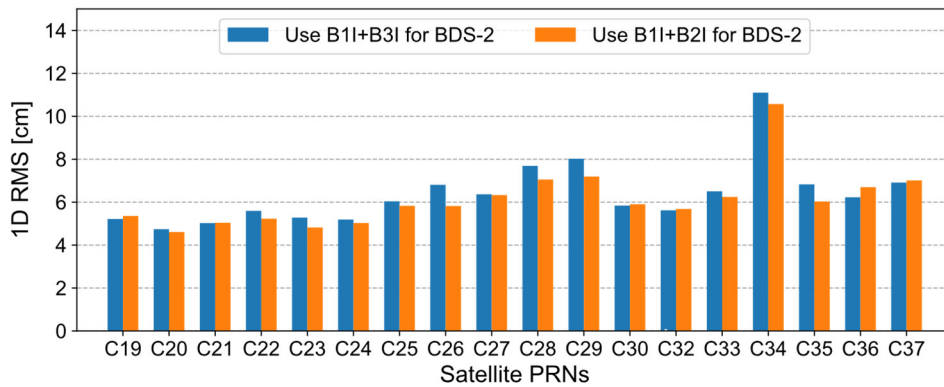
Figure 5.29 Comparisons of BDS-3 orbit DBD 1D RMS between solutions using B1I+B2I and B1I+B3I for BDS-2 in the integrated processing of BDS-2+BDS-3
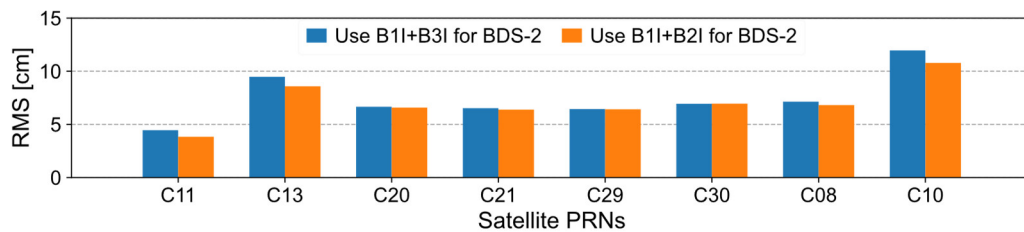
Figure 5.30 Comparisons of orbit SLR residual RMS between solutions using B1I+B2I and B1I+B3I for BDS-2 in the integrated processing of BDS-2+BDS-3

5.2.2.2 Receiver Biases

Figure 5.31 shows the estimates and formal errors of receiver biases between B1I+B2I of BDS-2 and B1I+B3I of BDS-3 on DOY 345, 2019. It shows that, receiver biases between B1I+B2I of BDS-2 and B1I+B2I of BDS-3 are much larger than that between the common signals B1I+B3I, especially for Septentrio and Trimble receivers. Within the group of receivers from the same manufacturer, quite a few stations' biases are different from that of others in size. In the cases of JAVAD and Septentrio receivers, biases with opposite signs to the majority are found for several stations. To a large extent, this difference originates from different antenna types. However, divergent antenna types could not explain all those irregular biases. Other equipment distinctions, like the receiver batch, firmware version, and the antenna radome type, could also contribute to that.
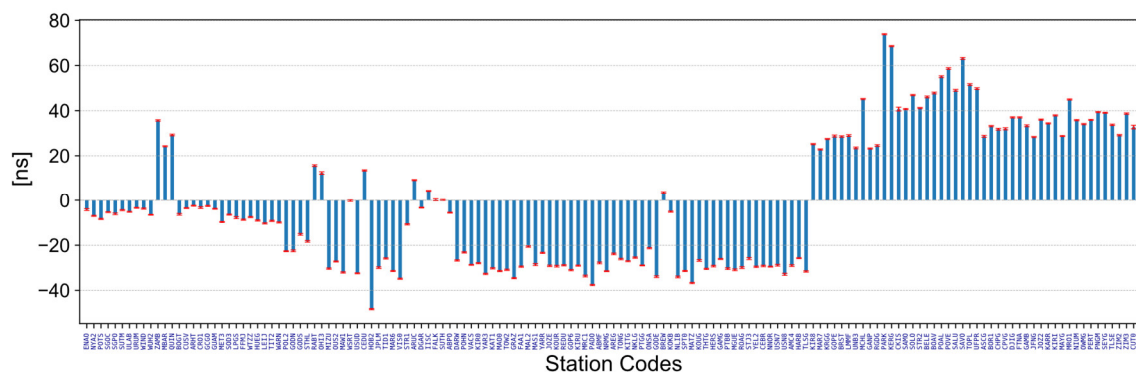
Figure 5.31 Estimates and formal errors of receiver biases between B1I+B2I of BDS-2 and B1I+B3I of BDS-3 on DOY 345, 2019

Similarly, the receiver biases between B1I+B2I of BDS-2 and B1I+B3I of BDS-3 were calculated indirectly by incorporating GPS observations into the processing for verification. Figure 5.32 shows the indirectly calculated receiver biases between B1I+B2I of BDS-2 and B1I+B3I of BDS-3 on DOY 345, 2019. No obvious differences between the results shown in Figure 5.32 and Figure 5.31 can be noticed. In Figure 5.33, daily estimates series as well as their means and STDs over DOY 335~365, 2019 of receiver biases between B1I+B2I of BDS-2 and B1I+B3I of BDS-3 are displayed. Depending on stations, the receiver bias ranges from -49 ns to +74 ns. Though with STDs varying within 0.1~1.0 ns, biases of most receivers can be regarded temporally stable, at least on the time scale of one month. The average standard deviation of all receivers is ~0.4 ns.
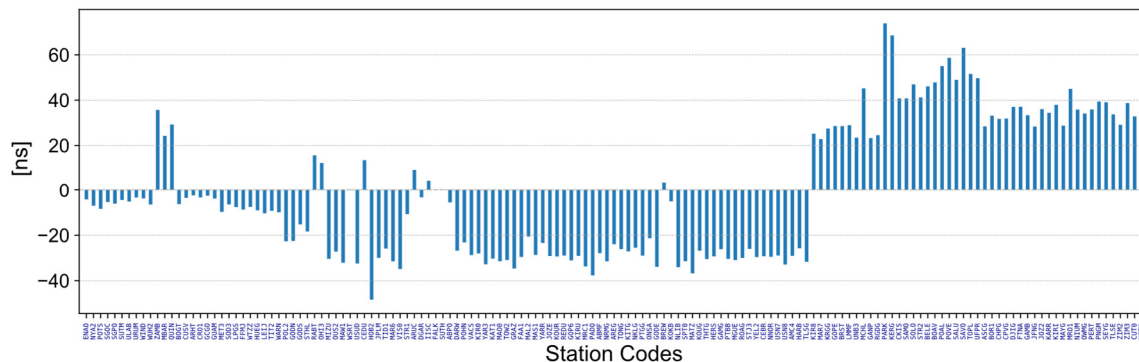
Figure 5.32 Indirectly calculated receiver biases between B1I+B2I of BDS-2 and B1I+B3I of BDS-3 on DOY 345, 2019
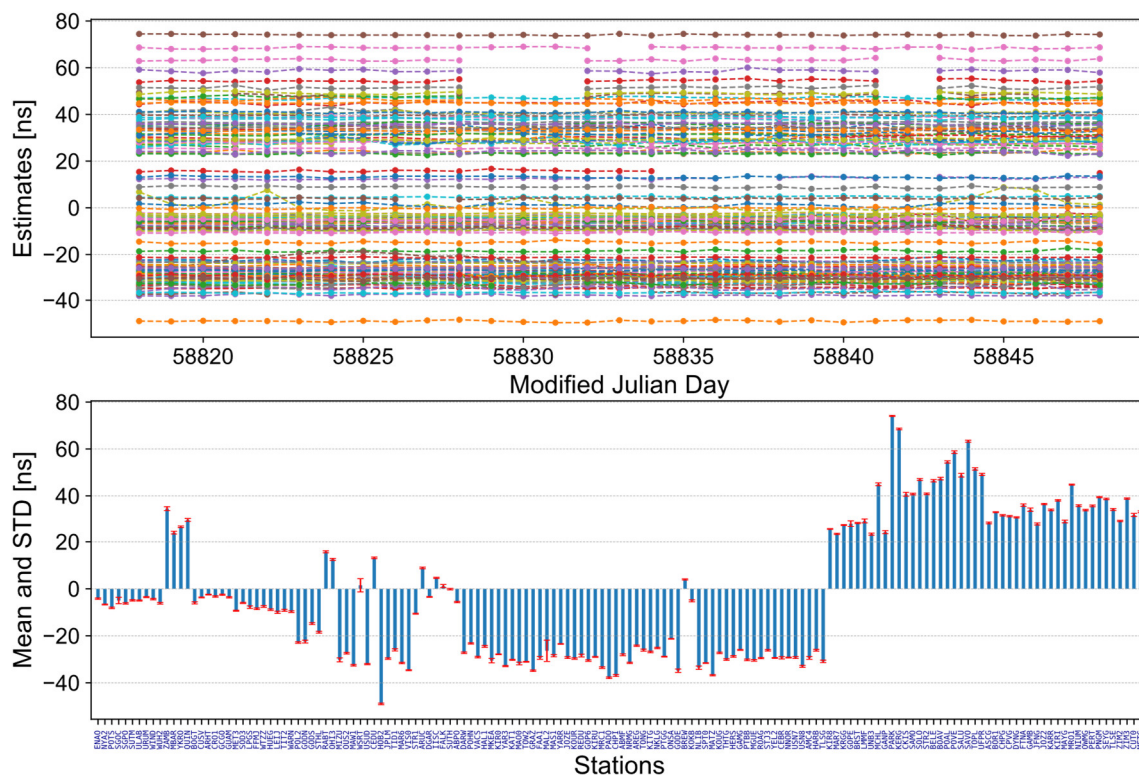
Figure 5.33 Estimated receiver biases between B1I+B2I of BDS-2 and B1I+B3I of BDS-3 over DOY 335~365, 2019

5.3 Conclusion

As the contributions of additional ISL observations will be investigated comprehensively in the following parts of this study, several critical concerns related to the orbit determination of BDS-3 using L-band ground tracking observations were addressed in this chapter.

The necessities of considering the Earth's albedo and antenna thrust perturbations are

confirmed by analyzing their impacts on the orbits. Based on the CSNO released parameters and box-wing satellite models, the Earth's albedo-caused accelerations reach up to $2 \sim 3$ nm/s^2 and thus, result in radial contractions of $1.4 \sim 2.6$ cm for BDS-3 MEOs. Similar effects can be expected from the antenna thrust. Using the values of transmit power archived in the IGS MGEX metadata file, radial accelerations of $0.9 \sim 1.1$ nm/s^2 are obtained for BDS-3 MEOs based on a simplified analytic model. Considering these accelerations decreases the radiuses by $1.7 \sim 1.9$ cm and ~ 1.6 cm for BDS-3 CAST and SECM satellites, respectively. Those systematic effects of Earth's albedo and antenna thrust are clearly reflected in the orbit SLR residuals. Then applicability of different empirical SRP models and the impacts of the additional a priori box-wing model are discussed for BDS-3. Without any a priori models, the ECOM2 is superior to ECOM1 for BDS-3 MEOs. When adding the a priori box-wing model based on the CSNO released satellite parameters, differences between the ECOM1 and ECOM2 are generally insignificant. The option of applying satellite-specific ECOMs for individual satellites is also experimented. It turns out to have a similar performance as ECOM2 in the orbit determination.

Finally, to generate products with better backward compatibility, frequencies choice of BDS-2 in the integrated processing of BDS-2 and BDS-3 is examined. Mostly because of stronger ground tracking support, using B1I+B2I for BDS-2 can get better orbit results than using B1I+B3I in the transition phase of BDS from the 2nd to 3rd generation. It is found that receiver biases of B1I+B3I between BDS-2 and BDS-3 do exist, and their magnitudes are around ±5 ns but may reach up to more than 20 ns, depending on the receiver types. However, the effects of those receiver biases on the ambiguity fixing can be neglected safely. Receiver biases between B1I+B2I of BDS-2 and B1I+B3I of BDS-3 are larger, ranging from -49 ns and +74 ns while stable with time, with an average monthly STD of around 0.4 ns. Slight orbit improvements can be observed for both BDS-2 and BDS-3 satellites if using B1I+B2I for BDS-2 in the integrated processing. This provides one possible solution to the concern of continuously reprocessing of historical BDS observations.

6 Contribution of ISL to Ground-based Precise Orbit Determination

In this chapter, numerical experiments and analyses are dedicated to investigating the improvement of ISL observations on BDS-3 orbit determination. Firstly, the contributions of the ISL range and clock observations are examined separately as those two observation types should be independent theoretically. Then, incorporating both the ISL range and clock observations with the L-band ground tracking measurements into an integrated estimator is studied.

6.1 Incorporate ISL Range Observations

Incorporating ISL range observations into the usual orbit determination processing, which uses only the ground tracking measurements, is investigated for BDS-3 in this section, including the impact of the modelling of the harmonic signals in ISL observations, weight allocation between different types of observations, and the improvement of ISLs under different ground network configuration conditions.

6.1.1 Impact of the Harmonic Signals

Before going forward further, it is better to confirm the effectiveness of the proposed periodic function model in Section 3.4. As there should not be any datum issue if an appropriate ground network is incorporated, validation of the advantage of the proposed model for absorbing harmonic signals found in the ISL observations would be more reliable and, therefore, should be more persuasive.

Four integrated solutions, which differ from each other only by the model used to deal with the harmonic signals in ISL range observations, are compared. For the convenience of referring, those solutions are named after the periodic function models adopted, i.e., Model 1 (with 1CPR terms only), Model 2 (with 2CPR terms only), and Model 3 (with both 1CPR and 2CPR terms, See Table 3-5). The solution designated as "**NONE**" refers to the processing scheme in which the harmonic signals in ISL range observations were ignored.

The ground network assigned as **GloA** in Section 6.1.3 was used in all cases. Since the issue of weight allocation will be addressed later, the a priori STD of 10 cm was used for ISL range observations in all four integrated solutions in this context.

6.1.1.1 Orbits

Figure 6.1 compares the orbit DBD 1D RMS of the four solutions. For individual satellites, a slight decrease in the orbit DBD 1D RMS could be observed in most cases if an appropriate model was applied. However, it is not easy to tell a uniform optimal model for all satellites. Relatively obvious improvement in the orbit precision can be found for satellites C28 and C30 if Model 2 or 3 and Model 1 or 3 are used, respectively. Although a marginal increase of the DBD can be noticed for some satellites when Model 3 was applied, it generally performs better than Model 1 and 2.
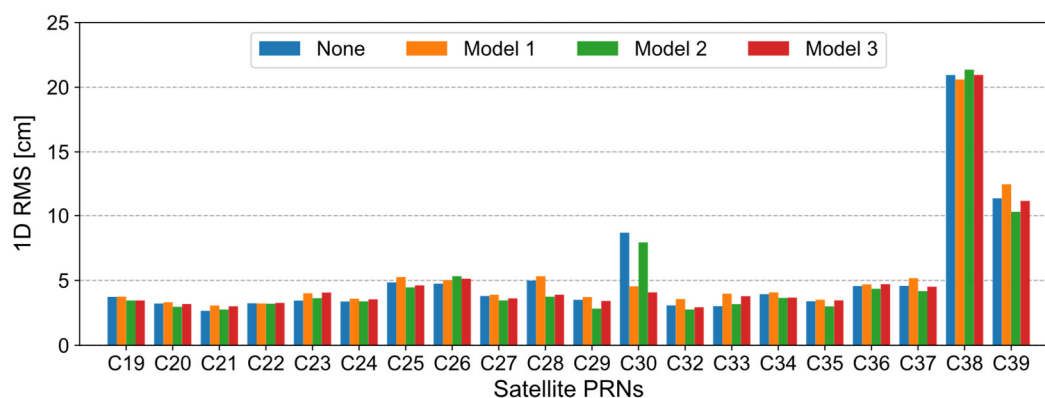
Figure 6.1 Comparison of orbit DBD 1D RMS from solutions with **Model 1** (1CPR), **Model 2** (2CPR), and **Model 3** (1CPR+2CPR) applied for ISL range observations. The solution referred to **None** ignores the harmonic signals in ISL observations. Legacy L-band observations from ground tracking were also incorporated in the processing.

In Figure 6.2, statistics of SLR residuals of orbits from different solutions are compared. For C20 and C21, the orbit accuracy is only slightly affected by the harmonic signals in ISL observations. But for satellite C30, ISL harmonic signals affect both the offset and noise of its orbit. Removing the 1CPR signal by Model 1 or Model 3 reverses the sign of the offset in SLR residuals. In other words, the orbit radial components are elongated by ~7 cm, decreasing the mean of SLR residuals from ~+4 cm down to -3 cm. A significant reduction of the residual STD of C30 can be found after eliminating the 1CPR signal.
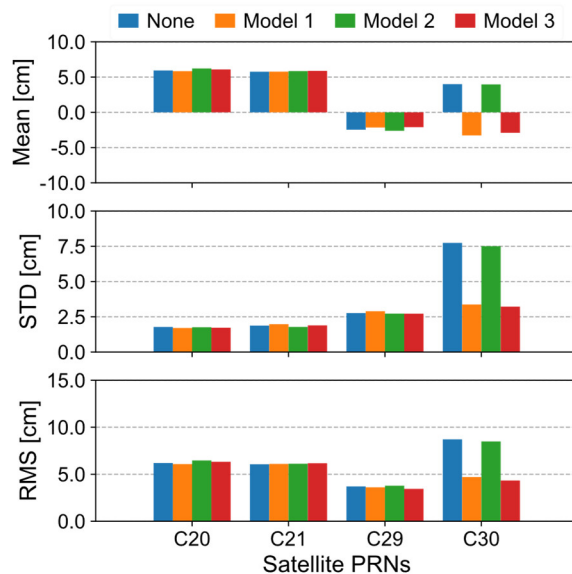
Figure 6.2 Statistics of SLR residuals of orbits from solutions with different periodic function models applied for ISL range observations. Observations from ground tracking were also incorporated in the processing.

Therefore, in the following processing involving ISL range observations, unless otherwise mentioned, Model 3 is always adopted to model the harmonic signals in ISL range observations.

6.1.1.2 ISL Hardware Delays

Figure 6.3 shows the comparison of STDs of daily ISL hardware delay estimates from different solutions. Effects from harmonic signals in the ISL range observations on the STDs of hardware delays get smaller when compared to cases not including observations from ground tracking (See Section 3.4.4). Although a slight rise of STD can be found for many satellites when Model 2 or 3 was adopted, the growth with a maximum of 0.04 ns, occurring when employing Model 3 for satellite C23, is insignificant.
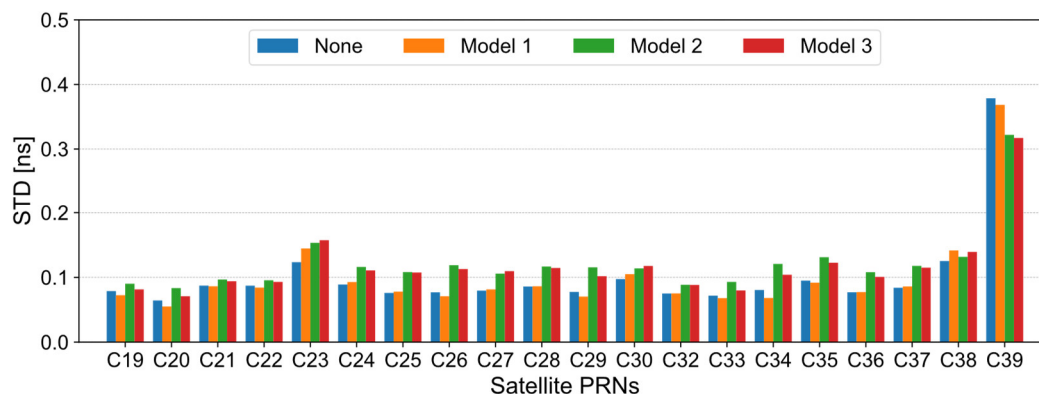
Figure 6.3 Comparison of STDs of ISL hardware delays from solutions with different periodic function models applied for ISL range observations. Observations from ground tracking were also incorporated in the processing.

6.1.2 Weight Allocation

As the ISL range observations and ground tracking L-band observations are processed in an integrated estimator, the concern of proper weight allocation between measurements of those different techniques arises naturally.

To search for the optimal weight ratio between ISL and ground tracking observations, various a priori STDs ranging from 1 cm to 25 cm were tested for ISL derived range observations. Those tests were conducted in the manner of trialing one by one. Based on the experience acquired from previous results in this study as well as from literature, the overall precision of current BDS-3 ISL range observations should be somewhere between 4.0 and 15.0 cm. But for the sake of completeness, the bounds of the search were extended.

The a-prior precision information of GNSS observations was fixed in all the integrated processings, i.e., 0.01 cycle and 0.50 m for the phase and pseudorange observations of each frequency, respectively, for all stations. Without elevation-related down-weighting, these a priori STDs correspond to ~7.28 mm and 1.76 m for the ionosphere-free carrier phase and code pseudorange observations, respectively, when frequencies B1I and B3I are used. Namely, a weight ratio of around 58696:1 between L-band carrier phase and code range ionosphere-free observations was fixed while testing different a priori STD for ISL range observations.

Theoretically, the weight ratio between ISL and ground tracking observations should have nothing to do with the size or distribution of the ground network. Therefore, a network consisting of all available BDS-3 tracking stations from the IGS MGEX during the study period (i.e., the network **GloA** in Section 6.1.3) has been used in all tests. Due to nonuniform noise levels of L-band observations among ground stations, the results as to the optimal weight

ratio might differ if different ground tracking networks are used.

6.1.2.1 A posteriori Standard Deviation

According to the least-square adjustment theory, the a posteriori STD of unit weight is the unbiased estimate of the a priori STD of unit weight. The closeness of post- and a priori STDs of the unit weight can be employed to evaluate the appropriateness of the weight ratios between various types of observations to some extent.

A posteriori STDs of the unit weight of integrated solutions with different a priori STDs used for ISL range observations are shown in Figure 6.4. In all the solutions, the a priori unit weight STD of 1.0 m was adopted, which means the weight of each observation involved in the adjustment is $1/\sigma^2$, where σ is the a priori STD in meters of the observation. Although almost every integer value in centimeters within the range of 1~25 was tried out, only results from several representative test solutions are shown here. And for reference, a posteriori STDs of the unit weight of the solution without ISL observations (**No ISL**) are also given.

It shows that all the a posteriori unit weight STDs are smaller than the a priori ones, i.e., one, if an ISL a priori STD of 4 cm or larger is adopted. And the a posteriori unit weight STDs decrease as the a priori STDs of ISL range observations increase. After the a priori STD of 12 cm, basically, all a posteriori unit weight STDs are within the range of 0.60~0.70, or more specifically, clustering around the value of ~0.65. When the a priori STD of 4 cm was employed for ISL range observations, estimates of a posteriori weight STDs are closest to 1, i.e., the a priori value. However, a posteriori unit weight STDs from the solution using no ISL observations are also much less than the a priori value. It might indicate the non-optimal weight ratio used even between the carrier phase and code pseudorange observations of ground tracking. Therefore, it seems risky to conclude 4 cm as the optimal a priori STD for ISL range observations. Investigation on the best weight ratio between the ground tracking carrier phase and code pseudorange observations of BDS-3 is beyond the scope of this study. Nevertheless, seeking the optimal (or as appropriate as possible) weight ratio between ISL and ground tracking measurements in this context still makes sense to acquire a better combined solution.
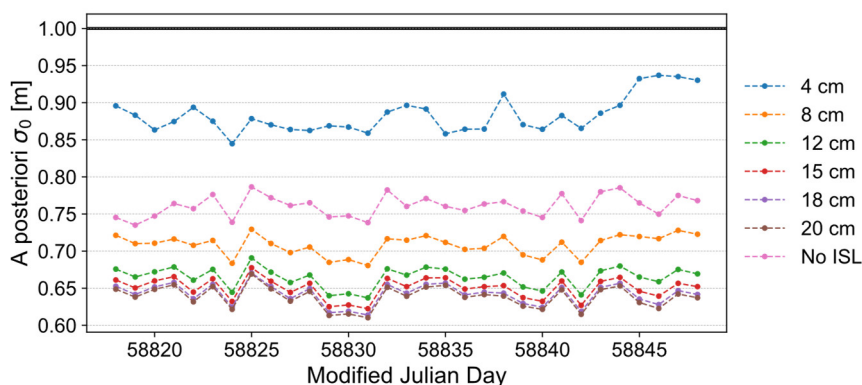
Figure 6.4 A posteriori unit weight STDs of solutions with various a priori STDs used for ISL range observations when processed together with ground tracking measurements

6.1.2.2 Orbits

Figure 6.5 displays the 1D RMS of orbit DBD of different solutions. Those solutions differ only in the a priori STD applied for ISL range observations in the combined processing. Only results of several representative solutions are shown without affecting the following discussion and conclusion. Orbit DBD 1D RMS of the solution without ISL observations involved are also given for reference.

It shows that the a priori precision information of ISL range observations has an apparent impact on the orbit precision. Not so surprisingly, using the a priori STD of 4 cm does not produce the best results in terms of the orbit DBD. Basically, among all the examined a priori STDs, i.e., 1~25 cm, the 1D RMS gets smaller when the a priori STD gets larger, until to the value of around 15 cm. Further increasing the a priori STD would either barely change or even degrade the results. When the a priori STD of 15 cm is used, most satellites get the smallest orbit DBD with a few exceptions with a negligible DBD difference to the smallest value. As will be more detailedly discussed later, incorporating ISLs noticeably improves the orbit precision of BDS-3 MEOs over that without ISL observations if appropriate a priori STDs were used. For IGSOs, i.e., satellites C38 and C39, the ground tracking solution is unavailable because of insufficient observations. But their orbits can still be determined via ISL measurements to other satellites. An optimal a priori STD of ISL observations also decreases the orbit DBD of IGSOs, especially for satellite C38.

124
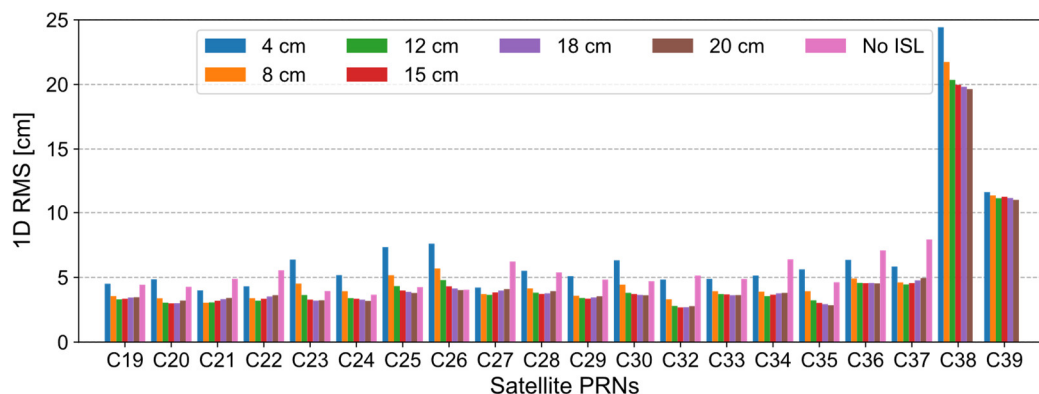
Figure 6.5 Orbit DBD 1D RMS of solutions with different a priori STDs used for ISL range observations

Statistics of orbit SLR residuals of different solutions are shown in Figure 6.6. Results of the solution using only ground tracking are also displayed for reference. Not as significant as on the orbit DBD, a priori STDs of ISL range observations show a much smaller effect on the SLR residuals. But similarly, it indicates the a priori STD of 4 cm is hardly the optimum. The improvement of ISLs on the accuracy of orbits, which will be addressed later, seems limited when a global tracking network is available.
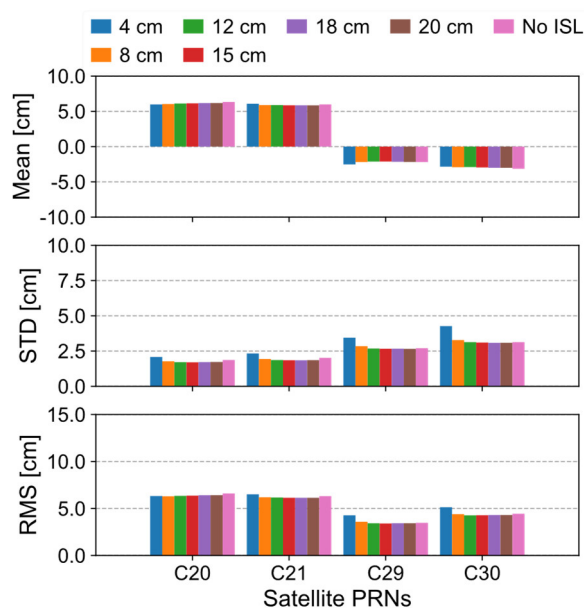
Figure 6.6 Statistics of SLR residuals of orbits from solutions with different a priori STDs used for ISL range observations

6.1.2.3 ISL Hardware Delays

The stability of ISL hardware delay estimates is also influenced by the a priori STD of ISL range observations. Figure 6.7 gives the comparison of STDs of ISL hardware delay estimates

from different solutions. Using an a priori STD larger than 15 cm does not change the STDs significantly.
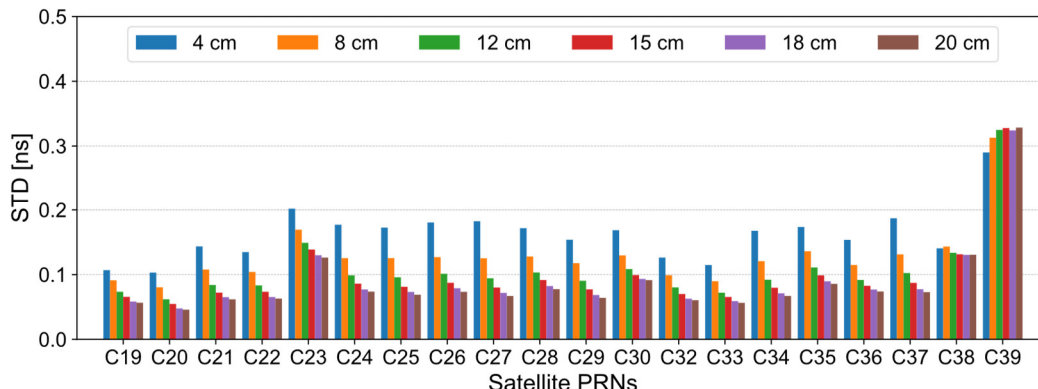
Figure 6.7 Comparison of STDs of ISL hardware delays from solutions with different a priori STDs used for ISL range observations

6.1.3 Improvement on Orbits

Three ground tracking networks, which differ in geographical coverage, number, and denseness of stations, were used to investigate the contribution of ISL range observations to the orbit determination. The geographical distribution of stations composing each network is displayed in Figure 6.8.
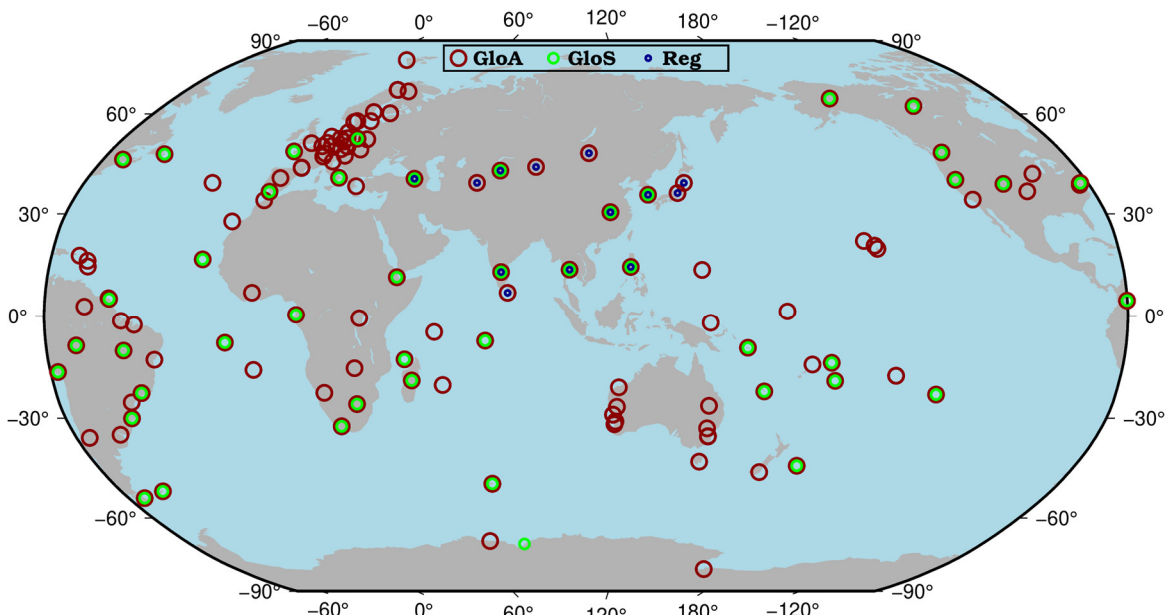
Figure 6.8 The three ground tracking networks used in this study to evaluate the improvement of ISL on BDS-3 orbit determination

A regional network consisting of 14 stations within the Asia-Pacific area (**Reg**) was used to

simulate as realistically as possible the current OCS monitoring facilities of BDS-3. Despite their close locations (114.5° E, 30.5° N), both station WUH2 and JFNG were used in the processing to provide as many observations as possible. A network with 45 sparsely but evenly distributed global stations (**GloS**) was adopted to provide moderately optimal ground tracking. The third network incorporating all available stations from the IGS MGEX ground facilities that can track BDS-3 (**GloA**) during the period DOY 335~365, 2019 provided probably the best ground tracking. Except for station DAV1 (78.0° E, 68.6° S), which was excluded from network GloA due to insufficient measurements, network GloS is a sub-network of GloA. Network GloA is comprised of 143 stations.

In each study case, unless otherwise mentioned, the only difference between solutions is whether the ISL range observations are used or not. The satellite-specific ECOM model, i.e., **SatE** developed in Chapter 5, has been used for modelling of the direct SRP perturbation in all solutions.

The proposed periodic model, i.e., Model 3 with both 1CPR and 2CPR terms was used in all solutions involving ISL range observations to eliminate the harmonic signals. The a priori STD of 15 cm was used for ISL range observations.

As for the two IGSOs, i.e., C38 and C39, due to lack of a priori orbits, never tracked by four or more ground stations, no enough actually valid observations, and other reasons, they were only involved in the solution using network GloA with additional ISL measurements.

6.1.3.1 In the Case of Network Reg

Depending on the availability of observations from individual stations, there were 12~14 stations used for each daily session of the network **Reg**. Figure 6.9 displays the orbit DBD 1D RMS of solutions with and without ISL observations using the right and left y-axis, respectively due to different magnitudes. Statistics of orbit DBD RMS in different orbital components, i.e., the Along-track (A), Cross-track (C), and Radial (R) directions, as well as the 1D RMS of those two solutions, are listed in Table 6-1. Due to weak observability, orbits of BDS-3 MEOs can only be determined with a precision of several to tens of meters by daily observing sessions from a regional network. Especially bad quality of the orbital along-track component can be observed. Adopting a longer processing arc, e.g., spanning two- or three-day might help. Nevertheless, the one-day processing arc was still maintained in this study. It can be seen that ISL measurements bring a huge improvement in the orbit precision. After adding the ISL range observations, the average orbit DBD 1D RMS decreases from ~16.3 m to ~7.5 cm, and that

of the along-track, cross-track, and radial components are reduced to 8.2, 9.0, 4.1 cm from 27.6, 1.8, and 5.0 m.
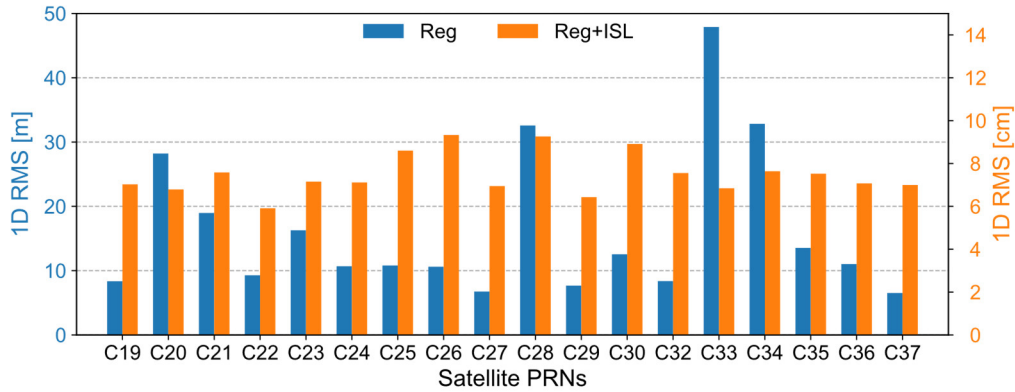
Figure 6.9 Orbit DBD 1D RMS of solutions **Reg+ISL** (right y-axis) and **Reg** (left y-axis) with and without ISL observations, respectively

Table 6-1 Statistics of orbit DBD RMS of solutions **Reg** and **Reg+ISL** [cm]

PRN	Reg				Reg+ISL			
	A	C	R	1D	A	C	R	1D
C19	1420.55	42.67	271.42	835.35	8.42	8.31	2.88	7.03
C20	4827.96	116.32	749.84	2821.64	8.17	7.88	3.06	6.79
C21	3250.92	110.85	470.82	1897.58	9.36	8.60	3.32	7.58
C22	1574.55	117.73	304.31	928.38	7.67	6.39	2.29	5.91
C23	2780.87	176.99	428.58	1627.70	6.59	9.26	4.95	7.16
C24	1809.96	128.43	365.64	1068.66	5.96	9.85	4.39	7.11
C25	1838.35	121.44	329.42	1080.56	11.28	8.15	5.31	8.60
C26	1779.84	178.78	422.16	1061.14	8.98	11.63	6.72	9.33
C27	1087.96	93.41	418.45	675.15	6.45	9.72	2.95	6.95
C28	5506.02	384.17	1176.48	3258.22	8.68	12.05	6.07	9.26
C29	1264.36	129.34	387.12	767.07	7.38	7.93	2.59	6.43
C30	2121.11	126.77	456.71	1254.83	11.89	8.54	4.89	8.91
C32	1429.55	83.23	236.76	837.97	8.87	9.01	3.40	7.56
C33	8235.55	185.81	987.62	4790.06	7.28	8.93	2.77	6.84
C34	5584.57	774.99	755.08	3284.21	9.02	8.47	4.70	7.64
C35	2279.19	149.83	532.39	1354.08	7.51	9.64	4.54	7.53
C36	1837.96	158.79	492.29	1102.37	5.81	10.18	3.56	7.07
C37	1091.37	82.81	280.18	652.29	7.80	7.60	5.32	7.00
Mean	2762.26	175.69	503.63	1627.63	8.17	9.01	4.10	7.48

Figure 6.10 shows the comparison of orbit SLR residual RMS of those two solutions. The

statistics, i.e., the mean, standard deviation, and RMS of SLR residuals, are summarized in Table 6-2. The numbers of SLR normal points excluded because of large residuals (i.e., over 1.0 m) for each satellite are also given for each solution. Because of poor orbit quality, more SLR normal points were excluded for the solution **Reg**. Adding ISL also shows a great improvement on the accuracy of orbits. The RMS of orbit SLR residuals decreases from ~30 cm to 4~7 cm. However, unlike the STDs, additional ISL observations do not always decrease the orbit radial offsets. Contrary to the significant reduction of orbit mean offsets of satellites C29 and C30, a radial bias of ~5.8 cm was found for satellite C21 after ISL observations were added into the processing. However, considering the orbit accuracy one might expect in this case, the overall improvement on the orbit of C21 brought by ISL should still be highly credited.

Figure 6.10 Orbit SLR residual RMS of solutions **Reg+ISL** and **Reg** with and without ISL observations, respectively

Table 6-2 Statistics of orbit SLR residuals of solutions **Reg** and **Reg+ISL** [cm]

PRN	NPT #	Reg				Reg+ISL			
		Mean	STD	RMS	Exl #	Mean	STD	RMS	Exl #
C20	297	6.19	29.18	29.83	12	6.49	2.35	6.90	0
C21	384	0.97	33.02	33.04	32	5.84	3.31	6.71	0
C29	251	13.52	28.31	31.37	18	0.18	4.63	4.64	2
C30	249	10.39	24.76	26.85	11	-4.87	5.17	7.11	0

6.1.3.2 In the Case of Network GloS

With the network **GloS**, the number of used stations for a daily orbit determination session was 39~45. In fact, the tracking geometry is still inadequate for BDS-3 MEOs in the case of ground network **GloS**. Large areas in the North Pacific, South Atlantic, and Russian territory with very sparse stations can be easily recognized. None or only a few stations are located in the Australia and North Africa continent.

Figure 6.11 shows the orbit DBD 1D RMS of solutions with and without ISL observations in the case of network **GloS**. The statistics of orbit DBD RMS in each orbital direction and 1D

RMS of both solutions are listed in Table 6-3. Percentages of RMS decrements of the solution **GloS+ISL** with respect to the solution **GloS** are appended at the end of the table. As can be seen, orbit DBD of all satellites gets considerably reduced by adding ISL observations. On average, the 1D RMS has been decreased by ~51%, from 8.22 cm to 4.05 cm. The inhomogeneity of orbit precision among different satellites which might be caused by the uneven tracking geometry, is also alleviated apparently. Among the three orbital components, the along-track and radial directions benefit more from the addition of ISL observations compared to the cross-track direction. Around 60% of RMS decrement is found in both of those two orbital components. As a result, the average orbit DBD RMSs fall from 11.32, 5.28, and 6.54 cm down to 4.47, 4.62, and 2.63 cm in the along-track, cross-track, and radial directions, respectively.
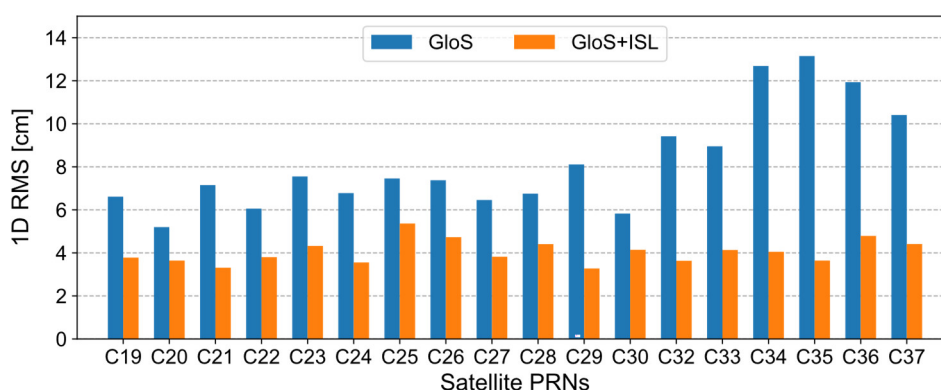
Figure 6.11 Orbit DBD 1D RMS of solutions **GloS+ISL** and **GloS** with and without ISL observations, respectively

Table 6-3 Statistics of orbit DBD RMS of solutions **GloS** and **GloS+ISL** [cm]

PRN	GloS				GloS+ISL				Decrease [%]			
	A	C	R	1D	A	C	R	1D	A	C	R	1D
C19	8.20	5.15	6.11	6.61	3.69	5.08	1.86	3.78	55.00	1.36	69.56	42.81
C20	6.11	4.71	4.65	5.20	3.68	4.63	2.19	3.64	39.77	1.70	52.90	30.00
C21	9.26	5.78	5.86	7.15	4.02	3.44	2.21	3.31	56.59	40.48	62.29	53.71
C22	7.23	5.28	5.47	6.06	4.11	4.78	1.91	3.80	43.15	9.47	65.08	37.29
C23	10.06	5.46	6.33	7.55	4.52	4.95	3.35	4.33	55.07	9.34	47.08	42.65
C24	9.49	4.58	5.18	6.78	4.10	3.29	3.20	3.56	56.80	28.17	38.22	47.49
C25	8.94	6.19	6.98	7.46	7.21	4.79	3.39	5.37	19.35	22.62	51.43	28.02
C26	9.93	4.80	6.44	7.38	4.45	5.69	3.86	4.73	55.19	-18.54	40.06	35.91
C27	8.84	5.23	4.43	6.46	4.20	4.57	2.31	3.82	52.49	12.62	47.86	40.87
C28	9.33	5.11	4.86	6.75	4.45	5.83	2.14	4.41	52.30	-14.09	55.97	34.67
C29	12.28	4.11	5.44	8.11	3.76	3.85	1.80	3.28	69.38	6.33	66.91	59.56
C30	8.29	3.94	4.19	5.83	4.90	4.54	2.62	4.14	40.89	-15.23	37.47	28.99

C32	12.47	5.07	9.22	9.42	4.82	3.35	2.27	3.64	61.35	33.93	75.38	61.36
C33	12.53	7.14	5.71	8.95	3.89	5.72	1.84	4.13	68.95	19.89	67.78	53.85
C34	19.52	5.09	8.72	12.69	5.16	4.14	2.35	4.05	73.57	18.66	73.05	68.09
C35	19.66	6.57	9.43	13.15	4.05	4.10	2.57	3.64	79.40	37.60	72.75	72.32
C36	18.51	5.04	7.68	11.93	5.34	5.17	3.68	4.79	71.15	-2.58	52.08	59.85
C37	13.07	5.78	10.98	10.41	4.11	5.22	3.78	4.41	68.55	9.69	65.57	57.64
Mean	11.32	5.28	6.54	8.22	4.47	4.62	2.63	4.05	60.51	12.50	59.79	50.73

The comparison of orbit SLR residual RMS between solutions **GloS** and **GloS+ISL** is shown in Figure 6.12. Statistics of SLR residuals of those two solutions are listed in Table 6-4. The RMS decrement percentages of the solution **GloS+ISL** relative to the solution **GloS** are also supplied at the end of the table. As used in earlier sections, the same procedure and criteria have been employed for the outlier detection and removal of SLR residuals. Only two SLR normal points, which are from satellite C29, were excluded in both solutions. Compared to the orbit precision represented by DBD, only slight accuracy improvements can be found after incorporating ISL observations. Note that, in the context of SLR residuals of GNSS satellite orbits, basically only the radial accuracy can be evaluated. For satellites C20 and C21, the SLR residual RMSs are lessened by 3.6% and 7.3%, respectively. And if inspected closely, most of those decrements are from the reduction of standard deviations of SLR residuals. Considering the low RMS of less than 5 cm, the small increase of 0.3 cm for satellite C30 is negligible.
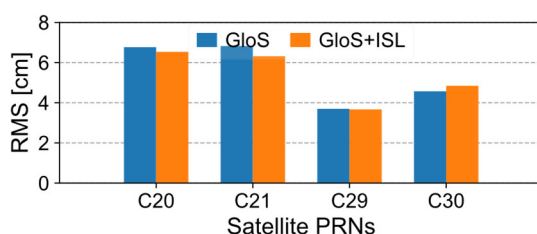
Figure 6.12 Orbit SLR residual RMS of solutions **GloS+ISL** and **GloS** with and without ISL observations, respectively

Table 6-4 Statistics of orbit SLR residuals of solutions **GloS** and **GloS+ISL** [cm]

PRN	GloS			GloS+ISL			RMS Decrease [%]
	Mean	STD	RMS	Mean	STD	RMS	
C20	6.37	2.28	6.77	6.30	1.75	6.53	3.55
C21	6.34	2.53	6.82	6.05	1.82	6.32	7.33
C29	-2.14	3.02	3.70	-2.06	3.04	3.67	0.81
C30	-3.12	3.34	4.57	-3.40	3.45	4.85	-6.13

6.1.3.3 In the Case of Network GloA

When the network **GloA** was used, the number of available stations in a daily solution is 118~131. Figure 6.13 compares the orbit DBD 1D RMS of solutions **GloA+ISL** and **GloA**. In Table 6-5, statistics of each component of orbit DBD RMS from those two solutions are listed. And decreasing percentages in orbit DBD RMS of the solution **GloA+ISL** relative to the solution **GloA** are also given. The two IGSO satellites, i.e., C38 and C39, are only available in the solution with ISL observations due to lack of ground tracking.

As one of the motivations of the deployment of ISLs is to compensate for the deficiency of local ground tracking, one may not expect significant orbit improvements when a global network is used. However, as shown in the results, even with a relatively complete ground tracking network, except for C26, orbit DBD of all other satellites get a clear reduction. The magnitude of decrements brought by ISL observations is different for individual satellites. Satellite C25 shows the minimum decrease of ~6% in orbit DBD 1D RMS, while C32 exhibits the maximum of ~48%. Except for satellites C23, C24, and C25, reductions over 21% and with an average of ~34% can be found for other MEO satellites. The average orbit DBD 1D RMS of BDS-3 MEOs declines by ~30%, from 5.12 to 3.59 cm.

Improvements in the orbital along-track and radial directions are more significant than that in the cross-track component. The maximum and average improvements in the along-track direction are ~59% (from satellite C37) and ~36%, respectively. And for the radial component, the maximum and average improvements are ~53% (from satellite C32) and ~32%, respectively. Accordingly, the average orbit DBD RMS in the along-track, cross-track, and radial components drop from 6.82, 3.81, and 4.02 cm to 4.11, 3.73, and 2.70 cm.
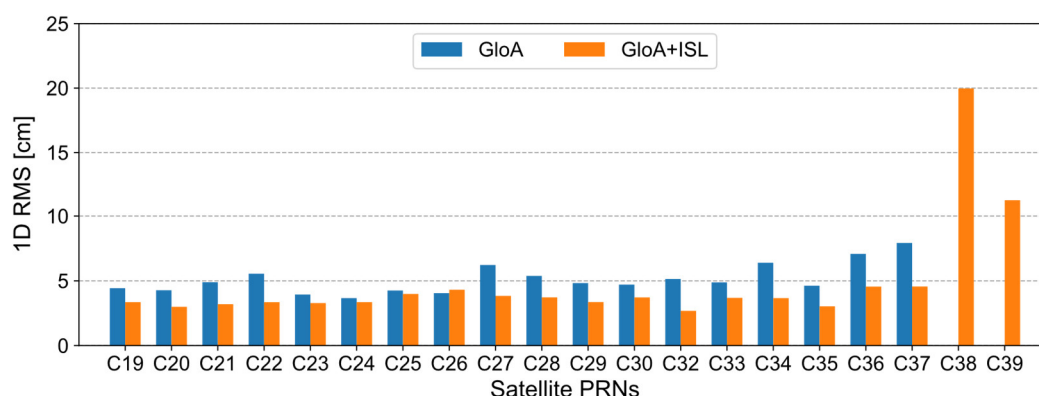
Figure 6.13 Orbit DBD 1D RMS of solutions **GloA+ISL** and **GloA** with and without ISL observations, respectively

Table 6-5 Statistics of orbit DBD RMS of solutions **GloA** and **GloA+ISL** [cm]

PRN	GloA				GloA+ISL				Decrease [%]			
	A	C	R	1D	A	C	R	1D	A	C	R	1D
C19	5.70	3.47	3.79	4.43	4.01	3.69	2.02	3.35	29.65	-6.34	46.70	24.38
C20	5.56	3.80	3.06	4.27	3.57	3.29	1.82	2.99	35.79	13.42	40.52	29.98
C21	6.63	3.26	4.14	4.89	3.98	3.01	2.39	3.20	39.97	7.67	42.27	34.56
C22	8.19	3.46	3.65	5.55	4.35	3.44	1.72	3.35	46.89	0.58	52.88	39.64
C23	4.32	3.21	4.20	3.94	3.14	3.29	3.41	3.28	27.31	-2.49	18.81	16.75
C24	4.59	3.20	3.01	3.67	3.60	3.31	3.15	3.36	21.57	-3.44	-4.65	8.45
C25	4.50	4.35	3.88	4.25	4.40	4.24	3.21	3.99	2.22	2.53	17.27	6.12
C26	4.23	4.18	3.71	4.05	3.94	5.26	3.56	4.31	6.86	-25.84	4.04	-6.42
C27	9.14	4.35	3.70	6.22	4.76	4.11	2.15	3.84	47.92	5.52	41.89	38.26
C28	6.99	4.27	4.44	5.38	4.09	3.97	3.01	3.72	41.49	7.03	32.21	30.86
C29	7.42	3.01	2.39	4.83	4.69	2.85	1.95	3.36	36.79	5.32	18.41	30.43
C30	6.72	2.93	3.58	4.71	4.57	3.04	3.37	3.72	31.99	-3.75	5.87	21.02
C32	6.94	3.45	4.39	5.14	3.09	2.80	2.05	2.68	55.48	18.84	53.30	47.86
C33	6.11	4.80	3.32	4.88	3.82	4.70	2.01	3.68	37.48	2.08	39.46	24.59
C34	9.63	3.11	4.52	6.40	4.70	3.34	2.65	3.66	51.19	-7.40	41.37	42.81
C35	5.50	4.16	4.07	4.62	3.44	3.16	2.39	3.03	37.45	24.04	41.28	34.42
C36	9.52	4.34	6.39	7.08	5.26	4.40	3.90	4.56	44.75	-1.38	38.97	35.59
C37	11.12	5.22	6.11	7.92	4.54	5.20	3.84	4.56	59.17	0.38	37.15	42.42
Mean	6.82	3.81	4.02	5.12	4.11	3.73	2.70	3.59	36.33	2.04	31.54	27.87
C38	-	-	-	-	32.77	6.83	8.75	19.97	-	-	-	-
C39	-	-	-	-	11.19	13.14	9.22	11.30	-	-	-	-

Figure 6.14 gives the RMS of orbit SLR residuals for solutions with and without ISL observations when using the ground network **GloA**. Detailed statistics of orbit SLR residuals are summarized in Table 6-6. Compared to the precision of orbits, the accuracy of orbits benefits limitedly from adding ISL observations. However, a decrease of 2~3% can still be clearly observed in the RMS of orbit SLR residuals.

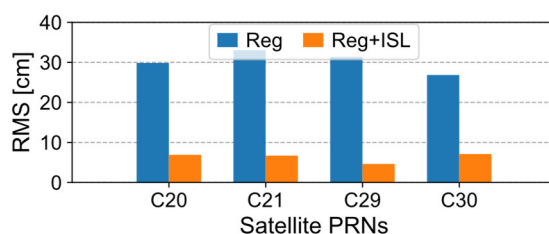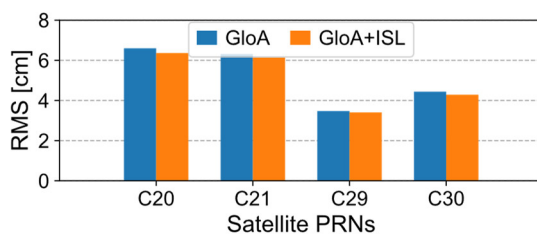Figure 6.14 Orbit SLR residual RMS of solutions **GloA+ISL** and **GloA** with and without ISL observations, respectively

Table 6-6 Statistics of orbit SLR residuals of solutions **GloA** and **GloA+ISL** [cm]

PRN	GloA			GloA+ISL			RMS Decrease [%]
	Mean	STD	RMS	Mean	STD	RMS	
C20	6.33	1.86	6.60	6.13	1.70	6.37	3.48
C21	5.98	2.02	6.31	5.86	1.85	6.14	2.69
C29	-2.19	2.70	3.48	-2.13	2.66	3.41	2.01
C30	-3.15	3.13	4.44	-2.96	3.10	4.29	3.38

6.2 Incorporate ISL Clock Observations

When incorporated into the processing of ground tracking measurements, the observation equation of ISL clock measurements as stated in Equation (2.17) can be rewritten as

$$\rho_-^{ij} = c[\delta t^j - \Delta^{j,PC_3}] - c[\delta t^i - \Delta^{i,PC_3}] + [(d_s^i - d_r^i)/2 - c\Delta^{i,PC_3}] \\ - [(d_s^j - d_r^j)/2 - c\Delta^{j,PC_3}] + (\varepsilon_*^{i,j} - \varepsilon_*^{j,i})/2 \tag{6.1}$$

Since ISLs are only established between BDS-3 satellites, superscripts used to discriminate BDS-3 from BDS-2 in Equations (5.6) and (5.7) are omitted. Thus, in Equation (6.1), Δ^{i,PC_3} and Δ^{j,PC_3} denote the ionosphere-free combinations of code pseudorange (PC) hardware delays of B1I and B3I of GNSS transmitters onboard satellite i and j, respectively.

As shown in Equation (6.1), in the integrated processing of ISL clock observations and ground tracking data, estimated parameters denoting the differences of ISL receipt and transmission hardware delays contain the delays of GNSS transmitters additionally. Thanks to the ground tracking observations, it is possible to estimate the ISL hardware delays in the relative sense. One of those hardware delay parameters should be fixed to serve as the datum to eliminate the rank deficiency of one degree of freedom (Ruan et al. 2014; Ruan et al. 2019).

This section is devoted to integrating ISL clock observations with ground tracking measurements in BDS-3 orbit determination. Specifically, the impact of harmonic signals found in ISL clock observations (See Section 4.4), weight allocation between ground tracking data and ISL clock observations, and the improvement brought by ISL clock observations on the orbit quality are investigated. Among the two types of derived ISL observations, only the clock observations are used in the integrated processing. As for the ground tracking, the network **GloA** (See Section 6.1.3) is used.

6.2.1 Impact of the Harmonic Signals

Same as the analysis conducted for ISL range observations, effectiveness of the proposed periodic function model in Section 3.4 for dealing with the harmonic signals is evaluated for ISL clock observations in the context of combined processing.

6.2.1.1 Orbits

Figure 6.15 displays the comparison of orbit DBD 1D RMS obtained from the engaged solutions. The only difference between those solutions is the specifically parameterized model used for absorbing harmonic signals in the ISL clock observations. Despite containing no direct geometric information, adding ISL clock observations still shows some effects on estimated satellite orbits. A small reduction in the orbit DBD can be observed for most satellites if the proper periodic function model is applied. Only negligible increases in the orbit DBD can be found for several satellites, like C20 and C22 using Model 1 or 3, C36 using Model 2 or 3. Similar to the case of ISL range observations, a significant improvement of the orbit precision of satellite C30 is found if the 1CPR signal is removed by Model 1 or 3. On the whole, Model 1 performs slightly better than Model 2. But on account of completeness, Model 3 could be taken as an overall optimal model if no severe resulted issue of over-parameterization. Based on the results shown here as well as that in Section 4.4, no seriously weaker solution is obtained when applying Model 3 instead of Model 1.
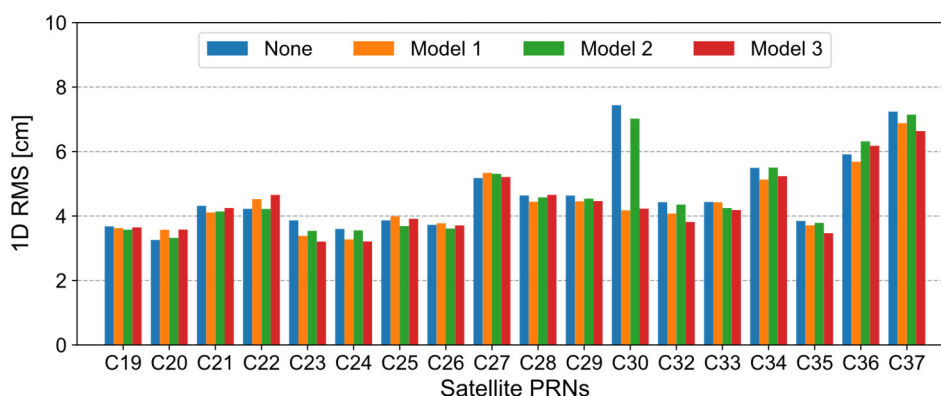
Figure 6.15 Comparison of orbit DBD 1D RMS obtained from solutions with different periodic function models applied for ISL clock observations. Observations from ground tracking were also incorporated in the processing.

Furthermore, statistics of SLR residuals of orbits from different solutions are compared in Figure 6.16. Much like ISL range observations, the 1CPR signal in the ISL clock observations has a significant impact on the orbit of C30. Both the precision and accuracy of C30 orbit

benefit remarkably from applying Model 1 or 3, with a reduction of ~7 cm in the SLR residual RMS. A slight offset decrease can be observed for satellite C29 when Model 1 or 3 is employed. For satellites C20 and C21, the effects of harmonic signals in the ISL clock observations are hardly visible.
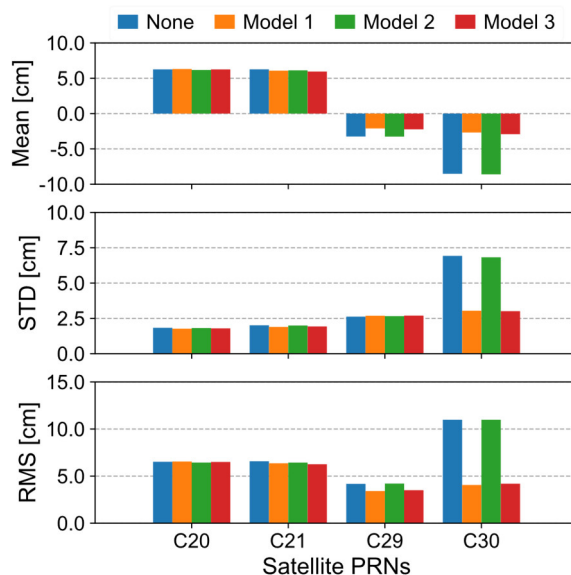
Figure 6.16 Statistics of SLR residuals of orbits from solutions with different periodic function models applied for ISL clock observations. Observations from ground tracking were also incorporated in the processing.

6.2.1.2 ISL Hardware Delays

Standard deviations of ISL hardware delay estimates are displayed in Figure 6.17 for the four different solutions. As satellite C19 was set as the reference, its estimates have been constrained to zero. It shows that the harmonic signals have only slight effects on the stability of hardware delay estimates. For some satellites, such as C23, C24, C27, and C30, a marginal increase in the STD of hardware delays can be seen after applying Model 1 or 3. Overall, those increments are very small, e.g., 0.01~0.02 ns, and therefore, are negligible.
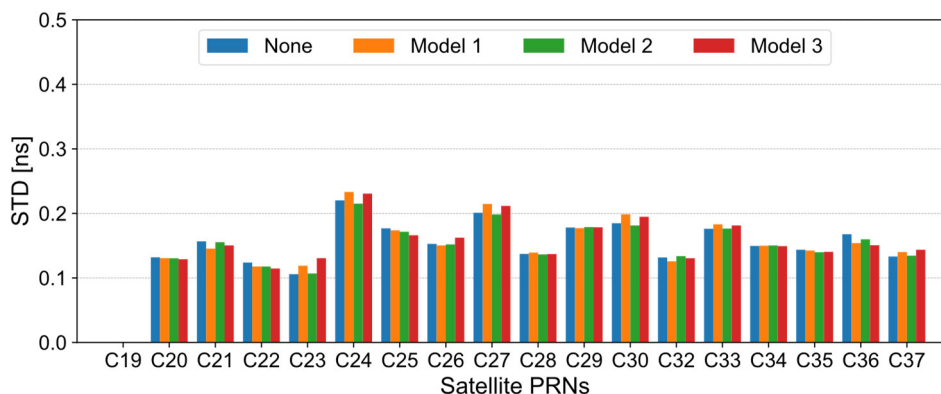
Figure 6.17 Comparison of STDs of ISL hardware delays from solutions with different periodic function models applied for ISL clock observations. Observations from ground tracking were also incorporated in the processing.

6.2.2 Weight Allocation

From the results obtained in Chapter 4, the clock observations of BDS-3 ISL appear to have a different noise level from the range observations. For this reason, the optimal a priori STD used for the range observations might not be appropriate for the clock observations. Similar to the case of ISL range observations, a series of tryouts of different a priori STDs for ISL clock observations have been conducted. Except for the a priori STD of ISL clock observations, there is no other difference among various integrated solutions. The a priori STDs of ground tracking carrier phase and code pseudorange observations were set to 0.01 cycle and 0.50 m, respectively, for each frequency of all stations. The ground tracking network **GloA** (See Section 6.1.3) was used in all the solutions.

6.2.2.1 A posteriori STD

The a posteriori unit weight STD series from the solutions with different a priori STDs for ISL observations are presented in Figure 6.18. Only a subset of the whole test solution set is shown. The solutions applying other a priori STDs not shown here have virtually no impact on the following discussion and conclusion. Additionally, the a posteriori STD series from the solution without ISL observations (**No ISL**) is also presented for reference.

Resembling the case of ISL range observations, the a posteriori STD of unit weight decreases as the a priori STD of ISL clock observations increases. Starting from the a priori STD of 4 cm, larger values for the a priori STD of ISL clock observations all get an a posteriori unit weight STD less than the a priori value, i.e., one. Starting from the a priori STD of 12 cm,

further down-weighting ISL clock observations only reduces the a posteriori unit weight STD very little, and at the end, basically, all the a posteriori unit weight STDs are stabilized within the range of 0.60~0.70. When the a priori STD of 4 cm was used for ISL clock observations, the generated a posteriori unit weight STDs were closest to the a priori unit weight STD among all solutions. It might indicate the optimal value to weight ISL clock observations in the integrated processing. However, just like for the range observations, more examination based on the estimates should be considered as to its appropriateness.
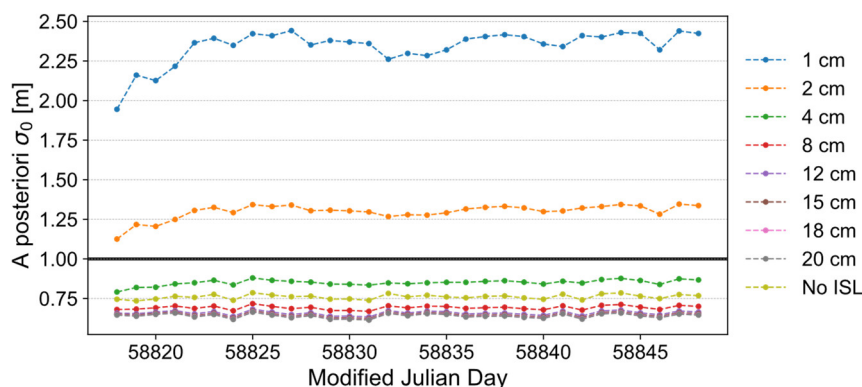
Figure 6.18 A posteriori unit weight STDs of solutions with various a priori STDs used for ISL clock observations when processed together with ground tracking measurements

6.2.2.2 Orbits

Orbit DBD 1D RMS from several tested solutions are displayed in Figure 6.19. The solution without any ISL observations is also given for reference. It shows that changing the weight of ISL clock observations affects the satellite orbits of the integrated processing. If an appropriate a priori STD is used, ISL clock observations exhibit clear benefits to the orbit precision of almost all satellites. Nevertheless, this will be discussed in a later section. From the comparison, the a priori STD of 4 cm for ISL clock observations seems the overall optimal weight since the resulted orbit DBD is the smallest for almost all satellites or very close to the smallest otherwise.

In Figure 6.20, statistics of orbit SLR residuals from the different solutions are shown together with that from the solution with only ground tracking observations. Slight influences from the weight of ISL clock observations on the accuracy of satellite orbits can be found. Also, if appropriately weighed, ISL clock observations show small while sound improvements on the accuracy of determined orbits. Though not much for each satellite, using 4 cm as the a priori STD gets the relatively smaller RMS of SLR residuals.
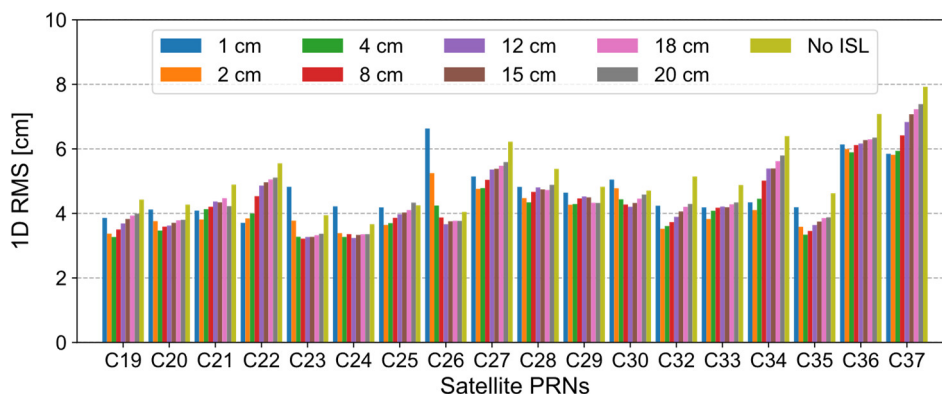
Figure 6.19 Orbit DBD 1D RMS of solutions with different a priori STDs used for ISL clock observations
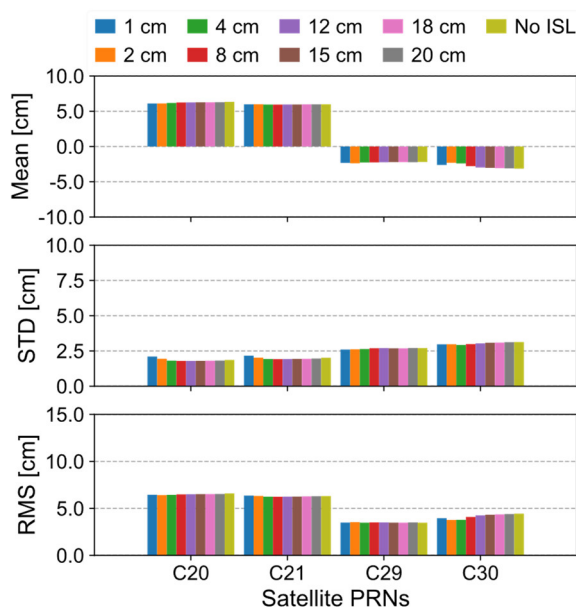
Figure 6.20 Statistics of SLR residuals of orbits from solutions with different a priori STDs used for ISL clock observations

6.2.2.3 ISL Hardware Delays

Figure 6.21 shows the comparison of STDs of ISL hardware delay estimates from different solutions. As taken as the reference, no estimates for satellite C19 are available. It doesn't show much difference among various solutions as to the stability of ISL hardware delay estimates. The largest variations of 0.02~0.03 ns occur only on a few satellites, like C25, C33, and C37, among all solutions. Therefore, using the a priori STD of 4 cm still seems optimum for ISL clock observations.
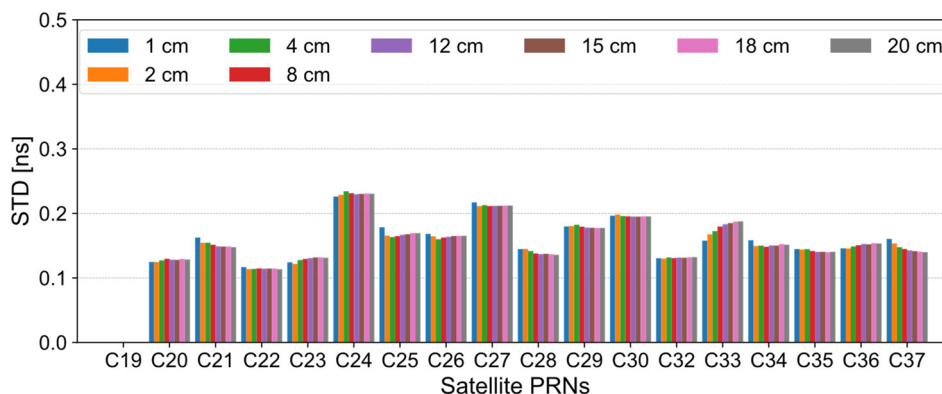
Figure 6.21 Comparison of STDs of ISL hardware delays from solutions with different a priori STDs used for ISL clock observations

6.2.3 Improvement on Orbits

Based on the results obtained in Section 6.2.2.2, adding ISL clock observations also improves the determined orbits as well. Hence, in this section, improvements brought by ISL clock observations on the orbit precision and accuracy are quantitatively evaluated and analyzed.

Figure 6.22 compares the orbit DBD 1D RMS of the solution using only ground tracking observations (**No ISL**) with the solution using additional ISL clock observations (**ISL Clk**). Statistics of orbit DBD RMS of the solution **ISL Clk** are listed in Table 6-7. Decreasing percentages of orbit DBD RMS of the solution **ISL Clk** with respect to the solution **No ISL** are also given. As the network **GloA** illustrated in Figure 6.8 was used in both solutions, solution **No ISL** is actually the solution **GloA** in Section 6.1.3.3. Therefore, orbit DBD RMS statistics of the solution **No ISL** are not listed here but referred to Table 6-5.

Except for C26, orbit precision of all other satellites profits clearly from the adding of ISL clock observations. The average 1D RMS of orbit DBD was decreased by ~19%, from 5.12 cm down to 4.14 cm. Because of direct enhancement on satellite clock parameters, the orbital radial component obtains the largest improvement consequently. An average reduction of ~39% can be found for the orbital radial DBD RMS, i.e., from 4.02 cm to 2.44 cm. Nevertheless, ISL clock observations also improve the along-track component by ~20%, i.e., reducing the DBD RMS from 6.82 cm to 5.49 cm.
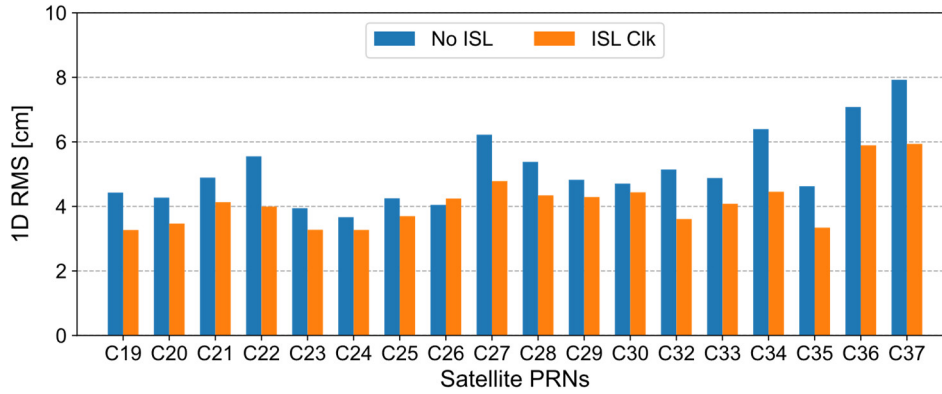
Figure 6.22 Comparison of orbit DBD 1D RMS between solutions incorporating ISL clock observations (**ISL Clk**) and not (**No ISL**)

Table 6-7 Statistics of orbit DBD RMS of solution **ISL Clk** [cm]

PRN	ISL Clk				Decrease [%]			
	A	C	R	1D	A	C	R	1D
C19	3.95	3.38	2.24	3.27	30.70	2.59	40.90	26.19
C20	4.58	3.60	1.47	3.47	17.63	5.26	51.96	18.74
C21	6.05	3.01	2.35	4.13	8.75	7.67	43.24	15.54
C22	5.93	3.06	1.85	4.00	27.59	11.56	49.32	27.93
C23	3.41	3.43	2.98	3.28	21.06	-6.85	29.05	16.75
C24	3.49	3.60	2.63	3.27	23.97	-12.50	12.62	10.90
C25	3.97	4.55	2.14	3.70	11.78	-4.60	44.85	12.94
C26	4.12	3.98	4.61	4.24	2.60	4.78	-24.26	-4.69
C27	6.79	4.06	2.47	4.79	25.71	6.67	33.24	22.99
C28	5.43	4.25	3.00	4.34	22.32	0.47	32.43	19.33
C29	6.59	2.98	1.71	4.29	11.19	1.00	28.45	11.18
C30	6.57	3.18	2.41	4.44	2.23	-8.53	32.68	5.73
C32	4.77	3.22	2.44	3.61	31.27	6.67	44.42	29.77
C33	5.04	4.53	2.02	4.08	17.51	5.62	39.16	16.39
C34	6.90	2.86	1.91	4.45	28.35	8.04	57.74	30.47
C35	4.27	3.39	1.93	3.34	22.36	18.51	52.58	27.71
C36	8.82	4.55	2.40	5.89	7.35	-4.84	62.44	16.81
C37	8.19	5.28	3.29	5.94	26.35	-1.15	46.15	25.00
Mean	5.49	3.72	2.44	4.14	19.50	2.36	39.30	19.14

Orbit SLR residual RMS of solutions **No ISL** and **ISL Clk** are compared in Figure 6.23. And the statistics of orbit SLR residuals are listed in Table 6-8. Decreasing percentages of orbit SLR residual RMS of the solution **ISL Clk** concerning the solution **No ISL** are also given. Except for C30, ISL clock observations have little impact on the orbit accuracy. An

improvement of ~15% can be found for satellite C30, lessening the residual RMS by 0.65 cm.
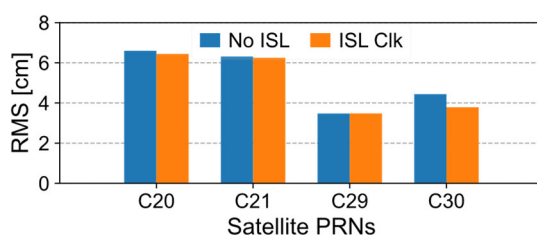
Figure 6.23 Comparison of orbit SLR residual RMS between solutions incorporating ISL clock observations (**ISL Clk**) and not (**No ISL**)

Table 6-8 Statistics of orbit SLR residuals of solutions **No ISL** and **ISL Clk** [cm]

PRN	No ISL			ISL Clk			RMS Decrease [%]
	Mean	STD	RMS	Mean	STD	RMS	
C20	6.33	1.86	6.60	6.18	1.81	6.44	2.42
C21	5.98	2.02	6.31	5.95	1.93	6.25	0.95
C29	-2.19	2.70	3.48	-2.27	2.64	3.48	0.00
C30	-3.15	3.13	4.44	-2.41	2.92	3.79	14.64

6.3 Incorporate both ISL Range and Clock Observations

An optimal solution should be obtained if both ISL derived range and clock observations are incorporated into the processing of L-band observations from ground tracking in a mathematically strict adjustment procedure. In this section, the benefits of integratedly processing ISL range and clock observations with ground tracking data are investigated. The optimal weights of 15 cm for ISL range and 4 cm for ISL clock observations are used as discussed in previous sections. As for periodic signals found in ISL measurements, the 1CPR and 2CPR signals are accounted via applying Model 3 for both ISL range and clock observations.

6.3.1 Improvement on Orbits

Improvement on orbits brought about by incorporating both ISL range and clock observations on the orbits is shown and discussed in this section. Network **GloA** as shown in Figure 6.8, has been used for providing ground tracking observations.

Figure 6.24 displays the comparison of orbit DBD 1D RMS between the solution using only ground tracking observations (**No ISL**) and the solution incorporating both ISL range and clock observations (**ISL Rng+Clk**). Solution **No ISL** is, in fact, the same as the solution **GloA**

in Section 6.1.3.3. Solutions, which are already discussed in previous sections, i.e., the solution adding only ISL range observations (**ISL Rng**, same as the solution **GloA+ISL** in Section 6.1.3.3) and the solution adding only ISL clock observations (**ISL Clk**, same as the solution **ISL Clk** in Section 6.2.3) are also shown for a complete comparison. Statistics of orbit DBD RMS of the solution **ISL Rng+Clk** are tabulated in Table 6-9. The statistics for solutions **No ISL** and **ISL Rng**, **ISL Clk** are referred to Table 6-5 and Table 6-7, respectively. Decreasing percentages of orbit DBD RMS of the solution **ISL Rng+Clk** regarding the solution **No ISL** are also noted in Table 6-9.

Compared to incorporating only ISL range or clock observations, processing integratedly both of these two types of ISL observations with the ground tracking measurements further improves the orbit precision for most satellites. However, for some satellites, such as C23, C30, C32, C35, and C36, a small increase against the solution with only ISL range observations, can be observed in the orbit DBD. Furthermore, for satellites C23 and C35, the orbit DBD 1D RMS of the solution **ISL Rng+Clk** is even slightly larger than that of either solution **ISL Rng** or **ISL Clk**. Nevertheless, in comparison to the solution without any ISL observations, the 1D RMS of BDS-3 MEO orbit DBD decreases by 29% on average, i.e., from 5.12 cm to 3.65 cm, after adding both ISL range and clock observations. The improvement is marginally lower than that using only ISL range observations (~30%, from 5.12 cm to 3.59 cm) while higher than the solution using only ISL clock observations (~19%, from 5.12 cm to 4.14 cm).

Significant reductions of orbit DBD occur in the orbital along-track and radial directions, which are around 39% and 42%, respectively. A rise of 0.16 cm in the orbital cross-track DBD RMS is negligible. To sum up, the average orbit DBD RMS of 4.19, 3.97, and 2.34 cm in along-track, cross-track, and radial directions can be reached after incorporating both the ISL range and clock observations.
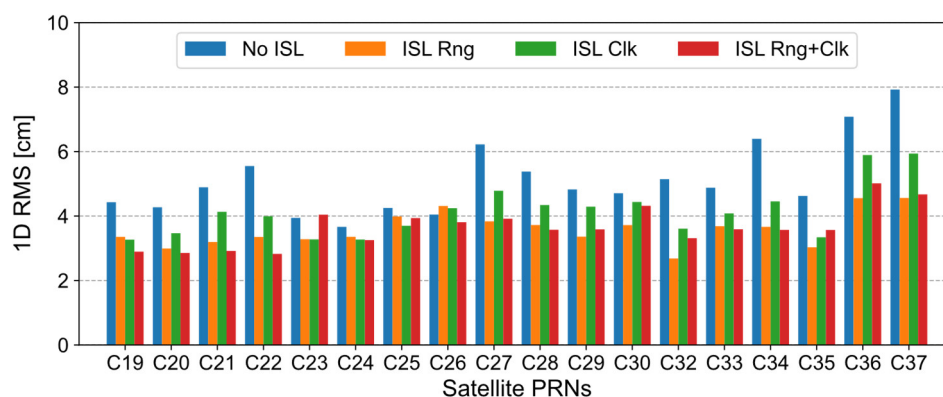
Figure 6.24 Comparison of orbit DBD 1D RMS of solutions incorporating only ISL range (**ISL Rng**), only ISL clock (**ISL Clk**), both ISL range and clock (**ISL Rng+Clk**), and no ISL observations (**No ISL**)

Table 6-9 Statistics of orbit DBD RMS of solution **ISL Rng+Clk** [cm]

PRN	ISL Rng+Clk				Decrease [%]			
	A	C	R	1D	A	C	R	1D
C19	2.84	3.74	1.76	2.90	50.18	-7.78	53.56	34.54
C20	3.39	3.28	1.49	2.86	39.03	13.68	51.31	33.02
C21	4.23	2.41	1.38	2.92	36.20	26.07	66.67	40.29
C22	3.31	3.36	1.31	2.83	59.58	2.89	64.11	49.01
C23	3.95	4.06	4.12	4.04	8.56	-26.48	1.90	-2.54
C24	3.83	3.22	2.60	3.25	16.56	-0.63	13.62	11.44
C25	3.97	4.76	2.85	3.94	11.78	-9.43	26.55	7.29
C26	3.00	5.24	2.65	3.81	29.08	-25.36	28.57	5.93
C27	5.13	4.10	1.71	3.92	43.87	5.75	53.78	36.98
C28	4.11	4.13	2.11	3.58	41.20	3.28	52.48	33.46
C29	5.17	2.86	1.91	3.59	30.32	4.98	20.08	25.67
C30	5.60	3.83	3.16	4.32	16.67	-30.72	11.73	8.28
C32	4.23	3.57	1.51	3.31	39.05	-3.48	65.60	35.60
C33	3.52	4.92	1.44	3.59	42.39	-2.50	56.63	26.43
C34	4.39	3.56	2.51	3.57	54.41	-14.47	44.47	44.22
C35	4.49	3.18	2.82	3.57	18.36	23.56	30.71	22.73
C36	5.91	5.16	3.73	5.01	37.92	-18.89	41.63	29.24
C37	4.40	6.03	3.12	4.67	60.43	-15.52	48.94	41.04
Mean	4.19	3.97	2.34	3.65	38.56	-4.20	41.79	28.71

The comparison of orbit SLR residuals from solutions **No ISL**, **ISL Rng**, **ISL Clk**, and **ISL Rng+Clk** are shown in Figure 6.25. The statistic values of solutions **No ISL** and **ISL Rng+Clk** are cataloged in Table 6-10. Decreasing percentages of SLR residual RMS of the solution **ISL Rng+Clk** concerning the solution **No ISL** are also given. Similar statistics of solutions **ISL Rng** and **ISL Clk** can be found in Table 6-6 and Table 6-8. Except for satellite C30, only small effects on orbit SLR residuals can be observed after incorporating both ISL range and clock observations. This is very similar to the situation of solutions in which only either the range or clock observations of ISL are added.
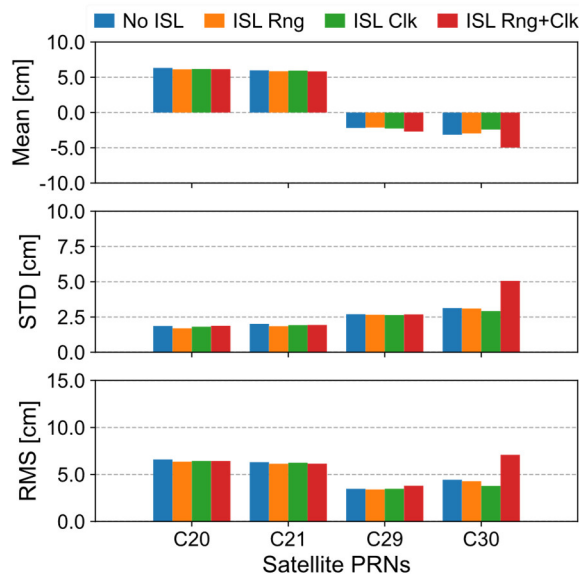
Figure 6.25 Comparison of orbit SLR residuals of solutions incorporating only ISL range (**ISL Rng**), only ISL clock (**ISL Clk**), both ISL range and clock (**ISL Rng+Clk**), and no ISL observations (**No ISL**)

Table 6-10 Statistics of orbit SLR residuals of solutions **No ISL** and **ISL Rng+Clk** [cm]

PRN	No ISL			ISL Rng+Clk			RMS Decrease [%]
	Mean	STD	RMS	Mean	STD	RMS	
C20	6.33	1.86	6.60	6.16	1.88	6.44	2.42
C21	5.98	2.02	6.31	5.84	1.94	6.15	2.54
C29	-2.19	2.70	3.48	-2.69	2.69	3.80	-9.20
C30	-3.15	3.13	4.44	-4.97	5.06	7.09	-59.68

However, an apparent change in the SLR residuals of satellite C30 can be noticed. Both its offset and standard deviation are enlarged, resulting in an increase of 60% in its SLR residual RMS. The increment of ~2.65 cm in the SLR residuals is found to be related to the satellite's on-orbit positions. Figure 6.26 displays orbit SLR residuals of solution **ISL Rng+Clk** relative to the Sun's elevation β regarding orbit planes and satellites' orbit angle μ concerning the Midnight points of orbits. Compared to satellites C20 and C21, C29 and C30 exhibit more degraded residual points around the orbit Midnight. In Figure 6.27, orbit SLR residuals of all four solutions in comparison are plotted against the ε angle, i.e., the angle between the Sun and Earth when seeing at the satellite. It shows that, for satellites C20, C21, and C29, no obvious difference respecting the variation pattern can be observed between various solutions. However, for satellite C30, the orbit quality was noticeably reduced at a low ε angle. The reason is not clear at this moment and needs further investigation.
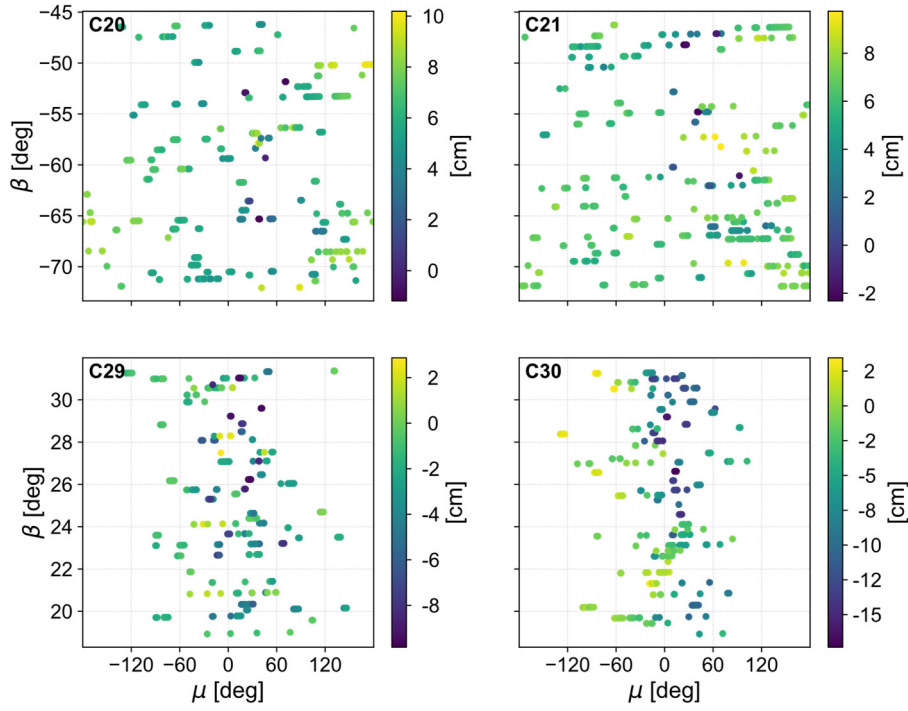
Figure 6.26 Orbit SLR residuals of solution **ISL Rng+Clk** displayed against satellites' on-orbit geometry. The β and μ angles, labeled along the y- and x-axes, are the Sun's elevation regarding the orbit plane and the orbit angle concerning the Midnight point of the orbit, respectively.
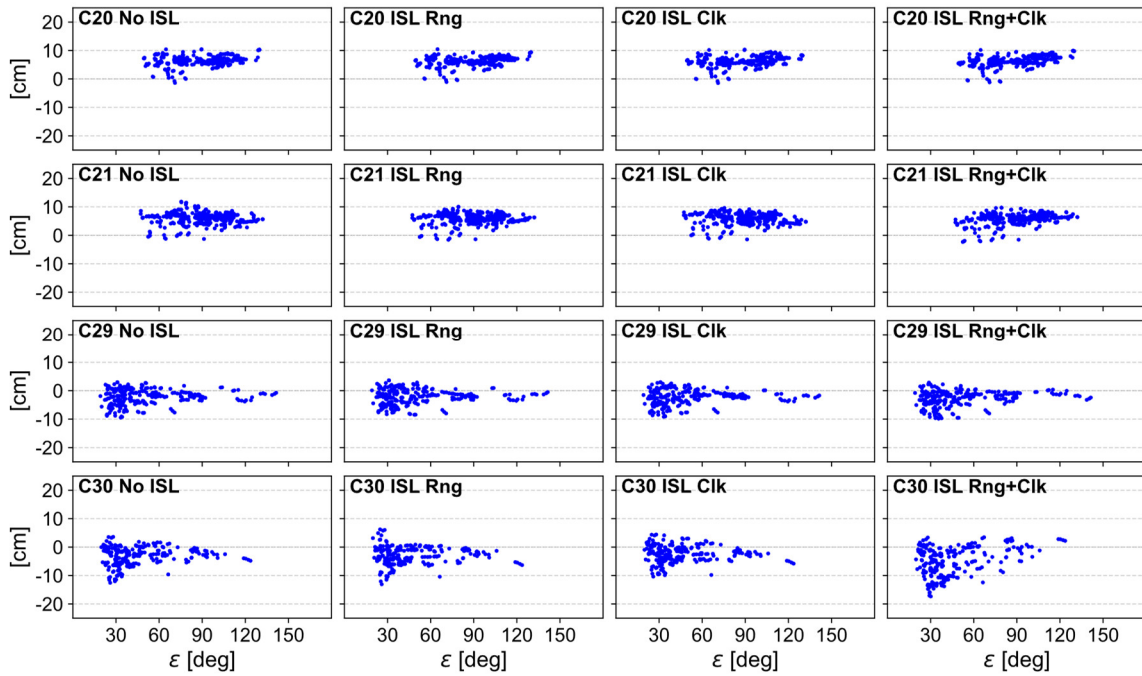
Figure 6.27 Orbit SLR residuals of all four solutions in comparison. The ε angle labeled along the x-axes is the angle between the Sun and Earth when seeing at the satellite.

6.3.2 Improvement on Geodetic Parameters

Another aspect to which the emerging ISL would potentially contribute is the estimating of geodetic parameters. As shown in the simulation study by (Glaser et al. 2020), compared with a GNSS composed of only MEOs, adding ISLs between MEOs can improve the precision of Earth Rotation Parameters (ERPs) by around 50% for pole motions and 70% for UT1-UTC, which are even more significant than that of incorporating LEOs.

As indicated by (Michalak et al. 2021), formal errors of geodetic parameters strongly depend on the a priori constraints of datum definition, i.e., constraints for the pseudo-observations resulting from the minimum constraints. As suggested in (Altamimi 2002), a standard deviation of 1.0 mm for the NNT constraint and an equivalent value for the NNR constraint (i.e., 0.03 mas, which is equivalent to 1mm at the equator) were applied to serve the datum definition in this study. Due to high correlations, the network scale is implicitly dominated by errors in the a priori satellite PCOs.

6.3.2.1 Earth Rotation Parameters

Figure 6.28 compares the average formal errors of estimated ERPs in solutions **GloA** and **GloA+ISL**. Clear reductions in formal errors can be observed for all ERPs. Compared to pole motions, pole motion rates benefit more from the added ISL observations. Formal errors of x- and y-pole rates decrease by ~35% and 40%, while the decreasing percentages of x-pole and y-pole are ~16% and 22%. Despite the much smaller magnitude than pole motions and their rates, a decrement of 24% can be found in the average formal error of the LOD parameter.
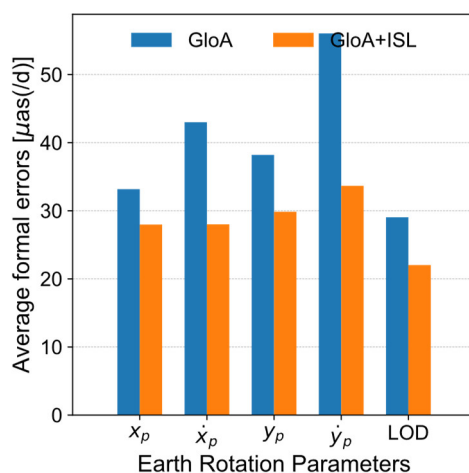
Figure 6.28 Average formal errors of estimated ERPs in solutions **GloA** and **GloA+ISL**

Taking the IGS combination solutions as references, ERPs estimated from solutions **GloA** and **GloA+ISL** are compared. Statistics of ERP differences are tabulated in Table 6-11. Unlike the formal errors shown in Figure 6.28, improvements in ERP estimates brought by ISL are not so encouraging. The RMS of the y-pole rate was significantly increased, though it was the worst determined parameter among the whole ERP set when using only the ground tracking measurements. The enlarged difference of the y-pole with respect to IGS combination solutions is caused mainly by the increased bias, whereas the STD of y-pole differences was slightly reduced. Similarly, increments in the mean values of other ERPs, such as x-pole, x-pole rate, and y-pole, can be also noticed while their STDs are either barely changed or clearly decreased. However, for the LOD parameter, the improvement of its accuracy is consistent with the formal error. Moreover, the offset of its estimates concerning IGS combination solutions was also clearly diminished.

Table 6-11 Statistics of ERP differences with respect to IGS combination solutions [μas, μas/d or μs]

ERPs	GloA			GloA+ISL		
	Mean	STD	RMS	Mean	STD	RMS
x_p	30.32	46.73	55.71	54.61	47.46	72.36
$\dot{x}_p$	0.94	308.22	308.22	-23.81	264.51	265.58
y_p	7.48	48.13	48.71	-15.58	45.17	47.79
$\dot{y}_p$	339.61	251.88	422.82	592.71	188.84	622.07
LOD	-7.33	13.89	15.71	-2.44	13.86	14.07

6.3.2.2 Geocenter Coordinates

Figure 6.29 shows the average formal errors of estimated geocenter coordinates from

solutions **GloA+ISL** and **GloA**. Formal errors of all three components of the geocenter were greatly reduced after incorporating ISL observations. Individually, decreasing percentages of 59%, 58%, and 55% can be found in the geocenter X, Y, and Z components.
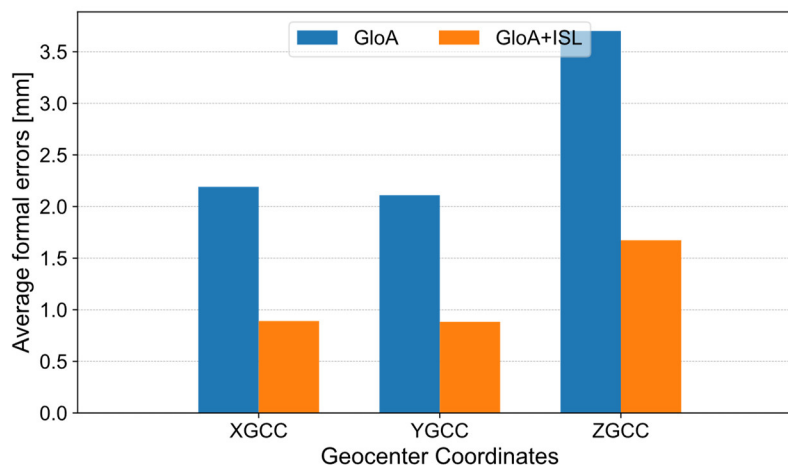
Figure 6.29 Average formal errors of estimated geocenter coordinates in solutions **GloA** and **GloA+ISL**

Usually, the geocenter Z component shows relatively high correlations with the D_0 and B_{c1} parameters of the ECOM SRP models (Meindl et al. 2013; Glaser et al. 2020). This correlation for satellite C19 from solutions **GloA** and **GloA+ISL** are compared in Figure 6.30 and Figure 6.31. It can be found that, for each daily session, correlations of the geocenter Z component with ECOM D_0 and B_{c1} parameters are very similar. Some variations along the date can be noticed for these correlations in both solutions. Incorporating ISL observations can considerably decrease the correlations, namely, decoupling the geocenter Z component from ECOM D_0 and B_{c1} parameters. The declines of these two correlations are also almost identical. Comparisons for satellites not shown here lead to a similar conclusion.
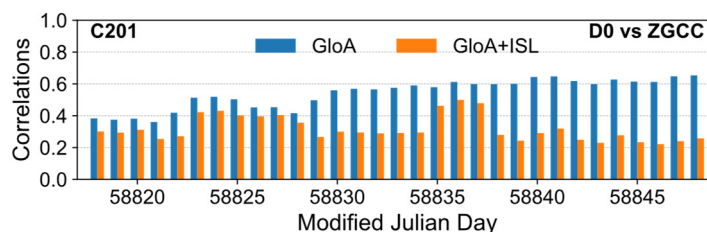
Figure 6.30 Correlation coefficients between the geocenter Z component and the ECOM D_0 parameter of SVN C201 (PRN C19) in solutions **GloA** and **GloA+ISL**
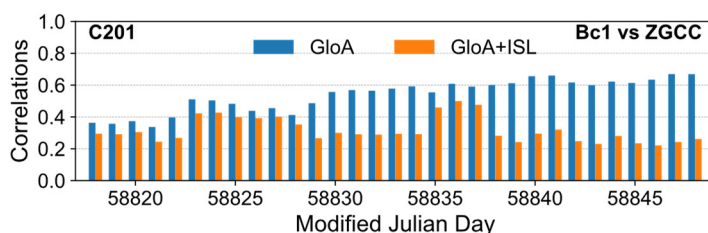
Figure 6.31 Correlation coefficients between the geocenter Z component and the ECOM B_{c1} parameter of SVN C201 (PRN C19) in solutions **GloA** and **GloA+ISL**

Under the assumption that the geocenter does not change too much during a short period, like one month, standard deviations of estimated geocenter coordinates can be served as the indicator of their precision. In Figure 6.32, STDs of geocenter coordinates estimated in solutions **GloA** and **GloA+ISL** are compared. Using only ground tracking observations, STDs of around 7, 8, and 55 mm were obtained for the X, Y, and Z components. After incorporating ISL observations, reductions of 46%, 77%, and 65% were found for these three components, respectively. Standard deviations of 4, 2, and 19 mm were reached in the X, Y, and Z coordinates of the geocenter when using additional ISL observations. These solid improvements brought by ISL are particularly promising if considering the weakness of GNSS in the contribution to the datum definition of ITRF.
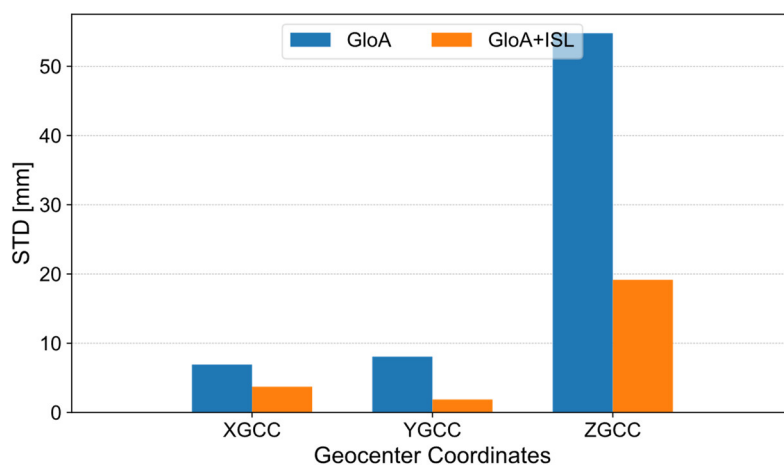
Figure 6.32 Standard deviations of the estimated geocenter coordinates in solutions **GloA** and **GloA+ISL**

6.3.2.3 Network Scale

Estimated network scales through GNSS are systematically affected by the biases in satellite PCOs, especially in the Z offsets (Zhu et al. 2003). Unless the mean PCO bias of the constellation have changed, which may happen if different satellite sets are observed from session to session, the PCO bias-induced offset in the scale estimation should keep constant

(Ge et al. 2005). And during a relatively short period, e.g., one month in this study, secular variation in the network scale induced by the PCO changes of individual satellites can be neglected. Therefore, regardless of the offset, variations in the network scale estimates should indicate the degree to which it is contaminated by the satellite PCO errors.

Estimates of network scale with respect to datum reference frames are displayed in Figure 6.33 and Figure 6.34 for solutions **GloA** and **GloA+ISL**, respectively. As mentioned earlier, a subset of stations from the IGS daily combination solution was used as the datum stations in the processing. Network scales of the IGS solutions are highly related to the PCOs of GPS satellites. Differences of estimated network scales by BDS-3 with that from IGS solutions should mainly reflect the inconsistency of BDS-3 PCOs with that of GPS. As can be seen, an offset of 1.3~1.5 ppb exists in the scales determined by BDS-3 no matter using additional ISL observations or not. However, it should be emphasized that this scale offset reflects more the inconsistency rather than the accuracy of satellites' PCOs of those two GNSS.

Simulations from (Glaser et al. 2020) show that adding ISLs between MEOs can improve the quality of network scale by 19% in the aspect of standard deviation. However, no significant difference between solutions **GloA** and **GloA+ISL** can be observed in the STDs of estimated network scales. This may be attributed to the extremely high accuracy of simulated ISL observations, i.e., 1mm, used in (Glaser et al. 2020).
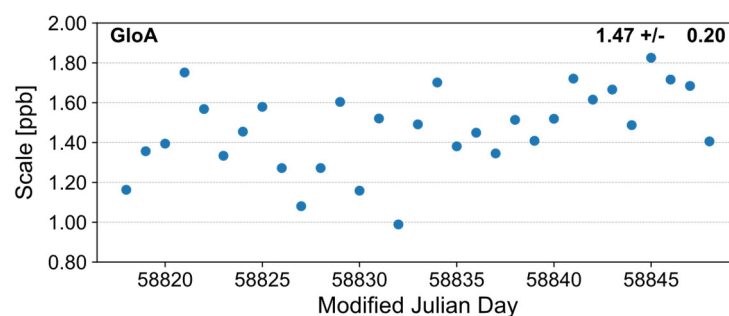
Figure 6.33 Network scales of solution GloA with respect to IGS daily combination solutions
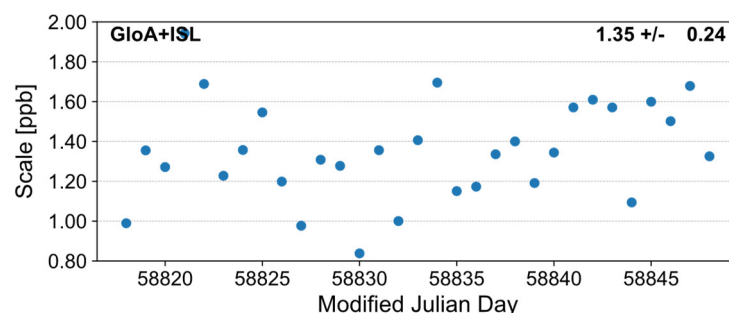
Figure 6.34 Network scales of solution GloA+ISL with respect to IGS daily combination solutions

6.4 Conclusion

The proposed periodic function model for absorbing the harmonic signals in ISL observations was checked to be effective for both the range and clock observations in the context of integrated processing. The a priori STDs of 15 cm and 4 cm for ISL range and clock observations, respectively, were found to be optimal when incorporated with the ground tracking observations.

For a regional ground network, adding ISL range observations improves the orbit precision from ~16.3 m to ~7.5 cm in the sense of orbit DBD 1D RMS. The orbit SLR residuals RMS was decreased from ~30 cm to 4~7 cm. In the case of a sparse global network, the average orbit DBD RMSs were reduced from 11.3, 5.3, 6.5 cm down to 4.5, 4.6, 2.6 cm in the along-track, cross-track, and radial directions. Even with all available ground tracking stations, adding ISL range observations can still further decrease the orbit DBD 1D RMS of BDS-3 MEOs by ~30%, i.e., decreasing the 1D RMS from 5.1 cm to 3.6 cm. As for the orbit accuracy indicated by the SLR residuals, the added ISL range observations only show limited improvements if a global network is available. The ISL clock observations were also demonstrated to benefit the orbit improvement. After incorporating only the ISL clock observations, orbit DBD RMSs decreased by ~20% and ~39% in the along-track and radial components. The average 1D RMS of orbit DBD was reduced from 5.1 cm to 4.1 cm. Similar to the range observations, the improvement from ISL clock observations in the orbit accuracy, i.e., SLR residuals, is slight, except for satellite C30, for which a decrement of ~15% was observed.

Integrating the ISL range and clock observations with ground tracking observations in a single least-square adjustment can further improve the orbits. Orbit DBD RMSs of 4.2, 4.0, and 2.3 cm in the along-track, cross-track, and radial directions were obtained. Significant improvements were found in the orbital along-track and radial directions, i.e., 39% and 42%, compared to the solution using only ground tracking observations. The cross-track component seems to benefit from the ISL observations hardly.

It is proven that the estimating of geodetic parameters profits from the ISL observations. Despite further investigations about the improvement in ERPs and network scale are needed, the enhancement on the geocenter coordinates is very encouraging. The correlations between the geocenter Z component and ECOM parameters can be greatly alleviated. After incorporating ISL observations, standard deviations of geocenter coordinates were reduced by 46%, 77%, and 65%.

7 Summary and Outlook

7.1 Summary

The new generation of BeiDou Navigation Satellite System (BDS-3) has been constructed completely and announced to provide global users with the legacy PNT as well as several featured services. Inter-Satellite-Links, which operate on the Ka-band, are carried by all BDS-3 satellites. High bandwidth communications within the constellation and precise relative ranging between satellites are realized by Inter-Satellite-Links, which not only increase the survivability but also improve the performance of a GNSS. Although the concept has been proposed for many years, it is the first time that those payloads are deployed constellation-wide in a GNSS. Therefore, ISLs from BDS-3 offer a great opportunity to comprehensively investigate the contributions of these new observations to precise orbit determination.

Following a detailed introduction of the current status of the system, the Inter-Satellite-Link of BDS-3 is thoroughly described, including the ranging system, the mathematical model of its one-way pseudorange, and various errors that the observations suffer. Assuming a maximum beam angle of 60°, only around 1.14% and 0.06% of daily ISLs between BDS-3 MEO satellites pass through Earth's ionosphere and troposphere, respectively. Therefore, atmospheric delays of ISLs between satellites are usually left unmodeled. The derivation of original dual one-way observations for decoupling the orbits and clocks is detailedly explained. Based on the law of error propagation, errors brought into the derived observations by the derivation pre-processing can be controlled within 1.0 cm given a priori ephemerides with the required accuracy. Calculated from the real ISL observations, the off-boresight angle of BDS-3 ISLs can be as small as 10° while as large as 60°, which results in a much wider beam range than the UHF cross-links designed for GPS Block IIR.

Autonomous orbit determination using only ISL ranging observations is investigated. The intrinsic insensibility of relative ranging observations to the constellation rotation can be demonstrated by the simplified Keplerian motion. When using Cartesian coordinates instead of osculating Keplerian elements, the direct consequence of the unobservability of absolute RAANs is the strong correlation of initial state vectors between satellites. In spite of the lack of enough datum, studying the orbit determination using ISL measurements solely can evaluate the performance of autonomous navigation of the system. The post-fit residuals of ISL derived range observations of BDS-3 are temporally homogeneous, with an overall daily

RMS less than 7 cm. The post-fit RMSs of individual satellites show obviously different. Orbit radial components do not suffer from the entire rotation of the constellation. For most MEO satellites, the radial components of orbit DBD are 2 ~ 4 cm. For the two considered IGSOs, the radial DBD RMS of 10~12 cm can be obtained. After eliminating the constellation rotation by Helmert transformations, orbit DBD RMS in the along-track, cross-track, and radial directions are 7, 5, and 4 cm on average. The hardware delays of Inter-Satellite-Links are very stable, with a monthly STD of 0.13 ns (~3.9 cm). Not clear about the exact reason, strong harmonic signals resonant with the orbit motions of BDS-3 MEO satellites are found in the link residuals. A Fourier-like periodic function model is proposed to absorb those signals and proved effective.

Autonomous time synchronization using only ISL clock observations is studied. By the derived clock measurements, clocks of satellites within the constellation can be precisely synchronized without ground tracking. The post-fit residuals of ISL clock observations are smaller than the range observations. The daily RMSs during the 31-days session are only slightly over 5 cm. Similar to the derived range observations, satellite-specific differences in the size of residuals can be found. When compared with IGS MGEX AC's products, differences of clock offsets estimated by ISL observations are only 0.01~0.02 ns larger than the comparison between various ACs. The hardware delays in the ISL derived clock observations are very stable, with an average STD of ~0.08 ns (~2.4 cm). Similar harmonic signals found in the derived range measurements are also encountered in the derived clock observations. By a simple correlation analysis, it shows that the derived range and clock observations are not really decoupled as intended. The proposed periodic function model turns out to be capable of absorbing those signals in the clock observations. Nevertheless, those harmonic signals have only minor effects on the precision of time synchronization.

Before moving on to the benefits of additional ISL observations, several critical issues related to the orbit determination of BDS-3 are addressed based on the L-band ground tracking data. Effects of non-conservative perturbations from Earth's Albedo and antenna thrust on orbits of BDS-3 are assessed. They both induce radial contractions of the orbits and, therefore, should be considered in orbit modelling. Differently parameterized empirical SRP models are examined as to the applicability to BDS-3 satellites. A satellite-specific SRP modelling approach that takes the different suitability of ECOMs into account is proposed though showing similar performance as the ECOM2. When ECOM2 or the proposed satellite-specific modelling is used, the a priori box-wing model has little effect on the orbit results. To cope with the backward compatibility issue caused by the switch of open service signals of BDS-3, the legacy B1I+B2I signals are recommended for BDS-2 in the combined processing of BDS-2 and

BDS-3.

Improvement of ISL observations on the orbit determination of BDS-3 is exhaustively assessed. The weights of ISL derived range and clock observations are determined to be 15 and 4 cm, respectively, after a series of tests. The benefits of additional ISL range measurements are evaluated in cases of different ground tracking networks. Interestingly, even on top of all available ground tracking stations from the IGS MGEX network, incorporating ISL derived range observation still decreases the orbit DBD noticeably. The average orbit DBD RMS in the along-track, cross-track, and radial components drop from 6.82, 3.81, and 4.02 cm to 4.11, 3.73, and 2.70 cm. As it benefits the decorrelation of orbit and clock information, incorporating only the ISL clock observations also improves the orbit precision. Integratedly processing the ISL derived range, ISL derived clock, and L-band ground tracking observations reduces the orbit DBD by ~39% and 42% in the along-track and radial directions, respectively, compared to using only ground-tracking data. Additionally, the ISL measurements can advantage the estimation of geodetic parameters. The strong correlations between empirical SRP parameters and geocenter coordinates are significantly reduced by adding ISL observations.

7.2 Outlook

Inspired by the work already done in this study, some of the future research around the ISLs of BDS-3 can be foreseen.

1) The effects of atmospheric delays on ISL observations should be quantitatively investigated. Because the affected measurements only take a small portion, atmospheric delays of ISLs between satellites are ignored. Though it might not necessarily improve the contribution a lot, detailed analyses of the magnitudes of tropospheric and ionospheric delays are indispensable for a type of new geodetic observation.

2) Optimal weighting among satellites should be sought unless the heterogeneity of ISL observations is solved. No matter for the range or clock observations, apparently heterogeneous ISL residual levels are noticed. In this study, only the relative weight ratios between ISL observations and L-band ground tracking measurements are determined. Towards the more rigorous and optimal processing, the clear nonuniformity of observation quality among satellites should be taken into account.

3) Original ISL dual one-way pseudoranges should be processed for orbit determinations and time synchronizations. Aimed at onboard processing for autonomous navigation,

almost all research around ISL observations is not directly based on the original observations. Theoretically, with the a priori ephemerides of enough accuracy, it is feasible to conduct all the analyses taking the original ISL observations as input. It is also the most natural as well as most rigorous way to evaluate the contribution of ISLs thoroughly. Although the harmonic signals existing in the derived observations are not likely introduced by the derivation pre-processing, processing the original observations would help scrutinize the cause of those periodic signals, at least narrowing down the possible error sources.

4) Limited by the data availability, only 31 days of BDS-3 ISL observations are used for investigations in this study. With measurements spanning over a longer period, the contribution of ISLs to the determination of geodetic parameters can be demonstrated more solidly, especially to the estimation of ERPs (and even the rates of Celestial Pole Offsets) and geocenter coordinates.

As the rigidity of the constellation is greatly enhanced, more trivial errors might be uncovered by incorporating precise ISL measurements. For example, any inconsistency between the PCOs of L-band and Ka-band antennas can be scouted up by integrated processing. On the other hand, it is naturally possible to calibrate one of those antennas by fixing the offsets of the other.

Bibliography

Abich K et al. (2019) In-Orbit Performance of the GRACE Follow-on Laser Ranging Interferometer. Physical Review Letters 123(3):031101. doi: https://doi.org/10.1103/PhysRevLett.123.031101

Altamimi Z (2002) Discussion on how to express a regional GPS solution in the ITRF. Paper presented at the Symposium of the IAG Subcommission for Europe (EUREF), Ponta Delgada, 5-8 June 2002

Altamimi Z, Boucher C, Sillard P (2002) New trends for the realization of the international terrestrial reference system. Adv Space Res 30(2):175-184. doi: https://doi.org/10.1016/S0273-1177(02)00282-X

Ananda MP, Bernstein H, Cunningham KE, Feess WA, Stroud EG (1990) Global Positioning System (GPS) autonomous navigation. Paper presented at the IEEE Position Location and Navigation Symposium, Las Vegas, Nevada, March 20-23

Arnold D et al. (2015) CODE's new solar radiation pressure model for GNSS orbit determination. Journal of Geodesy 89(8):775-791. doi: https://doi.org/10.1007/s00190-015-0814-4

Bar-Sever YE, Kroger PM, Borjesson JA (1998) Estimating horizontal gradients of tropospheric path delay with a single GPS receiver. Journal of Geophysical Research: Solid Earth 103(B3):5019-5035. doi: https://doi.org/10.1029/97JB03534

Bernstein H, Bowden AF, Gartside JH GPS User Position Accuracy with Block IIR Autonomous Navigation (AUTONAV). In: the 6th International Technical Meeting of the Satellite Division of the Institute of Navigation (ION GPS-93), Salt Lake City, Utah, September 22-24 1993. pp 1389-1399

Beutler G, Brockmann E, Gurtner W, Hugentobler U, Mervart L, Rothacher M, Verdun A (1994) Extended orbit modeling techniques at the CODE processing center of the international GPS service for geodynamic(IGS): theory and initial results. manuscripta geodaetica 19:367-386

Beyerle G (2009) Carrier phase wind-up in GPS reflectometry. GPS Solut 13:191-198. doi: https://doi.org/10.1007/s10291-008-0112-1

Bingbing D, Urs H, Inga S, Stefan M, Matthias K, Martin R (2022) BeiDou satellite radiation force models for precise orbit determination and geodetic applications. IEEE Transactions on Aerospace and Electronic Systems 58(4). doi: https://doi.org/10.36227/techrxiv.15111978.v1

Blewitt G (1990) An Automatic Editing Algorithm for GPS Data. Geophysical Research

Letters 17(3):199-202

Boehm J, Heinkelmann R, Schuh H (2007) Short Note: A global model of pressure and temperature for geodetic applications. Journal of Geodesy 81(10):679-683. doi: https://doi.org/10.1007/s00190-007-0135-3

Boehm J, Niell A, Tregoning P, Schuh H (2006) Global Mapping Function (GMF): A new empirical mapping function based on numerical weather model data. Geophysical Research Letters 33(7). doi: https://doi.org/10.1029/2005GL025546

Böhm J, Möller G, Schindelegger M, Pain G, Weber R (2015) Development of an improved empirical model for slant delays in the troposphere (GPT2w). GPS Solut 19(3):433-441. doi: https://doi.org/10.1007/s10291-014-0403-7

Butcher JC (2016) Numerical Methods for Ordinary Differential Equations. 3rd edn. John Wiley & Sons Ltd,

Cai C, Liu Z, Xia P, Dai W (2013) Cycle slip detection and repair for undifferenced GPS observations under high ionospheric activity. GPS Solut:247-260

Capderou M (2014) Handbook of Satellite Orbits: From Kepler to GPS. Springer,

Chen G, Herring TA (1997) Effects of atmospheric azimuthal asymmetry on the analysis of space geodetic data. Journal of Geophysical Research: Solid Earth 102(B9):20489-20502. doi: https://doi.org/10.1029/97JB01739

Chen J, Jiao W, Ma J, Song X (2005a) Autonav of Navigation Satellite Constellation Based on Crosslink Rang and Orientation Parameters Constraining. Geomatics and Information Science of Wuhan University 30(5)

Chen J, You Z, Jiao W (2005b) Research on Autonav of Navigation Satellite Constellation Based on Crosslink Range and Inter-satellites Orientation Observation. Journal of Astronautics 26(1):43-46

Cheng MK, Shum CK, Tapley BD (1997) Determination of long-term changes in the Earth's gravity field from satellite laser ranging observations. Journal of Geophysical Research: Solid Earth 102(B10):22377-22390. doi: https://doi.org/10.1029/97JB01740

Codik A (1985) Autonomous Navigation of GPS Satellites: A Challenge For The Future. NAVIGATION: Journal of The Institute of Navigation 32(3):221-232

Collaboration TA et al. (2013) Astropy: A community Python package for astronomy. A&A 558:A33

Colombo OL (1989) The dynamics of global positioning system orbits and the determination of precise ephemerides. Journal of Geophysical Research 94:9167-9182

CSNO (2013a) BeiDou Navigation Satellite System Open Service Performance Standard (Version 1.0). China Satellite Navigation Office

CSNO (2013b) BeiDou Navigation Satellite System Signal In Space Interface Control

Document—Open Service Signal (Version 2.0). China Satellite Navigation Office

CSNO (2016) BeiDou Navigation Satellite System Signal In Space Interface Control Document—Open Service Signal (Version 2.1). China Satellite Navigation Office

CSNO (2017a) BeiDou Navigation Satellite System Signal In Space Interface Control Document—Open Service Signal B1C (Version 1.0). China Satellite Navigation Office

CSNO (2017b) BeiDou Navigation Satellite System Signal In Space Interface Control Document—Open Service Signal B2a (Version 1.0). China Satellite Navigation Office

CSNO (2018a) BeiDou Navigation Satellite System Open Service Performance Standard （Version 2.0） . China Satellite Navigation Office

CSNO (2018b) BeiDou Navigation Satellite System Signal In Space Interface Control Document—Open Service Signal B3I (Version 1.0). China Satellite Navigation Office

CSNO (2019) BeiDou Navigation Satellite System Signal In Space Interface Control Document—Open Service Signal B1I (Version 3.0). China Satellite Navigation Office

CSNO (2020) BeiDou Navigation Satellite System Signal In Space Interface Control Document Open Service Signal B2b (Version 1.0) China Satellite Navigation Office

CSNO (2021) BeiDou Navigation Satellite System Open Service Performance Standard (Version 3.0). China Satellite Navigation Office

Davis JL, Herring TA, Shapiro II, Rogers AEE, Elgered G (1985) Geodesy by radio interferometry: Effects of atmospheric modeling errors on estimates of baseline length. Radio Science 20(6):1593-1607. doi: https://doi.org/10.1029/RS020i006p01593

Deng Z (2008) Preprocessing of high rate GPS data for real-time applications.

Desai S, Wahr J, Beckley B (2015) Revisiting the pole tide for and from satellite altimetry. Journal of Geodesy 89(12):1233-1243. doi: https://doi.org/10.1007/s00190-015-0848-7

Desai SD (2002) Observing the pole tide with satellite altimetry. Journal of Geophysical Research: Oceans 107(C11):7-1-7-13. doi: https://doi.org/10.1029/2001JC001224

Dilssner F (2017) A note on the yaw attitude modeling of BeiDou IGSO-6.

Dilssner F, Läufer G, Springer T, Schönemann E, Enderle W (2018) The BeiDou Attitude Model for Continuous Yawing MEO and IGSO Spacecraft Paper presented at the EGU 2018, Vienna,

Fehlberg E (1968) Classical fifth-, sixth-, seventh-, and eighth-order Runge-Kutta formulas with stepsize control. No.: NASA TR R-287

Fehlberg E (1970) Some experimental results concerning the error propagation in Runge-Kutta type integration formulas. No.: NASA TR R-352

Gao GX, Chen A, Lo S, Lorenzo DD, Walter T, Enge P (2009) Compass-M1 Broadcast Codes in E2, E5b, and E6 Frequency Bands. IEEE Journal of Selected Topics in Signal Processing 3(4):599-612. doi: https://doi.org/10.1109/JSTSP.2009.2025635

Ge M, Gendt G, Dick G, Zhang FP, Reigber C (2005) Impact of GPS satellite antenna offsets on scale changes in global network solutions. Geophysical Research Letters 32(6). doi: https://doi.org/10.1029/2004GL022224

Glaser S, Michalak G, Männel B, König R, Neumayer KH, Schuh H (2020) Reference system origin and scale realization within the future GNSS constellation "Kepler". Journal of Geodesy 94(12):117. doi: https://doi.org/10.1007/s00190-020-01441-0

Grelier T, Dantepal J, DeLatour A, Ghion A, Ries L (2007) Initial observations and analysis of compass MEO satellite signals. Inside GNSS 2(4):39-43

Hairer E, Nørsett SP, Wanner G (1993) Solving Ordinary Differential Equations I: Nonstiff Problems. Springer Series in Computational Mathematics, vol 8. Springer-Verlag Berlin Heidelberg. doi: 10.1007/978-3-540-78862-1

Han S, Gui Q, Li J (2013) Establishment criteria, routing algorithms and probability of use of inter-satellite links in mixed navigation constellations. Adv Space Res 51(11):2084-2092. doi: https://doi.org/10.1016/j.asr.2012.12.020

Herklotz RL (1987) Incorporation of Cross-Link Range Measurements in the Orbit Determination Process to Increase Satellite Constellation Autonomy. Massachusetts Institute of Technology

Hofmann-Wellenhof B, Lichtenegger H, Collins J (2001) GPS: Theory and Practice. 5th edn.,

Hofmann-Wellenhof B, Lichtenegger H, Wasle E (2008) GNSS-Global Navigation Satellite Systems GPS, GLONASS, Galileo, and more.

Hugentobler U, Rodríguez-Solano C, Steigenberger P, Dach R, Lutz S Impact of Albedo Modelling on GNSS Satellite Orbits and Geodetic Time Series. In: American Geophysical Union Fall Meeting 2009, 2009.

Jishen L (1995) Satellite Precision Orbit Determination. People's Liberation Army Press, Beijing, China

Kaplan ED, Hegarty CJ (eds) (2006) Understanding GPS: Principles and Applications. 2nd edn,

Kaula WM (1966) Theory of Satellite Geodesy: Applications of Satellites to Geodesy. Blaisdell Publishing Company,

Kleusberg A, Teunissen PJG (eds) (1996) GPS for Geodesy. Lecture Notes in Earth Sciences, vol 60. Springer-Verlag Berlin Heidelberg,

Kouba J (2009) Testing of global pressure temperature (GPT) model and global mapping function(GMF) in GPS analyses. Journal of Geodesy 83:199-208. doi: https://doi.org/10.1007/s00190-008-0229-6

Kouba J (2017a) Notes on December 2017 version of the ECLIPS subroutine.

Kouba J (2017b) Notes on May 2017 version of the eclips subroutine.

Leick A, Rapoport L, Tatarnikov D (2015) GPS Satellite Surveying. 4th edn.,

Li B (2018) Review of triple-frequency GNSS: ambiguity resolution, benefits and challenges. The Journal of Global Positioning Systems 16. doi: https://doi.org/10.1186/s41445-018-0010-y

Li J, Yang Y, He H, Guo H (2017) An analytical study on the carrier-phase linear combinations for triple-frequency GNSS. Journal of Geodesy 91:151-166. doi: https://doi.org/10.1007/s00190-016-0945-2

Li J, Yang Y, Xu J, He H, Guo H (2015) GNSS multi-carrier fast partial ambiguity resolution strategy tested with real BDS/GPS dual- and triple-frequency observations. GPS Solut 19(1):5-13. doi: https://doi.org/10.1007/s10291-013-0360-6

Li X et al. (2019) Precise orbit determination for BDS3 experimental satellites using iGMAS and MGEX tracking networks. Journal of Geodesy 93(1):103-117. doi: https://doi.org/10.1007/s00190-018-1144-0

Lin X, Baojun L, Yingchun L, Sujie X, Tao B Satellite Geometry and Attitude Mode of BDS-3 MEO Satellites Developed by SECM. In: ION GNSS+, 2018.

Liu C et al. (2020) Inter-satellite clock offsets adjustment based on closed-loop residual detection of BDS Inter-Satellite Link. Acta Geodaetica et Cartographica Sinica 49(9):1149-1157. doi: https://doi.org/10.11947/j.AGCS.2020.20200319

Liu L (1992) Orbital mechanics of artificial earth satellites. Higher Education Press, Beijing

Liu L (1998) Methods of Celestial Mechanics. Nanjing University Press,

Liu L (2000) Orbit Theory of Spacecraft. National Defense Industry Press, Beijing

Liu L, Liu Y-c (2000) On the Rank Deficiency of Autonomous Orbit Determination by Satellite-Satellite Relative Measuring. Journal of Spacecraft TT&C Technology 19(3):13-16

Liu L, Zhu L-F, Han C-H, Liu X-P, Li C (2009) The Model of Radio Two-way Time Comparison between Satellite and Station and Experimental Analysis. Chinese Astronomy and Astrophysics 33(4):431-439. doi: https://doi.org/10.1016/j.chinastron.2009.09.009

Liu Y-c, Liu l, Wang C-b (2000) On the Orbit Determination Combined the Satellite-Satellite Tracking and the Ground-based Tracking. Publications of Purple Mountain Observatory 19(2):117-120

Liu Z (2011) A new automated cycle slip detection and repair method for a single dual-frequency GPS receiver. Journal of Geodesy 85:171-183. doi: https://doi.org/10.1007/s00190-010-0426-y

Lomb NR (1976) Least-squares frequency analysis of unequally spaced data. Astrophysics and Space Science 39(2):447-462. doi: https://doi.org/10.1007/BF00648343

Lyard F, Lefevre F, Letellier T, Francis O (2006) Modelling the global ocean tides: modern insights from FES2004. Ocean Dynamics 56(5):394-415. doi:

https://doi.org/10.1007/s10236-006-0086-x

Martoccia D, Bernstein H, Chan Y, Frueholz R, Wu A (1998) GPS Satellite Timing Performance Using the Autonomous Navigation(Autonav). Paper presented at the ION 98,

Matas A (2011) Radio Navigation Satellite atellite Service and the ITU Radio Regulations. Paper presented at the United Nations International Meeting on the Applications of GNSS, Vienna, Austria, December 12-16

Meindl M, Beutler G, Thaller D, Dach R, Jäggi A (2013) Geocenter coordinates estimated from GNSS data as viewed by perturbation theory. Adv Space Res 51(7):1047-1064. doi: https://doi.org/10.1016/j.asr.2012.10.026

Meng W et al. (2013) Design and experiment of onboard laser time transfer in Chinese Beidou navigation satellites. Adv Space Res 51(6):951-958. doi: https://doi.org/10.1016/j.asr.2012.08.007

Menn MD (1986) Autonomous Navigation for GPS Via Crosslink Ranging. Paper presented at the IEEE Position Location and Navigation Symposium (PLANS), Las Vegas, Nevada, November 4-7

Menn MD, Bernstein H Ephemeris observability issues in the Global Positioning System (GPS) autonomous navigation (AUTONAV). In: IEEE Position Location and Navigation Symposium, 11-15 April 1994. pp 677-680. doi: https://doi.org/10.1109/PLANS.1994.303376

Michalak G, Glaser S, Neumayer KH, König R (2021) Precise orbit and Earth parameter determination supported by LEO satellites, inter-satellite links and synchronized clocks of a future GNSS. Adv Space Res. doi: https://doi.org/10.1016/j.asr.2021.03.008

Milani A, Gronchi GF (2010) Theory of Orbit Determination. Cambridge University Press, New York

Milani A, Nobili AM, Farinella P (1987) Non-gravitational perturbations and satellite geodesy. Adam Higer, Bristol, England

Montenbruck O, Gill E (2000) Satellite Orbits: Models, Methods, and Applications. Springer, Berlin, Heidelberg. doi: https://doi.org/10.1007/978-3-642-58351-3

Nerem RS, Chao BF, Au AY, Chan JC, Klosko SM, Pavlis NK, Williamson RG (1993) Temporal variations of the Earth's gravitational field from satellite laser ranging to Lageos. Geophysical Research Letters 20(7):595-598. doi: https://doi.org/10.1029/93GL00169

Niell AE (1996) Global mapping functions for the atmosphere delay at radio wavelengths. Journal of Geophysical Research: Solid Earth 101(B2):3227-3246. doi: https://doi.org/10.1029/95JB03048

Niell AE (2001) Preliminary evaluation of atmospheric mapping functions based on numerical weather models. Physics and Chemistry of the Earth, Part A: Solid Earth and Geodesy

26(6):475-480. doi: https://doi.org/10.1016/S1464-1895(01)00087-4

Noll CE, Ricklefs R, Horvath J, Mueller H, Schwatke C, Torrence M (2019) Information resources supporting scientific research for the international laser ranging service. Journal of Geodesy 93(11):2211-2225. doi: 10.1007/s00190-018-1207-2

Pan J et al. (2018) Time synchronization of new-generation BDS satellites using inter-satellite link measurements. Adv Space Res 61(1):145-153. doi: https://doi.org/10.1016/j.asr.2017.10.004

Pan J, Hu X, Zhou S, Tang C, Wang D, Yang Y, Dong W (2021) Full-ISL clock offset estimation and prediction algorithm for BDS3. GPS Solut 25(4):140. doi: https://doi.org/10.1007/s10291-021-01177-0

Parkinson BW, Jr. JJS, Axelrad P, Enge P (eds) (1996) Global Positioning System: Theory and Applications, Volume I. Progress in Astronautics and Aeronautics, vol 163. American Institute of Aeronautics and Astronautics, Inc.,

Pavlis NK, Holmes SA, Kenyon SC, Factor JK (2008) An Earth Gravitational Model to Degree 2160: EGM2008. Paper presented at the the 2008 General Assembly of the European Geosciences Union, Vienna, Austria, April 13-18

Pavlis NK, Holmes SA, Kenyon SC, Factor JK (2012) The development and evaluation of the Earth Gravitational Model 2008 (EGM2008). Journal of Geophysical Research: Solid Earth 117(B4). doi: https://doi.org/10.1029/2011JB008916

Pearlman MR, Degnan JJ, Bosworth JM (2002) The International Laser Ranging Service. Adv Space Res 30(2):135-143. doi: https://doi.org/10.1016/S0273-1177(02)00277-6

Petit G, Luzum B (2010) IERS Conventions 2010. Verlag des Bundesamts für Kartographie und Geodäsie, Frankfurt am Main

Price-Whelan AM et al. (2018) The Astropy Project: Building an Open-science Project and Status of the v2.0 Core Package. The Astronomical Journal 156(3):123. doi: https://doi.org/10.3847/1538-3881/aabc4f

Ray RD, Ponte RM (2003) Barometric tides from ECMWF operational analyses. Ann Geophys 21(8):1897-1910. doi: https://doi.org/10.5194/angeo-21-1897-2003

Rodríguez-Solano CJ (2009) Impact of Albedo Modelling on GPS Orbits. Technische Universität München

Rodríguez-Solano CJ, Hugentobler U, Steigenberger P Earth radiation pressure model for GNSS satellites. In: EGU 2011, 2011a.

Rodríguez-Solano CJ, Hugentobler U, Steigenberger P (2011b) Precise GNSS orbit determination using an adjustable box-wing model for solar radiation pressure. Paper presented at the IUGG 2011, Melbourne, Australia, 2011/07/01

Rodríguez-Solano CJ, Hugentobler U, Steigenberger P (2012) Adjustable box-wing model for

solar radiation pressure impacting GPS satellites. Adv Space Res 49(7):1113-1128. doi: https://doi.org/10.1016/j.asr.2012.01.016

Rothblatt MA (1987) Radiodetermination Satellite Services and Standards.

Ruan R, Feng L, Jia X (2014) Equipment Delay Estimation for GNSS Satellite Combined Orbit Determination with Satellite-ground Link and Inter-Satellite Link Observations. Acta Geodaetica et Cartographica Sinica 43(2):137-142

Ruan R, Wei Z, Jia X (2019) BDS-3 satellite orbit and clock determination with one-way inter-satellite pseudorange and monitoring station data. Acta Geodaetica et Cartographica Sinica 48(3):269-275. doi: https://doi.org/10.11947/j.AGCS.2019.20180483

Saastamoinen J (1972) Atmospheric Correction for the Troposphere and Stratosphere in Radio Ranging Satellites. In: The Use of Artificial Satellites for Geodesy, vol 15. Geophysical Monograph Series. pp 247-251. doi: https://doi.org/10.1029/GM015p0247

Sanz J, Miguel Juan J, Rovira-Garcia A, González-Casado G (2017) GPS differential code biases determination: methodology and analysis. GPS Solut 21(4):1549-1561. doi: https://doi.org/10.1007/s10291-017-0634-5

Scargle JD (1982) Studies in astronomical time series analysis. II. Statistical aspects of spectral analysis of unevenly spaced data. The Astrophysical Journal 263:835-853

Schmid R, Steigenberger P, Gendt G, Ge M, Rothacher M (2007) Generation of a consistent absolute phase-center correction model for GPS receiver and satellite antennas. Journal of Geodesy 81(12):781-798. doi: https://doi.org/10.1007/s00190-007-0148-y

Springer TA, Beutler G, Rothacher M (1999) Improving the orbit estimates of GPS satellites. Journal of Geodesy 73(3):147-157. doi: https://doi.org/10.1007/s001900050230

Standish EM (1998) JPL Planetary and Lunar Ephemerides, DE405/LE405.

Steigenberger P, Thoelert S, Montenbruck O (2018) GNSS satellite transmit power and its impact on orbit determination. Journal of Geodesy 92(6):609-624. doi: https://doi.org/10.1007/s00190-017-1082-2

Strang G, Borre K (1997) Linear Algebra, Geodesy, and GPS.

Tang C (2017) Generation of Precise Broadcast Orbits for Beidou Navigation Satellites with Multiple Tracking Measurements. University of Chinese Academy of Sciences

Tang C et al. (2016) Improvement of Orbit Determination Accuracy for Beidou Navigation Satellite System with Two-Way Satellite Time Frequency Transfer. Adv Space Res 58(7):1390-1400. doi: https://doi.org/10.1016/j.asr.2016.06.007

Tang C et al. (2018) Initial results of centralized autonomous orbit determination of the new-generation BDS satellites with inter-satellite link measurements. Journal of Geodesy 92(10):1155-1169. doi: https://doi.org/10.1007/s00190-018-1113-7

Tang C et al. (2017) Centralized autonomous orbit determination of Beidou navigation

satellites with inter-satellite link measurements: preliminary results. SCIENTIA SINICA Physica, Mechanica & Astronomica 47(2):1-11. doi: https://doi.org/10.1360/sspma2016-00355

Tang W, Deng C, Shi C, Liu J (2014) Triple-frequency carrier ambiguity resolution for Beidou navigation satellite system. GPS Solut 18(3):335-344. doi: https://doi.org/10.1007/s10291-013-0333-9

Tapley BD, Schutz BE, Born GH (2004) Statistical Orbit Determination. Elsevier Academic Press. doi: https://doi.org/10.1016/B978-0-12-683630-1.X5019-X

Teunissen PJG, Montenbruck O (eds) (2017) Handbook of Global Navigation Satellite Systems. Springer Handbooks. Springer. doi: https://doi.org/10.1007/978-3-319-42928-1

Teunissen PJG, Odolinski R, Odijk D (2014) Instantaneous BeiDou plus GPS RTK positioning with high cut-off elevation angles. Journal of Geodesy 88(4):335-350. doi: https://doi.org/10.1007/s00190-013-0686-4

VanderPlas JT (2018) Understanding the Lomb–Scargle Periodogram. The Astrophysical Journal Supplement Series 236(1):16. doi: https://doi.org/10.3847/1538-4365/aab766

Villiger A et al. (2020) GNSS scale determination using calibrated receiver and Galileo satellite antenna patterns. Journal of Geodesy 94(9):93. doi: https://doi.org/10.1007/s00190-020-01417-0

Walker JG (1984) Satellite constellations. Journal of the British Interplanetary Society 37:559-572

Wang C, Guo J, Zhao Q, Liu J (2018) Yaw attitude modeling for BeiDou I06 and BeiDou-3 satellites. GPS Solut 22(4):117. doi: https://doi.org/10.1007/s10291-018-0783-1

Wang C, Zhao Q, Guo J, Liu J, Chen G (2019) The contribution of intersatellite links to BDS-3 orbit determination: Model refinement and comparisons. Navigation 66(1):71-82. doi: https://doi.org/10.1002/navi.295

Wu A (1999) Estimate of the GPS Block IIR AutoNav Clock Behavior. Paper presented at the 1999 Joint Meeting of the European Frequency and International Frequency Control Symposium, Besancon, France, 13-16 April

Wu JT, Wu SC, Hajj GA, Bertiger WI, Lichten SM (1993) Effects of antenna orientation on GPS carrier phase. manuscripta geodaetica 18:91-98

Xia F, Ye S, Chen D, Jiang N (2019) Observation of BDS-2 IGSO/MEOs yaw-attitude behavior during eclipse seasons. GPS Solut 23(3):71. doi: https://doi.org/10.1007/s10291-019-0857-8

Xia R (2018) Research on the Theory and Method of BDS Autonomous Orbit Determination. Information Engineering University

Xie X, Geng T, Zhao Q, Cai H, Zhang F, Wang X, Meng Y (2019) Precise orbit determination

for BDS-3 satellites using satellite-ground and inter-satellite link observations. GPS Solut 23(2):40. doi: https://doi.org/10.1007/s10291-019-0823-5

Yan X, Liu C, Huang G, Zhang Q, Wang L, Qin Z, Xie S (2019) A Priori Solar Radiation Pressure Model for BeiDou-3 MEO Satellites. Remote Sensing 11(13). doi: https://doi.org/10.3390/rs11131605

Yang D, Yang J, Li G, Zhou Y, Tang C (2017a) Globalization highlight: orbit determination using BeiDou inter-satellite ranging measurements. GPS Solut 21(3):1395-1404. doi: https://doi.org/10.1007/s10291-017-0626-5

Yang D, Yang J, Xu P (2017b) Timeslot scheduling of inter-satellite links based on a system of a narrow beam with time division. GPS Solut 21(3):999-1011. doi: https://doi.org/10.1007/s10291-016-0587-0

Yang Y (2019) Research on the Method and Theory of BDS-3 PNT Service SIS Accuracy Improvement Using Inter-Satellite Link. Information Engineering University

Yang Y, Tang J, Montenbruck O (2017c) Chinese Navigation Satellite Systems. In: Teunissen PJG, Montenbruck O (eds) Handbook of Global Navigation Satellite Systems

Yang Y et al. (2021) BeiDou-3 broadcast clock estimation by integration of observations of regional tracking stations and inter-satellite links. GPS Solut 25(2):57. doi: https://doi.org/10.1007/s10291-020-01067-x

Zhang Y (2005) Study on Autonomous Navigation of Constellation using Inter-Satellite Measurement. National University of Defense Technology

Zhang Z et al. (2014) Design and performances of laser retro-reflector arrays for Beidou navigation satellites and SLR observations. Adv Space Res 54:811-817

Zhou S et al. (2012) Positioning accuracy assessment for the 4GEO/5IGSO/2MEO constellation of COMPASS. Science China Physics, Mechanics and Astronomy 55(12):2290-2299. doi: https://doi.org/10.1007/s11433-012-4942-z

Zhou S et al. (2016) Applications of two-way satellite time and frequency transfer in the BeiDou navigation satellite system. Science China Physics, Mechanics & Astronomy 59(10):109511. doi: https://doi.org/10.1007/s11433-016-0185-6

Zhou S et al. Accuracy Analyses of Precise Orbit Determination and Timing for COMPASS/Beidou-2 4GEO/5IGSO/4MEO Constellation. In: Sun J, Jiao W, Wu H, Shi C (eds) China Satellite Navigation Conference (CSNC), Wuhan, China, 2013. Lecture Notes in Electrical Engineering. Springer, Berlin, Heidelberg. doi: https://doi.org/10.1007/978-3-642-37407-4_8

Zhou Y, Wang Y, Huang W, Yang J, Sun L (2018) In-orbit performance assessment of BeiDou intersatellite link ranging. GPS Solut 22(4):119. doi: https://doi.org/10.1007/s10291-018-0784-0

Zhu SY, Massmann FH, Yu Y, Reigber C (2003) Satellite antenna phase center offsets and scale errors in GPS solutions. Journal of Geodesy 76(11):668-672. doi: https://doi.org/10.1007/s00190-002-0294-1

Ziebart M (2001) High Precision Analytical Solar Radiation Pressure Modelling for GNSS Spacecraft. University of East London

Ziebart M, Sibthorpe A, Cross P, Bar-Sever Y, Haines B Cracking the GPS - SLR Orbit Anomaly. In: the 20th International Technical Meeting of the Satellite Division of The Institute of Navigation, Fort Worth, TX, September 25-28 2007. pp 2033-2038

Appendix

A Status of the Space Segment of BDS

This section is dedicated to providing some information pertinent to the space segment of BDS, collected by the time of writing.

Table A-1 The 16 operational BDS-2 satellites in space as of December 2021

Sat. Type	SVN	ILRS Name	PRN[3]	Nominal clock[1]
BDS-2G	C003	compassg1	C01	RAFS[2]
	C016		C02	RAFS
	C018		C03	RAFS
	C006		C04	RAFS
	C011		C05	RAFS
	C020		C18	RAFS
BDS-2I	C005		C06	RAFS
	C007		C07	RAFS
	C008	compassi3	C08	RAFS
	C009		C09	RAFS
	C010	compassi5	C10	RAFS
	C017	compassi6b	C13	RAFS
	C019		C16	RAFS
BDS-2M	C012	compassm3	C11	RAFS
	C013		C12	RAFS
	C015		C14	RAFS

In Table A-2, SVNs of BDS-3 MEO satellites are colored according to their orbiting planes, i.e., plane A in red, plane B in green, and plane C in blue.

Table A-2 Current operational BDS-3 satellites in space

Sat. Type	SVN	PRN[3]	Nominal Clock	Mass [kg]
BDS-3G	C217	C59	PHM	2968.0

	C229	C60	PHM	2968.0
	C230	C61	PHM	2968.0
BDS-3I	C220	C38	PHM	2952.0
	C221	C39	PHM	2949.0
	C224	C40	PHM	2870.0
BDS-3M-CAST	C201	C19	RAFS	943.0
	C202	C20	RAFS	942.0
	C206	C21	RAFS	942.0
	C205	C22	RAFS	941.0
	C209	C23	RAFS	945.0
	C210	C24	RAFS	946.0
	C213	C32	RAFS	1007.0
	C214	C33	RAFS	1007.0
	C218	C36	RAFS	1061.0
	C219	C37	RAFS	1061.0
	C227	C41	PHM	1059.0
	C228	C42	PHM	1059.0
	C223	C45	RAFS	1058.0
	C222	C46	RAFS	1059.0
BDS-3M-SECM-A	C212	C25	PHM	1043.3
	C211	C26	PHM	1041.8
	C203	C27	PHM	1018.0
	C204	C28	PHM	1014.4
	C207	C29	PHM	1010.4
	C208	C30	PHM	1008.6
	C216	C34	PHM[4]	1046.6
	C215	C35	PHM[4]	1045.0
BDS-3M-SECM-B	C226	C43	PHM	1075.4
	C225	C44	PHM	1078.8

LRA offsets of CAST satellites given in Table 7 of (Yan et al. 2019) are close to that of CAST manufactured BDS-3 experimental satellites listed in Table 7 of (Li et al. 2019). And LRA offsets of SECM satellites in Table 7 of (Yan et al. 2019) coincide with those given by (Lin et al. 2018)

---

[4] Inconsistent between http://www.csno-tarc.cn/en/system/constellation and Table 1 from (Pan et al. 2021), former one is given here.

Table A-3 Offsets of Laser Retroflector Arrays (LRA) of BDS-3 MEOs

SVN	ILRS Name	LRA offset [m]			Note
		X	**Y**	**Z**	
C202	beidou3m2	0.5947	-0.0846	1.2644	CSNO
		0.6120	-0.0720	1.2230	(Yan et al. 2019)
C206	beidou3m3	0.5986	-0.0866	1.2650	CSNO
		0.6120	-0.0720	1.2230	(Yan et al. 2019)
C207	beidou3m9	0.6095	0.4260	0.6142	CSNO
		0.6646	0.4249	0.6427	(Yan et al. 2019)
C208	beidou3m10	0.6097	0.4273	0.6153	CSNO
		0.6646	0.4249	0.6427	(Yan et al. 2019)

Table A-4 L-band transmit power of BDS-3 MEOs extracted from the IGS MGEX metadata

Sat. Type	L-band transmit power [W]
BDS-3M-CAST	310
BDS-3M-SECM-A	280
BDS-3M-SECM-B	280

Table A-5 Frequency bands of BDS

Frequency Band	Frequency (MHz)
B1	1561.098
	1575.420
B2	1176.450
	1191.795
	1207.140
B3	1268.520

Table A-6 Open RNSS signals of current BDS-2/BDS-3

Frequency (MHz)[5]	Signal		Modulation	Symbol Rate [sps[6]]	Transmitted by
	Name	Component			

---

[5] Central frequency and bandwidth of signals

[6] Symbols Per Second

1561.098 (4.092)[7]	B1[8]	I	BPSK		BDS-2 MEO/IGSO/GEO BDS-3 MEO/IGSO/GEO
1575.420 (32.736)	B1C[9]	data pilot	BOC(1,1) QMBOC(6,1,4/33)	100 0	BDS-3 MEO/IGSO
1176.450 (20.46)	B2a[10]	data pilot	BPSK(10) BPSK(10)	200 0	BDS-3 MEO/IGSO
1207.140 (20.46)	B2b[11] B2[12]	I I	BPSK(10) QPSK	1000	BDS-3 MEO/IGSO BDS-2 MEO/IGSO/GEO
1268.520 (20.46)[7]	B3[13]	I	BPSK		BDS-2 MEO/IGSO/GEO BDS-3 MEO/IGSO/GEO

---

[7] See (CSNO 2021)

[8] See (CSNO 2019), the modulation of B1I signal is changed from QPSK in Version 2.1 (CSNO 2016), Version 2.0 (CSNO 2013b), and (CSNO 2013a)

[9] See (CSNO 2017a)

[10] See (CSNO 2017b)

[11] See (CSNO 2020)

[12] See (CSNO 2016)

[13] See (CSNO 2018b)

B Empirical SRP Models

Followings are the empirical SRP models tested for BDS-3 in this study, where the angular argument Δu is the orbital angle of the satellite concerning the Noon point.

The ECOM1 model

$$\boldsymbol{a}_{\mathrm{DYB}}(\Delta u) = \begin{cases} D_0 \\ Y_0 \\ B_0 + B_{1,c}\cos(\Delta u) + B_{1,s}\sin(\Delta u) \end{cases} \tag{B.1}$$

The 7-parameters version of the ECOM2 model, i.e., E2P7

$$\boldsymbol{a}_{\mathrm{DYB}}(\Delta u) = \begin{cases} D_0 + D_{2,c}\cos(2\Delta u) + D_{2,s}\sin(2\Delta u) \\ Y_0 \\ B_0 + B_{1,c}\cos(\Delta u) + B_{1,s}\sin(\Delta u) \end{cases} \tag{B.2}$$

The 9-parameters version of the ECOM2 model, i.e., E2P9

$$\boldsymbol{a}_{\mathrm{DYB}}(\Delta u) =$$
$$\begin{cases} D_0 + D_{2,c}\cos(2\Delta u) + D_{2,s}\sin(2\Delta u) + D_{4,c}\cos(4\Delta u) + D_{4,s}\sin(4\Delta u) \\ Y_0 \\ B_0 + B_{1,c}\cos(\Delta u) + B_{1,s}\sin(\Delta u) \end{cases} \tag{B.3}$$

C Box-Wing Model Parameters of BDS-3 Satellites

Here satellite parameters based on box-wing models released by CSNO and used in this study are given. As only the absorptivities were released by CSNO, the specularities and diffusivities, as shown in dark orange in the following tables, are guess values. On average, CAST satellites have a slightly higher area-to-mass ratio than SECM satellites.

Table C-1 Box-Wing model parameters for satellites C19, C20, C21, C22, C23, C24, C32, C33, C36, and C37 (BDS-3M-CAST) released by CSNO

Panel	Area (m^2)	α	ρ	δ
+X	2.860	0.350	0.000	0.650
-X	1.750	0.920	0.000	0.080
-X	1.110	0.135	0.000	0.865
+Y	3.630	0.135	0.865	0.000
-Y	3.630	0.135	0.865	0.000
+Z	2.180	0.920	0.000	0.080
-Z	2.180	0.350	0.000	0.650
SP	20.440	0.920	0.080	0.000

Table C-2 Box-Wing model parameters for satellites C25, C26, C27, C28, C29, C30, C34, and C35 (BDS-3M-SECM-A) released by CSNO

Panel	Area (m^2)	α	ρ	δ
+X	1.250	0.200	0.000	0.800
-X	1.250	0.200	0.000	0.800
+Y	3.130	0.200	0.800	0.000
-Y	3.130	0.200	0.800	0.000
+Z	2.590	0.200	0.000	0.800
-Z	2.590	0.200	0.000	0.800
SP	10.800	0.920	0.080	0.000

Table C-3 Box-Wing model parameters for satellites C43 and C44 (BDS-3M-SECM-B) released by CSNO

Panel	Area (m^2)	α	ρ	δ
+X	1.240	0.200	0.000	0.800

-X	1.240	0.200	0.000	0.800
+Y	3.780	0.200	0.800	0.000
-Y	3.780	0.200	0.800	0.000
+Z	2.570	0.200	0.000	0.800
-Z	2.570	0.200	0.000	0.800
SP	10.800	0.920	0.080	0.000

D Ground Tracking Networks of BDS
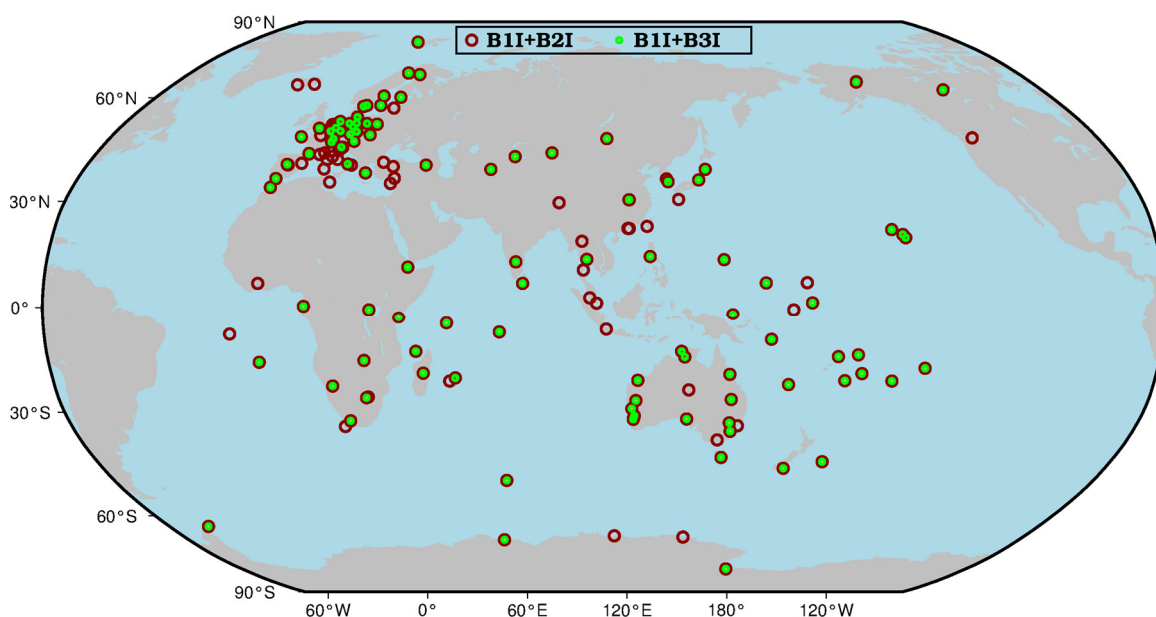
Figure D-1 IGS MGEX stations that can track BDS-2 on B1I+B2I or B1I+B3I during DOY 335~365, 2019

Table D-1 Receiver antenna+radome combinations that show up with Phase Center Corrections for BDS signals in the antenna file igsR3_2077.atx used by the IGS 3rd repro

Antenna+Radome		Frequencies	Calibration
ASH700936D_M	SCIS	C01/C05/C07/C08/C02/C06	a[1]
ASH701945B_M	NONE	C01/C05	b[2]
ASH701945B_M	SCIS	C01/C05/C07/C08/C02/C06	c[3]
ASH701945C_M	NONE	C01/C05	a
ASH701945E_M	NONE	C01/C05	a
ASH701945E_M	SCIS	C01/C05/C07/C08/C02/C06	a
ASH701945E_M	SCIT	C01/C05/C07/C08/C02/C06	a
CHCC220GR2	CHCD	C01/C05	a
JAV_GRANT-G3T	NONE	C01/C05/C07/C08/C02/C06	a
JAVRINGANT_DM	NONE	C01/C05/C07/C08/C02/C06	a
JAVRINGANT_DM	SCIS	C01/C05/C07/C02/C06	a
JAVRINGANT_G5T	NONE	C01/C05	a
JAVRINGANT_G5T	JAVC	C01/C05/C07/C08/C02/C06	a
LEIAR10	NONE	C01/C05	a

---

[1] ROBOT by Geo++
[2] Copied from ASH701945C_M   NONE
[3] Copied from ASH701945E_M   SCIS

LEIAR20	NONE	C01/C05/C07/C08/C02/C06	a
LEIAR20	LEIM	C01/C05/C07/C08/C02/C06	a
LEIAR25.R3	NONE	C01/C05/C07/C02/C06	a
LEIAR25.R3	LEIT	C01/C05/C07/C08/C02/C06	a
LEIAR25.R4	NONE	C01/C05/C07/C08/C02/C06	a
LEIAR25.R4	LEIT	C01/C05/C07/C08/C02/C06	a
LEIAT504	NONE	C01/C05	a
LEIAT504GG	NONE	C01/C05/C07/C08/C02/C06	a
RNG80971.00	NONE	C01/C05/C07/C08/C02/C06	d[4]
SEPCHOKE_B3E6	NONE	C01/C05	a
SEPCHOKE_B3E6	SPKE	C01/C05/C07/C08/C02/C06	a
TPSCR.G3	NONE	C01/C05/C07/C08/C02/C06	a
TPSCR.G3	SCIS	C01/C05/C07/C08/C02/C06	a
TPSCR.G3	TPSH	C01/C05/C07/C02	a
TPSCR.G5	TPSH	C01/C05/C07/C08/C02/C06	a
TPSCR.G5C	NONE	C01/C05	a
TRM115000.00	NONE	C01/C05/C07/C08/C02/C06	a
TRM29659.00	NONE	C01/C05	a
TRM55971.00	TZGD	C01/C05/C07/C02	a
TRM57971.00	NONE	C01/C05/C07/C08/C02/C06	a
TRM57971.00	TZGD	C01/C05	a
TRM59800.00	NONE	C01/C05/C07/C08/C02/C06	a
TRM59800.00	SCIS	C01/C05/C07/C08/C02/C06	a
TRM59800.80	NONE	C01/C05/C07/C08/C02/C06	e[5]
TRM59800.80	SCIS	C01/C05/C07/C08/C02/C06	f[6]
TRM59900.00	SCIS	C01/C05	a

Table D-2 Number of stations equipped with different Antenna+Radome combinations tracking BDS-3 with B1I+B3I signals and that having B1/B3 Phase Center Corrections in the antenna file igsR3_2077.atx on DOY 335, 2019

Antenna+Radome		Station Number	Whether having B1/B3 PCC in igsR3_2077.atx
AOAD/M_B	OSOD	1	
AOAD/M_T	AUST	1	
AOAD/M_T	DUTD	1	
AOAD/M_T	JPLA	2	
AOAD/M_T	NONE	5	

[4] Copied from TRM57971.00   NONE
[5] Copied from TRM59800.00   NONE
[6] Copied from TRM59800.00   SCIS

AOAD/M_T	OSOD	2	
ASH701945B_M	SCIS	1	Y
ASH701945C_M	NONE	3	
ASH701945C_M	SCIS	1	
ASH701945C_M	SCIT	1	
ASH701945E_M	NONE	2	
ASH701945E_M	SCIT	1	Y
ASH701945E_M	SNOW	2	
ASH701945G_M	NONE	2	
ASH701945G_M	SCIT	1	
JAVRINGANT_DM	NONE	8	Y
JAVRINGANT_DM	SCIS	7	Y
JAVRINGANT_G5T	NONE	11	
JNSCR_C146-22-1	OSOD	2	
LEIAR20	NONE	1	Y
LEIAR25	NONE	1	
LEIAR25.R3	LEIT	8	Y
LEIAR25.R3	NONE	3	Y
LEIAR25.R4	LEIT	8	Y
LEIAR25.R4	NONE	7	Y
LEIAT504	NONE	1	
SEPCHOKE_B3E6	NONE	7	
SEPCHOKE_B3E6	SPKE	4	Y
TPSCR.G3	NONE	2	Y
TPSCR.G3	SCIS	3	Y
TPSCR.G3	TPSH	1	
TPSCR.G5	TPSH	2	Y
TPSCR.G5C	NONE	1	
TRM115000.00	NONE	8	Y
TRM29659.00	SCIS	1	
TRM57971.00	NONE	4	Y
TRM57971.00	TZGD	1	
TRM59800.00	NONE	26	Y
TRM59800.00	SCIS	8	Y
Total		151	101

Table D-3 Receiver antenna+radome combinations that show up with Phase Center Corrections for BDS signals in the antenna file igs14_2148.atx used in this study

Antenna+Radome		Frequency	Calibration
CNTAT600	CNTS	C01/C02/C06/C07	a[1]
FOIA90	NONE	C01/C02/C06/C07	a
HGGCYH8372	HGGS	C01/C02/C06/C07	a
LEIAS11	NONE	C01/C02/C06/C07	g[7]
LEICGA100	NONE	C01/C02/C06/C07	a
LEIFLX100	NONE	C02/C07	a
SEPPOLANT_X_MF	NONE	C01/C02/C06/C07	a
TWIVC6050	NONE	C01/C02/C06/C07	a
TWIVC6050	SCIS	C01/C02/C06/C07	a
TWIVC6050	SCIT	C01/C02/C06/C07	a
TWIVSP6037L	NONE	C01/C02/C06/C07	a

Table D-4 Comparison of ionosphere-free linear combination PCOs of GPS L1+L2 with BDS B1+B3 based on igsR3_2077.atx file [mm]

Antenna+Radome		GPS L1+L2			BDS B1+B3			diff		
		N	E	U	N	E	U	N	E	U
ASH700936D_M	SCIS	0.9	0.5	42.6	1.0	0.0	44.7	0.1	-0.5	2.2
ASH701945B_M	SCIS	2.7	-1.6	42.0	3.7	-2.2	40.3	0.9	-0.6	-1.7
ASH701945E_M	SCIS	2.7	-1.6	42.0	3.7	-2.2	40.3	0.9	-0.6	-1.7
ASH701945E_M	SCIT	1.5	0.1	35.7	2.0	-1.7	41.7	0.4	-1.9	6.0
JAV_GRANT-G3T	NONE	4.4	7.0	54.2	4.1	-1.4	87.8	-0.3	-8.3	33.6
JAVRINGANT_DM	NONE	0.2	2.9	46.2	0.2	2.9	49.8	0.0	0.0	3.6
JAVRINGANT_DM	SCIS	0.5	3.6	38.5	1.0	4.4	47.5	0.5	0.8	9.0
JAVRINGANT_G5T	JAVC	-7.3	10.3	39.1	-17.8	16.1	62.0	-10.5	5.8	22.9
LEIAR20	NONE	1.0	1.2	107.5	3.5	1.7	126.2	2.5	0.4	18.7
LEIAR20	LEIM	1.1	0.7	111.5	1.4	0.5	132.1	0.3	-0.2	20.6
LEIAR25.R3	NONE	2.1	1.3	163.5	2.5	1.7	170.5	0.3	0.4	7.0
LEIAR25.R3	LEIT	0.5	2.3	165.9	-0.1	2.4	172.8	-0.7	0.0	6.9
LEIAR25.R4	NONE	0.2	2.3	165.0	-0.1	2.5	181.0	-0.2	0.2	16.0
LEIAR25.R4	LEIT	1.6	3.1	165.1	2.1	3.5	177.9	0.6	0.5	12.7
LEIAT504GG	NONE	2.0	3.2	44.8	1.7	3.7	53.7	-0.4	0.5	8.9
RNG80971.00	NONE	2.1	-0.9	73.5	3.9	-2.5	82.6	1.7	-1.6	9.2
SEPCHOKE_B3E6	SPKE	2.1	-1.0	105.6	0.1	-0.3	107.6	-2.0	0.7	2.0
TPSCR.G3	NONE	-1.0	2.2	37.8	-0.7	2.1	29.1	0.3	-0.1	-8.7
TPSCR.G3	SCIS	-1.0	2.4	32.3	-0.3	2.6	28.1	0.7	0.2	-4.2
TPSCR.G5	TPSH	-0.1	-0.1	50.3	0.0	0.1	51.8	0.2	0.2	1.4
TRM115000.00	NONE	-0.1	0.1	78.4	-1.2	-0.5	88.3	-1.1	-0.6	9.9

---

[7] Copied from LEICGA100 NONE

TRM57971.00	NONE	2.1	-0.9	73.5	3.9	-2.5	82.6	1.7	-1.6	9.2
TRM59800.00	NONE	2.0	3.4	45.4	2.2	3.0	50.9	0.2	-0.4	5.5
TRM59800.00	SCIS	1.3	0.6	39.5	2.7	-2.4	47.4	1.5	-3.0	7.9
TRM59800.80	NONE	2.0	3.4	45.4	2.2	3.0	50.9	0.2	-0.4	5.5
TRM59800.80	SCIS	1.3	0.6	39.5	2.7	-2.4	47.4	1.5	-3.0	7.9